

National Academy of Sciences of Ukraine  
Ministry of Education and Science of Ukraine  
Institute for Scintillation Materials NASU  
O.Ya. Usikov Institute for Radiophysics and Electronics of the NASU  
Kharkiv National University of Radio Electronics  
V. N. Karazin Kharkiv National University  
Odesa I.I. Mechnikov National University  
National Technical University "Kharkiv Polytechnic Institute"  
Ukrainian Physical Society

**Collection of scientific works**

**XI INTERNATIONAL SCIENTIFIC CONFERENCE**

# **Functional Basis of Nanoelectronics**

November 24-26  
Kharkiv – Odesa  
2020

XI International Scientific Conference “Functional Basis of Nanoelectronics” Collection of scientific works. – XI. : 2020. – 130 p.

Scientific works of the XI International Scientific Conference “Functional Basis of Nanoelectronics” are included in the collection

## **Program Committee of the Conference**

### ***Program Committee Co-Chairs:***

- Ya.I. Lepikh** Prof., Dr., Odesa I.I.Mechnikov National University, Odesa, Ukraine
- M.I. Slipchenko** Prof., Dr., Leading researcher, ISMA NASU, Kharkiv, Ukraine
- S.I. Tarapov** Correspondent member of NASU, Prof., Dr., O.Ya. Usikov Institute of Radio Physics and Electronics NASU, Kharkiv, Ukraine

### ***Program Committee Members:***

- N.A. Azarenkov** Academician of the NASU, Prof., Dr., Vice-Rector of the V.N. Karazin Kharkiv National University, Kharkiv, Ukraine
- A.E. Belyaev** Academician of the NASU, Professor, Director of the V.E. Lashkaryov Institute of Semiconductor Physics NASU, Kyiv, Ukraine
- I.N. Bondarenko** Professor, Head of Dep. in Kharkiv National University of Radio Electronics, Kharkiv, Ukraine
- B.N. Chichkov** Prof., Dr., Gottfried Wilhelm Leibniz Universität / Institut für Quantenoptik, Hannover, Germany
- V. Dyakonov** Prof., Dr., Head of Experimental Physics VI, Julius-Maximilians Universität Würzburg, Germany
- Fukai Shan** Prof., Vice Dean of College of Microtechnology and Nanotechnology, China
- Yu.E. Gordienko** Professor of Kharkiv National University of Radio Electronics, Kharkiv, Ukraine
- Z.Yu. Gotra** Professor, Head of dep. Lviv Polytechnic National University, Lviv, Ukraine
- B.V. Grynyov** Prof., Academician of NASU, Director of ISMA NASU, Kharkiv, Ukraine
- V.O. Katrich** Prof., Dr., Vice-Rector of the V.N. Karazin Kharkiv National University, Kharkiv, Ukraine
- V.P. Kladko** Correspondent member of the NASU, Prof., Deputy. Director of the V.E. Lashkarev Institute of Semiconductor Physics NASU, Kyiv, Ukraine
- V.P. Kostilyov** Dr., Head. of the lab. of V.E. Lashkaryov Institute of Semiconductor Physics NASU, Kyiv, Ukraine

- V.A. Kochelap** Correspondent member of the NASU, prof., Head of the Department of V.E. Lashkarev Institute of Semiconductor Physics NASU, Kyiv, Ukraine
- O.A. Kordyuk** Correspondent member NASU, Doctor, Prof., Director of Kyiv Academic University, Kyiv, Ukraine
- A.P. Kuznetsov** Professor, Vice-Rector of the Belarusian State University of Informatics and Radioelectronics, Minsk, Belarus
- A.L. Kukla** Dr., Head of the Department of the V.E. Lashkarev Institute of Semiconductor Physics. NASU, Kyiv, Ukraine
- A. Medvids** Dr., Prof., Riga Technical University, Latvia
- A.M. Negriyko** Correspondent member of NASU, Deputy Director of the Institute of Physics of NASU, Kyiv, Ukraine
- S.L. Prosvirnin** Professor of Radio Astronomy Institute of NASU, Kharkiv, Ukraine
- I. Yu. Protsenko** Prof., Dr., Head of dep. of Electronics, General and Applied Physics of Sumy State University, Sumy, Ukraine
- F.F. Sizov** Correspondent member of NASU, Prof., V.E. Lashkaryov Institute of Semiconductor Physics NASU, Kyiv, Ukraine
- V.A. Skryshevsky** Prof., Head. of dep. of the Institute of High Technologies, Taras Shevchenko National University, Kyiv, Ukraine
- O.V. Sorokin** Dr. Sci., Deputy Director of Science, Institute for Scintillation Materials National Academy of Sciences of Ukraine, Kharkiv, Ukraine
- E. Sheregij** Dr., Prof., Rzeszow University, Poland
- Yu.I. Yakimenko** Academician of NASU, Professor, Vice-President of NTUU "KPI", Kyiv, Ukraine
- V.A. Yampolsky** Correspondent member of NASU, Prof of O.Ya. Usikov Institute of Radio Physics and Electronics NASU, Kharkiv, Ukraine
- I.V. Zavislyak** Professor of Taras Shevchenko National University, Kyiv, Ukraine

**NANOELECTRONIC SENSORS AND  
INFORMATION SYSTEMS.**

**NANOELECTRONIC SENSORS FOR  
BIO-ENGINEERING**

# Recent research advances of usage of laser-fabricated nanomaterials in electroanalytical techniques

Chichkov Boris <sup>@</sup>, Muzyka Kateryna <sup>+</sup>, Slipchenko Mykola <sup>\*</sup>, Slipchenko Olena <sup>§</sup>, Vasylovskiy Volodymyr <sup>\*\*</sup>,  
Zholudov Yuriy <sup>+</sup>

<sup>@</sup> Leibniz University of Hannover, Institute of Quantum Optics

Welfengarten 1, 30167, Hannover, Germany, +49 511 2771666, chichkov@iqo.uni-hannover.de

<sup>+</sup> Kharkiv National University of RadioElectronics, Department of Biomedical Engineering  
Nauki Ave. 14, 61166, Kharkiv, Ukraine, +38057-7020369, myzika\_katya@ukr.net, yurets.zh@gmail.com,

<sup>\*</sup> Institute for Scintillation Materials NAS of Ukraine  
Nauky ave. 60, 61072, Kharkiv, Ukraine, naukovets.big@gmail.com, vasylovskiy.volodymyr@gmail.com,

<sup>§</sup> National Technical University "Kharkiv Polytechnic Institute"  
Kyrpychova str. 2, 61002, Kharkiv, Ukraine, Olena.Slipchenko@kphi.edu.ua

**Abstract** - Electroanalytical techniques have a broad application because of their advantages such as versatility and high sensitivity. Electrodes for such measurements can be modified by nanoparticles which enhance the performance of the analytical method. Laser synthesis is the best candidate to fabricate suitable nanoparticles and has numerous advantages. This Review presents a description of laser synthesis techniques of nanomaterials as well as achievements and prospects of usage of obtained nanoparticles in electroanalytical applications.

**Keywords** - laser synthesis, ablation, dewetting nanoparticles, electrode nanostructuration, electrochemical, electrochemiluminescence.

## I. INTRODUCTION

Electrochemistry is the branch of chemistry concerned with the interrelation of electrical and chemical effects. A large part of this field deals with the study of chemical changes caused by the passage of an electric current and the production of electrical or optical energy by chemical reactions. Namely, the measurement of electrical quantities, such as current, potential, or charge, as well as optical quantities and their relationship to chemical parameters [1,2]. A variety of modern research areas and industrial techniques are part of electrochemical science – energy storage and conversion, corrosion studies and protection, chemical synthesis and surface modification, and electroanalysis [2].

Electroanalytical techniques play a crucial role in modern analytical science due to their inherent advantages like simplicity, versatility, efficiency, sensitivity, rapidness, etc. To conduct electroanalytical measurements at least 2 electrodes and a sample solution are required. One of the electrodes, termed the reference electrode, is independent of the properties of the solution. The second one responds to the target analyte(s) and is thus termed the working electrode [1].

Modification of the working electrode surface is a way of creating electrochemical sensors – elements with new and interesting properties. Modified carbon and metal-based

electrodes are widely applied as a working electrode for electrochemical detection of the analytes. The material for electrode modification is applied to the electrode surface in the form of electroactive thin films, monolayers, or thick coatings. Modification of the electrode surface can enhance the performance of an electrode as a sensor device suitable for biological and environmental samples in many ways [3].

Nanoparticles (NPs) of different compositions and dimensions have become used as versatile and sensitive tracers [4]. The creation of NPs for enhanced sensitivity in electroanalytical applications greatly benefits from their nanoscale size, where their properties are strongly influenced due to high surface area to volume ratio. Also, NPs are one of the most exciting areas in modern electroanalytical chemistry because they offer excellent prospects for creating highly sensitive and selective electrodes (assays). Thus, the usage of NPs reduces the use of reagents and the required electroanalysis time. Many kinds of NPs, including metal, metal-oxide, semiconductor, and even composite-metal NPs, have been used for constructing electrochemical sensors [5].

A wide variety of methods is available for nanoparticle synthesis, affording a broad spectrum of chemical and physical properties. Laser synthesis is one of the best candidates, as compared to other methods. This method allows the preparation of stable colloids in pure solvents without using either capping and stabilizing agents or reductants [6].

This work is dedicated to reviewing the recent advances in the use of NPs that are generated by laser techniques for the development of new and efficient electrochemical methods for the analysis of liquids.

## II. LASER FABRICATION OF NANOMATERIALS

The synthesis of nanoparticles has attracted considerable interest due to their potential applications in a variety of areas including medicine, energy, and environmental remediation [9]. Numerous methods and techniques were presented to

synthesize nanoparticles including chemical, physical and biological techniques. However, the use of laser techniques for the synthesis of nanoparticles is of great interest due to a large number of advantages over other methods.

#### A. Pulsed laser ablation

Amongst the available techniques for synthesizing NPs, the pulsed laser ablation (PLA) route, either in liquid or solid phase, possesses several advantages over others [11]. PLA synthesis of nanoparticles is an interest in nanotechnology since pulsed laser synthesis is the fastest and green method to fabricate nanomaterials directly from bulk targets [8,7].

Laser ablation is a method that utilizes laser as an energy source for ablating solid target materials. During this process, extremely high energy pulses are concentrated at a specific point for a few nanoseconds on a solid surface to evaporate light-absorbing material [10,11]. Fig. 1 is a schematic of the nanoparticle formation by PLA. The laser systems for nanoparticle production consist of a pulsed laser, beam-handling optics, a target, and a substrate [7].

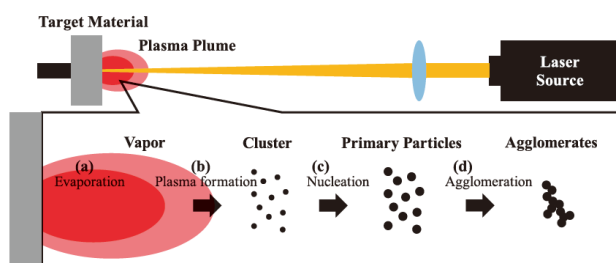


Fig. 1. Schematic of particle generation via laser ablation process [10]

Targets required for the synthesis are less expensive than the metal salts and other chemicals required in the chemical routes, which makes this method cost-effective comparing to other methods [11]. Laser ablation can generate high-purity nanoparticles because the purity of the particles is basically determined by the purity of the target and ambient media (gas or liquid) without contamination by the precursor chemicals and other reagents [10]. PLA demonstrates excellent suitability for the synthesis of a wide range of nanoparticles (semiconductor quantum dots (QDs), carbon nanotubes, nanowires, core-shell nanoparticles, etc.) in terms of the yield and size homogeneity of the produced nanomaterials [9,10]. Such nanomaterials can be effectively used for detection applications [13-19].

#### B. Laser dewetting method

The construction of metallic NPs of controlled size, spacing, and ordered distribution is essential for the modification of electrodes for electroanalytical purposes. [25] Self-assembly via laser dewetting of the heated thin film is a cost-effective and environmentally-friendly approach for nanostructures fabrication. Moreover, this method can be applied for dielectric, semiconductor, and multilayer substrates, allowing them to precisely control their microscopic properties [27]. Hence, dewetting can be an effective method to form nanoparticle arrays for electroanalytical applications [20-23].

Dewetting is a spontaneous phenomenon that refers to the decomposition of a film into droplets or other structures on an inert substrate. Its driving force is the minimization of the total energy of the free surfaces of the film and substrate, and of the film-substrate interface [12]. The dewetting is known to occur either through heterogeneous nucleation, which emanates from surface particles and impurities that grow into circular patches, or spinodal dewetting [24].

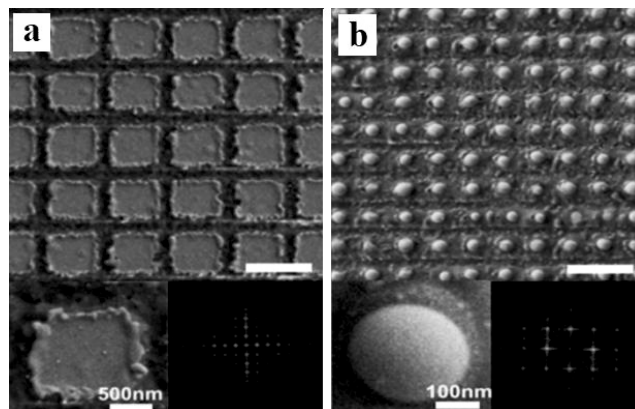


Fig. 2. Metal nanoparticles fabricated by laser dewetting a) SEM image before laser dewetting b) SEM image of an Au nanoparticle array made of a 30 nm film on a SiO<sub>2</sub> substrate at a fluence of 40 mJ/cm<sup>2</sup> [26]

### III. USAGE OF LASER-FABRICATED NANOMATERIALS IN ELECTROANALYTICAL METHODS

Modified electrodes are often used as a working electrode for electrochemical detection of a number of biomaterials, toxins, and other substances. Recently published articles on the usage of laser-fabricated nanoparticles in the electrochemical methods of the analysis show their versatility and multifunctionality (Table 1) [13-15, 18-21].

The most common electrodes for electrochemical detection are Indium tin oxide (ITO), carbon (glassy carbon, carbon fiber), graphene (graphene paper, graphene substrate), and silicon. ITO, graphene, and carbon electrodes are among the most widely used for electrochemical sensing of liquids. It is due to their high electrical conductivity, high chemical resistance, stable physical and electrochemical properties, a wide range of available potentials in the solvents of interest, and the possibility of a variety of chemical functionalization [21, 23, 28].

Recently, a number of works have demonstrated that hybrid structures that include nanoparticles can offer unique physicochemical properties that are desirable for sensing applications by enhancing achievable sensitivity.

The analyzed articles show that the most usable laser-fabricated nanomaterials for electrochemical analysis are Au NPs and Ni NPs that have drawn much attention in electrochemical fields because of their favorable properties which include: large surface-to-volume ratio, unique optical and electronic properties, high chemical stability, biocompatibility, and ability to facilitate transfer between biomolecules and electrodes [29, 30]. At present time, such NPs have the broadest range of detectable substances.

TABLE I. EXISTING ELECTROCHEMICAL SENSORS BASED ON LASER-FABRICATED NANOMATERIALS

Synthesis method	Type of Nanoparticles	Type of the electrode	Type of analysis	Detectable substance	References
Laser dewetting	Au NPs	ITO	Electrochemical	Ascorbic acid, glucose	[20], [21]
	Au NPs	Graphene	Electrochemical	Fructose, glucose	[22],[23]
Laser ablation	Au NPs	Carbon	Electrochemical	Glucose, ascorbic acid, Cd2+, Pb2+, Cu2+, Hg2+	[13],[14],[15]
	Ni NPs	Carbon	Electrochemical	Hydroquinone, glucose	[14],[19]
	Ni NPs	ITO	Electrochemical	Aflatoxin B1	[18]
	Pd NPs	Carbon	Electrochemical	Dopamine, ascorbic acid	[14]
	Cu NPs	Carbon	Electrochemical	Ascorbic acid	[14]
	CdSe QDs	ITO	Electrochemiluminescent	Tripropylamine	[31]
	TiO2/PbS, TiO2 NPs	-	Photoelectrochemical	-	[16], [17]
ZnO NPs	-	Photoelectrochemical	-	[17]	

Shabalina et.al [14] have shown that usage of laser-fabricated Pd NPs and Cu NPs is possible for the detection of ascorbic acid. In the case of Pd NPs, this nanomaterial has shown the best sensing efficiency of dopamine.

Regarding the usage of laser-fabricated nanomaterials in other sensing methods (Photoelectrochemical, Electrochemiluminescent), the number of research works is much lower.

In previous research, our research group has shown that deposited CdSe QDs on the ITO show ECL emission. This allows believing that such laser-fragmented fluorescent semiconductor nanoparticles are suitable for application in ECL experiments and the development of ECL assay procedures [31].

The usage of laser-fabricated nanomaterials in the detection of substances via photoelectrochemical method has not been studied. But the research of Hajjaji et. al. [16] showed that TiO2 nanotubes decorated by laser-fabricated PbS nanoparticles have a good photocatalytic efficiency and photoelectrochemical properties.

#### IV. CONCLUSION

Observed research works indicate that the utilization of the nanoparticles obtained by laser methods and the modification of electrodes by these modifiers are promising for electrochemical, electrochemiluminescent, and photoelectrochemical assays. Also, it has been shown the effectiveness of the detection of organic substances, toxins, and heavy metal ions in liquids by the use of these electrodes in electroanalytical methods.

#### ACKNOWLEDGMENT

This project was partly supported by The Ministry of Education and Science of Ukraine project №ДП 0118U002063 and the National Research Fund of Ukraine project (application reg. number 2020.02/0390).

#### REFERENCES

- [1] J. Wang, "Analytical Electrochemistry," Apr. 2006.
- [2] Allen J. Bard Larry R. Faulkner, "Electrochemical Methods. Fundamentals and Applications," 2001.
- [3] S. Sharma, N. Singh, V. Tomar, and R. Chandra, "A review on electrochemical detection of serotonin based on surface modified electrodes," *Biosensors and Bioelectronics*, vol. 107, pp. 76–93, Jun. 2018.
- [4] X. Zhang, Q. Guo, and D. Cui, "Recent Advances in Nanotechnology Applied to Biosensors," *Sensors*, vol. 9, no. 2, pp. 1033–1053, Feb. 2009.
- [5] W. Siangproh, W. Dungchai, P. Rattanasat, and O. Chailapakul, "Nanoparticle-based electrochemical detection in conventional and miniaturized systems and their bioanalytical applications: A review," *Analytica Chimica Acta*, vol. 690, no. 1, pp. 10–25, Mar. 2011.
- [6] M. Sportelli, M. Izzi, A. Volpe, M. Clemente, R. Picca, A. Ancona, P. Lugarà, G. Palazzo, and N. Cioffi, "The Pros and Cons of the Use of Laser Ablation Synthesis for the Production of Silver Nano-Antimicrobials," *Antibiotics*, vol. 7, no. 3, p. 67, Jul. 2018.
- [7] A. P. Caricato, A. Luches, and M. Martino, "Laser Fabrication of Nanoparticles," *Handbook of Nanoparticles*, pp. 407–428, 2016.
- [8] A. Reza Sadrolhosseini, M. Adzir Mahdi, F. Alizadeh, and S. Abdul Rashid, "Laser Ablation Technique for Synthesis of Metal Nanoparticle in Liquid," *Laser Technology and its Applications*, Jan. 2019.
- [9] K. Habiba, V. I. Makarov, B. R. Weiner, G. Morell, "Fabrication of nanomaterials by pulsed Laser Synthesis," *Manufacturing nanostructures*, 2014.
- [10] M. Kim, S. Osone, T. Kim, H. Higashi, and T. Seto, "Synthesis of Nanoparticles by Laser Ablation: A Review," *KONA Powder and Particle Journal*, vol. 34, no. 0, pp. 80–90, 2017.
- [11] H. Naser, M. A. Alghoul, M. K. Hossain, N. Asim, M. F. Abdullah, M. S. Ali, F. G. Alzubi, and N. Amin, "The role of laser ablation technique parameters in synthesis of nanoparticles from different target types," *Journal of Nanoparticle Research*, vol. 21, no. 11, Nov. 2019.
- [12] H. Oh, A. Pyatenko, and M. Lee, "Laser dewetting behaviors of Ag and Au thin films on glass and Si substrates: Experiments and theoretical considerations," *Applied Surface Science*, vol. 475, pp. 740–747, May 2019.
- [13] Y. Liu, B. J. J. Austen, T. Cornwell, R. D. Tilbury, M. A. Buntine, A. P. O'Mullane, and D. W. M. Arrigan, "Collisional electrochemistry of laser-ablated gold nanoparticles by electrocatalytic oxidation of glucose," *Electrochemistry Communications*, vol. 77, pp. 24–27, Apr. 2017.
- [14] A. V. Shabalina, I. N. Lapin, K. A. Belova, and V. A. Svetlichnyi, "Carbon electrodes modified by metal nanoparticles obtained by

- laser ablation method in organic substances determination," Russian Journal of Electrochemistry, vol. 51, no. 4, pp. 362–367, Apr. 2015.
- [15] X. Xu, G. Duan, Y. Li, G. Liu, J. Wang, H. Zhang, Z. Dai, and W. Cai, "Fabrication of Gold Nanoparticles by Laser Ablation in Liquid and Their Application for Simultaneous Electrochemical Detection of Cd<sup>2+</sup>, Pb<sup>2+</sup>, Cu<sup>2+</sup>, Hg<sup>2+</sup>," ACS Applied Materials & Interfaces, vol. 6, no. 1, pp. 65–71, Dec. 2013.
- [16] A. Hajjaji, S. Jemai, K. Trabelsi, A. Kouki, I. Ben Assaker, I. Ka, M. Gaidi, B. Bessais, and M. A. El Khakani, "Study of TiO<sub>2</sub> nanotubes decorated with PbS nanoparticles elaborated by pulsed laser deposition: microstructural, optoelectronic and photoelectrochemical properties," Journal of Materials Science: Materials in Electronics, vol. 30, no. 24, pp. 20935–20946, Nov. 2019.
- [17] M. Lau, S. Reichenberger, I. Haxhijaj, S. Barcikowski, and A. M. Müller, "Mechanism of Laser-Induced Bulk and Surface Defect Generation in ZnO and TiO<sub>2</sub> Nanoparticles: Effect on Photoelectrochemical Performance," ACS Applied Energy Materials, Sep. 2018.
- [18] P. Kalita, J. Singh, M. Kumar Singh, P. R. Solanki, G. Sumana, and B. D. Malhotra, "Ring like self assembled Ni nanoparticles based biosensor for food toxin detection," Applied Physics Letters, vol. 100, no. 9, p. 093702, Feb. 2012.
- [19] S. Kaneko, T. Ito, Y. Hirabayashi, T. Ozawa, T. Okuda, Y. Motoizumi, K. Hirai, Y. Naganuma, M. Soga, M. Yoshimoto, and K. Suzuki, "Optimizing coverage of metal oxide nanoparticle prepared by pulsed laser deposition on nonenzymatic glucose detection," Talanta, vol. 84, no. 2, pp. 579–582, Apr. 2011.
- [20] V. P. Hitaishi, I. Mazurenko, A. Vengasseril Murali, A. de Poulpiquet, G. Coustillier, P. Delaporte, and E. Lojou, "Nanosecond Laser-Fabricated Monolayer of Gold Nanoparticles on ITO for Bioelectrocatalysis," Frontiers in Chemistry, vol. 8, Jun. 2020.
- [21] K. Grochowska, K. Siuzdak, and G. Śliwiński, "Properties of an Indium Tin Oxide Electrode Modified by a Laser Nanostructured Thin Au Film for Biosensing," European Journal of Inorganic Chemistry, vol. 2015, no. 7, pp. 1275–1281, Aug. 2014.
- [22] A. Scandurra, F. Ruffino, M. Censabella, A. Terrasi, and M. G. Grimaldi, "Dewetted Gold Nanostructures onto Exfoliated Graphene Paper as High Efficient Glucose Sensor," Nanomaterials, vol. 9, no. 12, p. 1794, Dec. 2019.
- [23] A. Scandurra, F. Ruffino, S. Sanzaro, and M. G. Grimaldi, "Laser and thermal dewetting of gold layer onto graphene paper for non-enzymatic electrochemical detection of glucose and fructose," Sensors and Actuators B: Chemical, vol. 301, p. 127113, Dec. 2019.
- [24] E. Owusu-Ansah, C. A. Horwood, H. A. El-Sayed, V. I. Birss, and Y. J. Shi, "A method for the formation of Pt metal nanoparticle arrays using nanosecond pulsed laser dewetting," Applied Physics Letters, vol. 106, no. 20, p. 203103, May 2015.
- [25] H. A. El-Sayed, C. A. Horwood, E. Owusu-Ansah, Y. J. Shi, and V. I. Birss, "Gold nanoparticle array formation on dimpled Ta templates using pulsed laser-induced thin film dewetting," Physical Chemistry Chemical Physics, vol. 17, no. 16, pp. 11062–11069, 2015.
- [26] Yang, L., Wei, J., Ma, Z., Song, P., Ma, J., Zhao, Y., Wang, X., "The Fabrication of Micro/Nano Structures by Laser Machining," Nanomaterials, 9(12), p. 1789, 2019.
- [27] S. V. Makarov, V. A. Milichko, I. S. Mukhin, I. I. Shishkin, D. A. Zuev, A. M. Mozharov, A. E. Krasnok, and P. A. Belov, "Controllable femtosecond laser-induced dewetting for plasmonic applications," Laser & Photonics Reviews, vol. 10, no. 1, pp. 91–99, Jan. 2016.
- [28] S. Sharma, N. Singh, V. Tomar, and R. Chandra, "A review on electrochemical detection of serotonin based on surface modified electrodes," Biosensors and Bioelectronics, vol. 107, pp. 76–93, Jun. 2018.
- [29] M. Rizwan, N. Mohd-Naim, and M. Ahmed, "Trends and Advances in Electrochemiluminescence Nanobiosensors," Sensors, vol. 18, no. 2, p. 166, Jan. 2018.
- [30] D. Peng, B. Hu, M. Kang, M. Wang, L. He, Z. Zhang, and S. Fang, "Electrochemical sensors based on gold nanoparticles modified with rhodamine B hydrazide to sensitively detect Cu(II)," Applied Surface Science, vol. 390, pp. 422–429, Dec. 2016.
- [31] Y. Zholudov, A. S. Aljebur, and A. Kukoba, "Top-down Synthesized CdSe Nanoparticles for Electroanalytical and Labeling Applications," 2019 IEEE 39th International Conference on Electronics and Nanotechnology (ELNANO), Apr. 2019.

# Radiation Detector Based On The Symmetric Silicon Structure

A.V. Borisov, S.N. Osinov, V.F. Zavorotnyi

Microelectronics Department, National Technical University of Ukraine "Kyiv Polytechnic Institute named Igor Sikorsky", Kyiv, Ukraine

E-mail: a.borisov@kpi.ua, analog2@ukr.net, vizav@ukr.net

**Abstract** — A silicon structure with a symmetrical arrangement of Schottky barriers is proposed as a detector for detecting radiation intensity. The research results and established structural and technological limitations for a semiconductor structure are presented. A detection method using the proposed structure is described and a measurement scheme is synthesized. The possibility of increasing the sensitivity of the detector despite of a decrease in size of the active region is shown.

**Keywords** — semiconductor devices, Schottky diode, signal conversion, radiation detector.

## I. INTRODUCTION

The radiation detection process is the process of converting radiation energy (including ionizing radiation in the range of 0.1-100 A<sup>o</sup>) into a digital electrical signal. The number of physical phenomena allowing recording radiation is limited and is a consequence of the interaction of radiation with matter. Three classes of detectors are distinguished as the main ones, namely: gas-discharge detectors, scintillation detectors, and semiconductor detectors. In a wide frequency range, radiation registration is provided by an extensive range of radiation receivers that are constantly evolving. Among the existing traditional semiconductor detectors, four main groups are distinguished, namely silicon detectors, germanium detectors, p-i-n photodiodes, detectors based on other materials, in particular gallium arsenide (GaAs). In the last decade, there has also been a scientific interest in detectors based on organic semiconductors for environmental monitoring as available for mass application [1].

The main directions for constructive and technological improvement of the detectors are increased sensitivity of the detectors, achieving a high signal-to-noise ratio, temperature stability of the parameters, achieving an effective response to interaction with high radiation, up to 500 KeV of energy, cost of devices and geometric dimensions. An analysis of the design features of silicon detectors, based on the data presented in [2,], allows us to state the fact that the area of the sensitive region for recording short-range charged particles is from 20 to 50 mm<sup>2</sup>. To register the fast neutron flux, the sensitive area can reach 350 mm<sup>2</sup>. Such sensitive area geometry is burdensome for integrating detectors with digital signal processing circuits and requires the use of hybrid technology, while digital processing circuits are implemented using CMOS technology. In this regard, the urgent task is to reduce the area of the sensitive element of silicon detectors for recording short-range charged particles by at least an order of magnitude without losing the detector's sensitivity. In this case, the technological

implementation of the detectors is carried out using planar technology methods.

## II. DETECTION OF RADIATION ON SILICON STRUCTURES

The main principle that is realized when radiation is detected in silicon structures is the registration of the photocurrent during the entire time of absorption of radiation pulses, i.e., a continuous process is considered. The appearance of the photocurrent is the result of the interaction of radiation with the silicon structure and the generation of charge carriers, and the generation conditions are predetermined by the detector design itself. For example, under the action of irradiation, the electrical conductivity of the photoresistor increases by increasing the number of non-basic charge carriers while absorbing the quanta of radiation. The photoresistor contains a semiconductor with ohmic contacts. A DC voltage is applied to the ohmic contacts and the value of the DC current through the semiconductor is recorded. This method uses the dependence of current on the intensity of the irradiation, which generates non-basic carriers in the volume of the semiconductor. To increase the sensitivity of the device choose semiconductors with a large value of the lifetime of non-basic charge carriers and such geometric dimensions of the active area of the semiconductor, which provide a high gain of photocurrent. Photoresistors are characterized by geometric dimensions usually larger than those of photodiodes. A significant reduction in the size of the photoresistor leads to a decrease in sensitivity.

The radiation intensity can be detected by determining the constant photocurrent through a photodiode with a p-n junction, through a p-i-n diode, or through a metal-semiconductor structure (with Schottky barrier) [3]. In this case, the diode is applied a constant voltage in the opposite direction and record the amount of current caused by the generation of electron-hole pairs in the region of p-n junction, which are generated by irradiation. At sufficiently high rates of photo response, the disadvantage of this method is the low sensitivity compared with the method of determining the electrical conductivity of the photoresistor due to the lack of gain and small quantum efficiency due to the small size of the transition and small depleted region in which the absorption of light quanta. Generated non-basic charge carriers quickly leave the active region of the p-n junction due to its small size, and then fall into the region of its own conductivity, where they no longer affect the current, since in these areas the concentration of the main charge carriers significantly exceeds the concentration generated by the internal photoelectric effect.

### III. SYMMETRIC SILICON STRUCTURE WITH TWO SCHOTTKY BARRIERS

#### A. Design Features Of The Detector

A symmetrical detector structure is proposed to increase the sensitivity for small areas of the sensitive area. A symmetric silicon structure with two Schottky barriers is such that it contains two identical Schottky barriers that are technologically formed simultaneously and in a stationary mode are interconnected with respect to each other and represent their own or impurity (p-type) a semiconductor with a symmetrically located pair of layers of metal, which is created with the Schottky barrier semiconductor, Fig. 1.

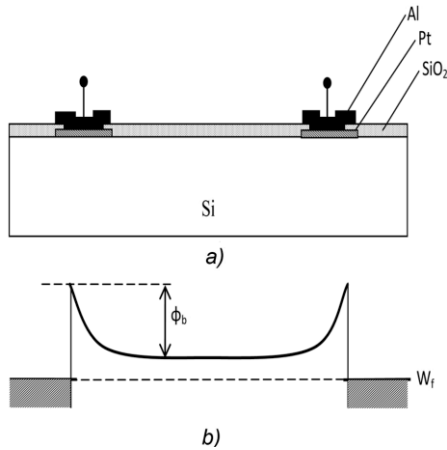


Fig.1. Cross section of a radiation sensitive device with Schottky barriers (a) and an energy diagram (b),  $\phi_b$  is the height of the energy barriers that form a potential well for charge carriers (electrons), and  $W_f$  is the Fermi level.

When radiation is dropped to the surface of a semiconductor, charge carriers are generated in the latter due to interband transitions (own excitation), or transitions involving energy levels in the band gap (impurity excitation). In the presence of a voltage on a semiconductor, these excessive charge carriers take the lead in creating an electric current.

These excessive charge carriers are stored (and generate photocurrent) in the semiconductor until they are recombined in volume or out of the external circuit through electrical contacts. Two symmetrical Schottky barriers form a potential well, FIG. 1, b, for unprofitable charge carriers and prevent them from entering the external circuit and reducing photocurrent due to this.

In order that the excess charge carriers in the potential well contribute to the photocurrent all the time, the voltage is supplied with a variable with a period less than the time of carrier flow between the contacts (Fig. 2).

The potential well prevents the charge carriers from leaving the active region. This eliminates their premature recombination and continues their role in generating current.

This gives additional advantages, which are expressed in the fact that the technological size of the active area of the device can be reduced without loss of sensitivity, moreover, the response on radiation can be significantly enhanced using an AC amplifier and synchronous detection, which increases the overall noise immunity of detection.

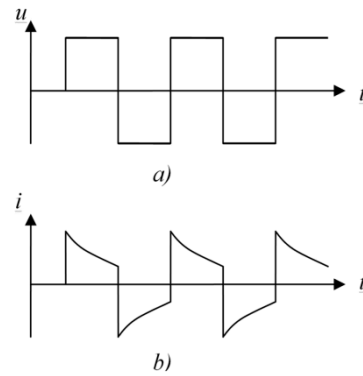


Fig. 2. Voltage diagrams on the detector (a) and current through the detector (b) in the steady state of the structure (the processes of generation and recombination are balanced).

Thus, the control of the process of photocurrent formation in a silicon structure with two Schottky barriers is associated with such parameters as:

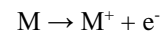
- Schottky barrier height,
- the lifetime of the main carriers and the transit time of the active region of the detector,
- concentration of the main charge carriers.

The peculiarity of the structure presented above is that the requirement is imposed on the barrier height - to be greater than the thermal energy of the charge carriers. The concentration of carriers in the active detection region is ultimately an appropriate choice of material and organization of the manufacturing technological route. Practically important is the need to establish the geometric dimensions of the active detection region, and the rationale for reducing the size is associated with such parameters as the lifetime of the main carriers and the transit time of the active region of the detector.

#### B. Modeling And Numerical Estimation

For detectors detecting radiation, three time-sequential processes are characteristic - this is the generation of carriers under the influence of external radiation; carrier transfer and their multiplication due to a certain mechanism of current amplification and the interaction of current with an external circuit to obtain an information signal.

Indeed, at the time moment  $t_0$ , in the interaction of radiation with the semiconductor structure, ionization of atoms occurs, which consists in the separation of at least one electron from the atom, which is schematically represented as



The resulting electron has an energy  $E_e$ , in accordance with the expression

$$E_e = E_y - E_c \quad (1)$$

Here  $E_y$  is the quantum energy,  $E_c$  is the binding energy of an electron with an atom. Expression (1) is valid under the condition that  $E_y > E_c$ .

Also, the formed electron is characterized by a lifetime  $\tau$ , which is an established fact, when exposed to radiation on a substance, it amounts to no more than  $\tau = 10^{-6}s$ . Under the conditions of a stationary radiation flux and real geometry of the semiconductor structure, a definite charge packet  $Q$  is formed which is represented by the expression

$$Q = q n A x \quad (2),$$

where  $q$  is the unit charge;  
 $n$  is the number of charges per unit volume;  
 $A$  is the cross-sectional area of the active zone of the structure;  
 $x$  is the length of the active region of the structure.

Charge localization in the semiconductor structure under consideration in a one-dimensional version is shown in Fig. 3, an argument in favor of such a representation is the fact that the metal – semiconductor transition has a capacitance and this leads to charge localization near the barrier, region  $\delta$  [4].

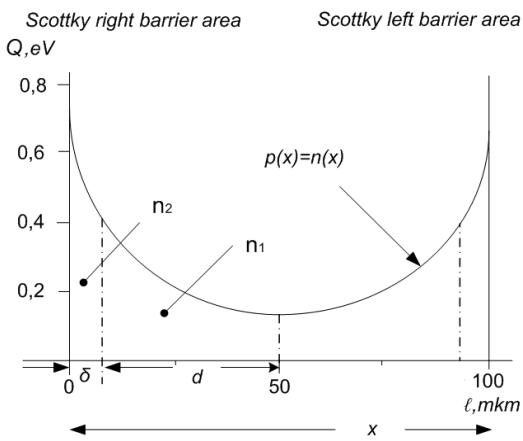


Fig. 3. Charge localization in the active region of the semiconductor structure [8].

At time  $t_1$ , a positive wave of a periodic alternating signal acts on the semiconductor structure. Since the semiconductor structure in the equivalent is two counterclockwise Schottky diodes, then, as a result, one diode turns out to be forward biased, and the second in the reverse biased state. The consequence of this is a significant drop in the applied voltage at the reverse biased diode, which virtually eliminates the possibility of a through conductivity current, but the presence of a pulling electric field, capacitive couplings, and a charge packet in the active zone provide the formation of a bias current and the charge of the active region flows to the boundary of the first barrier.

At time  $t_2$ , the polarity of the synchronous signal changes and since the semiconductor structure is symmetrical, the bias current is of a similar nature, but its direction is reversed. In the future, this process has a periodic character and is synchronized with an external alternating signal.

The bias current  $I_s$  is defined as  $I_s = dQ/dt$ , or taking into account (2) we will present it in the form

$$I_s = q(n_2 - n_1)A(x/\Delta t),$$

where  $x/\Delta t$  is the flight speed of the active region in the semiconductor structure.

Based on ideal case, it can be assumed that the formed charge packet in the potential well can be infinitely long time, but in reality, a very specific time elapses before it degrades or recombines beyond the potential well and it is

associated with the carrier lifetime,  $\tau$ . It is advisable to limit the time of flight of the active region of the detector by the condition

$$t_p < 0.3 \tau \quad (3).$$

For this parameter, this is important for two reasons, namely: controlling the current sensitivity of the detector by choosing a constructive solution for the semiconductor structure and setting the boundary synchronization frequency for the external control signal.

Current sensitivity is defined as the ratio of the change in the energy characteristic at the detector output with respect to the radiation flux. Under the conditions of a stationary radiation flux, a semiconductor structure with a geometry for which condition (3) will be satisfied will have an advantage. At a value of the effective electron flow velocity of the order of  $10^5$  m/s the length of the active region of the semiconductor structure will be no more than 100  $\mu\text{m}$ , which is a practically important result.

A numerical estimate of the current sensitivity for such a structure gives a five-fold increase in the parameter, which is a good result and is an occasion for experimental verification. The generation of a synchronization signal with a detection edge frequency of  $10^{-6}$  Hz and TTL level amplitude is almost completely affordable, and considering that modern processors provide data processing in the GHz range, the viability of the presented detection method is quite justified.

For detecting charge carriers that are generated by radiation and are located in a potential well between Schottky barriers, AC is used, followed by synchronous detection to increase noise immunity and signal to noise ratio. In Fig. 4 shows a diagram of the voltage (a) on the detector and the current (b) through it from the beginning of the generation of carriers by external radiation and to balance the processes of generation and recombination.

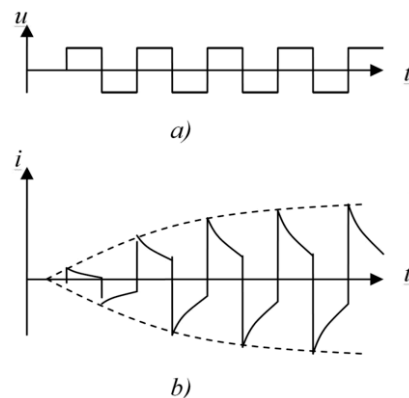


Fig. 4. Voltage diagrams  $u(t)$  on the detector (a) and current  $i(t)$  through the detector (b) in the process of balancing generation and recombination.

The diagram is for the case when the lifetime of the generated media exceeds the period of AC voltage on the detector several times. If the intensity of the radiation does not change, then the mechanisms of generation and recombination of charge carriers are balanced and the concentration of carriers goes to the equation, proportional to the intensity of the radiation, and the amplitude of the current pulses for several periods - to the saturation level.

#### IV. EXAMPLE OF THE DETECTOR SCHEME USING A SINGLE CRYSTAL

Since AC voltage is required to power the detector, a scheme is proposed that allows all the necessary components for power, amplification and synchronous detection to be implemented on a single chip of a programmable system on a PSoC crystal, such as CY8C29466-24PX1, (Fig5).

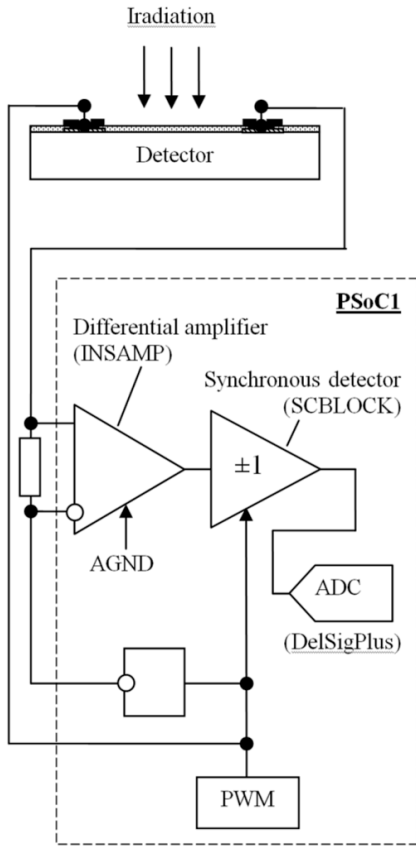


Fig. 5. Schematic diagram of the detector

To measure the detector current, a resistor R is included in the circuit of the device, the voltage at which is proportional to the current. To remove the maximum signal power from the device, the resistance R must be of the same order as the internal resistance of the device.

To amplify the signal of the detector using instrumental differential amplifier (INSAMP), implemented on two operational amplifiers with the possibility of connecting the reference voltage (the reference voltage is taken half of the power supply  $AGND = 1/2 V_{dd}$ ). Synchronous detection implemented on an analog block (SCBLOCK) with switching capacitors. A delta-sigma analog-to-digital ADC converter (DelSigPlus) was used to digitize the detector signal.

One phase of AC voltage is fed directly to the device from the PWM Pulse Modulator, the other phase through the phase inverter FI (which is also configured in the PSoC1 chip). The signal proportional to the current through the device is amplified on the differential amplifier and fed to the synchronous detector. In parallel, a PWM synchronization signal is applied to the synchronous detector. At the output of the synchronous detector receive a voltage proportional to the radiation intensity. To register the signal, it is digitized using

ADC, or used in analog form. You can use the same chip for multiple analog sensors to take signals from multiple radiation sensitive devices.

#### V. CONCLUSIONS

The new method of detection radiation intensity with help of symmetrical silicon structure with a potential well between two Schottky barriers is proposed [5]. The mechanism of interaction of the synchronizing signal and charge in the active region of the detector is presented. The conditions for the formation of the information signal recording the photocurrent of the detector in dynamic mode are determined. A numerical assessment of the detector topology is performed.

The obtained result, despite its qualitative nature, is of practical importance and is a scientific justification for increasing the sensitivity of the ionizing radiation detector and reducing the geometric dimensions of the detectors. It should be noted that the process of radiation exposure is complex and it is necessary to take into account other processes occurring in the structure of the substance, except for the photoelectric effect. It is necessary to clarify the relationships in the dynamic states of the detector, in particular, outside the scope of this study, the question remains what will happen in the structure when exposed to radiation with variable energy.

The advantage of the proposed structure and method of registration the signal is that the radiation generated charge carriers are in the potential well and repeatedly drifting from barrier to barrier in an external AC electric field, creating a photocurrent, while the useful signal is variable, which allows significant amplification and synchronous detection. This provides high sensitivity and noise immunity to detect radiation intensity.

#### ACKNOWLEDGMENT

This research was supported by Laboratory of Medical Sensors the Department of Microelectronics, National Technical University of Ukraine "Kyiv Polytechnic Institute named Igor Sikorsky" in part research works 0117U5112 "Dynamic processes in integral devices of the information electronics" and 0117U005113 "Energy-saving adaptive microprocessor control systems for renewable light sources".

#### REFERENCES

- [1] Marcia Dutra R. Silva/ Evolution of Ionizing Radiation Research\ Charter 8/ Ionizing Radiation Detectors. pp. 189-209, 2015. <http://dx.doi.org/10.5772/60914>
- [2] Baranochnikov M. L. Receivers and radiation detectors. Directory. - M. DMK Press, 2012. ISBN 978-5-94074-564-8
- [3] Firago V. A. Radiation receivers: Lecture notes - Mn.: Belarusian State University, 2004.
- [4] Messaadi Lotfi, Dibi Zohiar. Analog behavioral Modeling of Shottky Diode Using Spice/- Journal of Nano- and Electronic Physics v. 9. No. 1 01002 (4pp), 2017.
- [5] V.F. Zavorotnyi, S.N. Osinov, A.V. Borisov. The method of detecting the radiation intensity. Patent of Ukraine №139816 valid of 27.01.2020.

# Carbon Nanotube Based Nanobiosensors For The Detection Of Viruses: Achievements And Prospects

B.N. Chichkov<sup>1</sup>, N.I. Slipchenko<sup>2</sup>, V.G. Udovitskiy<sup>3,4</sup>, P.V. Turbin<sup>3,4</sup>, A.Yu. Kropotov<sup>4</sup>, E.V. Slipchenko<sup>5</sup>

<sup>1</sup>Leibniz University, Hannover, Germany, E-mail: b.chichkov@lzh.de

<sup>2</sup>Institute of Scintillation Materials, NAS of Ukraine 61001, Kharkiv, Nauky Ave., 60, Ukraine,  
E-mail: naukovets.big@gmail.com

<sup>3</sup>Scientific Center of Physical Technologies MES and NAS of Ukraine  
61022, Kharkiv, Svobody Sq., 6, a/c 4499, Tel. (057)707-53-82, E-mail: udovvg@meta.ua, petro\_turbin@ukr.net

<sup>4</sup>V.N. Karazin Kharkiv National University, 61022, Kharkiv, Svobody Sq., 6, Ukraine

<sup>5</sup>National Technical University "Kharkiv Polytechnic Institute"  
61000, Kharkiv, Kyrpychova str., 2, Ukraine, E-mail: Olena.Slipchenko@kpi.edu.ua

## I. INTRODUCTION

The COVID-19 pandemic, which rapidly swept the whole world due to the spread of the highly pathogenic SARS-CoV-2 virus, made all the issues of combating this viral disease very relevant for humanity. In particular, the issues of its rapid and reliable detection in environmental objects and the human body, as well as antibodies to it in the blood of humans and animals [1]. One of the main methods for the detection of the SARS-CoV-2 virus is now a technique based on the polymerase chain reaction, which, along with the undoubted advantages (high sensitivity and selectivity), requires complex laboratory equipment and special expensive reagents, as well as significant time and labor costs.

Nanobiosensors, the work of which is based on the use of new functional nanomaterials, in particular, carbon nanotubes (CNTs), open up wide possibilities for the successful solution of problems of fast and rather reliable detection of pathogenic viruses in various environments [2]. Pure CNTs are biologically inert nanoscale structures. For use in biosensors, various kinds of biological receptors must be immobilized on their surface, which will provide selective interaction with the desired analyte in the analyzed medium. This will lead to a change in any property of the CNT-receptor-analyte system (for example, a virus), which is converted into an electrical signal by a highly sensitive transducer, see scheme in Fig. 1 [3]. Therefore, the process of CNT functionalization is one of the most important for their use in biosensors. In our previous work, various methods of functionalization and dispersion of CNTs [4] were considered for their use in electronics. In this work, a wide range of issues related to the creation of biosensors based on CNTs for the detection of viruses, in particular, the functionalization of CNTs by selective bioreceptors, methods for converting and recording signals from bioreceptors, applied design and technological solutions, etc., are considered.

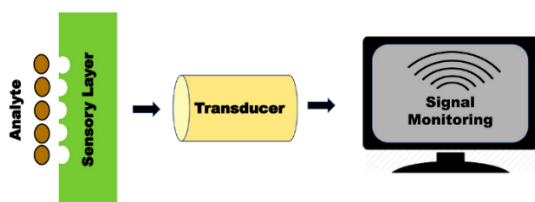


Fig. 1. General monitoring scheme with the use of biosensors [3].

## II. MAIN PART

### A. Types of used bioreceptors

The purpose of CNTs functionalization is to ensure their sensitivity to some biological analyte. The general scheme of classification of a huge family of biosensors for the detection of various bioanalytes according to the types of bioreceptors used in them, as well as the types and design of transducers, is shown in Fig. 2 [5].

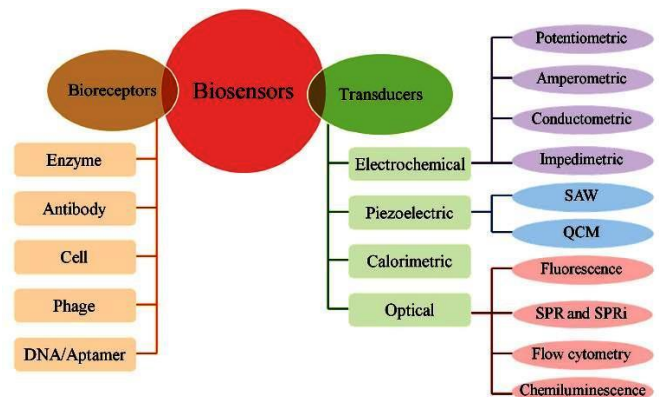


Fig. 2. Classification of biosensors by structural elements of their construction [5].

According to the analysis of publications for the detection of viruses, sensors that react to fragments of nucleic acids (DNA / RNA) of virus particles (Nucleic acid-based biosensors), sensors using antibodies to antigens of virus particles (Antibody-based biosensors), as well as sensors using the so-called. aptamers (Aptamer-based biosensors) are most often used.

At the fabrication of biosensors that react to fragments of nucleic acids of viral particles, it is required to immobilize a single-stranded oligonucleotide (DNA probe) on the CNTs surface, which is complementary to the target DNA / RNA molecule (its fragment) of the viral particle that needs to be detected in the sample. When such a particle interacts with the probe, hybridization complexes are formed on the surface

of the sensors, which change some of its characteristics, which is then recorded by the transducer. The choice of an oligonucleotide and its immobilization on the CNTs surface, which can be both covalent and non-covalent, are the most important in the sensor fabrication technology and determine the specificity and sensitivity of detection.

The working principle of Antibody-based biosensors is based on the immobilization of antibodies to the antigens of the pathogenic viruses to be detected on the CNT surface. When antibodies interact with antigens, so-called binding complexes are formed on the surface of the sensor, which change the characteristics of the sensor. The interaction "antibody-antigen" is very specific and therefore biosensors of this type are highly selective. It works on the principle of recognizing a pathogenic virus, producing antibodies to it and selectively binding for the purpose their inactivation by the immune system of humans and animals. Therefore, biosensors of this type are also called immunosensors. Currently, for the detection of antibodies in human blood, for example, to the SARS-CoV-2 virus, the most commonly used enzyme immunoassay (ELISA-Enzyme Linked Immune Sorbent Assay). The ELISA method allows to diagnose a viral infection not at the very beginning, but after the infection has occurred and the human immune system has developed antibodies to this antigen. Biosensors containing immobilized on their surface antibodies to a specific virus make it possible to detect this virus immediately after its appearance in the analyzed samples of the biological fluid of an infected person, without waiting for him to develop antibodies to this antigen.

In the establishment of Aptamer-based biosensors, the so-called aptamers are used. Aptamers are three-dimensional spatial structures formed by nucleic acid molecules. They are capable of specifically interacting with various particles. Single-stranded DNA molecule assembled from individual fragments contained in the so-called. "Library of DNA" is formed in such a way that it tightly fits mutually corresponding to it (complementary) in size and structure of a nanoparticle. The aptamers got their name from the Latin word *aptus* - to approach. The formed complexes "aptamer - nanoparticle", being in contact with the sensitive surface of the biosensor, change its characteristics and, according to the magnitude of this change, determine their number (concentration).

#### *B. Methods for converting and registering signals in transducers*

The non-electrical signal obtained as a result of the interaction of the analyte with the sensor receptor is further converted in the transducer by various methods into an electrical signal convenient for displaying in the final device, for example, on the display. Depending on the conversion method, transducers are divided into the following types: electrochemical, piezoelectric, calorimetric, optical. Depending on the characteristics of the measurement, each of the types named above is also divided into a number of separate subtypes (see Fig. 2).

Methods of transformation in biosensor transducers are being developed together with the development of the biosensors themselves. They are well described in various

publications. Conversion methods implemented in viral biosensor transducers do not fundamentally differ from conversion methods in biosensors designed to control other bioanalytes. Therefore, we will not dwell on these methods in more detail in this work.

### III. CONCLUSIONS

The COVID-19 pandemic, which rapidly swept the entire world due to the spread of the highly pathogenic SARS-CoV-2 virus, has now significantly changed life and created many problems for all of humanity. At the end of 2019, the term "coronavirus" was familiar only to specialists and a relatively small number of other people. Now almost everyone knows about him - from young children to people of venerable age.

For the first time, coronaviruses were discovered and classified back in the 1960s of the last century. Until the beginning of this century, they did not create any special problems. But in the 21st century, this is already the third serious outbreak of diseases caused by coronaviruses. In 2002/2003, there was SARS-CoV (Severe Acute Respiratory Syndrome) disease in China, which took more than 1000 lives. In 2012, a second outbreak occurred in South Asia and the Middle East - MERS-CoV (Middle East Respiratory Syndrome), in which there was a very high mortality rate (up to 35%), but the number of cases was relatively small. And now we are experiencing an outbreak of SARS-CoV-2, from which more than a million people have already died and the pandemic continues.

The above makes the task of fast and reliable detection of pathogenic viruses, currently SARS-CoV-2, very actual. The already achieved results of research and development show that CNTs, due to their special physicochemical properties, make it possible to create small-sized, sensitive, fast-acting and relatively inexpensive biosensors of various analytes, in particular, viruses. Moreover, such sensors can be successfully used both in specialized diagnostic laboratories and at the place of providing medical care to a patient at home.

### REFERENCES

- [1] Y. Jin, H. Yang, W. Ji, Weidong et al. Virology, Epidemiology, Pathogenesis, and Control of COVID-19 // *Viruses*, **2020**, 12, 372 (17 p.).
- [2] K. Katsarou, E. Bardani, P. Kallemi et al. Viral Detection: Past, Present, and Future // *BioEssays* **2019**, 41, 1900049 (18 p.).
- [3] Singh S., Kumar V., Dhanjal D.S et al. (2020) Biological Biosensors for Monitoring and Diagnosis. In: Singh J., Vyas A., Wang S., Prasad R. (eds) *Microbial Biotechnology: Basic Research and Applications*. Environmental and Microbial Biotechnology. Springer, Singapore. 2020, 370 p.
- [4] V. G. Udovitskiy, N. I. Slipchenko, A. Yu. Kropotov, B. N. Chichkov Physical, chemical and plasmochemical methods of functionalisation and dispersion of carbon nanotubes for their application in electronics // *Journal of Surface Physics and Engineering* **2017**, Vol.2, №2-3, P.144-164 (in rus.).
- [5] Q. Wu, Y. Zhang, Q. Yang et al, Review of Electrochemical DNA Biosensors for Detecting Food Borne Pathogens // *Sensors* **2019**, 19, 4916.
- [6] T. Ozer, B. J. Geiss, C. S. Henry Review. Chemical and Biological Sensors for Viral Detection // *Journal of The Electrochemical Society*, **2020**, 167, 037523.

# Electrochemiluminescent detection of tryptophan aminoacid

Yuriy Zholudov\*, Ali Salman Aljebur\*, Dmytro Snizhko\*, Guobao Xu<sup>+</sup>

\* Kharkiv National University of Radio Electronics, Biomedical Engineering Department  
Nauki Ave., 14, 61166, Kharkiv, Ukraine, +38(057)7020369, yurets.zh@gmail.com,

<sup>+</sup> Changchun Institute of Applied Chemistry, Chinese Academy of Sciences, State Key Laboratory of Electroanalytical Chemistry  
Renmin Street, 5625, 130022, Changchun, Jilin, China, +86-43185262747, guobaoxu@ciac.ac.cn

**Abstract** — The work describes application of electrogenerated chemiluminescence (ECL) method for detection of fluorescent aromatic amino acid tryptophan in aqueous solutions. It was discovered that ECL emission is observed upon oxidation of tryptophan at glassy carbon electrode in the presence of sodium tetraphenylborate co-reactant when potential pulses are applied to the electrode. The ECL intensity is proportional to the concentration of amino acid and allows its detection in a broad concentration range with high selectivity.

**Keywords** — electrogenerated chemiluminescence, sensors, tryptophan, amino acid, biosample

## I. INTRODUCTION

Tryptophan (Trp) is an essential amino acid that plays an important role in human and animal growth and metabolism and is required for the biosynthesis of certain proteins. It is classified as a non-polar aromatic amino acid containing an indole side chain (Fig. 1) that gives fluorescent properties to the molecule [1]. Trp is also a precursor in the biosynthesis of important species, such as serotonin (a neurotransmitter) and melatonin (a hormone). The deficiency of tryptophan intake with foods or disorder of its metabolism in the human organism is associated with certain diseases [2, 3]. Therefore a number of techniques were developed for Trp detection in body fluids, pharmaceuticals, and food samples. Among them electrochemical, fluorescent, chromatographic, colorimetric techniques are just few to mention [4].

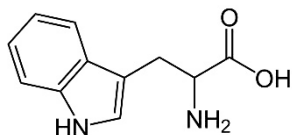


Fig. 1. Structure of Trp molecule

Among detection techniques special attention should be paid to electrogenerated chemiluminescence (ECL) - a technique combining advantages of electrochemistry and chemiluminescence and essentially eliminating their drawbacks [5, 6]. There are two basic ways ECL can be used for Trp detection. One is based on the fact that Trp as well as many other amine compounds can be used as an oxidative reduction type coreactant for ECL excitation of luminophore (mostly tris(2,2'-bipyridine)ruthenium,  $\text{Ru}(\text{bpy})_3^{2+}$ ) [7 - 9]. Another approach is using luminescent property of Trp

species. Previously a few works reporting ECL emission from Trp were published [10, 11]. In both cases the reaction was performed in alkaline medium in the presence of some oxidizing agents like hydrogen peroxide or oxygen. Studies of Sacura's group identified the reaction as chemiluminescence enhanced by electrochemical energy [10].

At the same time in the course of studies of tetraphenylborate ECL coreactant [12, 13] it was found that it can excite ECL emission in reaction with Trp in dimethylformamide solution on the rotating glassy carbon disk electrode. Here we report about aqueous ECL emission from Trp in reaction with sodium tetraphenylborate (TPB) and its use for fast, selective and sensitive detection of this aminoacid.

## II. EXPERIMENTAL

Electrochemical and ECL measurements were performed in a 3-electrode electrochemical cell containing glassy carbon disk working electrode (3mm in diameter), Pt foil counter electrode (approx. 375 mm<sup>2</sup> area) and Ag/AgCl reference electrode with Autolab PGSTAT 128N potentiostat coupled to ФЭУ-136 PMT module (multialkali SbNaKCs photocathode, 1400V) in home designed lightproof chamber.

In all ECL measurements the deoxygenation of solutions was made by nitrogen bubbling for at least 10 minutes. The electrode was cleaned prior to each experiment by polishing with  $\text{Al}_2\text{O}_3$  slurry (0.05 $\mu\text{m}$ ) and rinsing with distilled water.

0.1M  $\text{NaClO}_4$  (Sinopharm Chemical Reagent Co.) was used as a supporting electrolyte for electrochemical and ECL experiments unless otherwise stated. Solutions of L-Tryptophan (Beijing Dingguo Biotechnology Co.) and sodium tetraphenylboron (Shanghai Zhanyun Chemical Co.) were prepared as follows: Trp or TPB was dissolved in 0.1M aqueous solution of  $\text{NaClO}_4$  to give a stock standard solution containing 30 mM of appropriate substance. Aliquots of stock solutions were added to 0.1M aqueous solution of  $\text{NaClO}_4$  to obtain the required concentration.

Most ECL measurements were carried out in unbuffered solution. For measurements involving pH effect study the pH was adjusted by adding NaOH or  $\text{HClO}_4$ .

### III. RESULTS AND DISCUSSION

In neutral medium Trp exists in a zwitterionic form with its carboxylic acid group deprotonated ( $pK_a = 2.38$ ) and its amino group protonated ( $pK_a = 9.39$ ). Oxidation of Trp on carbon electrodes in neutral aqueous media is believed to be a  $2e^-$  process with accompanying loss of 2 protons [14]. Fig. 1a shows cyclic voltammetry of 0.3 mM Trp in deaerated aqueous solution containing 0.1M  $NaClO_4$  supporting electrolyte in neutral, basic ( $pH=11$ , addition of  $NaOH$ ) and acidic ( $pH=2$ , addition of  $HClO_4$ ) media. Oxidation of Trp is irreversible and in neutral media is accompanied by certain electrode fouling that leads to slight increase of peak potential and decrease of its amplitude from scan to scan. No ECL emission is observed under such conditions.

Electrochemical oxidation of 0.3 mM TPB solution is shown in Fig. 2b. At such concentrations it is also characterized by certain electrode fouling with gradual shift of electrode potentials and amplitudes of oxidation current between the scans [13 - 16]. Earlier studies suggest that the first wave at  $\sim 0.47V$  is an oxidation of TPB giving diphenylborinic acid and biphenyl as the products while the second wave is a pH dependent oxidation of diphenylborinic acid [15]. Here it should be noted that according to literature data [15] and our own studies the second pH dependent oxidation wave of TPB is well defined in phosphate buffer and its amplitude is similar to the first wave while in  $NaClO_4$  solution it is very weak (small feature at about 0.6V, 0.85V and 1.05V for basic, neutral and acidic media correspondingly in Fig. 2b).

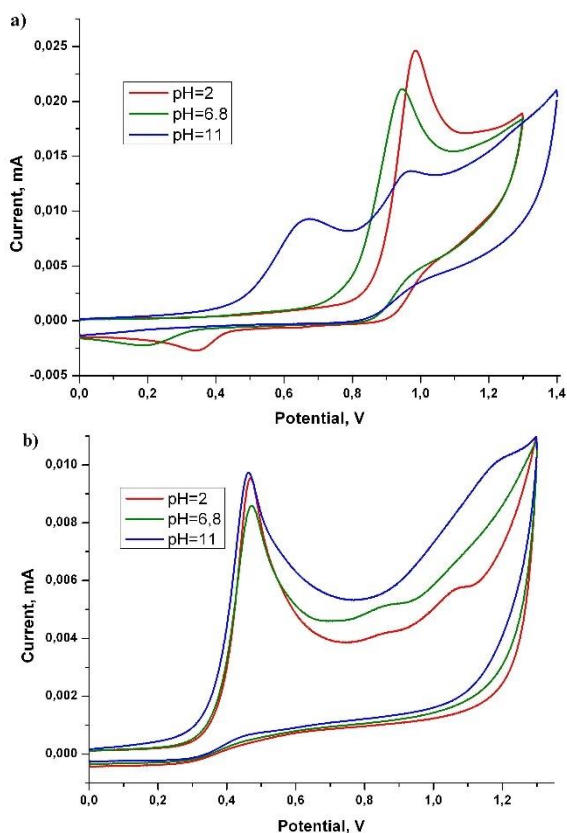


Fig. 2. Cyclic voltammetry of a) 0.3 mM Trp; b) 0.3 mM TPB solution at  $pH=2$  (red), neutral unbuffered solution (green),  $pH=11$  (blue). Scan rate 100 mV/s.

When both Trp and TPB are present in the solution a weak ECL emission is observed when oxidation of aminoacid occurs. This emission was found to be dependent on the concentrations of aminoacid and coreactant, solution pH and scan rate. Fig. 3 shows typical emission for 0.1M Trp and 3mM TPB solution at 250 mV/s scan rate.

In accordance to previous studies TPB belongs to ECL coreactants working according to oxidative reduction mechanism [13]. Proposed mechanism of TPB reaction suggests that its oxidation at the electrode does not contribute to ECL emission and only depletes TPB near the electrode. Thus, assuming that TPB oxidation occurs much before oxidation of Trp, it is quite expectable that ECL will increase with the increase of the scan rate and will reach maximum in case of pulsed excitation. Example of light emission from solutions containing varying Trp concentration and 2 mM of TPB when potential step of 1.3V and 0.1s duration is applied to the electrode is shown in Fig. 4. Analysis of ECL response shows that its amplitude and kinetics strongly depend on the concentrations of aminoacid and coreactant.

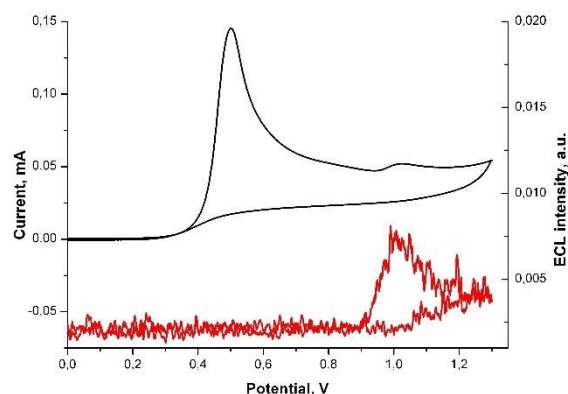


Fig. 3. Cyclic voltammetry and ECL response of 0.1mM Trp solution containing 3mM TPB coreactant, scan rate 250 mV/s.

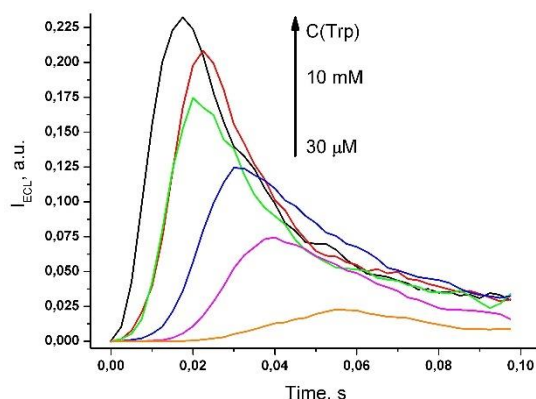


Fig. 4. Pulsed ECL response of 2mM TPB solution containing Trp: 30 μM, 100 μM, 300 μM, 1mM, 3mM, 10mM. Pulse amplitude 1.3V, pulse duration 0.1 s.

For the purpose of Trp detection in aqueous media a number of experimental parameters was optimized: coreactant concentration, potential pulse duration and amplitude. It was found that peak value of ECL emission under pulsed excitation is not as stable and reproducible as an integral of ECL response during pulse interval. It was noted that pulsed ECL response has a tendency of variation in both increasing and decreasing between the pulses depending on experimental conditions. Thus it was reasonable to use the

average value of light response during several consecutive pulses (3 pulses were used as an optimal condition).

Using the optimized detection conditions the calibration plot of Trp ECL quantification was built using series of potential pulses (1.3V, 0.1s) in 0.1M NaClO<sub>4</sub> solution containing 2mM of TPB coreactant. The integral ECL response averaged for the first 3 pulses is shown in Fig. 5. It allows detection of Trp in the range of 0.3μM - 0.3 mM with the detection limit of 0.2 μM (S/N=3). The fitting equation in the log-log coordinates is:

$$\log(I_{ECL}) = 0.85 \log(C_{TRP}) + 1.78 \quad (R^2 = 0.993) \quad (1)$$

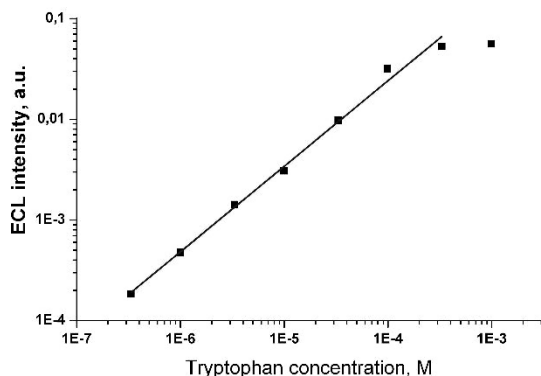


Fig. 5. Dependence of ECL intensity vs. tryptophan concentration. 2mM TPB. Supporting electrolyte 0.1 M NaClO<sub>4</sub>, pulse amplitude 1.3V, pulse duration 0.1 s, pulse interval 10s.

Weak emission intensity did not allow the use of ordinary spectrometer so estimation of emission spectra was done using a set of rather broadband glass filters. It was found that ECL spectrum of Trp/TPB system has a maximum within 525-575 nm range which does not coincide with the fluorescence spectrum of Trp amino acid (maximum at 350 nm). Such emission is similar to ECL and chemiluminescence of Trp where pyrrole ring opening takes place [10, 17 - 19]. At the same time in most chemiluminescent studies the proposed mechanism involves Trp oxidation by strong oxidant while TPB was shown to behave as oxidative reduction kind of ECL coreactant [12, 13]. This suggests that essentially different reaction mechanism is involved in our case.

ECL emission of Trp/TPB system is present in a rather broad pH range. A slight maximum is observed near Trp isoelectric point. Fast decay of ECL activity in basic solutions above pH 9 is accompanied with the decrease of Trp oxidation wave at 0.95 V (Fig.2) and corresponds to deprotonation of Trp's amino group (pKa = 9.39). Decay of ECL signal in the acidic pH range is not so rapid. It is accompanied with certain increase of Trp redox activity and growth of oxidation wave at 0.95V (some shift of peak potential to 0.99V is observed). Except protonation of Trp carboxylic group (pKa = 2.38) such behavior could also be caused by changes in TPB coreactant mechanism but proving this requires further studies.

Weak emission intensity did not allow the use of ordinary spectrometer so estimation of emission spectra was done using a set of rather broadband glass filters. It was found that ECL spectrum of Trp/TPB system has a maximum within 525-575 nm range which does not coincide with the fluorescence spectrum of Trp amino acid (maximum at 350

nm). Such emission is similar to ECL and chemiluminescence of Trp where pyrrole ring opening takes place [10, 17 - 19]. At the same time in most chemiluminescent studies the proposed mechanism involves Trp oxidation by strong oxidant while TPB was shown to behave as oxidative reduction kind of ECL coreactant [12, 13]. This suggests that essentially different reaction mechanism is involved in our case.

The ECL reaction of tryptophan with TPB appears to be quite selective. No ECL emission was found under the same conditions with a number of other aminoacids including fluorescent tyrosine and phenylalanine, as well as methionine, proline, alanine, histidine. Under the same conditions optimized for Trp detection 0.3 mM indole solution also shows pulsed ECL response with similar kinetics and about 50 times lower intensity that is accompanied by much more severe electrode fouling from pulse to pulse. This suggests the responsibility of indole group of tryptophan for observed ECL emission.

#### IV. CONCLUSION

Thus a new simple method of sensitive and selective identification and quantification of L-tryptophan in aqueous solutions was developed based on its ECL reaction with TPB coreactant. It has an application potential in a number of areas including biological samples assay, pharmacy and foods industry.

Presented results suggest that ECL reaction mechanism is essentially different from those reported earlier for Trp in aqueous media and also differs from ordinary oxidative reduction mechanism typical for Trp coreactant. Thus further studies are necessary to reveal its details.

#### ACKNOWLEDGMENT

The work was supported by the Ministry of Education and Science of Ukraine (joint Ukraine-China research project M/97-2020) and Ministry of Science and Technology of the People's Republic of China (CU03-02).

#### REFERENCES

- [1] Wagner and H. Musso, "New Naturally Occurring Amino Acids," *Angewandte Chemie International Edition in English*, vol. 22, no. 11, pp. 816-828, Nov. 1983.
- [2] Slominski, I. Semak, A. Pisarchik, T. Sweatman, A. Szczesniowski, and J. Wortsman, "Conversion of L-tryptophan to serotonin and melatonin in human melanoma cells," *FEBS Letters*, vol. 511, no. 1-3, pp. 102-106, Jan. 2002.
- [3] E. R. Radwanski and R. L. Last, "Tryptophan Biosynthesis and Metabolism: Biochemical and Molecular Genetics," *The Plant Cell*, vol. 7, no. 7, p. 921, Jul. 1995.
- [4] S. Jia, and X. Dong, "Study on detection methods for tryptophan in food and biological samples," *International Journal of Current Research in Chemistry and Pharmaceutical Sciences*, vol. 3, no. 9, pp. 27-31, Sep. 2016.
- [5] M. Hesari and Z. Ding, "Review—Electrogenerated Chemiluminescence: Light Years Ahead," *Journal of The Electrochemical Society*, vol. 163, no. 4, pp. H3116-H3131, Dec. 2015.
- [6] Z. Liu, W. Qi, and G. Xu, "Recent advances in electrochemiluminescence," *Chemical Society Reviews*, vol. 44, no. 10, pp. 3117-3142, 2015.
- [7] K. Uchikura and M. Kirisawa, "Electrochemiluminescence Determination of D,L-Tryptophan Using Ligand-Exchange High-Performance Liquid Chromatography," *Analytical Sciences*, vol. 7, no. 6, pp. 971-973, 1991.
- [8] W.Y. Lee and T.A. Nieman, "Evaluation of use of tris(2,2'-bipyridyl)ruthenium(III) as a chemiluminescent reagent for

- quantitation in flowing streams," *Analytical chemistry*, vol. 67, pp. 1789-1796, 1995.
- [9] S. Brune and D. Bobbitt, "Effect of pH on the reaction of tris(2,2'-bipyridyl)ruthenium(III) with amino-acids: Implications for their detection," *Talanta*, vol. 38, no. 4, pp. 419-424, Apr. 1991.
- [10] S. Sakura, "Chemiluminescence of tryptophan enhanced by electrochemical energy," *Electrochimica Acta*, vol. 37, no. 15, pp. 2731-2735, Dec. 1992.
- [11] G. N. Chen, R. E. Lin, Z. F. Zhao, J. P. Duan, and L. Zhang, "Electrogenerated chemiluminescence for determination of indole and tryptophan," *Analytica Chimica Acta*, vol. 341, no. 2-3, pp. 251-256, Apr. 1997.
- [12] O. M. Bilash, Y. T. Zholudov, and M. M. Rozhitskii, "Electrochemiluminescent detection of labile radical intermediates of electrochemical reactions," *Journal of Solid State Electrochemistry*, vol. 15, no. 10, pp. 2127-2131, Jul. 2011.
- [13] Y. Zholudov, O. Bilash, A. Kukoba, and M. Rozhitskii, "Electrogenerated chemiluminescence in systems with tetraphenylborate anion as a co-reactant," *The Analyst*, vol. 136, no. 3, pp. 598-604, 2011.
- [14] N. T. Nguyen, M. Z. Wrona, and G. Dryhurst, "Electrochemical oxidation of tryptophan," *Journal of Electroanalytical Chemistry and Interfacial Electrochemistry*, vol. 199, no. 1, pp. 101-126, Feb. 1986.
- [15] W. R. Turner and P. J. Elving, "Electrooxidation of Tetraphenylborate Ion at the Pyrolytic Graphite Electrode.," *Analytical Chemistry*, vol. 37, no. 2, pp. 207-211, Feb. 1965.
- [16] P. K. Pal, S. Chowdhury, M. G. B. Drew, and D. Datta, "The electrooxidation of the tetraphenylborate ion revisited," *New Journal of Chemistry*, vol. 26, no. 3, pp. 367-371, Feb. 2002.
- [17] P. F. de Violet, B. Veyret, P. Vincendeau, and A. Caristan, "Chemiluminescence induced by oxidation of tryptophan by singlet oxygen and by hypochlorous acid. implications in the luminescence emitted in phagocytosis," *Photochemistry and Photobiology*, vol. 39, no. 5, pp. 707-712, May 1984.
- [18] M. Kaczmarek and S. Lis, "Influence of Lanthanide(III) Ions on the Reaction System Tryptophan-H<sub>2</sub>O<sub>2</sub>-Fe(II)," *International Journal of Photoenergy*, vol. 2007, pp. 1-7, 2007.
- [19] Y.-D. Liang and J.-F. Song, "Flow-injection chemiluminescence determination of tryptophan through its peroxidation and epoxidation by peroxyntitrous acid," *Journal of Pharmaceutical and Biomedical Analysis*, vol. 38, no. 1, pp. 100-106, Jun. 2005.

# Carbon nanotube electrodes for nanoelectrochemical sensors

Dmytro Snizhko\*, Yuriy Zholudov\*, Iaroslav Gnilitzkyi#, Alexander Kuznetsov#, Guobao Xu<sup>+</sup>

\* Kharkiv National University of Radio Electronics, Biomedical Engineering Department  
Nauki Ave., 14, Kharkiv, 61166, Ukraine, +38(057)7020369, dmytro.snizhko@nure.ua, yurii.zholudov@nure.ua

#Limited Liability Company Novinanolab (LLC Novinanolab)

Pasternaka str., 5, Frankivskiy district, Lviv, 79015, Ukraine, iaroslav.gnilitzkyi@novinano.com

<sup>+</sup> Changchun Institute of Applied Chemistry, Chinese Academy of Sciences, State Key Laboratory of  
Electroanalytical Chemistry

Renmin Street, 5625, 130022, Changchun, Jilin, China, +86-43185262747, guobaoxu@ciac.ac.cn

**Abstract** — The given work is considered to the investigation of the carbon nanotube modified nanoelectrodes for electrochemical sensors. The combination of nanoelectrodes with ultra-fast electrochemical (EC) and electrochemiluminescent (ECL) assays. Their utilization opens new advantages for its applications in biology and medicine. In this work classification of nanodes, their fabrication technology, characterization and application for analytics are discussed. The developed the laboratory setup for ultramicroelectrodes and nanodes characterization by ultra-fast voltammetry and electrogenerated chemiluminescent methods are shown and the data of its investigation and testing are presented.

**Keywords** — nanodes, ultra-fast voltammetry, electrogenerated chemiluminescence, sensors

## I. INTRODUCTION

In the development of modern electrochemical sensors, much attention is paid to the possibility of miniaturizing electrodes to the nano level. This task is relevant to the possibility of obtaining unique features of new devices and systems that use electrodes with characteristic dimensions down to nanometers. Today, the use of microelectrodes and ultra-microelectrodes for studying the composition of liquid, solid and gaseous media by methods of electrochemical analysis is increasingly being implemented not only in the form of single laboratory specimens of microsensor devices, but also as specific commercial proposals of analytical instruments and systems. Undoubtedly, the search for the possibility of realizing electrodes with minimum sizes, namely, nanoscale electrodes - nanodes, and with maintaining their functional purpose, for example, as a sensor element in electrochemical analysis, is one of the main directions of nanosensor analytics.

The aim of this work is to develop an experimental setup for electrochemical and electrochemiluminescent studies of micro- and nanoelectrodes (nanodes), including techniques with a high rate of polarization potential sweep and a high time resolution of recording an analytical signal.

In this work, the classification of nanodes is considered, the analysis of existing methods of manufacturing, testing and areas of use of nanodes is carried out. Aspects of the application of such devices and their advantages in analytics

are discussed, including the use of ultrafast voltammetry in the method. A model system was studied - a solution of 9,10-diphenyl anthracene in a solution of a mixture of acetonitrile with benzene (3: 1 by volume) with the addition of a background electrolyte 0.5 M tetrabutyl ammonium perchlorate, which combines the possibilities of recording single-photon events and carrying out ultra-fast voltammetry to study ECL reaction.

To understand the problem of creating nanodes, let us consider the main criteria for the classification of electrodes for electrochemical analysis. One of the most important features used to classify electrodes is the geometry of the working surface. For electrochemical analysis, good geometry reproducibility and manufacturability are important factors. The simplicity of the shape makes easy the modeling of mass-transport processes of electroactive substances, which is an important aspect of the use of electrodes in modern analytics. According to this parameter, the electrodes can be divided into a few groups. For these reasons, the most widespread are electrodes with the following geometry: spherical, hemispherical, disk, cylindrical, annular, slotted, channel, tubular, and matrix of electrodes [1]. So, according to [1], the share of microelectrodes in the form of a disk out of the total number of the most used microelectrodes is 50%, for cylindrical microelectrodes - 20%, electrode matrices - 20%, about 10% are slot and ring electrodes, a small percentage of microelectrodes falls on other types of geometry of the working surface, for example, spherical and quasi-spherical.

The main requirements for nanodes were formed on the basis of the experience of using classical electrodes and ultra-microelectrodes. However, further miniaturization of electrodes down to nanoscale imposes additional requirements due to the specific fabrication and operation of these devices. Today, the creation of nanodes remains at the level of unique innovative technologies of laboratory samples. Accordingly, their research, as well as the improvement of manufacturing technology, will expand the scope of application.

Frequently the main nanode fabrication aspect is device feasibility, the rest are secondary. Work continues on the development of a simple reproducible technology for nanodes fabrication, the research of technologies for the

manufacture of electrodes with different materials of the working surface. To date, nanode samples have been obtained for materials such as platinum [2-5], carbon [6, 7].

However, of considerable interest is the integration of technologies for new nanomaterials producing, for example, carbon nanotubes, into nanode, which are being actively studied as an electrode material for electrochemical analytics by many groups [8-10].

The presence of specific properties, such as the catalytic effect, which allows the electrochemical oxidation of non-electroactive substances on classical electrodes, for example, biomacromolecules, makes this material very promising for use in bio analyses [11-16].

## II. NANODES PROPERTIES

One of the important properties that stimulate interest in the use of ultramicroelectrodes is the intense transport of matter in the diffusion region at the working surface of the electrode, since the transport of matter changes from linear to spherical. Due to the intensification of transport, the limitation imposed by the limiting factor - diffusion - on the processes accompanying electrolysis is reduced. Thus, on these electrodes, it becomes possible to study heterogeneous rate constants of electron transfer, which is difficult or impossible with the use of electrodes of the classical type.

Another aspect of the ultra-microelectrodes and nanodes use is the ability to perform voltammetry without adding a background electrolyte to the system. In the process of electrolysis, charge carriers are required for the passage of currents through the electrochemical system, i.e. ions. In non-polar solvents, it becomes problematic to implement a traditional voltammetric experiment without an excess of the supporting electrolyte, which reduces the ohmic voltage drop in the electrochemical cell. However, the negative factor is involving contaminant substances of the background electrolyte in the investigated electrochemical processes. A change in the physicochemical characteristics of the test sample under the influence of the addition of a supporting electrolyte makes it impossible to obtain adequate results. Since a much lower current flows through microelectrodes than through macro-sized electrodes, it is possible to neglect the ohmic voltage drop due to its smallness when using microelectrodes. Nanodes have the same property to an even greater extent, since their currents are even lower than those of microelectrodes. Thus, the range of investigated electrochemical systems expands and the need to use a supporting electrolyte is eliminated.

The improvement in the temporal resolution of electrochemical methods is associated with the rate of recharge of the double electric layer formed at the working electrode/solution interface. At large capacitive (non-Faraday) currents in the electrochemical cell, other (Faraday) processes are masked, and it becomes more difficult to separate them. Thus, decrease of the electrode size reduces the electric double layer size, the value of its capacitance and capacitive currents, therefore, the rate of formation of a useful (Faraday) analytical signal increases. Thanks to this, it becomes possible to obtain a better signal-to-noise ratio, to carry out studies of faster stages of electrochemical reactions, and to detect short-lived reaction products.

Localization of research in a small volume of solution is an additional argument for the use of microelectrodes and

nanoelectrodes, respectively. With a decrease in the size of the electrode, it becomes possible to realize a higher rate of the electrochemical experiment. The experiment time is proportionally related to the size of the diffuse region near the electrode for substances involved in the electrochemical process at the stage of electrolysis and diffusion of products. By reducing the size to 5  $\mu\text{m}$  and the electrolysis time to 1  $\mu\text{s}$ , it becomes possible to limit the area of the solution involved in the experiment to a volume of several picoliters. The implementation of such experimental parameters makes it possible to study by the electrochemical method the chemical components involved in the metabolism of an individual cell, without the need to extract the cell from the culture or sample.

One of the main difficulties in using electrochemical methods in medicine is the impossibility of realizing a redox reaction for a substance in the window of working potentials available for an aqueous solvent, i.e. until the moment when the electrochemical decomposition of the solvent itself begins to occur. The solution to this problem is the use of intermediates in the chemical stage of the redox process or electrodes with catalytic properties. Carbon nanotubes, possessing a catalytic effect, are of interest for studying the prospects of their use as an electrode material. One of the technological difficulties is the production of nanoscale electrodes from this material. The study of carbon nanotubes as an electrode material has been carried out in a number of works, where it is noted that it is promising due to the manifestation of such properties as the catalytic effect of redox reactions for a number of substances, good electrical conductivity, etc. The use of this material in the analysis of biologically important substances remains limited [11-16]. The study of the main methods of obtaining this material made it possible to single out, as the most promising technology for creating nanodes with carbon nanotubes, chemical attachment of carbon nanotubes selectively to the surface of a gold nanoelectrode.

## III. EXPERIMENTAL

The use of nanodes in the method of electrogenerated chemiluminescence makes it possible to study small sample sizes or physically small volumes, for example, several picoliters, involving only individual pairs of reagents in the ECL reaction. Through the ECL signal, it becomes possible to control the transfer of one electron in electrochemical reactions. Thus, a transition from statistical observations in classical electrochemistry to stochastic studies on individual molecules is possible. This aspect is especially important for nanoelectrochemical studies, where the manifestation of properties is determined by the solitary nature of nanoobjects, which are in nanoscale constraints.

To investigate the possibilities of integrating micro- and nanodes into the methods of electrogenerated chemiluminescence and high-speed scanning of the electrode potential, an experimental setup shown in Fig. 1. Along with the electrochemical equipment Autolab PGSTAT 128N, Metrohm A.G. it includes equipment for recording single photons H-10682 Hamamatsu Photonics K.K., as well as equipment of its own design for synchronizing electrochemical and optical measurements in one experimental setup.

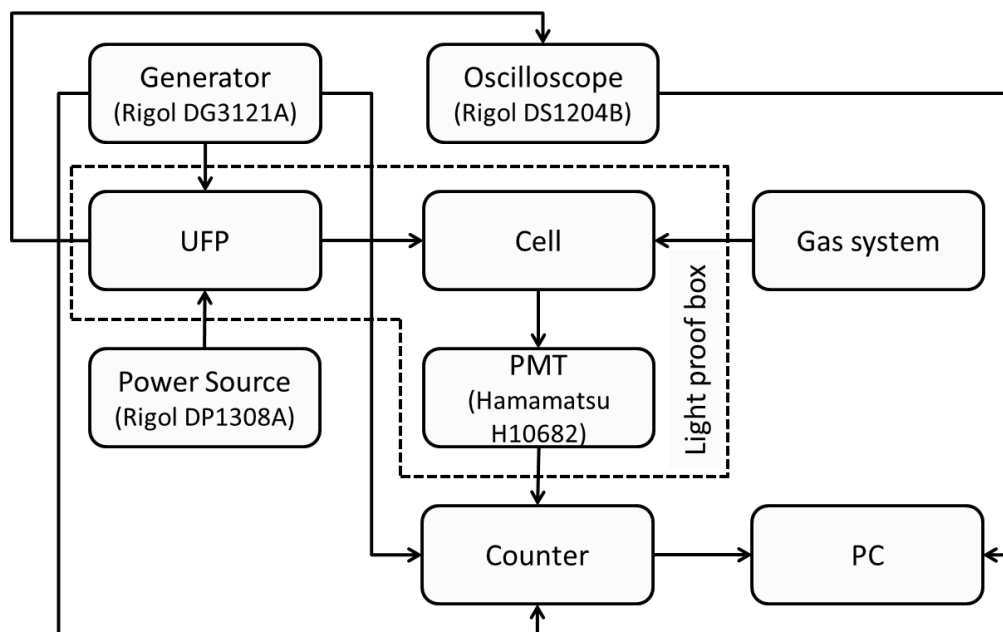


Fig. 1. Laboratory setup structure: UFP – Ultra-fast potentiostat, PMT – photomultiplier tube, PC – personal computer.

#### IV. CONCLUSION

The use of nanodes in non-stationary methods of electrochemical analysis, especially in high-speed modifications of pulse potentiometry, scanning linear and cyclic voltammetry, has high potential due to the use of the unique properties of nanodes in the implementation of new analytical capabilities. Their integration into new devices and systems opens up new promising areas of research in biology and medicine.

#### ACKNOWLEDGMENT

This project was partly supported by The Ministry of Education and Science of Ukraine project (reg. number 0118U002063) and National Research Fund of Ukraine project (application reg. number 2020.02/0390). The work was supported by the Ministry of Education and Science of Ukraine (joint Ukraine-China research project M/97-2020) and Ministry of Science and Technology of the People's Republic of China (CU03-02).

#### REFERENCES

- [1] Allen J. Bard, Martin Stratmann, Patrick R. Unwin "Encyclopedia of Electrochemistry", Vol. 3, Instrumentation and Electroanalytical Chemistry, Wiley-VCH, New-York, 2003, P. 160. ISBN: 978-3-527-30395-3
- [2] P. A. Christensen "Electrochemical aspects of STM and related techniques," Chem. Soc. Rev., 1992, Vol. 21, pp. 197-208. DOI: 10.1039/CS9922100197
- [3] Lee, C.J. Miller, A.J. Bard "Scanning electrochemical microscopy: preparation of submicrometer electrodes", Analytical Chemistry Vol.63, No.1, pp. 78-83, 1991. DOI: 10.1021/ac00001a016
- [4] M. Wong, J. D. McNeill, K. J. Gaffney, N.-H. Ge, A. D. Miller, S. H. Liu, and C. B. Harris "Femtosecond Studies of Electron Dynamics at Dielectric-Metal Interfaces", The Journal of Physical Chemistry B, Vol.103, No.2, pp. 282-292, 1999. DOI: 10.1021/jp983913c
- [5] Y. Shao, M.V. Mirkin, G. Fish, S. Kokotov, D. Palanker, A. Lewis "Nanometer-Sized Electrochemical Sensors", Analytical Chemistry Vol. 69, No. 8, pp. 1627-1634, 1997. DOI: 10.1021/ac960887a
- [6] D.K.Y. Wong, L.Y.F. Xu "Voltammetric studies of carbon disk electrodes with submicrometer-sized structural diameters", Analytical Chemistry Vol. 67, Iss. 22, pp. 4086-4090, 1995. DOI: 10.1021/ac00118a009
- [7] X. Zhang, W. Zhang, X. Zhou, and B. Ogorevc, "Fabrication, Characterization, and Potential Application of Carbon Fiber Cone Nanometer-Size Electrodes", Analytical Chemistry, Vol. 68, Iss. 19, pp. 3338-3343, 1996. DOI: 10.1021/ac9600969
- [8] R. L. McCreery "Advanced Carbon Electrode Materials for Molecular Electrochemistry", Chemical Reviews, vol.108, iss.7, pp.2646-2687, 2008. DOI : 10.1021/cr068076m
- [9] Heller, J. Kong, K.A. Williams, C. Dekker, S.G. Lemay "Electrochemistry at single-walled carbon nanotubes: the role of band structure and quantum capacitance", Journal of the American Chemical Society, Journal of the American Chemical Society Vol. 128, Iss. 22, pp. 7353-7359, 2006. DOI: 10.1021/ja061212k
- [10] N.G. Tsierkezos, E. Rathsmann, U. Ritter "Electrochemistry on Multi-walled Carbon Nanotubes in Organic Solutions", J Solution Chem, Vol. 40, No. 1645, 2011. DOI: 10.1007/s10953-011-9735-x
- [11] Hall, W. G. Matthews, R. Superfine, M. R. Falvo, and S. Washburn "Simple and efficient method for carbon nanotube attachment to scanning probes and other substrates", Appl. Phys. Lett. Vol. 82, No. 2506, 2003. DOI: 10.1063/1.1567049
- [12] Ebbesen, T., Lezec, H., Hiura, H. et al. "Electrical conductivity of individual carbon nanotubes", Nature, Vol. 382, pp. 54-56, 1996. DOI: 10.1038/382054a0
- [13] Y. Saito, K. Hamaguchi, K. Hata, K. Uchida, Y. Tasaka, F. Ikazaki, M. Yumura, A. Kasuya and Y. Nishina "Conical beams from open nanotubes", Nature, Vol. 389, pp. 554-555, 1997. DOI: 10.1038/39221
- [14] N.G. Tsierkezos, S.H. Othman, U. Ritter "Nitrogen-doped multi-walled carbon nanotubes for paracetamol sensing" Ionics, Vol. 19, pp. 1897-1905, 2013. DOI: 10.1007/s11581-013-0930-1.
- [15] J. Kruusma, V. Sammelselg, S.E. Banks "A systematic study of the electrochemical determination of hydrogen peroxide at single-walled carbon nanotube ensemble networks", Electrochemistry Communication, Vol. 10, Iss. 12, pp. 1872-1875, 2008. DOI: 10.1016/j.elecom.2008.09.033
- [16] M.D. Rubianes, G.A. Rivas "Dispersion of multi-wall carbon nanotubes in polyethylenimine: A new alternative for preparing electrochemical sensors" Electrochemistry Communications, Vol. 9, Iss. 3, pp. 480-484, 2007. DOI: 10.1016/j.elecom.2006.08.057

# Nanomaterials In Optical And Optical-Electronic Instrument

V.N. Borschev<sup>1</sup>, A.M. Listratenko<sup>1</sup>, A.V. Kravchenko<sup>1</sup>, A.V. Syddia<sup>2</sup>, N.I. Slipchenko<sup>2</sup>, B.N..Chichkov<sup>3</sup>

<sup>1</sup>LLC «Research and Production Enterprise «LTU»  
st. Novgorodskaya, 3, 1st floor, office 104, Kharkov 61145, Ukraine, tel. +38 (050) 591-24-55  
E-mail: info@ltu.ua

<sup>2</sup>Institute for Scintillation Materials National Academy of Sciences of Ukraine  
Nauky ave. 60, Kharkiv 61072, Ukraine, tel. +38 (057) 341-01-61;  
E-mail: isma@isc.kharkov.com

<sup>3</sup>Institute of Quantum Optics, Leibniz Universität Hannover,  
Welfengarten strasse 1, 30167 Hannover, Germany, tel. +49(511)2771666,  
E-mail: chichkov@iqo.uni-hannover.de

**Abstract** - The current state and development trends of transparent polymer compositions containing nanosize fillers that open up new prospects for optical and optoelectronic instrumentation are considered. Examples of some currently existing polymer and nanopolymer optical systems are given, which clearly show that complexity of structures and microsized of modern optical and optoelectronic products for their successful implementation and wide application require new easy-to-use and not costly optically transparent nanomaterials and their manufacturing technologies.

**Keywords:** - nanoparticles, nanomaterials, nanopolymer optically transparent composites

## I. INTRODUCTION

The priority scientific directions actively developing in recent years include the creation of transparent polymer compositions containing nanosize fillers, which also open new prospects for optical and optoelectronic instrumentation [1].

High-technology and relatively low-cost polymer optics are the means for solving technical problems associated with reducing the labor intensity of assembly, improving the design and reliability of various optical devices.

At the same time, the new polymeric materials have proven to be promising not only for traditional optics, but also for laser optics and technology, which uses polymeric lenses, deflecting plates, prisms.

Luminophor containing polymers and composites are very attractive as luminescent probes, optical media for luminescent solar concentrators, electroluminescent organic LEDs.

The current trend is to create photochrome and other so-called "smart" materials based on optically transparent polymers.

The aim of the work carried out is to search and analyze the results of theoretical and experimental research, literary sources and patents for the last two decades in the field of optical and optical-electronic instrumentation.

Generalizations of the obtained data and recommendations for creating optically transparent nanocomposites of wide application.

## II. POLYMER OPTICALLY TRANSPARENT COMPOSITES

Polymer nanocomposites are polymeric materials that are filled with particles that have at least one of the sizes in the nanometer range. When creating polymer nanocomposites, the primary objective of the polymer matrix is to ensure compatibility with nanoparticles, ensuring uniformity of nanoparticles distribution. As a polymer, filler nanoparticles of noble metals or semiconductors of size 1-20 nm are used, in which strong spatial localization of valence electrons leads to properties different from those of both solid and isolated molecules. The most promising for obtaining quantum-size effects are particles whose size does not exceed 10 nm [2, 3].

With uniform distribution of nanocrystals, absence of their coagulation and monodispersion, nanomaterial is a homogeneous optical environment whose light scattering and rheological properties are similar to those of a polymer matrix even at high concentrations of nanocrystals, while optical and physical properties represent a superposition of properties of the both components. The small size of nanoparticles leads to the fact that polymer nanocomposites can be considered as an optical environment and optical parameters - index of refraction and index of absorption - can be applied for it as a uniform environment. In this respect, nanostructuring is a new way to create optical environments in which the resulting set of properties cannot be achieved by other means. The general property of optical nanocomposites is that the injection of large concentrations of nanocrystals into the matrix leads to changes in the properties and structure of the matrix. The higher the concentration of nanocrystals injected, the greater the changes. This effect is observed regardless of the method of synthesis and composition of the nanocomposite.

The nanoparticles embedded in the polymer do not induce light diffusion if they are distributed uniformly and their size is much smaller than the radiation wavelength. The index of refraction of a polymer with built-in nanoparticles is determined by the next expression:

$$n = \frac{n_1 V_1 + n_2 V_2}{V_1 + V_2} \quad (1)$$

where  $V_1$  and  $V_2$  as well as  $n_1$  and  $n_2$  are the volumes of source material and nanoparticles and the refractive index of source material and nanoparticles respectively.

At a high concentration of nanoparticles, the index of refraction of a nanocomposite with built-in nanoparticles can be much higher than that of the source material, which increases the light output of light-emitting semiconductor light-emitting diodes or light transmission for semiconductor light receivers and optical systems [3, 4, 5].

#### A. Organosilicon composite for connecting optical elements.

The components of some nodes of optical systems are connected together in monoblocks. Various organosilicon compounds are used as a binding substance.

For connection and sealing of optical elements on the basis of a plastic base and a thickener in work [6] a new composition consisting of a base - a mixture of polydimethylsiloxane and polymethylphenylsiloxane liquid with viscosity from 3000 to 40000 mm<sup>2</sup>/sec. at temperature 20°C and a silicon dioxide thickener is offered. At the same time, the composition has a index of refraction of 1.41-1.43. And it works in the temperature range from minus 70°C to plus 300°C. The base of the silicon organic composition is a mixture of polymethylsiloxane liquid (PMS), a general formula:  $\text{CH}_3)_3\text{SiO}[(\text{CH}_3)_2\text{SiO}]_n \text{Si}(\text{CH}_3)_3$ , with a viscosity between 1000 and 50,000 mm<sup>2</sup>/sec and a polymethylphenylsiloxane liquid (PFMS), the general formula:  $(\text{CH}_3)_3 \text{SiO} [(\text{CH}_3)_2\text{SiO}]_k [\text{CH}_3(\text{C}_6\text{H}_5)\text{SiO}]_m \text{Si}(\text{CH}_3)_3$ , where  $k/m = 10/1$ , with viscosity from 10,000 to 20,000 mm<sup>2</sup>/sec in the ratio PMS-60-40%, PFMS - 40-60%.

High viscosity of the base of the composition (3000-40000 mm<sup>2</sup>/sec) and a small change in its value with temperature ensures normal operation of optical devices, smooth running and clear fixation of moving parts in winter and summer.

### III. NANOPOLYMER MATERIALS FOR LIGHTING EQUIPMENT

Nanoparticles such as quantum dots (QDs) are of high interest for use in lighting devices. They can, for example, serve as a non-organic luminophore in the transformation of blue light into other colors with a narrow bandwidth and adjustable frequency of radiation using QDs, in order to be able to obtain high quality white color.

However, the introduction of nanoparticles in many types of polymers leads to the clumping of nanoparticles. Therefore, the relevant technical task is to create an alternative system of nanoparticle - polymer, especially a polymer system with quantum dots, in which the causes of aggregation of nanoparticles would be eliminated, and polymer matrices had high values of glass transition temperature  $T_g$  to 150-200 ° C, for example, photochemically stable silicon-containing polymers. Silicon-containing polymers can have much higher thermal stability and an acceptable light transmission ratio than other organic polymers. However, QDs with conventional surface

protective molecules are not dispersed in silicones and show aggregation resulting in reduced light transmission. Thus, there is a problem of mixing nanoparticles into silicon-containing polymers. The phase separation between nanoparticles and polymers causes QDs agglomeration and drastically reduces the quantum yield and the light transmission ratio through nanoparticle/polymer mixtures.

In [7] we propose a technical decision that allows to obtain well dispersed QD layers in silicones using protective molecules that can be attached to the QDs surface by themselves. A group of silicone-compatible protective molecules was developed. These protective molecules can easily coat QDs and provide formation of uniform QDs/silicone polymer composites. These protective molecules consist of two parts; one part is connected to external unprotected atoms on the QDs crystal surface and the other part is compatible with the silicon matrix. With surface modification, the nanoparticles can be easily mixed with the silicone matrix. The films have high thermal stability and can be used as new phosphors to transform light. When selecting a combination of silicone polymers and surface protective molecules for nanoparticles, it is possible to homogenously mix most common nanoparticles in any specified organosilicon matrix. The formed thin films of the matrix nanoparticles/silicones have a high ratio of light transmittance and are as stable as nanoparticles in purely non-organic matrices.

Such luminescent materials can also be used successfully in lighting devices. This technical decision can be applied in lighting devices that include light sources and light converters. Luminescent nanoparticles can be, for example, include compounds of semiconductor nanoparticles of groups II-VI selected from a group consisting of CdS, CdSe, CdTe, ZnS, ZnSe, ZnTe, HgS, HgSe, HgTe, CdSeS, CdSeTe, ZnSeTe, HgSeTe, ZnSeTe, ZnSeTe, etc.

In another variant of implementation of luminescent nanoparticles can be, for example, compounds of semiconductor nanoparticles of III-V groups, selected from the group consisting of GaN, GaP, GaAs, AlN, AlP, AlAs, InN, InP, InAs, GaNP, GaNAs, GaPAs, AlNP, AlNAs, AlNAs, AlNAs, etc.

Thus, the silicone nanocomposite used in the lighting device according to the proposed technical decision is able to transmit light radiation with high efficiency with a wavelength selected from the range of 420-750 nm at temperatures up to 100°C - 200°C.

#### A. LED with variable index of refraction.

The technical decision proposed in [8] refers generally to light emitting diodes (LEDs) and in particular to LEDs with improved radiation output.

Figure 1 shows an LED with a multi-layer diffuser. The multi-layer LED includes semiconductor material **1**, which forms a p-n transition. Semiconductor material **1** includes GaAsP and GaN semiconductor layers.

Semiconductor material **1** is encapsulated with three optically transparent polymer layers **2**, **3** and **4**. The materials of layers **2**, **3** and **4** are selected so that the index of refraction of the layers gradually decreases from the layer close to semiconductor material **1** to the layer adjacent to the air. This

leads to a reduction in the difference between the index of refraction of semiconductor material **1** and the capsule first layer **2**, between the first layer **2** and the second layer of material **3**, between layer **3** and the third layer **4** and finally, between the third layer **4** and air. Although the technical implementation example consists of three layers, any number of layers can be used to achieve the required technical result. In this example, layers **2**, **3** and **4** have an index of refraction of 3.3, 2.49 and 1.5 respectively, the index of refraction of the semiconductor material GaAsP is 3.4.

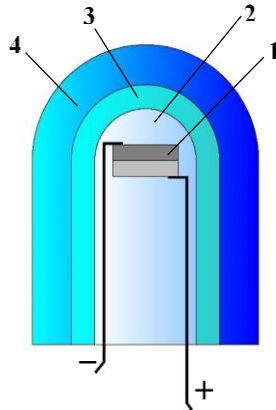


Fig. 1 - LED with multi-layer light diffuser.

Theoretical losses due to Fresnel reflection are determined from the expression:

$$nFr = \frac{4}{2 + \frac{n_2}{n_1} + \frac{n_1}{n_2}} \quad (8)$$

Where  $n_1$  and  $n_2$  are the index of refraction of the adjoining optical layers.

For multi-layer optical coatings, theoretical losses are determined for each boundary layer with a different index of refraction, and by multiplying them, the total light losses in the luminous system are obtained.

Nanoparticles can be obtained using various transparent metal oxides such as  $\text{TiO}_2$ ,  $\text{MgO}$ ,  $\text{ZrO}_2$  and  $\text{Al}_2\text{O}_3$  or a combination of metal oxides. Group II-VI materials that have relatively low light scattering can also be used, including  $\text{ZnSe}$ ,  $\text{ZnS}$  and alloys from Zn, Se, S and Te (Tellurium).

#### B. Optical composition for the light-emitting device.

The technical decision [9] refers to optical compositions and the method of their production for light-emitting devices. The optical composition is a transparent matrix containing organic anionic fragments and metal cations distributed in a matrix. Organic anion fragments and metal cations form a metal-organic complex, while metal cations are able to form transparent nanocrystals when in contact with an agent containing at least one element from the sulfur and selenium group. The method of obtaining the optical composition includes the stages of providing a transparent matrix containing organic anionic fragments; dispersion of metal cations in the matrix; providing contact of the metal-organic complex with the agent to convert at least part of the metal cations into transparent nanocrystals directly in the matrix.

The technical decision allows increasing the index of refraction and reducing excessive scattering in light-emitting devices. In many light-emitting devices that contain a solid-state light source, such as a light-emitting diode, a solid-state light source is encased in a shell of transparent material to increase light extraction from the device and protect the solid-state light source. As a sealing material it is important to use materials with a high index of refraction, such as silicones, as well as with high photochemical stability. A sealing material containing a material with a high index of refraction can significantly increase the efficiency of the system when used in a composite element, such as a wavelength conversion element, or a transparent covering element of such light-emitting devices.

In this technical decision, it was proposed to disperse nanocrystals in the matrix from a material with a high index of refraction, such as a silicone matrix, to further increase the index of refraction of the matrix.

This technical decision proposes the formation of nanocrystals directly inside a transparent matrix. This provides a composition containing a transparent matrix and organometallic complex. As a result, nanocrystals can form directly in a transparent matrix as the organometallic complex contacts an agent containing at least one element, selected from a group of sulphur and selenium. Low mobility of the organometallic complex inside the transparent matrix makes it difficult and prevents aggregation of nanocrystals. The advantages of the composition according to this technical decision are that there is no need for formation or surface modification of nanocrystals before obtaining the optical composition. In addition, the index of refraction of the composition is regulated depending on the time of exposure of the agent containing at least one element selected from the group consisting of sulfur and selenium. In addition, the organometallic complex is not aggregated in the composition, and thus nothing makes nanocrystals prone to aggregation when exposed to this agent. Preventing aggregation leads to the prevention of excessive light diffusion. Nanocrystals are selected from a group consisting of  $\text{ZnS}$ ,  $\text{CdS}$ ,  $\text{ZnSe}$ ,  $\text{CdSe}$  and  $\text{PbS}$ .

A transparent covering element such as a silicone dome can contain an optical composition.

The light-emitting device can contain a solid-state light source and an optical composition located on top of the specified solid-state light source. The light sources can be light-emitting diodes, light-emitting diodes, light-emitting diodes or laser diodes, but other light sources are equally acceptable. For example, LEDs can be semiconductor chips with flat surface, RGB (red, blue, green) LEDs, luminophoric or blue LEDs, purple or UV LEDs in combination with remote luminophor technology. The light-emitting surfaces can be non-coated, coated, etc.

In other applications of the proposed technical decision, the wavelength conversion element for a light-emitting device can contain an optical composition and wavelength conversion material. The wavelength conversion element can be located in direct contact, close to or away from a solid-state light source. In some implementation options, the wavelength conversion material may be quantum dots or quantum rods. When excited by falling light, the quantum dot emits light with a color determined by the size and substance of the crystal. Therefore, by adjusting the size of the dots,

you can obtain light of a certain color. The most famous quantum dots with radiation in the visible range are CdSe dots with the shell, dots from CdS and ZnS. In addition, non-cadmium containing quantum dots such as InP, CuInS<sub>2</sub> or AgInS<sub>2</sub> can be used. The quantum dots have a very narrow emission band and therefore have saturated colours. In addition, the emission colour can be easily adjusted by adjusting the quantum dot size.

The conversion element can also contain non-organic wavelength conversion materials. For example, Ce doped with YAG (Y<sub>3</sub>Al<sub>5</sub>O<sub>12</sub>) or LuAG (Lu<sub>3</sub>Al<sub>5</sub>O<sub>12</sub>). Legalized YAG Ce, legalized by LuAG, ECAS and BSSN.

### C. Optical composition for lighting devices.

The efficient high-power LEDs are often built on blue InGaN emitting materials. In order to obtain a lighting device with an output of the desired colour (e.g. white), suitable wavelength-converting luminophores can be used, which convert part of the light- emitted with long wavelengths to obtain a combination of light with the desired spectral characteristics. Luminophor can for example, be embedded in an organic encapsulating material such as an epoxy resin applied on top of an LED, or it can be preformed into a ceramic self-adhesive layer that can be applied to an LED. The ceramic luminophoric layer is stronger and less temperature-sensitive than conventional organic luminophoric layers. This ceramic luminophore layer is attached to the LED using an optical connection. Traditional materials used for such compounds include optical silicones, which have high photothermal stability required by LED operating conditions and high transparency. However, optical silicones have a relatively low index of refraction, usually between 1.4 and 1.58, compared to the index of refraction of the upper LED layer through which light exits (which can be the upper contact, e.g. GaN (refractive index approximately 2.42) or a growth substrate made of sapphire (refractive index approximately 1.77)). As a result, the critical angle of total internal reflection of light falling on this connection from the LED is relatively small. The light falling on the connection at angles above the critical angle does not come straight out of the LED. In addition, the low index of refraction of the connection compared to the index of refraction of ceramic luminophorus leads to limited transmission due to reflections at the interface. Therefore, a normal optical connection results in a limited output and light transmission.

The objective of the proposed technical decision [10] is to at least partially overcome the above problem and to create an optical connection that can provide improved light output or light transmission from an LED-based lighting device.

Figure 2 shows a lighting device containing LED 4 with an inverted crystal on holder 1 and electrically connected via electrical contacts 2 to contact pads 3 located on the holder. An optical element 6 in the form of a dome is attached to the crystal using compound 5 containing a nanocomposition.

The nanocomposition has a first index of refraction ( $n_1$ ) of at least 1.65 for light with a first wavelength of 350-500 nm and a second index of refraction ( $n_2$ ) of 1.60-2.2 for light with a second wavelength of 550-800 nm. The difference between ( $n_1$ ) and ( $n_2$ ) is at least 0.03. In this case, the first and second index of refraction can be adjusted by changing the volume ratio of nanoparticles to the binding material. The

difference between index of refraction  $n_1$  and  $n_2$  provides different critical angles of total internal reflection for light with different wavelengths at the interface with the material on which this composition is applied. The critical angles can be adjusted for any specific application by adapting the first and second index of refraction of the composition.

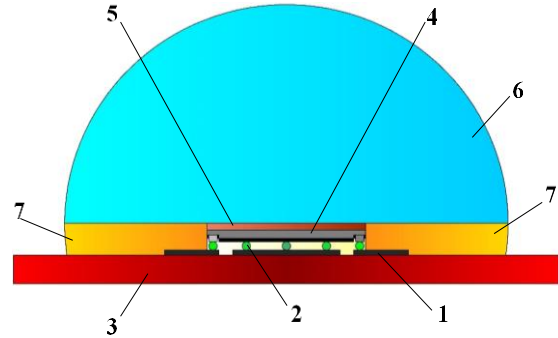


Fig. 2 - Lighting device.

The nanoparticles of the composition can be selected from the group consisting of TiO<sub>2</sub>, ZrO<sub>2</sub>, Y<sub>2</sub>O<sub>3</sub>, Ta<sub>2</sub>O<sub>5</sub>, Nb<sub>2</sub>O<sub>5</sub>, TeO<sub>2</sub>, BaTiO<sub>3</sub> and SiC. Normally nanoparticles contain TiO<sub>2</sub>. TiO<sub>2</sub> has an absorption band in the near UV wavelength range, thus providing high dispersion at desired wavelengths without too much absorption. In addition, TiO<sub>2</sub> is cheap and easily available from commercial suppliers. The volume content of nanoparticles is in the range from 15 to 75% and preferably from 30 to 60% of the composition volume. In addition, the volume ratio of nanoparticles: the binder is from 15:85 to 99:1.

For example, a composition can contain up to 70 vol.% nanoparticles, up to 10 vol.% binder and 20 vol.% air. It is preferable to include at least approximately 5 vol.% binder to have acceptable adhesive or bonding properties. The amount of binder can be very small, only covering the surface of the nanoparticles. The binding component of the composition according to the variants of this technical decision can contain silicates, alkyl silicate and/or alkyl polysiloxane.

Optical element 6 of the lighting device is shaped like a hemisphere. Optical element 6 can contain ceramic material such as YAG or sapphire, or glass with high index of refraction. The index of refraction of the composite constituting compound 5 with a high index of refraction is consistent with the index of refraction of the optical element 6 for the first wavelength, or the index of refraction of the composite can be slightly higher than that of the optical element. Connection 5 with high index of refraction can only be located between the optical element and LED, and conventional filler or binder 7, such as conventional silicone connection, can fill any remaining space between optical element 6 and holder 1. The common filler or binder mentioned above may be transparent or can contain diffusion elements. Alternatively, connection 5 with a high index of refraction, containing a composition according to the variants of this technical decision, can be applied to the entire area of the optical element 6 facing LED 4 and holder 1.

For the preparation of a silicone compound filled with TiO<sub>2</sub> nanoparticles, the polysiloxane silicone fluid medium

was dissolved in a non-polar dispersion of TiO<sub>2</sub> nanoparticles using xylene as a solvent. Dispersant agent was used to stabilize TiO<sub>2</sub> particles in the dispersion. The dispersion was prepared by grinding TiO<sub>2</sub> nanopowder with initial particles of <50 nm size in xylene with addition of dispersing agent. The resulting dispersion was translucent. The silicone resin was a one-component silicone. Alternatively, a two-component silicone could be used and either both components or one of the components could be mixed with the TiO<sub>2</sub> dispersion. After dispersion, most of the solvent was removed by evaporation and the resulting silicone fluids filled with TiO<sub>2</sub> were used for LED contact with the ceramic luminophoric body. In the case of two-component silicone with nanoparticles added to one of the components, the second component was added to the compound. At the end the compound was cured at 150°C for 1 hour. Alternatively, the dispersion of TiO<sub>2</sub> could be obtained by mixing the nanoshredded TiO<sub>2</sub> powder with the silicone resin and dispersing agent. Some solvent could have been added to reduce viscosity. The composition described here can be used to optically connect ceramic elements to LEDs. The composition can also be used as a coating or binder for ground luminophore, particularly for lighting devices with remote luminophore.

#### IV. CONCLUSIONS

The analysis of some existing polymer and nanopolymer optical systems and their applications has shown that the complexity of structures and micro sizes of today's optical systems require new easy-to-use and not costly optical materials. New types of polymer materials are replacing the traditional optical material (glass). In addition to the fact that they make it possible to obtain structures of micro and nanosizes, there is already a real opportunity to select their physical and optical properties - index of refraction, optical uniformity, light transmission, light scattering, stiffness and

others, depending on the specific task. Nanostructured optical polymer materials are increasingly being used to further improve and enhance the efficiency of not only optical devices, but also products of scintillation technology, lighting engineering, photovoltaic, as well as applications in other fields of science and technology.

In this regard, the research aimed at finding new approaches to the creation of nanocomposites on the basis of a wide range of polymers and nanoparticles becomes relevant.

#### REFERENCES

- [1] Smirnov V.I. "Physical foundations of nanotechnology and nanomaterials: a training manual". - Ulyanovsk: UISTU, 2017. - 240 p. (in Russian)
- [2] Serova V.N. "Optical and other materials based on transparent polymers. Serova: monograph". Feder. Agency for Education, Kazan. Gos. Technol. Un-t. - Kazan: KSTU, 2010. - 540 p. (in Russian)
- [3] Burunkova, Yu.E., Denisyuk, I.Yu., Shekhanova EB, Fokina, M.I. "Optical polymer nanocomposites". - St. Petersburg: ITMO University, 2017. - 80 p. (in Russian)
- [4] Burunkova. Yu. E., Semina S.A., Kaporsky L.N., Levichev V.V. "Nanomodified optical acrylate composites". Optich. J. 2008 - v. 75, No. 10 p. 54-58. (in Russian)
- [5] Vilchinskaya S.S., Lisitsyn V.M. "Optical materials and technologies: a training manual". Tomsk Polytechnic University. Tomsk: Publishing House of Tomsk Polytechnic University. 2011.- 107 p. (in Russian)
- [6] Patent RF № 2505569 "Organosilicon composition". Patent publication: January 27, 2014 (in Russian)
- [7] Patent RF № 2627378 "New materials and methods for dispersing nanoparticles". Patent Publication: 08/16/2017 (in Russian)
- [8] Patent US № US6717362 "LED with variable refraction". Patent Publication: 04/06/2004
- [9] Patent RF № 2655358 "Optical composition". Patent Publication: 05/30/2018 (in Russian)
- [10] Patent RF № 2567915 "Optical composition". Patent publication: November 9, 2015 (in Russian)

# Short Review of Features a Low Dimensional Electron Systems on Helium Layers at Experimental Study. Possible Applications

Nikolaenko V. A.

B. Verkin Institute for Low Temperature Physics and Engineering of NAS of Ukraine, Prospekt Nauky, 47,  
Kharkov - 61103, Ukraine  
E-mail: nikolaenko@ilt.kharkov.ua

**Abstract** — a new glance study of row the physical effects and models for practice realization give the modern nanotechnologies. The phenomena the phase boundaries as well as the phase transitions attract the special attention of researchers condensed matter physics. Using surface electrons (SEs) over layer helium on substrate as model can aid to study some fundamental and applied questions nano-electronic. This short review considers some experimental studies the low-dimensional electronic systems over helium layers on substrates. A number possible application of SEs over helium layers for creating nano-devices and sensors is presented.

**Keywords** — quantum dot, quantum wire, liquid helium, surface electrons, IR detector, quantum bit

## I. INTRODUCTION

A modern nanotechnologies lead to new understanding laws of the low dimensional electron systems and they applications. The especial properties of the two-dimensional layer of surface electrons over helium (SEs) at theoretical analysis were noticed by Cole and Cohen (USA, 1969) [1] and Shikin (Ukraine, 1970) [2]. A many of articles and a number of monographs are devoted this topic (for example, [3]). The surface electron is localized in a shallow potential well at a relatively large distance from the surface because to the low permittivity of liquid helium and its weak polarization. The motion SEs along the surface is quasi-free. The limitation caused only by both the scattering on helium atoms in vapor at temperatures above 0.9 K and on riplons (quantized oscillations of surface) at a lower temperature. The presence of a solid rough substrate under helium surface leads to a thermo- activation carry of electrons. The motion of the SE transverse to the surface is quantized by the hydrogen-like spectrum. Modulation of surface properties in one or two directions reduces the dimension of the electronic system to one-dimensional (1D, quantum wire) or to zero-dimensional (0D, quantum dot, an artificial atom). Among conducting matter the SEs has preferable because high homogeneity carriers and possibility broad changing in one experiment both the charge density and the type of scatters. The disadvantage the system of surface electron over helium is the limitation of the electron concentration due to the development of electro-hydrodynamic instability with the loss of electrons. The peculiarity of classical and quantum manifestations take a place at both the restrict system of SEs and the phase transitions there. The analysis a quantum

characteristic of SE over various substrates was carried out in [4]. The system SEs is as well as the object of research and the classical model of the conducting solid-state matter and the basis for the construction chips of the sensitive devices and the quantum bits.

The results experimental studies by transport method the low-dimensional SEs are given below. Some the features low-dimensional SEs proposed to use for the creating nano-devices. The structure of review is next. 1. Introduction. The experimental setup and measurement methods at study low dimensional electron systems over substrates are given in subparagraph 2. The row factors leading to restrict of the SEs including the dipton system and the features manifestations of specific properties is considered in 3(A-D). In 4(A-D) proposed possibilities to use of physical properties SEs in restrict geometry for creating nano-electronic devices.

## II. EXPERIMENTAL SETUP AND MEASUREMENT METHODS

The simplest methodology for the experimental study of the electronic systems is the transport method. The Sommer-Tanner method [5] is preferred for study surface electrons, which considered the conductance of the electrons coupled in

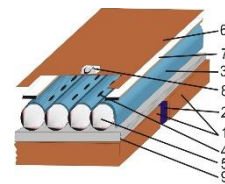


Fig. 1. Sketch of Sommer-Tanner device. 1D system of SE (for example). 1 - measurement electrodes; 2 - screening stripe; 3 - He film; 4 - Q1D system of surface electrons; 5 - substrate (row of light guides); 6 - upper pressing electrode; 7 - guard ring; 8 - electron source (tungsten thread); 9 - Si-plate.

capacitive manner with measuring electrodes. The system SEs from a source of free electron formed above the helium layer in the gap of a charged capacitor (Fig.1). The electron concentration,  $n$  is set by the compensation the external electric field,  $E$  by SEs field and definite by expression  $E=ne$ . Another, more sensitive but more complicated method for studying SEs is microwave - resonant one where SE are localized above the substrate inside resonator (Fig. 2,). The quality of loaded cavity is determined by decreasing signal from  $V_1$  to  $V_2$  as  $Q = \omega_0 \tau / [2 \ln(V_1 / V_2)]$  (here  $\omega_0$  and  $\tau$  are the resonance frequency and the damping decrement

correspondently).

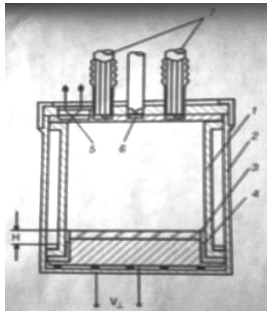


Fig. 2. Sketch of HF resonator for SEs study. 1 - cavity; 2 - vacuum chamber; 3 - substrate; 4 - bottom of cavity; 5 - heating filament; 6 - tungsten needle as source ions; 7 - HF-coaxial coupling lines.

The method was tested early by loading SEs [6].

A novel of this method was proposed as next [7]. The cavity bottom is coplanar combination of rings insulated to one other that is the Corbino geometry. It is the measurement system of the matter analyzes up to 50 MHz. Here the conducting properties of SEs definite by Sommer-Tanner method. There is too the possibility besides the low frequency analyze of matter to perform the modulation of cavity HF signal enhancing sensitivity of measurement.

### III. EXPERIMENTAL STUDIES SOME PROPERTIES OF SEs IN RESTRICTED GEOMETRY

#### A. Quantization conductivity of surface electrons over superfluid helium in potential wells of charged profiled substrate [8]

The modern nano-technologies have lead to creating 1D conducting systems: charges move free in one direction and

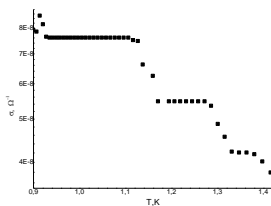


Fig. 3. The temperature dependence Q1D conductivity of surface electrons over helium in potential wells of charged profiled substrate. The potentials of charge both the substrate and SE is near 15V.

others displacement are quantized. The study of a quasi-one-dimensional (Q1D) system in semiconductors motivated creating this system based on SEs. The Q1D-SE system over helium in grooves of profiled substrate at pressing field,  $E$  was proposed and realized in [9, 10] and detailed in [11]. The SE's system is high homogeneity and here can be changed in separate experiment both the electron density and the width lines. The depth of potential well Q1D-SE system estimated as  $\varphi \sim e E \delta$  ( $\delta$  is deflection of liquid surface of radius,  $R$  in groove). The equidistant quantized 1D spectrum is  $\omega^2 = eE/mR$ .

In this experiment electrons from a source emitted to substrate forming charge stripes and then into grooves with helium for forming SE lines. The charged stripes shift Q1D-SE spectrum on the value  $\omega^2 \sim \pi^2 e^2 n_x / m a^2$  ( $n_x$  is the density of linear charge and  $a$  is distance between charges). The temperature dependence of conductivity,  $\sigma$  is here step-like at  $T < 1.4K$  (Fig. 3). Observed feature isn't described by scattering SE on helium atoms in gas or on ripples. The inter-level interval  $\hbar \cdot \omega$  ( $\hbar$  is Plank's constant) corresponds a plateau of dependence. Parameters of steps in various experiments were various.

#### B. The conductivity phenomena in Q1D electron system over superfluid helium at crystallization [12].

The conductivity,  $\sigma$  of 1D (Q1D) is sensitive to both the boundary conditions and the phase transitions of the electron system. The special place there is Q1D electron system over liquid helium. The system is formed by SEs pressed by electric field to the bottom of the liquid grooves in profiled substrate.

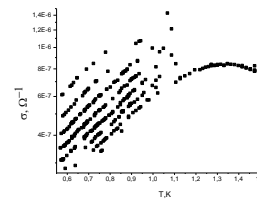


Fig. 4. The conductivity Q1D electron system over superfluid helium at crystallization (dependence  $\sigma$  vs  $T$ ).

In present work for investigation of value  $\sigma$  has been used the Q1D-SEs channels by the width of  $3 \times 10^{-5}$  m (near to 2D system). The experiment performed at temperature range  $T = 0.5 - 1.5K$  with the effective electron density  $2.4 \cdot 10^{13} m^{-2}$ . The result measurement is shown on graph 3. Here a transition to the electron crystal,  $T_c$  is 1.1K. One can see lower  $T_c$  eight parallel tilted lines. The lines of  $\sigma$  vs  $T$  decrease exponential with decreasing temperature. The thermo activation energy expressed as  $\Delta^* = (T1 \cdot T2) \cdot \exp(\sigma1 / \sigma2) / (T2 - T1)$  (here  $\sigma1$  and  $\sigma2$  are the conductivities corresponded to  $T1$  and  $T2$ ) is about 1 K. The effect can relate Volf-Bregg constructive interference of an electron waves in the lines of Q1D at Wigner crystallization. The experimental investigations are continuing.

#### C. Transition to the self-localized state of electrons over thin helium film on the structures substrate [13]

Above the surface of liquid helium in a strong effective electric field, there is a formation of a disk-like surface anion (SA): the complex, consisting of an electron and deformation of the liquid surface below it [14]. SA has a low mobility and easy definite by transport method.

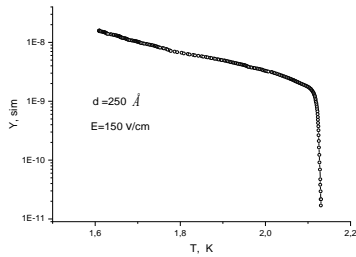


Fig.5 Transition to the self-localized state of electrons over thin helium film on the structures substrate (transport method measurement).

According to the experimental and the theoretical data the SE – SA transition depends on the thickness of the film,  $d$ , the effective electric field,  $E$ , and temperature,  $T$  (or a density of the gas phase). The value  $E$  as function  $d$  is expressed  $(Q_d \cdot e) / (4\pi \epsilon_0 d^2)$ . (here  $Q_d$  is effective polarization of substrate). The ratio of SE/SA – mobility's at low temperature is  $(4 \eta e E) / (\pi \alpha^{3/2} m^{1/2})$ , here  $\eta$  and  $\alpha$  is the viscosity and the surface tension of liquid helium accordingly.

This work concedes transition to the surface anion state (SA) on the helium film in the pores of a structured substrate. For plate was selected of mono-crystal Si an orientation of 1-0-0. The size of plate is  $5 \times 6 \times 0.3 \text{ mm}^3$ . The substrate is structured by grid of pore by diameter of  $2 \mu\text{m}$  in  $4 \mu\text{m}$  steps. The electrostatic modeling of a cylindrical pore shows the preferential localization of electrons on the thin film inside pore. Figure 5 presents the experimental dependence of conductivity  $Y$  vs  $T$  at conditions  $d = 25\text{nm}$  and outer field  $E = 150\text{V/cm}$ . The transition SE – SA takes a place at temperature  $\sim 2.1\text{K}$ . Others study show shift of SE – SA transition to lower  $T$  at decreasing in  $d$ .

#### D. The dipton system in helium film over substrate

The experimentally was appointed the dielectric substrate can be charged by positive ions and the helium film charged by SE forming dipton system [15, 16]. The positive ion (+ i) is "snowball" with radius  $0.6\text{-}0.7 \text{ nm}$  and mass like  $\sim 40M_4$  ( $M_4$  is mass of He atom) which strong coupled with dielectric substrate. Because large mass of

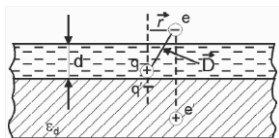


Fig.6 Sketch of the dipton system in helium film over substrate.

ions the electron system on surface helium film is adiabatic like in atom of solid state. The main electric field of dipton system is  $E_l = 2e / [(1 + \epsilon_s) d^2]$  (here  $\epsilon_s$  is the substrate dielectric constant) and be in superposition with outside electric field,  $E$ . In parabolic potential well induced by positive ion the quasi-harmonic spectrum SE along surface takes a place. The spectrum depends on thickness helium film,  $d$  and the basic frequency is  $\omega_d^2 = 2e^2 / [(1 + \epsilon_s) m d^3]$ . The SE-QD localization size is  $L = L = (\hbar / m\omega_d)^{1/2}$ . For  $d \sim 30\text{nm}$  and  $\epsilon_s \sim 4$  the value of  $L$  is  $\sim 8 \text{ nm}$ .

## IV. APPLIED OF THE PHYSICAL PROPERTIES SE IN RESTRICT CONDITIONS OVER SUBSTRATES FOR THE PRACTICE REALIZATION (PROPOSITIONS)

### A. Selective MW detecting using the surface electrons over liquid helium into pores of the structured substrate [17].

As signed upper the modulation of the substrate properties lowers the dimensionality of

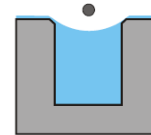


Fig.7 Surface electron over liquid helium in pore of substrate..

the SE system up to quantum dot (QD). Here proposed for the detecting of a microwave (MW) radiation utilized the harmonic spectrum of QD - SEs over the distorted helium surface in pores of structured substrate (figure). The transport of SE over silicon structured substrate was considered early [18]. The selective MW frequency coincides with a along harmonic spectrum of SE expressed as  $\omega = (eE/mR)^{1/2}$ . Here the value  $R = 2\alpha/\rho gH$  is the radius distortion of helium surface over pores ( $\alpha$  and  $\rho$  are surface tension and density of helium, correspondently;  $g$  is acceleration of gravity force and  $H$  is distance between surfaces of the substrate and of helium under it). The spectrum scale  $0.1 - 1\text{K}$  is governed by values  $R, E$  and by charge on substrate too. The stimulated by MW- radiation the transition between a longitudinal SE states changes the local potential is fixed by sensitive chip. It is possible the selective detecting of sub-mm radiation too by SE hydrogen like energy spectrum of SE. The Umov-Poiting vector must be tilted to surface here. The composition of device is: the porous silicon substrate; reading electrodes (pixels) which connected to potential sensitive sensors (field effect transistors, one-electron transistor - SET, or others) on the rear side; the potential grid above the substrate and a source of free electrons.

### B. IR detector using transitions to the self-localized state of electrons over helium film on the structures substrate (see subparagraph 3C).

The IR detector based on stimulate by radiation transition from a surface electron state (SE) to surface anion state (SA) on the helium film in the pores of a structured substrate [19]. As considered in [13] the transition depends on parameters  $d, E$ , and  $T$

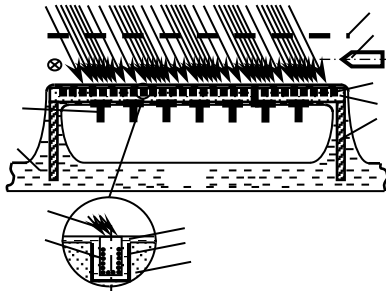


Fig.8. The composition of IR detector with SE in porous of structured substrate (see text and subparagraph 3c).

The electrostatic modeling of a cylindrical pore show the preferential localization of electrons on the thin film inside pore. The IR image is corresponds to the equipotential relief of the substrate, induced by the contrast of the conductivity of the electrons in the pores. The frequency range and the sensitivity of the detector are determined by the thermal sensibility to the radiation of the nano-covering of the pore walls and the operating temperature. The basic composition of device can be follows (see figure 8): the porous silicon substrate with reading electrodes (pixels) on the rear side, a collector grid above the substrate and a source of free electrons. Estimates demonstrate that the sensitivity of the IR detector reaches the quantum limit and that exceeds the semiconductor analog, the feature of which is both the formation of wave modes of radiation and the electro-optical effects in a porous substrate.

So the basic composition of device (figure 8) can be universal tool for study and applied of interaction microwave irradiation with surface electrons.

### C. Sub-mm detecting using diplons in helium film [20]

In the parabolic potential well over positive ion the quasi-harmonic spectrum SE along surface is formed as  $\hbar\omega_l$  (like in 1D system). The quantized spectrum depends on thickness helium film,  $d$  and the basic frequency is considered in subparagraph 1D. The energy  $\hbar\omega_d$  depends as  $d^{3/2}$  and the estimates give the energy scale near 50K at  $d = 30\text{nm}$  and  $\sim 250\text{K}$  at  $d = 10\text{nm}$ , accordingly. So the spectrum corresponds to terahertz (THz) range and can be shifted either to area "soft" or area "hard" irradiation by changing the helium film thickness at smooth substrate. The normal directed electromagnetic irradiation corresponding frequency causes change both the electron state in diplon system and the potential relatively substrate. The main electric field of diplon system  $E_l = 2e/[(1+\epsilon_s) d^2]$  be in superposition with outside electric field,  $E$ . The change of value,  $E$  leads to adjusting irradiation frequency to harmonic frequency of diplon system. The experiment shown the density of the diplons varies in wide range up to  $10^{15} \text{m}^{-2}$ . The composition of device can be slimily to one for electrons over helium film on the structures substrate (figure 8). The CCD matrix as substrate with the individual pixels control makes device to read the charging relief under the thin substrate formed by irradiation image.

### D. Longitudinal quantum oscillations of surface electrons over helium film on a structured substrate for quantum computing [21]

Modeling the micro- nano-objects and the complex physical processes revolutionize quantum computer (QC). The quantum bit (QB) operates in superposition of two quantum states. The quantum entanglement of  $n$  bits for some time is essence of QC with  $2^n$  basis vector in opposite to classical logic with  $n^2$  basis. The quantum dots for QBs are preferred. The concept of Platzman and Dykman (Science., 284, p. 1967 (1999)) considers for QC a hydrogen-like levels of the surface electrons (SEs) on helium covered lattice of microelectrodes. Using both the Stark's shift of Ridberg's levels into resonance with mkm-radiation and the normal tunneling the SEs is the essence of QB tuning and reading the results. Here proposed the use of the longitudinal spectrum of SEs over the lattice of governing microelectrodes coated with thin helium film on the dielectric plate. The longitudinal spectrum of electrons depending on the film thickness  $d$  is  $\omega_d^2 = e^2 / [(1 + \epsilon_s) m d^3]$  (here  $\epsilon_s$  is the dielectric constant of plate). The energy of the inter-level transition vs  $d$  is shown

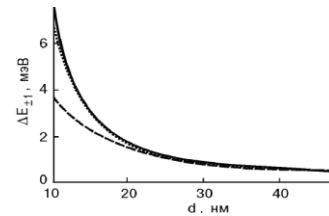


Fig.9. Dependence of energy interval,  $\Delta E$  from thickness of helium film,  $d$ .

in the figure 9 (bottom curve is smooth He film and He film with dimple is upper curve). The size of localization of electron in potential well,  $L$  is like in subparagraph 2D. The Wigner crystallization (WC) temperature at the electron density  $n_s$  is  $T_c < 0.226 n_s^{1/2}$ . The quantum melting of WC and overlapping of the electron wave functions in periodic potential of a lattice takes place at energy of the electron  $\epsilon > (\pi n_s \hbar^2 / 2 m)$ . Like theory is in work [22]. The smoothly of plate surface is additional need and this is achievable with modern nanotechnology. On estimates, at  $n_s = 10^{14} - 10^{15} \text{m}^{-2}$  interval of  $T_c = (2.6 - 7.15) \text{K}$  and  $\epsilon \sim (0.14 - 1.4) \text{K}$ ; the value of  $L \sim 10\text{nm}$  at  $d \sim 30\text{nm}$ . The QC can operate at super-low temperatures ( $\sim 10 \text{mK}$ ).

## V. CONCLUSIONS

Among conducting matter the SEs has preferable because high homogeneity carriers and possibility broad changing in one experiment both the charge density and the type of scatters. The electrons (SEs) over layer helium on substrate as ideal model can aid to study some fundamental and applied questions nano-electronic. Modulation of surface properties under SE in one or two directions reduces the electronic system to one-dimensional (1D, quantum wire) or to zero-dimensional (0D, quantum dot, an artificial atom).

This short review considers preparation, experimental studies of row the low-dimensional electronic systems over helium layers on substrates. A number possible application of

SEs over helium layers for creating nano-devices and sensors is presented.

The review is based on the materials of experimental studies by the method of SEs transport under conditions of quantum constraints and phase transitions. The works considered in the brief review were carried out over a long period of time, tested at a number of international conferences and confirmed by publications. A number of them are given in the references. The review is divided into two sub-topics: experimental studies and possible applications the SEs in restricted conditions.

The section "Experimental studies some properties of SEs in restricted geometry" concerns next questions.

- Quantization conductivity of surface electrons over super fluid helium in potential wells of charged profiled substrate.
- The conductivity phenomena in Q1D electron system over superfluid helium at crystallization.
- Transition to the self-localized state of electrons over thin helium film on the structures substrate.
- The diplo system in helium film.

The last object take a place number of advantages. For example, the high limiting concentration which leads to the lifting of degeneracy electron system and the band motion of electrons in it, also here has place an ideal parabolic potential well for electron over ion. The studies in the above questions are not closed.

In the section "Applied of the physical properties SE in restrict conditions over substrates for the practice realization" was proposed next.

- Selective MW detecting using the surface electrons over liquid helium into pores of the structured substrate.
- IR detector using transitions to the self-localized state of electrons over helium film on the structures substrate.
- Sub-mm detecting using diploons in helium film.

The review is completed with a proposal for use without loss of electrons next idea.

- Longitudinal quantum oscillations of surface electrons over helium film on a structured substrate for quantum computing.

#### ACKNOWLEDGMENT

The author hopes that this work will be stimulating for further research and use in nanoelectronic of the unique features of surface electrons under quantum conditions.

#### REFERENCES

- [1] M.W.Cole, M.H Cohen,"Image-potential-induced surface bands in insulators," Phys. Rev. Lett. vol. 23, 1969, p.1238.
- [2] V.B. Shikin "About moving of the helium ions near boundary vapor-liquid," JETPH, v. 58, 1970, p. 1748. (in Russian).
- [3] V.B. Shikin and Yu.P Monarkha, "Two-dimensional charged systems in liquid helium," Moscow, 'Nauka', 1989.
- [4] V.A.Nikolaenko, and A.G.Pashchenko,"Detectors of infrared radiation at the surface electrons for registration and visualization",

- Telecommunications and Radio Engineering, v.75(6), 2016, pp.549-562 .
- [5] W.T.Sommer and D.J.Tanner,"Mobility of electrons on the surface of liquid 4He," Phys. Rev. Lett.,v.27(30), 1971, pp.1345-1349.
- [6] Yu.Z. Kovdrya, F.F.Mende, and V.A. Nikolaenko, "High-frequency conductivity of electrons above helium film in the regime of localization on substrate potential inhomogeneities", Phys. Nizk. Temp., v.10 (11), 1984, pp. 1129–1140 (in Russian).
- [7] I.N. Bondarenko, V.A. Nikolaenko, A.V. Polishchuk,. "The cavity with the Tunnel Diodes and Corbino-Electrodes for Analyze Dielectrics and Semiconductors." Proceedings of the IEEE 9th International Conference on Nanomaterials: Applications and Properties, 2019, 9075672.
- [8] A. Nikolaenko, A. S. Smorodin, S. S. Sokolov. "Differential conductivity of surface electrons over superfluid helium in potential wells of charged profiled substrate" International research and practice conference. Nanotechnology and Nanomaterials (NANO2018), 2018, abstract book, p.637.
- [9] Yu. Z. Kovdrya, Yu.P.Monarkha, "1D electron system over liquid helium" Fiz. Nizk.Temp., v.12, 1986, pp.1011-1015.
- [10] Yu. Z. Kovdrya, V.A. Nikolaenko,"Q1D electron system over liquid helium",Fiz. Nizk.Temp., v.18, 1992, pp.1278-80.
- [11] S.S. Sokolov, Guo-Qiang Hai and Nelson Studart,"Mobility of electrons in Q1D channel on the liquid helium surface",PRB, v.51, 1995, pp.5977-5988.
- [12] A. Nikolaenko, A. S. Smorodin, S. S. Sokolov," The conductivity phenomena in Q1D electron system over superfluid helium at crystallization", International research and practice conference Nanotechnology and Nanomaterials (NANO2019), 2019, abstract book, p.591.
- [13] A. Nikolaenko, Ya. Yu. Bezsmolnyy, S. S. Sokolov,"IR detector using transitions to the self-localized state of electrons over helium film on the structures substrate"
- [14] V.B. Shikin," Disk-shaped electron bubbles in gas helium," JETP-Lett. v.80(6), 2004, pp. 472-476.
- [15] Yu.P. Monarkha, Yu. Z. Kovdrya,"Dipol complexes in superfluid helium film," Low Temp.Phys. , v.8, 1982, pp. 215-218 (in Russian).
- [16] V.I. Karamushko, Yu.Z. Kovdrya, F.F. Mende, V.A. Nikolaenko, "UHF electromagnetic absorption by electrons above the helium film", Fiz. Nizk.Temp., v.8(2), 1982, pp.219-222.
- [17] Ya. Yu. Bezsmolny V. A. Nikolaenko, "Selective MW detecting using the surface electrons over liquid helium on structured substrate," International research and practice conference Nanotechnology and Nanomaterials (NANO2018), 2018, abstract book, p.756.
- [18] A.V. Smorodin, V.A. Nikolaenko, S.S. Sokolov, L.A. Karachevtseva, and O.O. Lytvynenko, "Transport properties of surface electrons over structurized substrate", Low Temp. Phys., v.38, 2012, pp. 1158-1166.
- [19] V.A. Nikolaenko, A.G. Pashchenko, Ya.Yu. Bessmolny,"Infrared Receiver On Electron Transitions Into The Autolocalized State Over The Helium Film On The Structured Substrate", Telecommunications and Radio Engineering, v.77, 2018, pp. 47-60. (DOI: 10.1615/TelecomRadEng.v77.i1.50) .
- [20] V.A. Nikolaenko, A.G. Pashchenko, "The selective detecting of the sub- mm band irradiation by the dyplon system in superfluid helium film", Proceedings of the IEEE 8th International Conference on Nanomaterials: Applications and Properties, 2018, P5-18, 04MIT20.
- [21] V.A. Nikolaenko, A.G. Pashchenko,"Longitudinal quantum oscillations of surface electrons over helium film on a structured substrate for quantum computer", International research and practice conference. Nanotechnology and nanomaterials (NANO2020), 2020, (to be published in abstract book).
- [22] V.I.L Ginzburg., Yu.P. Monarkha, "Surface electrons in helium over macroscopic structures" Fiz. Nizk. Temp., v.4, 1978, pp. 1236-1239.

# RECURSIVE DEVICES OF BINARY DATA SORTING DEVICES

Volodymyr Hryha, Taras Benko, Igor Kogut, \*Oksana Dolishnyak

Vasyl Stepanyuk Precarpatian National University, Computer Engineering and Electronics Department  
 \*Ivano-Frankivsk National Medical University  
 V.Stusa 17-59, Ivano-Frankivsk, Ukraine, 76006, +38(096)- 0147200, igorkohut2202@gmail.com

**Abstract** — Features of construction of recursive devices on the basis of space-time graphs for synthesis of specialized devices of sorting of numbers are considered. As a result, a comparative analysis of the synthesized models of recursive devices on PLIC was performed.

**Keywords** — sspace-time graph, tier-parallel form, algorithm, sorting, synthesis, PLIC.

## I. INTRODUCTION

In general, computer systems are divided into universal and specialized. Many of the computer elements of these systems are used to solve various problems of digital signal and image processing, automated control problems, computer modeling problems and others. The use of universal single and multiprocessor systems to solve the above problems is sometimes limited to achieving the required technical parameters that these systems may not provide in real time and also shows the cost price of these systems. The use of specialized computer systems involves the creation of new computer elements focused on the execution of specific algorithms or a class of algorithms, which will no longer run on existing but on created computer tools. Currently, using powerful CAD to design a variety of devices, this approach is a serious alternative to the first approach. This paper considers methods for constructing recursive specialized sorting devices based on the technique of space-time graphs, which are applied to invariant to the offset or independent of the input data algorithms.

This article investigates the methods of constructing recursive devices on the example of the algorithm for sorting numbers using the technique of spatio-temporal graphs, and also attempts to synthesize the obtained recursive sorting devices on PLIC by Xilinx.

## II. ALGORITHM SELECTION AND DESCRIPTION

To study the methods and ways of construction recursive devices based on space-time graphs selected algorithm for sorting data by the method of "bubbles". Sorting is the most commonly used data processing operation used in scientific calculations. In Fig.1. the graph of the algorithm for sorting the sequence of input numbers is shown.

The output of the graph is a new sequence of output numbers  $y_i$ , which consists of input numbers rearranged in the desired order.

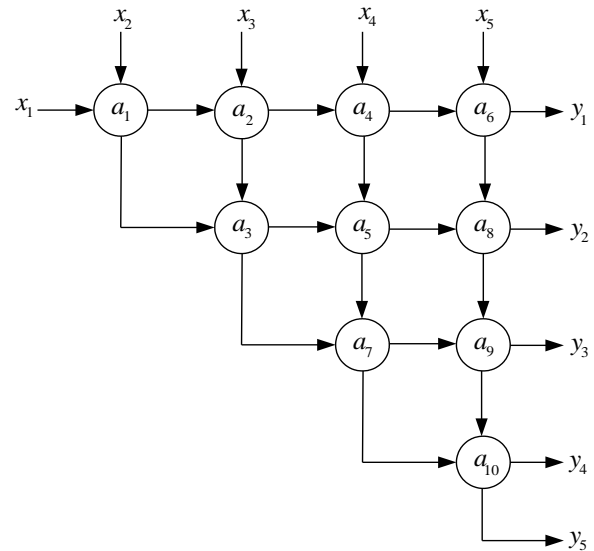


Fig.1. Graph of the algorithm for sorting numbers by the method of "bubbles"

The computational graph of this algorithm consists of ten vertices that are used to sort the five input numbers. Each of the vertices performs the operation of comparing two input numbers and at the corresponding outputs we obtain the maximum and minimum number.

In Fig.2. the structural scheme of one operation of comparison of the described algorithm of sorting of numbers by a method of "bubbles" is represented.

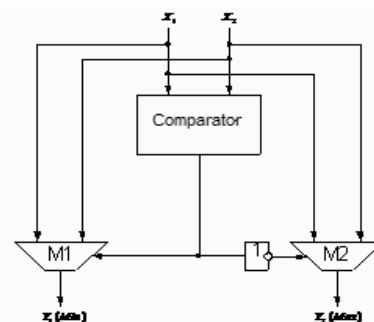


Fig.2. Block diagram of the operation of comparing the sorting algorithm.

This block diagram consists of a comparator whose inputs are fed two numbers for comparison, and two multiplexers, which are controlled by the output signal of the comparator and simultaneously output their maximum and minimum number.

### III. SPATIO-TEMPORAL DESIGN OF RECURSIVE SORTING DEVICES.

The technique of spatio-temporal transformation of graphs will be used to construct recursive sorting devices. This requires a graph of the computational algorithm for sorting numbers, which is presented above in parallel, so as to see which operations are performed in parallel. The image of the computational graph of the algorithm in tier-parallel form allows to reveal parallelism and to find compromise space-time relations. In the tier-parallel form of the computational graph of the algorithm, all vertices of one tier depend on the results of the vertices of the previous tier, and do not depend on the vertices of the next tiers. The tier-parallel form determines the degree of parallelism of the graph (maximum number of vertices on one tier), as well as the minimum possible calculation time of this algorithm (number of tiers). Note that information and bypass vertices will be used to convert the computational graph of the number sorting algorithm into a tiered-parallel form.

In fig. 3. the tiered-parallel form of the selected sorting algorithm is shown.

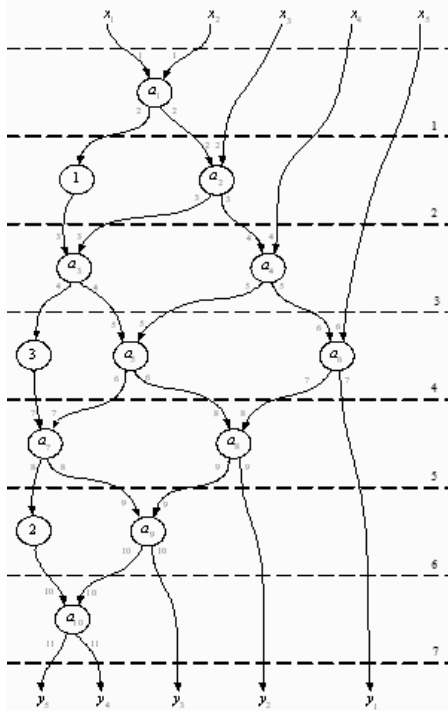


Fig. 3. Tiered-parallel form of number sorting algorithm.

The tier-parallel form of this graph of the algorithm is divided into seven tiers and consists of ten operational vertices and three bypass vertices. The operational vertices perform a comparison operation and the bypass vertices with the specified numerical values of the delay cycles delay the data that passes in an arc through the corresponding tier and do not participate in the processing on this tier. It should be noted that the submission of input data and the issuance of results should also be delayed on the column bypass vertices. In order to construct a recursive device, it is necessary to perform a spatio-temporal transformation of the tier-parallel form of the algorithm to obtain a recursive spatio-temporal graph. To this end, in Fig.3. next to each operational vertex the numerical values of cycles of giving and giving out of

data taking into account consecutive time execution of each vertex as the recursive space-time graph will consist of one vertex are represented.

In fig. 4. shows a minimized recursive space-time graph.

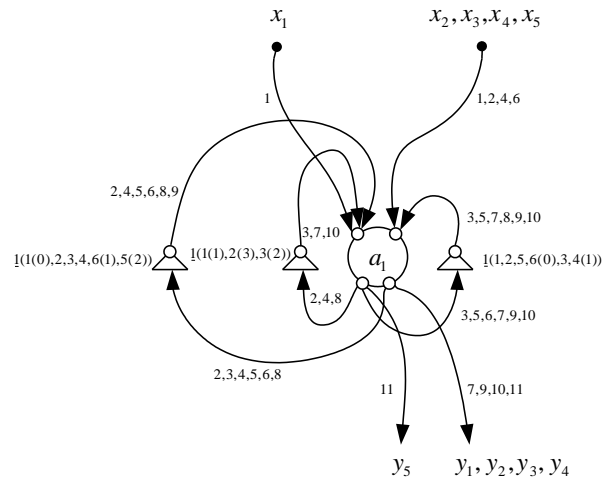


Fig.4. Minimized recursive space-time graph of number sorting algorithm.

This graph consists of one vertex, which sequentially in time performs each operation of the selected algorithm. The top of the graph has 2 input and 2 output nodes. Near the arcs that come to the input and output nodes recorded clock numbers during which the necessary data is given, and near the triangular delay elements recorded the sequence of numbers coming to the vertices of the graph and their delay for the required number of cycles. Note that having a recursive space-time graph, you can proceed to the construction of the structure of the recursive device. We distinguish two methods of constructing recursive devices. The essence of the first method is to build a recursive device based on a basic recursive space-time graph. The basic recursive space-time graph consists of one vertex and the number of its arcs corresponds to the number of arcs in the tier-parallel form of the graph given above. In Fig.5. the basic structure of the recursive device of sorting of numbers constructed on the basis of the basic recursive space-time graph is shown.

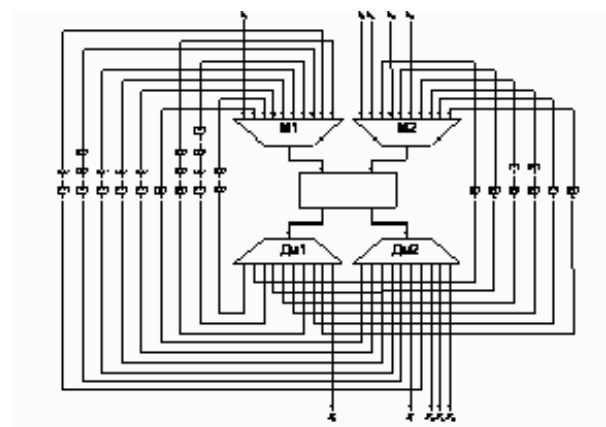


Fig.5. Basic structure of a recursive device.

The basic structure of the recursive number sorting device consists of an operating unit, two multiplexers that supply data for processing, two demultiplexers with which the

issuance of intermediate and main results and 29 registers that delay the data for the appropriate number of cycles. It should be noted that the input and output nodes of the space-time graph in the diagram correspond to multiplexers and demultiplexers. The top of the graph, which sequentially performs all the necessary operations in time, corresponds to the operational unit of comparison of numbers, and the arcs with delay elements correspond to the feedback with the registers of data delay.

The second method of constructing recursive devices follows from the first. In Fig.4. shows a minimized recursive space-time graph in which the temporal minimization of arcs is performed. Output arcs that exit from the same output node and enter the same input node of the space-time graph can be combined into one arc, as each of these arcs is triggered at different times.

In Fig.6. the minimized structure of the recursive device of sorting of numbers constructed on the basis of the minimized recursive space-time graph is shown.

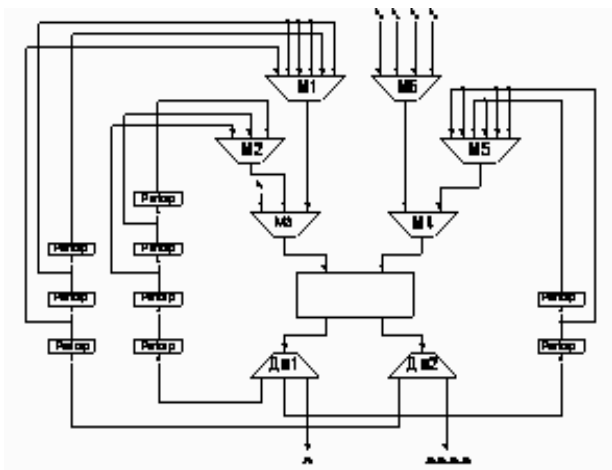


Fig.6. Minimized structure of recursive device

The minimized structure of the recursive device, in contrast to the basic structure, consists of nine registers that delay intermediate data and intermediate processing results, two demultiplexers with fewer outputs and six multi-input multiplexers, which allows you to design a recursive device with less hardware.

#### IV. RESEARCH RESULTS.

In this paper, using the Aldec Active-HDL tool, models of basic and minimized recursive sorting devices were developed. The operation of the main devices at the

functional level was simulated, and also, with the help of the Xilinx ISE software package, the synthesis of devices on the programmable logic integrated circuits of Xilinx was performed. Table 1. presents the results of maximum speed and equipment costs obtained during the synthesis of these devices on the FPGA family Virtex5 company Xilinx.

TABLE 1 THE RESULTS OF THE SYNTHESIS OF DEVICES ON PLIC.

Device name	Speed	Equipment costs
Basic recursive device	105MH z	20% Slices
Minimized recursive device	108MH z	6% Slices

As can be seen from Table 1. the speed of the basic and minimized recursive devices is almost the same and the cost of equipment is better than the minimized recursive device.

#### V. CONCLUSION

As a result of using the technique of space-time graphs in the work the structures of basic and minimized recursive devices are constructed and a comparative assessment of speed and hardware costs is made by means of synthesis of these devices on PLIC. The obtained results of the synthesis of models of basic and minimized recursive devices allow us to conclude that these devices have almost the same speed, and in terms of equipment costs the best results are given by minimized recursive sorting devices.

#### REFERENCES

- [1] Kuhn. C. Matrix processors. Moscow. Mir, 1991.
- [2] Melnik A.O. "Specialized real-time computer systems", "LP", Lviv, 1996, 53p.
- [3] Dunets R.B. Analysis and synthesis of topologies of computer publishing and printing systems: Monograph - Lviv: NVF "Ukrainian Technologies", 2003.
- [4] Gryga, I. Kogut, V. Holota, R. Kochan, S. Rajba, T. Gancarczyk, U. Iatskovska Spatial-Temporal Transformation of Matrix and Multilayer Algorithms of Binary Number Multiplications // Proceedings of 10<sup>th</sup> IEEE International Conference on Intelligent Data Acquisition and Advanced Computing Systems: Technology and Applications. IDAACS'2019. – Metz, France, September 18-21, 2019. – P. 691-694.
- [5] V. Gryga, Y. Nykolaichuk, L. Nykolaichuk, N. Vozna, H. Klym Structuring of Algorithms for Data sorting and New Principles of Their Parallelization // Advanced Computer Information Technologies. International Conference. ACIT 2019. – Ceske Budejovice, Czech Republic, 2019. – P. 205-208.

**METHODS OF FORMATION, DIAGNOSIS, AND  
RESEARCH OF NANOSTRUCTURES AND NANO-  
OBJECTS INCLUDING BIOLOGICAL**

# BiO<sub>2</sub> and RuO<sub>2</sub> based nanocomposites for hybrid integrated circuits

Yaroslav Lepikh, Vitalii Borshchak, Nina Sadova, Nataliya Zatovskaya

Interdepartmental Scientific and Educational Physical-Technical Center  
of the MES and NAS of Ukraine at the Odessa I.I. Mechnikov National University,  
Odessa / 65028 / Ukraine / +38 048 723 34 61 / ndl\_lepikh@onu.edu.ua

**Abstract** — Nanocomposites are a multiphase heterogeneous system, which includes components with different physical and chemical properties. The investigation of the starting material properties, the organic and inorganic binding agent compositions, the conductive and dielectric phases, their particle morphology and geometric dimensions becomes a priority in the production of hybrid integrated circuits as far as such composites complex electrophysical properties first of all is determined by the conductive (functional) components and glass chemical-physical nature

**Keywords** — nanocomposites, nanomaterials, multiphase heterogeneous system, metal oxides

## I. INTRODUCTION

The functional basis of the nanocomposites that are widely used at present are, as a rule, metal oxides – a functional material, as a permanent binding agent – special glasses from the group of lead-boron-aluminosilicate glasses. As shown in [1], the glass has two functions: they hold the conductive particles in contact and provide the composition adhesion to the substrate. When choosing a permanent binding agent, the most important characteristics are the temperature glass viscosity dependence, which determines the composition annealing mode, the surface tension value, chemical activity and thermal expansion coefficient. The glass surface tension and its conductive particles wetting determine the mechanical properties of the contacts between the conductive particles [2, 3]. In these latter days there has been an increase in the number of publications devoted to the investigations of the possibility of using ruthenium compounds in nanocomposites as strain sensor sensitive elements [4, 5]. A sufficiently large ruthenium chemical and thermal inertness together with its obtainable price, makes this element the basis of a new class of nanocomposite materials [6 - 14]. In composite systems based on ruthenium compounds the resistors resistivity function dependence on the conducting phase concentration is smoother, and the resistance temperature coefficient is a narrower range of changes. The electrophysical properties of nanocomposite systems based on ruthenates are much more stable. All this makes the new nanocomposites extremely promising materials for use in the development of various microelectronic elements.

## II. RESULTS AND DISCUSSIONS

In the work, functional materials (the conducting phase — ruthenium oxides) were introduced into the paste in the form of small particles, the maximum size of which did not exceed

5 microns. Compositions based on ruthenium dioxide (RuO<sub>2</sub>) are distinguished by good electrophysical properties, low sensitivity to high temperatures, since ruthenium dioxide does not dissolve in the glass matrix, this allows you to increase the annealing temperature of resistive pastes of 1000 ° C. Fusible glasses (SiO<sub>2</sub> - B<sub>2</sub>O<sub>3</sub> - Bi<sub>2</sub>O<sub>3</sub> - BaO - ZnO - CdO) were used as a permanent binder. Bismuth oxide was introduced into the glass composition because it helps to stabilize the dielectric constant of the pastes and does not affect the electrical conductivity, being neutral. Bismuth oxide promotes fusibility, improves the wetting of particles and adhesion to the substrate. Studies have shown that on the basis of bismuth it is possible to create insulating coatings that do not cause corrosion of the schemes. Glass frit, on the one hand, provides adhesion of metal-enamel elements to the lining, on the other hand, creates a "rigid frame", fixing the position of the conductive particles in it. Studies of the electrical conductivity of nanocomposites based on ruthenium oxides showed a mixed nature of their conductivity as a combination of processes occurring in the conducting phase and in glass fiber. The conductivity of nanocomposite layers is determined by the height of the potential barrier of the dielectric layer between the conducting particles. If the interlayer of the dielectric between the conducting particles is less than 100 Å, then the main mechanism of conductivity is tunneling. With an interlayer size of more than 100 Å, tunneling is unlikely and only charge carriers whose energy exceeds the height of the barrier can overcome the potential barrier, i.e., thermionic becomes the main conduction mechanism. Thus, the movement of charges through the thin layers of the glass phase that surrounds the conducting phase is carried out using the tunneling effect in the energy-narrow zone. The influence of a permanent binder (glass) is manifested not so much in the chemical interaction with the conducting phase, but through the wetting and dissolution of its particles. Of great importance is the wetting of the functional material with glass and the chemical activity of the glass. If the glass forms a thick continuous layer around each conductive particle, then the contact between the particles is broken. Therefore, it is necessary that the glass does not completely wet the particles, but to such an extent that the particles are fixed in the matrix. It should be noted that the electrophysical properties of the resistive elements depend to a large extent on the ratio of the concentration of the conducting phase to the constant binder. The paper shows the dependences of the parameters of composite structures based on "glass-ruthenium dioxide" on the ratio of the conducting phase — RuO<sub>2</sub> and the constant binder — glass at a fixed annealing temperature of 8700C (Fig. 1.2). The glass fiber particle size largest influence on the resistance of

nanocomposites occurs in samples with a low ruthenium dioxide content. With an increase in the RuO<sub>2</sub> concentration, the resistance approaches a constant value and does not depend on the glass frit particle size.

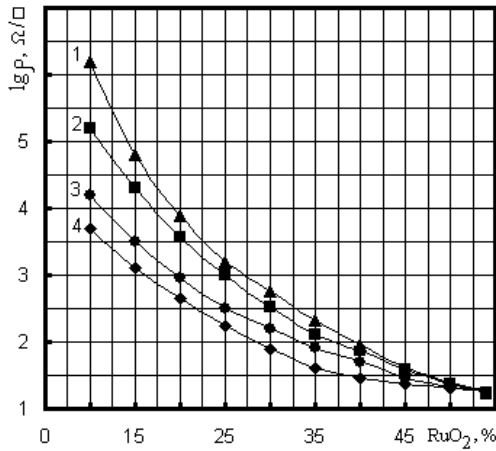


Fig. 1 RuO<sub>2</sub> based thick films surface resistivity dependence on the ratio of the conductive phase and glass concentrations. The glass particle sizes, microns: 1 - 0.5; 2 to 1; 3 to 3; 4 - 5.

The resistance dependence on the particle sizes for high-resistance films can be related to the processes of sintering and the influence of the component dispersion on of current-carrying chains geometric dimensions. In the films with high resistance, the main contribution to the conductivity is made by glass-frit; therefore, this phase state plays a significant role in the process of current transfer. In the investigation process, it was found that glasses can crystallize under the influence of heat treatment, forming the crystalline phase of α-SiO<sub>2</sub>. Particles of the functional material can also become centers of crystallization of the glass matrix. The presence of crystalline of inclusions in the matrix leads to local changes in the of glass melting conditions and flashing the functional material particles during heat treatment, which cannot but affect the formed film parameters. Thus, the heat treatment causes the new phase formation, as well as the system energy zone restructuring. Since the α-SiO<sub>2</sub> crystalline phase found in glass has a melting point above 15000C, and the resistive layer sintering occurs, as a rule, at temperatures up to 8700C, the glass crystalline phase does not melt and the local structural disturbances occur in the matrix body, which influence the conditions for the conductive chain formation. In addition, occasional breaks in the conductive chains make the overall conductivity chains structure in the film body disordered. It was established that the α-SiO<sub>2</sub> crystalline phase in the glass presence increases the film resistance (~10%). In connection with the aforesaid, it is of interest to consider a model that explains the α-SiO<sub>2</sub> crystalline phase in an amorphous glass matrix influence on the of thick films based on the glass - RuO<sub>2</sub> cluster system electrical conductivity.

A thick-film element can be represented as a assembly of conductive chains from one electrode to another, which consist of functional material conductive particles. A conducting i-chain is formed with a probability  $p_i$ , which includes the probability that all chain elements are conductive ( $p_1$ ) and the probability of continuity of the chain in the glass matrix from one electrode to another ( $p_2$ ), i.e.  $p_i = p_1 \cdot p_2$ . In this model, the probability  $p_1$  of all chain

elements conductivity is proportional to the functional material mass part  $m_f$  in the mass of the dry powder in the paste  $m_p$ :  $p_1 = k_1 m_f / m_p$ . Here  $k_1$  is the proportionality coefficient. The probability of obtaining a continuous chain from one electrode to another is proportional to the mass of the functional material  $m_f$  and inversely proportional to the glass frit mass  $m_g$ :  $p_2 = k_2 m_f / m_g$ . Here  $k_2$  is the proportionality coefficient. Powder mass is  $m_p = m_f + m_g$ .

If there is a crystalline phase in the glass, one more factor must be taken into account. The presence of the α-SiO<sub>2</sub> crystalline phase in low-melting glass is equivalent to the introduction of unmelted particles into it, since the melting temperature of any of the SiO<sub>2</sub> modifications is much higher than the layer sintering temperature. During sintering, in this case, local regions of "non-melts" are formed in the glass, which disrupt the structure formation process in limited regions. "Non-melts" impede the spread of liquid glass and create a uniform sintered structure. of The functional material particles in these areas do not form tight contacts due to the absence of compressive forces that occur during glass sintering. Thus, unsintered and therefore non-conductive contacts are formed in the system, which in essence represent breaks in current-carrying circuits.

To calculate the non-conductive contact formation possibility, it is necessary to introduce  $p_3$  into the relation for  $p_i$  - the probability that all contacts between the elements of the chain are conductive, that is,  $p_i = p_1 \cdot p_2 \cdot p_3$ . With an increase in the mass of the crystalline phase  $m_{cr}$  in the mass of the glass  $m_p$  powder  $m_p$  and the functional material, the probability  $p_3$  decreases:  $p_3 = 1 - k_3 \cdot m_{cr} / m_p$ . Here  $k_3$  is the coefficient of proportionality. From the above relations for  $p_1$ ,  $p_2$  and  $p_3$  it is easy to obtain  $p_i$ .

Since the thick-film resistor in this case is presented as a system that consists of conductive chain set, its conductivity,

$$\sigma = \sum_{i=1}^N \sigma_i p_i$$

where  $\sigma_i$  is the  $i$ -th chain conductivity,  $N$  is the number of chains.

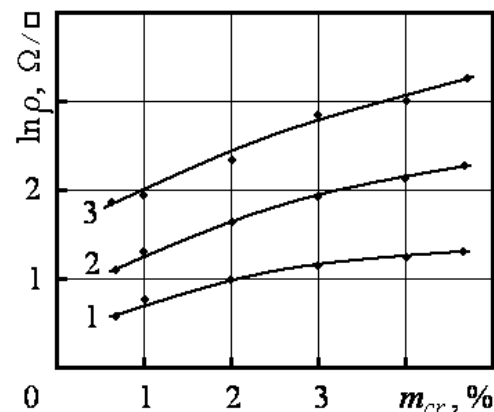


Fig. 2. The film specific surface resistance dependence on the percentage concentration of the crystalline phase  $m_{cr}$  in glass frit. The glass frit content in the system "glass - clusters RuO<sub>2</sub>"  $m_g$ , %: 1 - 60; 2 to 50; 3 to 40

If all chains are formed under the same conditions, then we can assume that  $p_i = p$ . Then

$$\sigma = p \sum_{i=1}^N \sigma_i = k_1 k_2 \frac{m_f^2 (m_f + m_g - k_3 m_{cr})}{m_g m_p^2} \sum_{i=1}^N \sigma_i$$

It can be seen from this expression that an increase in the crystalline component content  $m_{cr}$  in the glass phase  $m_g$  leads to an increase in the thick film resistance, which is confirmed experimentally (Fig. 2).

Thus, at a fixed annealing temperature the glass-frit particle size has the greatest influence on the resistor resistance of samples with a low content of ruthenium dioxide. The layer resistance increases with the glass content increasing. For given values of the functional material mf ( $\text{RuO}_2$ ) content and the glass phase masse  $m_g$ , the crystalline phase mass  $m_{cr}$  increase leads to the conductivity value decrease, i.e., to the resistive film resistance increase.

### III. CONCLUSIONS

Thus, the general influence of the particle size distribution, the ratio of the starting component concentrations and the annealing temperature on the parameters of the glass-metal oxide compositions was studied. The influence of the glass physicochemical properties on the phase composition formation, microstructure, and electrophysical properties of elements based on the obtained nanocomposites is shown. It has been established that, as a permanent binding agent, low-melting glass  $\text{SiO}_2\text{-B}_2\text{O}_3\text{-Bi}_2\text{O}_3\text{-BaO-ZnO-CdO}$  gives the best results, the advantage of which is to reduce the onset softening temperature (400-4500C), increase the specific surface resistance, and the absence of toxic lead compounds, which leads to the environmental pollution reduction. Glasses have high moisture resistance. Studies of the nanocomposite electrical conductivity mechanism showed a mixed nature of their conductivity as a combination of processes occurring in the conducting phase and in glass fiber.

### REFERENCES

[1] Технология толсто пленочных гибридных интегральных схем / Д.Хамер, Дж.Биггерс. – Изд-во «Мир» Москва, 1975.495 с.  
[2] Патент на винахід № 113565 А2017 10203, Легкоплавке скло для нанокompозитів // Лепіх Я.І., Лавренова Т.І.// Опубл. Бюл. № 3/2017 від 10.02.2017. заявл. 08.11.2017  
[3] Патент України на Корисну модель № 103231 "Скляне зв'язуюче для нанокompозитів на базі системи "скло-оксиди металів"// Я.І. Лепіх, Т.І. Лавренова. Публ. 10.12.2015, Бюл. № 23.

[4] Belavic D., Pavlin M., Gramc S., Santo-Zarnic M., Some Applications of Thick-Film strain Gauge// In Pros.of 24th Intern. Conf.and Exhib..IMAPS, Poland.-2000.-P.1999-202.  
[5] Grimaldi C., Ryser P., Strdssler S. Gange factor enhancement driven by heterogeneity in thick-film resistors // J.Appl. Phys. 2001.-v.90.-№ 1.-P. 322-327/  
[6] Курмашев Ш.Д. Влияние кристаллической фазы SiO2 на электрофизические компоненты композиционных структур на базе стекло-Bi2Ru2O7// Ш.Д.Курмашев, Т.И.Лавренова, Т.Н.Бугаева// Тезисов. докл. XXII научн. конф. стран СНГ "Дисперсные системы".- Одесса, 2006.- С. 215.  
[7] Курмашев Ш.Д., Садова Н.Н., Лавренова Т.И., Бугаева Т.Н. Исследование воспроизводимости электрофизических параметров толсто пленочных структур "RuO2 – стекло" // Технология и конструирование в электронной аппаратуре. – 2005. - №4(58). - С. 62-64  
[8] Патент України на винахід № 110982 "Резистивний матеріал для товстоплівкових елементів"// Я.І. Лепіх, Т.І. Лавренова, Т.М. Бугайова. Публ. 10.03.2016, Бюл. № 5/2016.  
[9] Ya.I.Lepikh, T.I. Lavrenova, N.M. Sadovaja Structural-phase and Electrophysical Properties of Nanocomposites Based on the "Glass-Ni3B" System, Received by the Cathode Beam Annealing// Journal of nano- and electronic physics, (Журнал нано- та електронної фізики) Vol. 9 No 5, 05005-1 – 05005-4(4pp) (2017), Sumy State University  
[10] Ya.I.Lepikh, T.I. Lavrenova, T.N. Bugayova., N.P. Zatovskaya, P.O. Snigur Annealing temperature modes influence on properties of heterophase nanocomposites based on ceramics "glass – Ag-Pd" systems// J. Functional Materials.- Vol. 21, No. 3 (2014). – P. 297-301.  
[11] Ya.I.Lepikh, Сантоній В.І., Янко В.В., Будянська Л.М., Іванченко І.О. Influence of the current-carrying phase dispersity on the electrophysical parameters of nanocomposites on the basis of "glass – ru compounds"// Abstract book of Intern. research and practice conference: Nanotechnology and nanomaterials (NANO-2019), 27-30, P. 130-131  
[12] Ya.I.Lepikh, Lavrenova T.I., Borshchak V.A., Sadova N.M., Zatovskaya N.P. Restoring and protection of the low temperature solder from oxidation// The Fourth Internat.Conf. on Information end Telecommunication Technologies and Radio Electronics (UkrMiCo'2019), 09-13 Sept. 2019, Odesa, Ukraine  
[13] L.M. Filevska. Luminescence of nanoscale tin dioxide. Review. Photoelectronics. 27 (2018), p.52-59.  
[14] V.S. Grinevych, L.M. Filevska, V.A. Smyntyna, M.O. Stetsenko, S.P. Rudenko, L.S. Maksimenko, and B.K. Serdega. Characterization of SnO2 Sensors Nanomaterials by Polarization Modulation Method. Springer Science+Business Media Dordrecht 2016 J. Bonca, S. Kruchinin (eds.), ~ Nanomaterials for Security, NATO Science for Peace and Security Series A: Chemistry and Biology, DOI 10.1007/978-94-017-7593-9, p.259-266.

# Formation of Cyanine Dyes J-aggregates in Thin Polymer Films

Alexander Sorokin\*, Irina Ropakova\*, Roman Grynyov<sup>+</sup>, Irina Bespalova\*, Svetlana Yefimova\*, Yuri Malyukin\*

\* Institute for Scintillation Materials of NAS of Ukraine, 60 Nauky ave., 61072 Kharkiv, Ukraine

<sup>+</sup> Ariel University, Natural Science Faculty, Physics Department, P.O.B. 3, 407000, Ariel, Israel

e-mail: sorokin@isma.kharkov.ua

**Abstract** — The formation of molecular aggregates in thin polymeric films is very useful for the development of functional materials for photonic and optoelectronic applications. However, in charged layered films the fluorescence of J-aggregates is often significantly quenched. As it was demonstrated using PIC and TDBC J-aggregates, one of the main process, which is quenching the fluorescence, is the exciton self-trapping.

**Keywords** — J-aggregates, layered polymer films, exciton, exciton-phonon coupling, exciton self-trapping

## I. INTRODUCTION

Nanostructured organic materials have attracted intense research interest as a very promising subject for optoelectronic and photonic applications [1]. Organic molecules exhibit high fluorescence efficiencies at low particle densities, a wide variety of optical properties, and are easy and cheap to process, resulting in extremely large design flexibility, very good possibilities for integration into devices, and an impressive performance of organic materials. In the active organic devices, including organic light-emitting diodes, organic photovoltaic cells, organic field-effect transistors, electrochromic devices, and organic nonlinear optics, the material is typically applied in form of thin films [1]. In this case, special efforts should be taken to prevent concentration quenching due to energy transfer to weakly or non-fluorescent states like dimers or excimers. However, there is an example of aggregates consisting of organic fluorophores which, contrary to concentration quenching, exhibit strong fluorescence, namely J-aggregates [2–4]. J-aggregates are highly ordered nanostructures of non-covalently coupled dyes such as cyanines, porphyrins, merocyanines, perylenes, and others [2–4]. They were independently discovered in the late 1930s by E. Jelley and G. Scheibe by the appearance of a novel bathochromically shifted band (called J-band) in the absorption spectra of pseudoisocyanine dyes in water solutions upon increasing their concentration. The observed changes were ascribed to the formation of dye aggregates which were henceforth called J-aggregates (Jelley's aggregates) or sometimes Scheibe aggregates (Scheibe polymers) [2–4]. Due to the translational symmetry within the molecular chains of a J-aggregate, the electronic excitations of the monomers are delocalized over chain segments and molecular (Frenkel) excitons are formed. The distinctive feature of J-aggregates

is the J-band which results from electric dipole transitions into the low energy edge of the exciton band [2–4]. Depending on the molecular packing within the chains also a hypsochromic excitonic band (H-band) or both J- and H-bands can appear [2–4].

J-aggregates exhibit many unique spectroscopic properties, which are distinctly different from those of the individual molecules constituting the aggregates: very narrow absorption and fluorescence line widths as for organic compounds (down to tens of  $\text{cm}^{-1}$  at low temperatures), near-resonant fluorescence, large extinction coefficients (up to  $10^6 \text{ cm}^{-1}\cdot\text{M}^{-1}$ ), giant third-order optical nonlinearities (up to  $10^{-5}$  esu), exciton superradiance, and energy migration up to micron distances [2–4]. Thus, they are ideal candidates for novel photonic materials, especially for thin-film applications. Unfortunately, pure aggregate films are often not stable enough. Polymer-based thin films with incorporated J-aggregates could be more durable and might be an attractive alternative [4].

There are two main approaches to form polymer films containing J-aggregates: spin-coating and layer-by-layer assembly [4]. In both cases the optical properties of the J-aggregates are affected by the polymer medium, resulting, for example, in a strong decrease of the fluorescence quantum yield or a transformation of the aggregate structure [4]. In the layer-by-layer self-assembly (LbL) technique alternating multilayer polymer films can be deposited onto an electrically charged substrate using electrostatic attraction dipping the substrate sequentially in aqueous solutions of polycations and anions, here the aggregating dye molecules. The samples consist of a sequence of successive monolayers of a polymer and of the aggregates, which are within their layers densely packed [4].

J-aggregates formed in LbL films are perspective for different photonic and photoelectronic applications, for example, for organic photovoltaics [5]. Therefore, the optical properties and structures of J-aggregates in layered films are of great interest.

In the present report, we summarize data obtained in our previous studies concerning the optical characteristics transformation for J-aggregates of two cyanine dyes, namely PIC and TDBC, under formation in LbL films [6,7].

## II. EXPERIMENTAL SECTION

PIC dye (pseudoisocyanine, 1,1'-diethyl-2,2'-cyanine iodide, Chart 1a) dye, cationic polyelectrolyte PDDA (poly(diallyldimethylammonium chloride), average  $M_w < 100000$  g/mol, solution 35 wt. % in  $H_2O$ , Chart 1c) and anionic polyelectrolyte PSS (poly(sodium 4-styrenesulfonate), average  $M_w \sim 70000$  g/mol, powder, Chart 1d) were purchased from Sigma Aldrich (USA) and used as-received. The TDBC dye (1,1'-disulfobutyl-3,3'-diethyl-5,5',6,6'-tetrachlorobenzimidazoly-carbo-cyanine sodium salt, Chart 1b) was purchased from Few Chemicals GmbH (Germany) and used as-received.

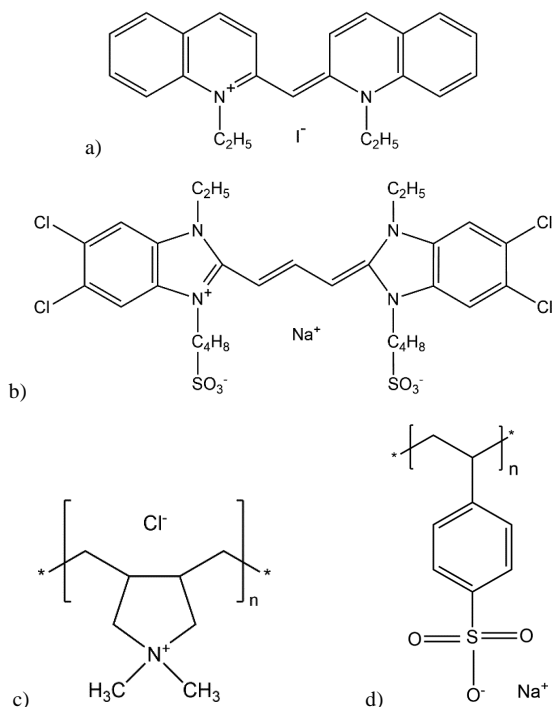


Chart 1. Structural formulas of the dyes and polymers: a) PIC, b) TDBC, c) PDDA, d) PSS.

To prepare polymer films containing PIC J-aggregates the spray layer-by-layer (LbL) assembly method was used [6]. For this purpose, commercially available paintbrush 80-897 (Miol, China) was used. A substrate glass plate was preliminarily treated with hot (95 °C) piranha etch ( $H_2SO_4 + H_2O_2 = 2:1$ ). The treatment with piranha etch cleans organic residues off the substrate and hydroxylate the surfaces, making it highly hydrophilic. Then, an aqueous polycation PDDA solution (2 wt. %) was sprayed on the substrate for coating with a positively charged film with successive deposition of a negatively charged polymer layer from an aqueous polyanion PSS solution (2 wt. %). As PIC dye is a cationic one (Chart 1a), the PIC J-aggregates layer was deposited on the PSS layer. The J-aggregates layer was coated with the PSS layer to provide isolation from the surrounded air. Each deposited layer was rinsed with sprayed distilled water. To prepare PIC monomers in the polymer film, the stock solution of the dye in DMF (1 mM) was added to an aqueous polyvinyl alcohol (PVA) solution (2 wt. %) and then the mixture was drop-casted on a glass substrate with subsequent slow drying at normal conditions.

For the preparation of LbL polymer films with TDBC J-aggregates dipping method was used [7]. First, the clean substrate was immersed for 20 seconds in the aqueous PDDA (0.5 wt. %) solution agitated by a magnetic stirrer (at 1000 rpm) to deposit a positively charged polymer monolayer. After that, the substrate covered by the PDDA film was dipped into the TDBC (1 mM) J-aggregate stock solution for 10 min (without agitation) to deposit a layer of J-aggregates. Finally, the J-aggregate layer was covered by a PDDA layer immersing the sample for 20 seconds in the agitated PDDA solution. Each layer deposition was followed by rinsing the substrate for 10 seconds in agitated distilled water and drying it with dry air. To obtain multilayer films the procedure was repeated several times.

Absorption spectra were obtained using an incandescent lamp and a fiber-coupled USB4000 microspectrometer (OceanOptics, USA) using a home-made fiber-optic adapter attached to a 20X eyepiece. Fluorescence spectra were recorded applying a monochromator (MDR-23, LOMO, Russia) and a diode-pumped  $Nd^{3+}$ : YAG laser ( $\lambda_{exc} = 532$  nm, 5 mW) or a xenon lamp as the excitation source. The spectral output of the monochromator was calibrated using a calibrated tungsten halogen lamp (HL-2000-CAL, OceanOptics, USA). Low-temperature spectra were measured using a nitrogen cryostat. The temperature was controlled within 1 K.

Fluorescence decay spectra were obtained by a FluoTime 200 fluorescence lifetime spectrometer (PicoQuant, Germany) equipped with a solid sample holder and for excitation, a picosecond laser diode emitting at 531 nm with a pulse energy of 13 pJ. The width of the instrument response function (IRF) for the whole setup was 100 ps and below. For the analysis of the decay curves, the FluoFit software (PicoQuant, Germany) was used.

## III. RESULTS AND DISCUSSION

Both types of J-aggregates formation in LbL films significantly affect their morphologies and optical characteristics [6,7]. Indeed, in solutions PIC J-aggregates have thread-like morphology [4,6] and TDBC J-aggregates have rod-like one [7], so exciton dynamics in both aggregate types were quasi-one-dimensional. However, in LbL films the J-aggregates revealed two-dimensional island-like morphologies [6,7] (Fig. 1).

Two-dimensional morphologies were confirmed by AFM microscopy [6,7]. The aggregate morphology changing in combination with a more rigid environment in the polymer film comparing with the water solution results in the spectral properties transformation typical for J-aggregates formation in polymer films [6,7] (Fig. 2).

For example, for PIC J-aggregates the main changes are the following: in LbL film the J-band becomes wider ( $\Delta\nu_J^{LbL} = 330$   $cm^{-1}$ ), the fluorescence quantum yield strongly decreases ( $\eta^{LbL} \sim 0.005$ ) and the lifetime is also significantly shortened ( $\tau_{av}^{film} \sim 40$  ps) (Fig. 2a). For comparison, in an aqueous NaCl (0.2 M) solution, PIC J-aggregates at the used dye concentration ( $C = 0.5$  mM) demonstrate such characteristics:  $\Delta\nu_J = 180$   $cm^{-1}$ ,  $\eta \sim 0.38$  and  $\tau \sim 1.39$  ns. In the case of TDBC J-aggregates, in water solution they exhibit a very narrow J-band ( $\lambda_{max} = 585$  nm,  $\Delta\nu_{FWHM} = 280$

$\text{cm}^{-1}$ ) and a nearly resonant, narrow fluorescence band ( $\lambda_{\text{max}} = 586.5 \text{ nm}$ ,  $\Delta\nu_{\text{FWHM}} = 320 \text{ cm}^{-1}$ ).

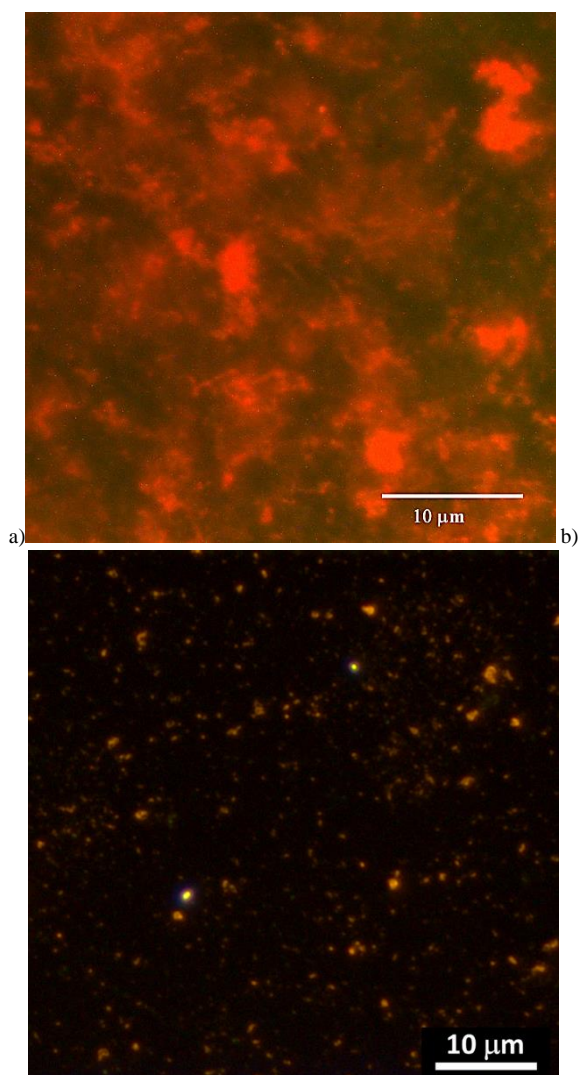


Fig. 1. Fluorescent microscopy images of PIC (a) and TDBC (b) J-aggregates.

The J-aggregate fluorescence is bright with a quantum yield of  $\eta \sim 0.31$  and a quite short lifetime of  $\tau_{\text{av}} \sim 60 \text{ ps}$ . In LbL film the absorption maximum is at  $\lambda_{\text{max}}^{\text{LbL}} = 587.5 \text{ nm}$  and the bandwidth amounts  $\Delta\nu^{\text{LbL}} = 300 \text{ cm}^{-1}$ , while for fluorescence  $\lambda_{\text{max}}^{\text{LbL}} = 588.5 \text{ nm}$  ( $\Delta\nu_{\text{FWHM}}^{\text{LbL}} = 270 \text{ cm}^{-1}$ ),  $\eta^{\text{LbL}} \sim 0.5\%$  and the decay curve is so short, that not distinguished from our setup response function curve. Therefore, the main spectral changes are related to fluorescence signal and reveal drastical quenching.

We suppose, that the main origin of exciton dynamics modification is the efficient exciton self-trapping due to a more rigid environment and, hence, stronger exciton-phonon coupling [6,7]. Indeed, the exciton-coupling constants estimated for both J-aggregates appeared to be much larger than 1 (1.97 for PIC [6] and 1.35 for TDBC [7]) in LbL films unlike the solution case [6,7].

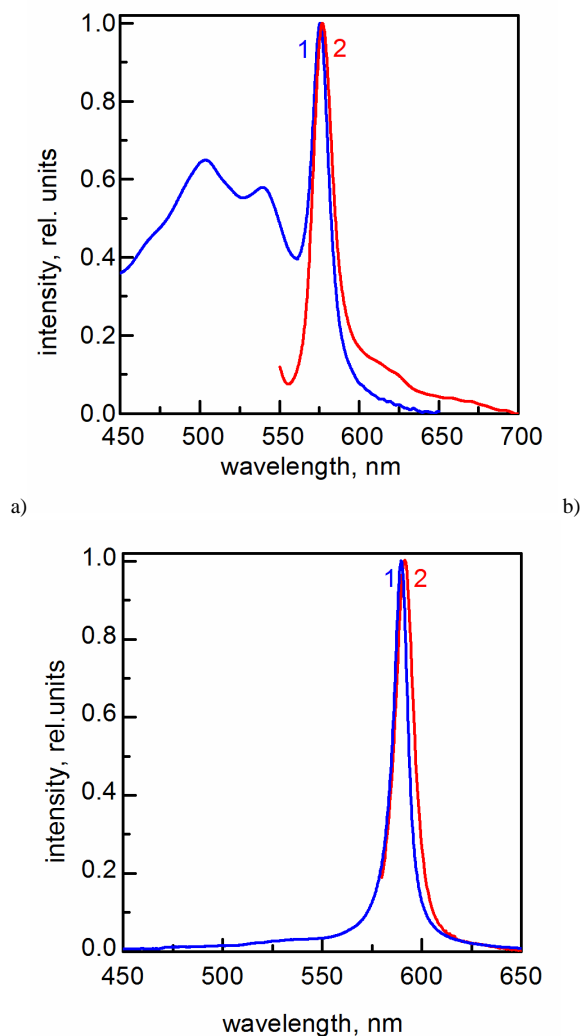


Fig. 2 Absorption (1) and fluorescence spectra (2,  $\lambda_{\text{exc}} = 530 \text{ nm}$ ) of PIC (a) and TDBC (b) J-aggregates in LbL films at room temperature.

Because of strong exciton-phonon coupling and 2D morphology of the J-aggregates in LbL films, the fluorescence of self-trapped excitons can be seen at low temperatures [6,7] (Fig. 3).

One could see, that the red-shifted wide fluorescence band of self-trapped excitons is much more intense for PIC J-aggregates comparing with TDBC ones, because of stronger exciton-phonon coupling (Fig. 3). So, exciton self-trapping is one of the processes which significantly influence the exciton dynamics in J-aggregates formed in LbL films and needs to be taken into account at the development of functional materials on their base.

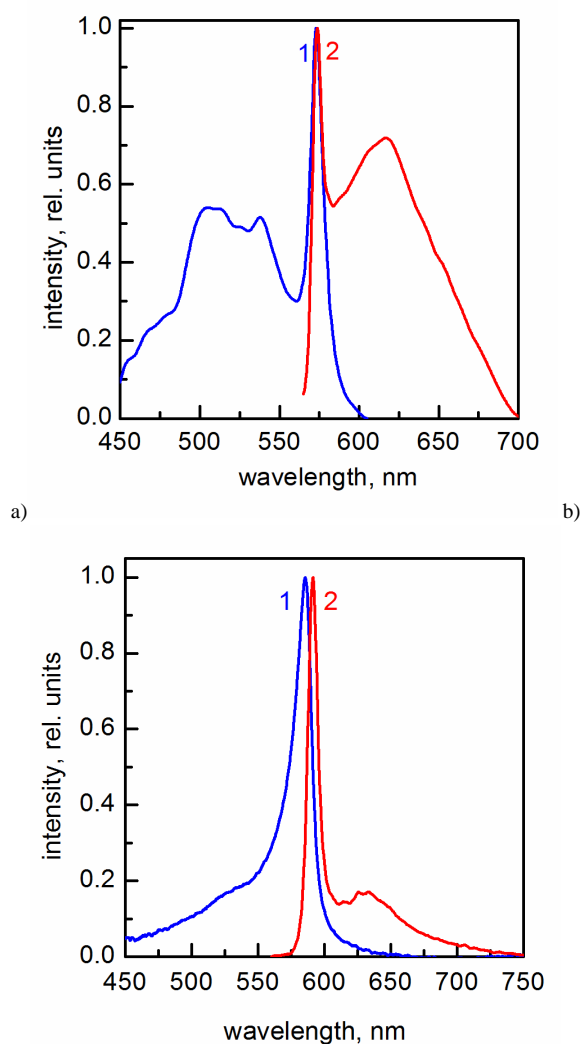


Fig. 3 Absorption (1) and fluorescence spectra (2,  $\lambda_{exc} = 530$  nm) of PIC (a) and TDBC (b) J-aggregates in LbL films at 80 K.

#### IV. CONCLUSIONS

We studied the morphologies and optical properties of PIC and TDBC J-aggregates formed in charged layer-by-layer PDDA films. It was found that despite the similarity of the main steady-state spectral characteristics of the J-aggregates in the solutions and polymer films their

fluorescence quantum yields are much smaller than in solutions due to efficient fluorescence quenching. It was found, that in LbL films the morphology of the J-aggregates transforms into two-dimensional, island-like structures. Due to the more rigid environment in the polymer films, the exciton-phonon coupling constant of the J-aggregates becomes quite large resulting in efficient exciton self-trapping. The latter is supposed to be responsible for the lower quantum yields in the films compared to the solution. Exciton self-trapping manifests itself at low temperatures ( $\sim 80$  K) in a red-shifted fluorescent band with a long decay time for both types of J-aggregates. For the development of thin polymer film materials based on the J-aggregates, the ways to suppress the exciton self-trapping need to be found.

#### REFERENCES

- [1] K. H. Al-Shamery, H.-G. Rubahn, and H. Sitter, Eds., *Organic nanostructures for next generation devices*. Berlin, Heidelberg: Springer, 2008.
- [2] F. Würthner, T. E. Kaiser, and C. R. Saha-Möller, "J-Aggregates: From Serendipitous Discovery to Supramolecular Engineering of Functional Dye Materials," *Angew. Chemie Int. Ed.*, vol. 50, no. 15, pp. 3376–3410, Apr. 2011.
- [3] J. L. Bricks, Y. L. Slominskii, I. D. Panas, and A. P. Demchenko, "Fluorescent J-aggregates of cyanine dyes: basic research and applications review," *Methods Appl. Fluoresc.*, vol. 6, no. 1, p. 012001, Dec. 2017.
- [4] A. V. Sorokin, S. L. Yefimova, and Y. V. Malyukin, "Polymer-Bound Supramolecular J-Aggregates: Optical Properties and Applications," in *Encyclopedia of Polymer Science and Technology*, Hoboken, NJ, USA: John Wiley & Sons, Inc., 2018, pp. 1–33.
- [5] Y. Wang and X. Zhan, "Layer-by-Layer Processed Organic Solar Cells," *Adv. Energy Mater.*, vol. 6, no. 17, p. 1600414, Sep. 2016.
- [6] A. V. Sorokin, N. V. Pereverzev, I. I. Grankina, S. L. Yefimova, and Y. V. Malyukin, "Evidence of Exciton Self-Trapping in Pseudocyanine J-Aggregates Formed in Layered Polymer Films," *J. Phys. Chem. C*, vol. 119, no. 49, pp. 27865–27873, 2015.
- [7] A. V. Sorokin, I.Yu. Ropakova, S. Wolter, R. Lange, I. Barke, S. Speller, S.L. Yefimova, Yu.V. Malyukin, S. Lochbrunner, "Exciton Dynamics and Self-Trapping of Carbocyanine J-Aggregates in Polymer Films," *J. Phys. Chem. C*, vol. 123, no. 14, pp. 9428–9444, Apr. 2019.

# Estimation of Wave Pressure on Scattering Carbon Nanotubes in THz Range

Yevhenii Antonenko, Sergey Berdnik, Victor Katrich, Mikhail Nesterenko, Yuriy Penkin, Sergey Shulga

V. N. Karazin Kharkiv National University  
4 Svobody Sq. / 61022 / Kharkiv / Ukraine / mikhail.v.nesterenko@gmail.com

**Abstract** — Electromagnetic wave pressure on scattering carbon nanotubes was estimated based on a rigorous solution of the diffraction problem. Thin vibrators with distributed constant reactive impedance were used as physically adequate models of the carbon nanotubes. It was shown that under resonant condition the wave pressure acting on impedance vibrators was lower as compared to that acting on perfectly conducting vibrators. The numerical estimates of the ponderomotive effect on the carbon nanotubes confirm that the wave pressure can be controlled by frequency tuning.

**Keywords** — electromagnetic wave pressure, carbon nanotubes, ponderomotive effect, thin vibrator

## I. INTRODUCTION

Wave pressure is interpreted as mechanical effect of electromagnetic waves on scattering inhomogeneities in propagation media. This is one of the fundamental physical phenomena known as a ponderomotive effect [1-4]. The term also relates to the other phenomenon such as torques generation by circularly polarized waves, the recoil effect for directional radiation systems, and others [2].

The hypothesis of light pressure on gases received theoretical and experimental substantiation, starting with the work of P. N. Lebedev [1]. The light pressure measured in [1] was about  $10^{-7}$  [H/m<sup>2</sup>]. Until the 40th years of the 19th century, studies of the mechanical effects of electromagnetic radiation were carried out exclusively in the light wavelength range. Apparently, the wave pressure at radio frequencies was measured by Hasson in 1930 [3]. In this experiment, a half-wave dipole made of aluminum foil suspended on a quartz filament was irradiated at a wavelength of 0.175 m.

Subsequently, thin vibrator scatterers in the microwave range were repeatedly studied by other authors (see, for example, [2]). In these studies, only well-conducting vibrators were considered, in which impedance is an objective disadvantage. Indeed, energy losses in the vibrator decrease the mechanical effect of the incident field, and, consequently, decrease the sensitivity of devices intended for measuring the ponderomotive effect [4]. Most likely, this can explain the lack of study devoted to analyses of the ponderomotive properties for vibrators characterized by purely reactive impedances.

Recently, the interest to this issue has increased again due to the use of carbon nanotube elements in various THz applications. As is known [5], single-walled carbon nanotubes (SWNT) located in free space characterized by a

constant complex impedance  $\bar{Z}_s$  distributed over its surface is defined by the formula

$$\bar{Z}_s = \frac{i\pi\hbar^2(\omega - i\nu)}{240e^2v_F}, \quad (1)$$

where  $v_F \approx 9.71 \cdot 10^5$  m/s is Fermi speed,  $\nu = 3.33 \cdot 10^{11}$  Hz is relaxation frequency,  $e$  is electron charge,  $\hbar$  is Planck constant, and  $\omega$  is angular frequency of the monochromatic wave. As known, the value of the intrinsic impedance defined by the formula (1) does not depend upon SWNT length, and the inequality  $\text{Im}\bar{Z}_s \gg \text{Re}\bar{Z}_s$  holds in the frequency range from 1 THz to 100 THz [5]. Therefore, in this frequency range, the carbon tubes can be modeled by thin vibrator scatterers with the purely inductive surface impedance.

The report is aimed at estimating the wave pressure magnitude on the scattering SWNT in the THz frequency range, based on the numerical simulation results.

## II. PROBLEM FORMULATION AND SOLUTION

Let us consider a carbon nanotube model based on a linear impedance vibrator located in an infinite medium with material parameters  $(\epsilon_1; \mu_1)$ . The vibrator length and radius are  $2L$  and  $\rho$ . The vibrator is characterized by a constant distributed impedance  $\bar{Z}_s$  normalized to the medium wave resistance  $Z_0 = \sqrt{\mu_1/\epsilon_1}$  [Ohm]. The vibrator dimensions satisfy the thin wire approximations,  $\frac{\rho}{2L} \ll 1$  and  $\frac{\rho\sqrt{\epsilon_1\mu_1}}{\lambda} \ll 1$ , where  $\lambda$  is the wavelength in free space.

Let us analyze the vibrator excited by a monochromatic plane linearly polarized wave  $E_y^{ex} = E_0 e^{ik_1 z}$  or  $H_x^{ex} = -\frac{E_0}{Z_0} e^{ik_1 z}$  which normally incident on the vibrator from half-space  $z \leq 0$  (Fig. 1). The fields and currents depend on time  $t$  as  $e^{i\omega t}$ . The real wave amplitude is  $E_0$ ,  $k_1 = k\sqrt{\epsilon_1\mu_1}$  and  $k = \omega/c$  are the wave numbers, and  $c \approx 2.998 \cdot 10^8$  [m/s] is the speed of light in vacuum.

According to classical concepts [4], the ponderomotive force  $F$  acting on a current element with length  $ds$ , along

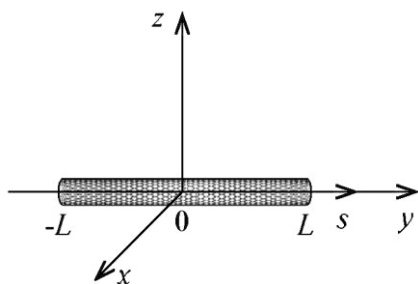


Fig. 1. The carbon nanotube geometry.

which the electric current  $J$  flows in the magnetic field with intensity  $\vec{H}$ , is determined by the following expression

$$F = J \left[ d\vec{s}, \mu_1 \vec{H} \right]. \quad (2)$$

As can be seen, the force  $F$  is proportional to the sine of the angle between the vectors  $\vec{H}$  and  $d\vec{s}$ , and its direction is determined by the right-hand screw rule.

The magnetic field  $\vec{H}$  on the vibrator surface is the sum of the incident field  $\vec{H}^{ex}$  and the secondary scattered field  $\vec{H}^{dif}$ , that is  $\vec{H} = \vec{H}^{ex} + \vec{H}^{dif}$ . Since the symmetric vibrator excitation uniquely determines the symmetry of the spatial radiation pattern (RP) of the secondary vibrator radiation, the resultant ponderomotive forces defined by the field  $\vec{H}^{dif}$  acting on the scattering vibrator is zero [2]. Then  $\vec{H} = \vec{H}^{ex}$  and the formula (2) can be rewritten as

$$F = J \left[ d\vec{s}, \mu_1 \vec{H}^{ex} \right] = J \left[ \frac{\mu_1 E_0}{Z_0} e^{ik_1 z} \vec{x}^0, d\vec{s} \right]. \quad (3)$$

Since the temporal representation of a monochromatic physical quantity  $V(t)$  is related to its amplitude  $V(\omega)$  as

$$V(t) = \text{Re} \left\{ V(\omega) e^{i\omega t} \right\}, \quad (4)$$

the expression (3) for the ponderomotive force acting on the unit surface of the impedance vibrator can be represented in the coordinate system shown in Fig. 1 as

$$F(t) = \text{Re} \left\{ J_y(s) e^{i\omega t} \right\} \cdot \text{Re} \left\{ \frac{\mu_1 E_0}{Z_0} e^{i(\omega t + k_1 z)} \right\}. \quad (5)$$

Since the free space parameter is  $\mu_1 = \mu_0 = 1.257 \cdot 10^{-6} [(V \cdot s)/(A \cdot m)]$ , the expression (5) can be simplified to

$$F(t) = \frac{\mu_0 E_0}{Z_0} \text{Re} \left\{ J_y(s) e^{i\omega t} \right\} \cdot \cos(\omega t + k_1 z). \quad (6)$$

Let us represent the complex current  $J_y(s)$  by using the Euler's formula as  $J_y(s) = |J_y(s)| e^{i\psi(s)}$  where  $|J_y(s)|$  is the current modulus and  $\psi(s) = \arctg [\text{Im} J_y(s) / \text{Re} J_y(s)]$ . Then the expression (6) can be rewritten as

$$F(t) = \frac{\mu_0 E_0}{Z_0} |J_y(s)| \cos(\omega t + \psi(s)) \cos(\omega t + k_1 z) \quad (7)$$

and the density of the ponderomotive force (7) averaged over the period of high-frequency oscillations  $T$  can be calculated by the formula [4]

$$\begin{aligned} F &= \bar{F}(t) \\ &= \frac{\mu_0 E_0}{TZ_0} |J_y(s)| \int_0^T \cos(\omega t + \psi(s)) \cos(\omega t + k_1 z) dt \\ &= \frac{\mu_0 E_0}{2Z_0} |J_y(s)| \cos(\psi(s) - k_1 z) \end{aligned} \quad (8)$$

The ponderomotive force (2) acting on a thin linear vibrator scatterer can be estimated if the operation of one-dimensional averaging over the vibrator length is carried out taking into account the relation  $k_1 z \approx 0$ . Then the formula (8) takes the form

$$\bar{F} = \frac{\mu_0 E_0}{4LZ_0} \int_{-L}^L |J_y(s)| \cos(\psi(s)) ds. \quad (9)$$

It is quite clear that the force  $\bar{F}$  is applied to the mass center of the vibrator  $s = 0$ .

Expression (9) allows us to correctly calculate the ponderomotive impact of the incident wave on the impedance vibrator if the current distribution is defined as a rigorous solution of the diffraction problem. In what follows, the analytical solution of the electrodynamic problem obtained by the asymptotic averaging method (up to the term  $\alpha^2$ ) [6] will be used as the initial expression defining the vibrator current  $J_y(s)$

$$\begin{aligned} J_y(s) &= \alpha \frac{i\omega E_0}{kk} \left\{ 1 - \cos \tilde{k}(s+L) \right. \\ &\quad \left. - \frac{\sin \tilde{k}(L+s) + \alpha P^s [k\rho, \tilde{k}(L+s)]}{\sin 2\tilde{k}L + \alpha P^s(k\rho, 2\tilde{k}L)} (1 - \cos 2\tilde{k}L) \right\}, \end{aligned} \quad (10)$$

where  $\alpha = \frac{1}{2 \ln[\rho / (2L)]}$  is the natural small parameter

$$(|\alpha| \ll 1), \quad \tilde{k} = k + i(\alpha / \rho) \bar{Z}_s,$$

$$\begin{aligned} &P^s [k\rho, \tilde{k}(L+s)] \\ &= \int_{-L}^s \left[ \frac{e^{-ikR(s',-L)}}{R(s',-L)} + \frac{e^{-ikR(s',L)}}{R(s',L)} \right] \sin \tilde{k}(s-s') ds' \Big|_{s=L} \\ &= P^s(k\rho, 2\tilde{k}L), \end{aligned} \quad (11)$$

$$R(s',s) = \sqrt{(s'-s)^2 + \rho^2}.$$

Taking into account the formulas (10), (11), and the equality  $\omega\mu_0 = 120\pi k$ , the final form of the expression (9) can be presented as

$$\bar{F} = \alpha \frac{E_0^2}{4L} \times \int_{-L}^L \frac{i}{\tilde{k}} \left[ \frac{1 - \cos \tilde{k}(s+L)}{\sin 2\tilde{k}L + \alpha P^s(k\rho, 2\tilde{k}L)} - \frac{\sin \tilde{k}(L+s) + \alpha P^s[k\rho, \tilde{k}(L+s)]}{\sin 2\tilde{k}L + \alpha P^s(k\rho, 2\tilde{k}L)} \right] \cos(\psi(s)) ds. \quad (12)$$

### III. RESULTS OF THE NUMERICAL MODELLING

The structure of the expression (12) allows us to state that the force  $\bar{F}$  depends upon the amplitude  $E_0$  and frequency  $\omega$  of the incident wave, vibrator length,  $2L$ , and impedance  $\bar{Z}_S$  which is function of the vibrator current distribution  $J_y(s)$ . On the other hand, it is known [6] that inductive impedance of the scattering vibrator results in enlargement of its resonance length  $2L_{res}$ . Therefore, it is a good idea to carry out assessment of the field forces acting on the scattering vibrators of equal length, but characterized by different reactive impedances, and, hence, by different resonant wavelengths  $\lambda_{res}(2L; \bar{Z}_S)$ . The analytical relationship between  $\lambda_{res}$  and  $2L$ ,  $\bar{Z}_S$  was obtained in the monograph [6] for the case of the reactive impedance

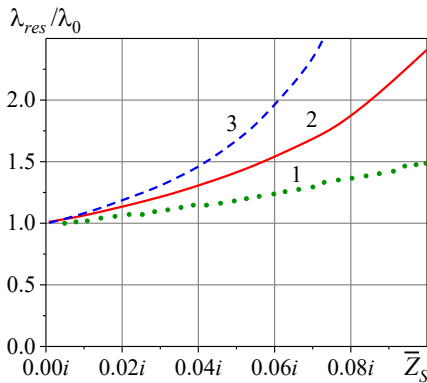


Fig. 2. Resonance characteristics of the carbon nanotube: 1 –  $2L/\rho=100$ ; 2 –  $2L/\rho=200$ ; 3 –  $2L/\rho=300$ .

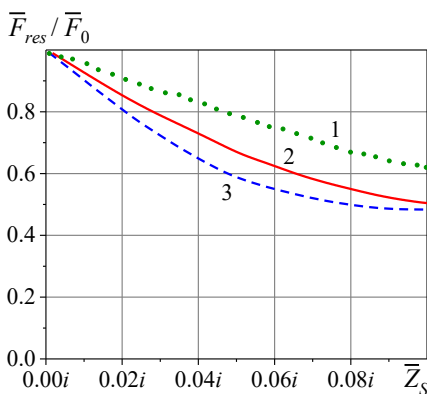


Fig. 3. The ponderomotive effect on the carbon nanotubes: 1 –  $2L/\rho=100$ ; 2 –  $2L/\rho=200$ ; 3 –  $2L/\rho=300$ .

$|\bar{Z}_S| \ll 1$ . This relation can be written in the following form

$$(\tilde{k}L)_{res} \approx \frac{\pi}{2} + \alpha \left[ \frac{1}{2} \text{Si}(2\pi - 2\alpha \frac{iL\bar{Z}_S}{\rho}) - \frac{1}{2} \text{Si}(2\alpha \frac{iL\bar{Z}_S}{\rho}) \right], \quad (13)$$

where  $\text{Si}(x)$  is the integral sine of the complex argument.

The expression for  $\lambda_{res}$  can be easily obtained based on (13):

$$\lambda_{res} \approx \left( \frac{1}{4L} + \frac{\alpha}{2\pi} \left[ \frac{1}{2L} \text{Si} \left( 2\pi - 2\alpha \frac{iL\bar{Z}_S}{\rho} \right) - \frac{1}{2L} \text{Si} \left( 2\alpha \frac{iL\bar{Z}_S}{\rho} \right) - \frac{i\bar{Z}_S}{\rho} \right] \right)^{-1}, \quad (14)$$

which allows us to calculate the resonant wavelength of the impedance vibrator with the parameters  $2L$ ,  $\rho$  and  $\bar{Z}_S$ . For clarity of analysis based on the formula (14), the plots of the ratio  $\lambda_{res}/\lambda_0$  as the function of the reactive impedance  $\bar{Z}_S$  are shown in Fig. 2. In this ratio  $\lambda_0$  is the resonant wavelength of the perfectly conducting vibrator,  $\lambda_0 = \lambda_{res}|_{\bar{Z}_S=0}$ . These curves are universal since their form depends only upon the ratio  $2L/\rho$ . This conclusion can be also verified analytically based on the expression (14). As can be seen from Fig. 2, the function  $\lambda_{res}/\lambda_0$  is rapidly increasing function of the reactive impedance  $\bar{Z}_S > 0$ . The slopes of the curves rapidly increase when the vibrator radius is decreased.

Let us compare based on the formula (12) the simulation results concerning the magnitude of the ponderomotive forces  $\bar{F}_0$  acting on the perfectly conducting vibrator at the resonant wavelength  $\lambda_0$  and  $\bar{F}_{res}$  acting on the impedance carbon nanotube vibrator at the resonant wavelength  $\lambda_{res}$ . Of course, if the vibrator length  $2L$  is constant, the energy flow intercepted from the incident wave is also does not vary if the impedance belongs to the interval  $0.0 \leq \bar{Z}_S \leq 0.1i$ . The ratio  $\bar{F}_{res}/\bar{F}_0$  as function of the reactive impedance  $\bar{Z}_S$  is plotted in Fig. 3.

As can be seen from Fig. 3, the impedance modulus  $|\bar{Z}_S|$  increase causes weakening the ponderomotive effect. It should be borne in mind that such behavior can be explained by decrease of the ponderomotive force component associated with the weakening of the vibrator recoil effect caused by the secondary vibrator radiation. Since this decreasing is not associated with direct energy losses in the vibrator material, it can be interpreted as redistributing the diffracted field in favor of the reactive part of the field concentrated near the scatterer. The level of additional energy captured by the vibrator from the reradiated field which is defined by the transformation near field structure is directly proportional to the impedance modulus. As seen from Fig. 3, decreasing the ratio  $\rho/(2L)$  causes decreasing the wave pressure force acting on the vibrator. It can be also concluded based on the simulation results that there exists an objective limit of this decrease equal to  $\bar{F}_{res}/2\bar{F}_0$ .

#### IV. CONCLUSION

For the first time, the comparative analysis of the wave pressure on scattering carbon nanotubes based on the rigorous solution of the electrodynamic diffraction problem has been carried out. The carbon nanotube was modelled by the thin vibrator with constant reactive impedance distributed over its surface. It was found that in the THz frequency range, the ponderomotive force acting on the nanotube vibrator scatterer under the resonant conditions is lower as compared to that acting on the perfectly conducting vibrator in the same condition. The observed effect has been interpreted from the physical point of view. The obtained results have both fundamental and applied values.

#### REFERENCES

- [1] P. N. Lebedev, Selected Works. Moscow-Leningrad: Gostekhizdat, 1949. (in Russian)
- [2] Ponderomotive Action of the Electromagnetic Field (Theory and Applications). R. A. Valitov (ed.). Moscow: Sovetskoye radio, 1975. (in Russian)
- [3] S. Husson, "Action me'canic exerce'e sur un conducteur parles ondes electromagnetiques," Comptes Rendues, No. 191, 1930.
- [4] Tamm, Fundamentals of the Theory of Electricity, Moscow: Nauka, 1989. (in Russian)
- [5] G. W. Hanson, "Radiation efficiency of nano-radius dipole antennas in the microwave and far-infrared regimes," IEEE Antenn. Propag. Mag., vol. 50, pp. 66-77, 2008.
- [6] M. V. Nesterenko, V. A. Katrich, Yu. M. Penkin, V. M. Dakhov, and S. L. Berdnik, Thin Impedance Vibrators: Theory and Applications, Springer Science+Business Media, New York, 2011.

# Electrical Conductivity Of $(\text{Cu}_{1-x}\text{Ag}_x)_7\text{SiS}_5\text{I}$ -Based Ceramics Prepared From Nanopowders

A. Pogodin, I. Shender, S. Bereznyuk, M. Filep, O. Kokhan, I. Studenyak

Uzhhorod National University

Pidhirna St. 46 / 88000 / Uzhhorod / Ukraine / +380953310773 / artempogodin88@gmail.com

$(\text{Cu}_{1-x}\text{Ag}_x)_7\text{SiS}_5\text{I}$ -based ceramics with argyrodite structure were prepared from nanopowders. The structural studies were performed by XRD technique and microstructural analysis. The total electrical conductivity of ceramics was measured by impedance spectroscopy in the frequency range from 10 Hz to  $2 \times 10^6$  Hz and temperature interval from 292 K to 383 K. The contributions of ionic and electronic components into the total electrical conductivity were separated as well as their temperature behavior was studied. The influence of  $\text{Cu}^+ \rightarrow \text{Ag}^+$  cationic substitution on electrical parameters of  $(\text{Cu}_{1-x}\text{Ag}_x)_7\text{SiS}_5\text{I}$ -based ceramics was investigated.

**Keywords** — argyrodite; superionic conductor; ceramic; ionic conductivity; activation energy

## I. INTRODUCTION

$(\text{Cu}_{1-x}\text{Ag}_x)_7\text{SiS}_5\text{I}$  mixed crystals belong to the superionic compounds with argyrodite structure [1, 2]. Due to the high values of electrical conductivity argyrodites are the promising materials for solid state ionics [3]. On the basis of argyrodites the new types of solid state batteries, supercapacitors, electrochemical sensors, etc. can be created. In recent years they have been obtained in the forms of composites, ceramics and thin films [4-7]. Copper-containing argyrodites in ceramic form were studied in Ref. [6]. The electrical properties of  $(\text{Cu}_{1-x}\text{Ag}_x)_7\text{SiS}_5\text{I}$  mixed crystals were investigated by impedance spectroscopy in Ref. [8].

In this paper, we will focus on investigating new  $(\text{Cu}_{1-x}\text{Ag}_x)_7\text{SiS}_5\text{I}$ -based ceramics. It should be noted that among ceramic materials, electrochemical ceramics have recently been widely studied in order to develop the latest technologies of electrochemical energy storage, which is caused by the rapid development of alternative energy sources, electric vehicles and portable electronic devices [9-11]. The most promising materials in this regard are solid electrolytes used in all-solid-state batteries. It should be noted that the use of solid electrolyte instead of liquid one not only increases the safety of batteries, but also simplifies the design of the battery itself [11-13].

Thus, this paper is devoted to preparing  $(\text{Cu}_{1-x}\text{Ag}_x)_7\text{SiS}_5\text{I}$ -based ceramics from nanopowders, measuring their electrical conductivity, separating the contributions of ionic and electronic components of conductivity, and studying the influence of  $\text{Cu}^+ \rightarrow \text{Ag}^+$  cationic substitution on their electrical parameters.

## II. EXPERIMENTAL

The nanocrystalline powders obtained by grinding of the synthesised  $(\text{Cu}_{1-x}\text{Ag}_x)_7\text{SiS}_5\text{I}$  compounds in a planetary ball mill PQ-N04 for 60 min with a speed of 200 rpm. The  $(\text{Cu}_{1-x}\text{Ag}_x)_7\text{SiS}_5\text{I}$  powders were investigated using XRD method (DRON 4-07,  $\text{CuK}\alpha$  radiation, angle scanning speed  $2\theta$  is 0.02 deg., exposure is 1 s) and SEM technique. Comparison of diffractograms indicates that the expansion of lines occurs with particles size decrease (Fig.1). This is confirmed by the results of SEM, with the use of which it was established that at a grinding time of 60 min the average particle size is  $\sim 100$  nm.

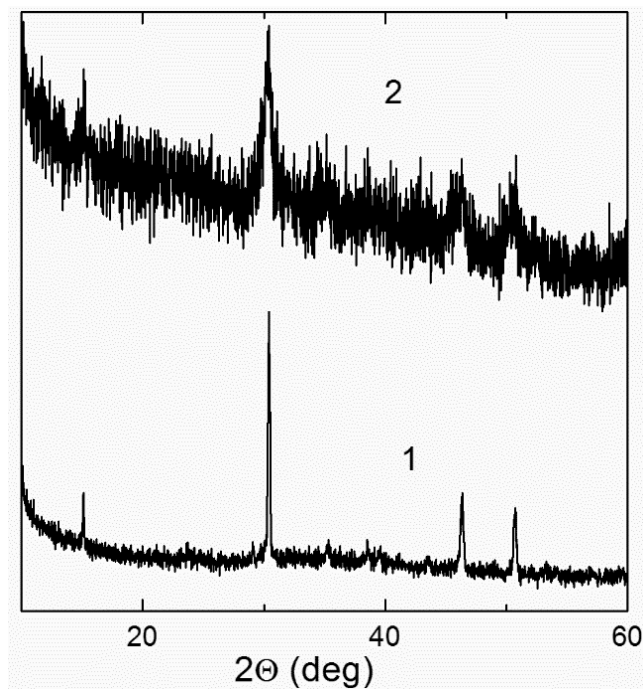


Fig. 1. Diffractograms of  $(\text{Cu}_{0.5}\text{Ag}_{0.5})_7\text{SiS}_5\text{I}$  powders with different average particles size: (1)  $\sim (10-50\mu\text{m})$ ; (2)  $\sim 100$  nm.

Pressing of samples was carried out at a pressure of  $\sim 400$  MPa, annealing - at 973 K during 36 hours. As a result, polycrystalline  $(\text{Cu}_{1-x}\text{Ag}_x)_7\text{SiS}_5\text{I}$  ceramic samples were obtained in the form of disks with a diameter of 8 mm and a thickness of 3-4 mm. To determine the size of crystallites after annealing, the obtained ceramic samples were investigated by microstructural analysis using metallographic microscope METAM - R1 (Fig.2). According to the results of the analysis of the obtained microstructure, histogram of particles size distribution was constructed. It is established that ceramic samples obtained by sintering nanocrystalline powder are characterized by homogeneous microstructure,

characterized by the distribution of particles in a narrower range. As a result of recrystallization, the average size of crystallites for obtained ceramics is  $\sim 3 \mu\text{m}$ .

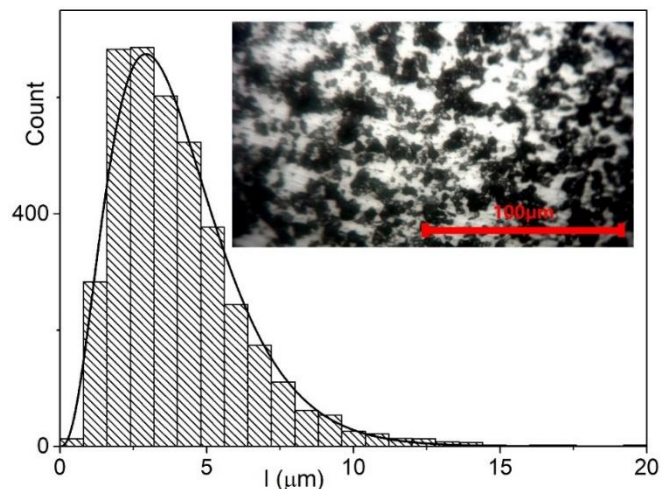


Fig. 2. Dependence of size distribution for crystallites of  $(\text{Cu}_{0.5}\text{Ag}_{0.5})_7\text{SiS}_5\text{I}$ -based ceramic, obtained from nanopowder which was milled in planetary ball mill for 60 min. The inset shows the microstructure image for  $(\text{Cu}_{0.5}\text{Ag}_{0.5})_7\text{SiS}_5\text{I}$ -based ceramic.

Investigations of the electrical conductivity of ceramic samples were carried out by impedance spectroscopy method in frequency (10 Hz -  $3 \times 10^5$  Hz; 20 Hz -  $2 \times 10^6$  Hz) and temperature (292 - 383 K) ranges with combination of high-precision LCR meters: Keysight E4980A and AT-2818. The amplitude of the alternating current constituted 10 mV. Measurement was carried out by a two-electrode method, on blocking (electronic) gold contacts. Gold contacts for measurements were applied by chemical precipitation from solutions [8].

### III. RESULTS AND DISCUSSION

For all ceramic samples, the obtained dependences of the total conductivity on the frequency are of a typical nature (Fig.3a):

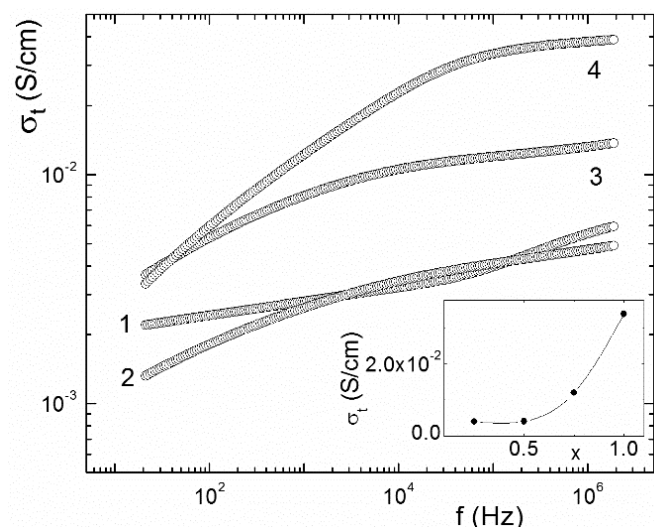


Fig. 3. Frequency dependences of total electrical conductivity at  $T=298$  K for  $(\text{Cu}_{1-x}\text{Ag}_x)_7\text{SiS}_5\text{I}$ -based ceramics:  $(\text{Cu}_{0.75}\text{Ag}_{0.25})_7\text{SiS}_5\text{I}$  (1),  $(\text{Cu}_{0.5}\text{Ag}_{0.5})_7\text{SiS}_5\text{I}$  (2),  $(\text{Cu}_{0.25}\text{Ag}_{0.75})_7\text{SiS}_5\text{I}$  (3),  $\text{Ag}_7\text{SiS}_5\text{I}$  (4). The inset shows the compositional dependence of total electrical conductivity for  $(\text{Cu}_{1-x}\text{Ag}_x)_7\text{SiS}_5\text{I}$ -based ceramics at 100 kHz.

an increase in conductivity with a frequency is observed, being characteristic of materials with ionic conductivity in

solid state [14]. The inset in Fig.3 presents the compositional dependence of the total electrical conductivity for  $(\text{Cu}_{1-x}\text{Ag}_x)_7\text{SiS}_5\text{I}$ -based ceramics at 100 kHz. It is shown that at  $\text{Cu}^+ \rightarrow \text{Ag}^+$  cationic substitution the nonlinear increase of electrical conductivity is observed (inset to Fig. 3).

For the detailed study of frequency behavior of electrical conductivity and its separation into ionic and electronic components, a standard approach using electrode equivalent circuits and their analysis on Nyquist plots was used [14-16]. The parasitic inductance of the cell ( $\sim 2 \times 10^{-8}$  H) is taken into account during the analysis of all ceramic samples. We will illustrate such analysis on  $(\text{Cu}_{0.25}\text{Ag}_{0.75})_7\text{SiS}_5\text{I}$ -based ceramic for which at  $Z''$ - $Z'$  dependence two semicircles are observed (Fig.4).

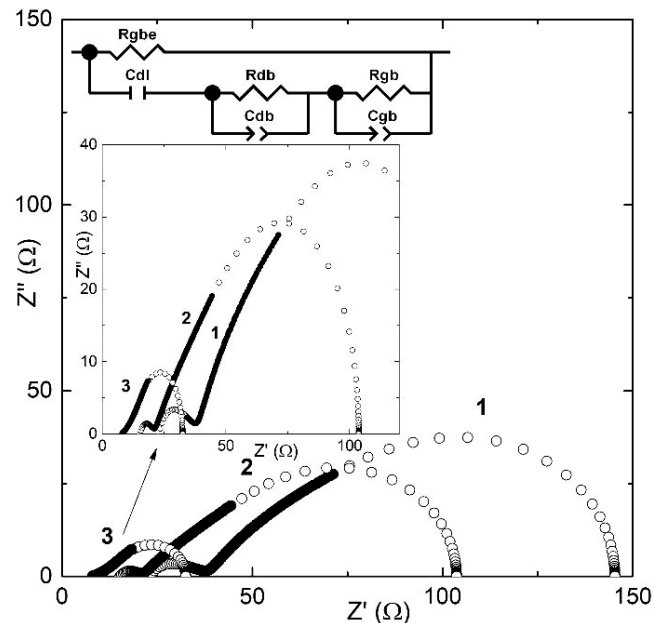


Fig. 4. EEC and Nyquist plots for  $(\text{Cu}_{0.25}\text{Ag}_{0.75})_7\text{SiS}_5\text{I}$ -based ceramic at different temperatures: (1) 298 K, (2) 323 K, (3) 373 K. Experimental data correspond to the solid dots, calculated data correspond to the open dots.

The EEC, which described the Nyquist plots, can be divided in two parts: one of them relates to ionic processes, another one - to electronic processes. Low-frequency semicircles on the Nyquist plots correspond to the diffusion relaxation processes at the electrode/crystal boundary which is described by the capacity of the double diffusion layer  $C_{dl}$  (Fig. 4). Serial to them were included the elements with  $R_{gb}/C_{gb}$  parameters which related to resistance and capacity of the grain boundaries of ceramic samples (the end of low-frequency semicircles) (Fig. 4). High-frequency semicircles correspond to the conductivity processes determined by the resistance of intra-grain boundaries, which is marked by  $R_{db}$  on the EEC, with parallel included capacity  $C_{db}$  (Fig. 4). It should be noted that on EEC parallelly to the elements responsible for ion processes the electronic resistance  $R_{gbe}$  is included and determined electronic conductivity of the samples (Fig.4).

Temperature studies have shown that with increasing temperature, the increase of electronic conductivity gradually eliminates the influence of diffusion ionic processes at the boundaries of ceramics crystallites, as evidenced by the decrease of the high-frequency semicircle at 323 K (Fig.4, curve 2). With further increase of temperature up to 373 K (Fig. 4, curve 3) there is a further reduction of the influence of diffusion ionic processes, which, together with the

decrease in the thickness of the double diffusion layer, lead to the significant decrease of the high-frequency semicircle.

Fig.5a presents the compositional dependences of the ionic and electronic components of electrical conductivity for  $(\text{Cu}_{1-x}\text{Ag}_x)_7\text{SiS}_5\text{I}$ -based ceramics. With  $\text{Cu}^+ \rightarrow \text{Ag}^+$  cationic substitution the nonlinear increase of ionic component and nonlinear decrease of electronic component are observed. At the same time the ratio of ionic and electronic components nonlinearly increases (inset to Fig. 5a). It is revealed that with silver content increase in  $(\text{Cu}_{1-x}\text{Ag}_x)_7\text{SiS}_5\text{I}$ -based ceramics the above mentioned ratio changed from  $\sigma_{\text{ion}} < \sigma_{\text{el}}$  ( $\text{Cu}_{0.75}\text{Ag}_{0.25}$ ) $_7\text{SiS}_5\text{I}$  to  $\sigma_{\text{ion}} \gg \sigma_{\text{el}}$  ( $\text{Ag}_7\text{SiS}_5\text{I}$ ).

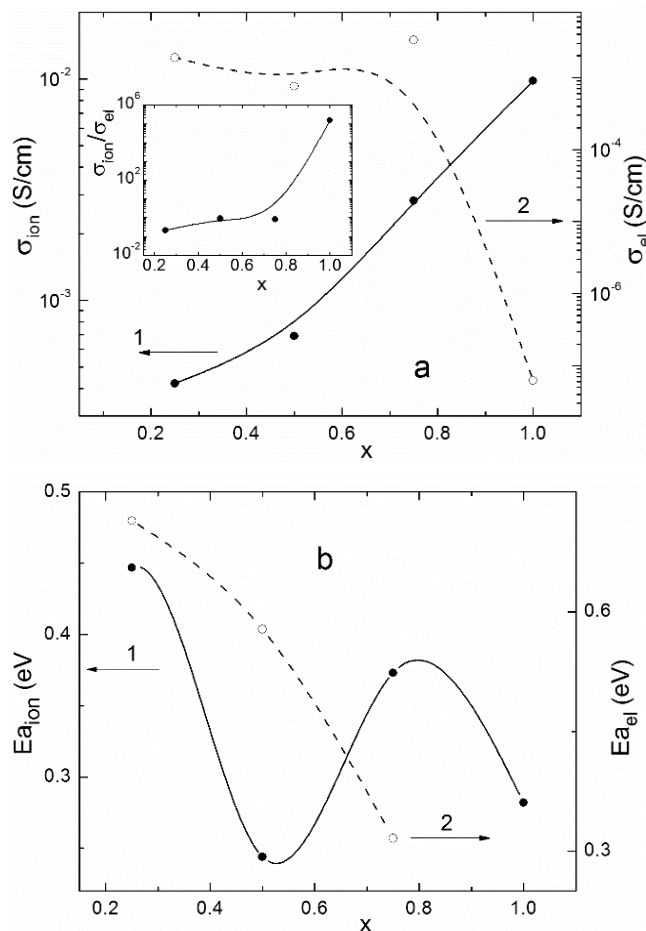


Fig. 5. (a) Compositional dependences of ionic (1) and electronic (2) components of electrical conductivity at  $T=298$  K for  $(\text{Cu}_{1-x}\text{Ag}_x)_7\text{SiS}_5\text{I}$ -based ceramics, the inset shows the compositional dependences of the ratio of the conductivity components; (b) Compositional dependences of the activation energies of ionic (1) and electronic (2) components of electrical conductivity for  $(\text{Cu}_{1-x}\text{Ag}_x)_7\text{SiS}_5\text{I}$ -based ceramics.

The temperature dependences of the ionic and electronic components of electrical conductivity in the Arrhenius coordinates for  $(\text{Cu}_{1-x}\text{Ag}_x)_7\text{SiS}_5\text{I}$ -based ceramics are presented on Fig.6.

The linear behavior of above mentioned dependences confirmed the thermoactivating character of electrical conductivity. From the presented temperature dependences of the ionic and electronic conductivity the activation energies were determined (Fig. 5b).

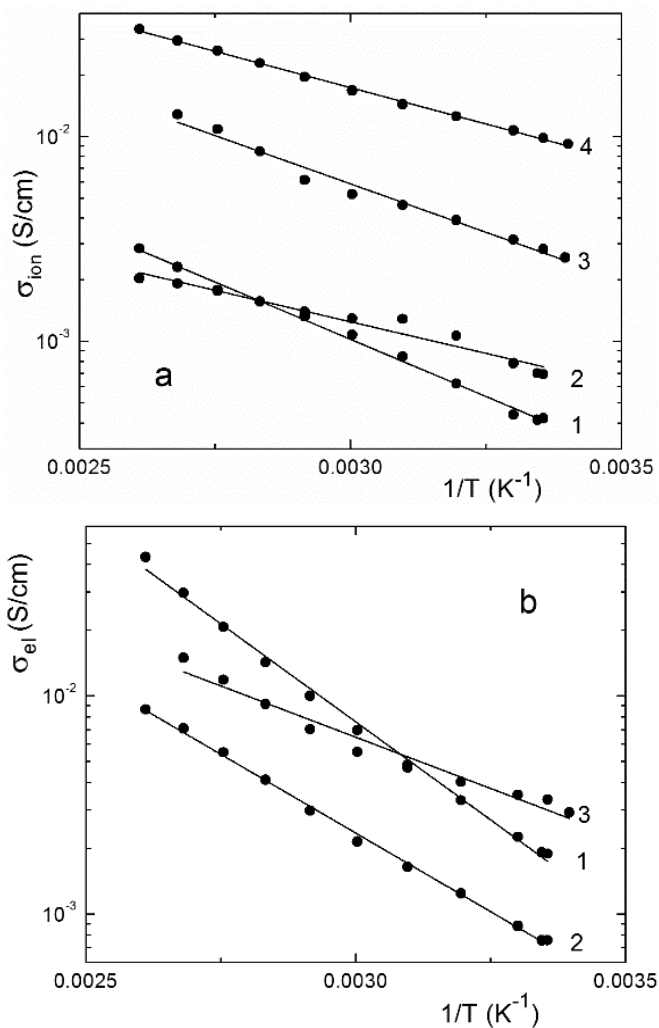


Fig. 6. Temperature dependences of ionic (a) and electronic (b) components of electrical conductivity for  $(\text{Cu}_{1-x}\text{Ag}_x)_7\text{SiS}_5\text{I}$ -based ceramics:  $(\text{Cu}_{0.75}\text{Ag}_{0.25})_7\text{SiS}_5\text{I}$  (1),  $(\text{Cu}_{0.5}\text{Ag}_{0.5})_7\text{SiS}_5\text{I}$  (2),  $(\text{Cu}_{0.25}\text{Ag}_{0.75})_7\text{SiS}_5\text{I}$  (3),  $\text{Ag}_7\text{SiS}_5\text{I}$  (4).

It is shown that the activation energy of ionic component of electrical conductivity for  $\text{Cu}_{1-x}\text{Ag}_x)_7\text{SiS}_5\text{I}$ -based ceramics at  $\text{Cu}^+ \leftrightarrow \text{Ag}^+$  cationic substitution nonlinearly decreases with minimum for  $(\text{Cu}_{0.5}\text{Ag}_{0.5})_7\text{SiS}_5\text{I}$ -based ceramic (Fig.5b). At the same time with silver content increase the activation energy of electronic component of electrical conductivity monotonously decreases (Fig.5b).

#### IV. CONCLUSIONS

$(\text{Cu}_{1-x}\text{Ag}_x)_7\text{SiS}_5\text{I}$ -based ceramics were prepared from nanocrystalline powders which were obtained by grinding in a planetary ball mill. Nanopowders were pressed out at a pressure of  $\sim 400$  MPa and were annealed at 973 K during 36 hours. X-ray diffraction spectra of nanopowders have shown that they preserved the argyrodite structure, however, as the particles size decreases, the diffraction bands expand. From microstructural analysis the dependences of size distribution and average crystallites size for  $(\text{Cu}_{1-x}\text{Ag}_x)_7\text{SiS}_5\text{I}$ -based ceramics were investigated. Electrical conductivity of ceramic samples was measured in the frequency range from 10 Hz to  $2 \times 10^6$  Hz and temperature interval from 292 K to 383 K. It is shown that the total electrical conductivity at  $\text{Cu}^+ \rightarrow \text{Ag}^+$  cationic substitution was nonlinearly increased. Using Nyquist plots the total electrical conductivity was separated into ionic and electronic components. It is revealed that with  $\text{Cu}^+ \rightarrow \text{Ag}^+$  cationic substitution the ionic component

nonlinearly increases, the electronic component nonlinearly decreases, and their ratio  $\sigma_{\text{ion}}/\sigma_{\text{el}}$  nonlinearly increases from  $\sigma_{\text{ion}} < \sigma_{\text{el}}$  ( $\text{Cu}_{0.75}\text{Ag}_{0.25}\text{Si}_7\text{S}_5\text{I}$ ) to  $\sigma_{\text{ion}} \gg \sigma_{\text{el}}$  ( $\text{Ag}_7\text{Si}_5\text{I}$ ). Temperature studies have shown that the temperature dependences of ionic and electronic components are described by the Arrhenius law, which confirms the thermoactivating character of conductivity.

#### REFERENCES

- [1] W.F. Kuhs, R. Nitsche, K. Scheunemann, "The argyrodites – a new family of the tetrahedrally close-packed structures", *Mater. Res. Bull.*, vol. 14, pp. 241–248, February 1979.
- [2] T. Nilges, A. Pfitzner, "A structural differentiation of quaternary copper argyrodites: Structure – property relations of high temperature ion conductors", *Z. Kristallogr.*, vol.220, pp. 281–294, April 2005.
- [3] I.P. Studenyak, M. Kranjčec, M.V. Kurik, "Urbach rule and disordering processes in  $\text{Cu}_6\text{P}(\text{S}_{1-x}\text{Se}_x)_5\text{Br}_{1-y}\text{I}_y$  superionic conductors", *J. Phys. Chem. Solids.*, vol. 67, pp. 807-817, April 2006.
- [4] A.F. Orliukas, E. Kazakevicius, A. Kezionis, T. Salkus, I.P. Studenyak, R.Yu. Buchuk, I.P. Prits, V.V. Panko, "Preparation, electric conductivity and dielectrical properties of  $\text{Cu}_6\text{PS}_5\text{I}$ -based superionic composites", *Solid State Ionics.*, vol. 180, pp. 183-186, March 2009.
- [5] I.P. Studenyak, V.Yu. Izai, V.I. Studenyak, O.V. Kovalchuk, T.M. Kovalchuk, P. Kopčanský, M. Timko, N. Tomašovičová, V. Zavisova, J. Miskuf, I.V. Oleinikova, "Influence of  $\text{Cu}_6\text{PS}_5\text{I}$  superionic nanoparticles on the dielectric properties of 6CB liquid crystal", *Liquid Crystals.*, vol. 44, pp. 897-903, November 2017.
- [6] T. Šalkus, E. Kazakevicius, J. Banys, M. Kranjčec, A.A. Chomolyak, Yu.Yu. Neimet, I.P. Studenyak, "Influence of grain size effect on electrical properties of  $\text{Cu}_6\text{PS}_5\text{I}$  superionic ceramics", *Solid State Ionics.*, vol. 262, pp. 597-600, September 2014.
- [7] I.P. Studenyak, M. Kranjčec, V.Yu. Izai, A.A. Chomolyak, M. Vorohta, V. Matolin, C. Cserhati, S. Kökényesi. "Structural and temperature-related disordering studies of  $\text{Cu}_6\text{PS}_5\text{I}$  amorphous thin films", *Thin Solid Films.*, vol. 520, 1729-1733, January 2012.
- [8] I.P. Studenyak, A.I. Pogodin, V.I. Studenyak, V.Yu. Izai, M. J. Filep, O.P. Kokhan, M. Kranjčec, P. Kúš, "Electrical properties of copper- and silver-containing superionic ( $\text{Cu}_{1-x}\text{Ag}_x$ ) $_7\text{Si}_5\text{I}$  mixed crystals with argyrodite structure", *Solid State Ionics.*, vol. 345., №.115183, February 2020.
- [9] Fernao Pires, E. Romero-Cadaval, D. Vinnikov, I. Roasto, J.F. Martins, "Power converter interfaces for electrochemical energy storage systems – A review", *Energy Conversion and Management.*, vol. 86, pp. 453–475, October 2014.
- [10] H. Li, X. Zhang, Z. Zhao, Z. Hu, X. Liu, G. Yu, "Flexible Sodium-Ion Based Energy Storage Devices: Recent Progress and Challenges", *Energy Storage Materials.*, vol. 26, pp. 83-104, April 2020.
- [11] Z. Wu, Z. Xie, A. Yoshida, Z. Wang, X. Hao, A. Abudula, G. Guan, "Utmost limits of various solid electrolytes in all-solid-state lithium batteries: A critical review", *Renewable and Sustainable Energy Reviews* ., vol. 109, pp. 367–385, July 2019.
- [12] J.W. Fergus, "Ceramic and polymeric solid electrolytes for lithium-ion batteries", *Journal of Power Sources.*, vol. 195, pp. 4554–4569, August 2010.
- [13] Z. Zhang, Q. Zhang, C. Ren, F. Luo, Q. Ma, Y.-S. Hu, Z. Zhou, H. Li, X.e Huang, L. Chen, "A ceramic/polymer composite solid electrolyte for sodium batteries", *J. Mater. Chem. A.*, vol. 4., pp. 15823-15828, September 2016.
- [14] A.K. Ivanov-Schitz, I.V. Murin, "Solid State Ionics", vol. 1, S.-Petersburg Univ. Press, 2000 (in Russian).
- [15] M.E. Orazem, B. Tribollet, "Electrochemical Impedance Spectroscopy", John Wiley & Sons, New Jersey, 2008.
- [16] R.A. Huggins, "Simple method to determine electronic and ionic components of the conductivity in mixed conductors: a review", *Ionics.*, vol.8, pp. 300-313, May 2002.

# Optical Properties of X-Ray Irradiated (Ga<sub>0.1</sub>In<sub>0.9</sub>)<sub>2</sub>Se<sub>3</sub> Thin Films

M. Pop<sup>1</sup>, M. Kranjčec<sup>2</sup>, A. Bendak<sup>1</sup>, A. Solomon<sup>3</sup>, L. Suslikov<sup>1</sup>, I. Studenyak<sup>1</sup>

<sup>1</sup>Uzhhorod National University, Uzhhorod, Ukraine  
Pidhirna St. 46 / 88000 / Uzhhorod / Ukraine / mykhaylo.pop@uzhnu.edu.ua

<sup>2</sup>University North, Varazdin, Croatia

<sup>3</sup>Institute of Electron Physics, Uzhhorod, Ukraine

**Abstract** — Thermal evaporation technique was used to deposit (Ga<sub>0.1</sub>In<sub>0.9</sub>)<sub>2</sub>Se<sub>3</sub> thin films. As-deposited thin films were irradiated using wideband radiation of Cu-anode X-ray tube at different exposition times. Refractive index and extinction coefficient dispersions were obtained from the spectral ellipsometry measurements. Optical transmission spectra of X-ray irradiated (Ga<sub>0.1</sub>In<sub>0.9</sub>)<sub>2</sub>Se<sub>3</sub> thin films were measured depending on irradiation time. Parameters of Urbach absorption edge for X-ray irradiated (Ga<sub>0.1</sub>In<sub>0.9</sub>)<sub>2</sub>Se<sub>3</sub> thin films were studied. The nonlinear decrease of energy pseudogap as well as nonlinear increase of Urbach energy and refractive index with increase of X-ray irradiation time are revealed.

**Keywords** — thin film, spectral ellipsometry, transmission spectra, X-ray irradiation, refractive index, energy pseudogap

## I. INTRODUCTION

(Ga<sub>x</sub>In<sub>1-x</sub>)<sub>2</sub>Se<sub>3</sub> solid solutions in the compositional range of 0.02 < x < 0.55 crystallize in the defect wurtzite structure with hexagonal symmetry (P<sub>6</sub><sub>1</sub> or P<sub>6</sub><sub>5</sub> space group) and belong to the γ<sub>1</sub>-phase of Ga<sub>2</sub>Se<sub>3</sub>-In<sub>2</sub>Se<sub>3</sub> system [1]. They are characterized by the high concentration of vacancies that can form spirals along the optical axis *c* of the crystal [2]. Alternation of cations and vacancies results in random fluctuations of lattice electric potential which, in turn, affects physical processes in these materials.

γ<sub>1</sub>-(Ga<sub>x</sub>In<sub>1-x</sub>)<sub>2</sub>Se<sub>3</sub> solid solutions possess the low electrical conductivity (~10<sup>-10</sup> Ω<sup>-1</sup>×cm<sup>-1</sup>), whereas photoconductivity in the γ<sub>1</sub>-phase is almost by three orders of magnitude higher than in other phases [1]. Optical absorption edge in γ<sub>1</sub>-(Ga<sub>x</sub>In<sub>1-x</sub>)<sub>2</sub>Se<sub>3</sub> crystals at low absorption levels is shown to be formed by indirect interband optical transitions [3], temperature effect on the absorption edge being studied in Ref. [4]. Interrelation between photoluminescence and optical absorption spectra were investigated in Ref. [5]. Refractometric, birefringent and gyrotropic properties of γ<sub>1</sub>-(Ga<sub>x</sub>In<sub>1-x</sub>)<sub>2</sub>Se<sub>3</sub> crystals were studied in detail in Refs. [6–8]. Besides, γ<sub>1</sub>-(Ga<sub>x</sub>In<sub>1-x</sub>)<sub>2</sub>Se<sub>3</sub> crystals are characterized by high optical activity along the optical axis and are promising materials for acousto-optical modulators of laser irradiation [9].

In recent years the studies for obtaining (Ga<sub>x</sub>In<sub>1-x</sub>)<sub>2</sub>Se<sub>3</sub> solid solution in the form of thin films were performed for their effective practical application [10]. In the present paper we report on the ellipsometric studies of optical constants,

the influence of X-ray irradiation on the optical transmission spectra, Urbach absorption edge parameters and refractive indices in (Ga<sub>0.1</sub>In<sub>0.9</sub>)<sub>2</sub>Se<sub>3</sub> thin films.

## II. EXPERIMENTAL

(Ga<sub>0.1</sub>In<sub>0.9</sub>)<sub>2</sub>Se<sub>3</sub> crystals were obtained by Bridgman technique. (Ga<sub>0.1</sub>In<sub>0.9</sub>)<sub>2</sub>Se<sub>3</sub> thin films were sputtered onto a quartz glass substrate by thermal evaporation, their thickness being 2.4 μm. The structure of the deposited films was analyzed by X-ray diffraction; the diffraction spectra show the films to be amorphous. The composition of the thin films was determined by EDX on Hitachi S4300 SEM.

X-ray irradiation was performed for the different exposition times (30, 60 and 120 min) using wideband radiation of Cu-anode X-ray tube with approx. 400 W of power applied (33 kV, 13 mA). Spectroscopic ellipsometer Horiba Smart SE was used for the measurements of the optical constants of (Ga<sub>0.1</sub>In<sub>0.9</sub>)<sub>2</sub>Se<sub>3</sub> thin films. Measurements were carried out in the spectrum region from 440 nm to 1000 nm at an incident angle of 70°. Optical transmission spectra of (Ga<sub>0.1</sub>In<sub>0.9</sub>)<sub>2</sub>Se<sub>3</sub> film were measured by using LOMO KSVU-23 grating monochromator. The spectral dependences of the absorption coefficient were derived from the interference transmission spectra [11].

## III. RESULTS AND DISCUSSION

(Ga<sub>0.1</sub>In<sub>0.9</sub>)<sub>2</sub>Se<sub>3</sub> crystals were obtained by Bridgman technique. (Ga<sub>0.1</sub>In<sub>0.9</sub>)<sub>2</sub>Se<sub>3</sub> thin films were sputtered onto a quartz glass substrate by thermal evaporation, their thickness being 2.4 μm. The structure of the deposited films was analyzed by X-ray diffraction; the diffraction spectra show the films to be amorphous. The composition of the thin films was determined by EDX on Hitachi S4300 SEM.

X-ray irradiation was performed for the different exposition times (30, 60 and 120 min) using wideband radiation of Cu-anode X-ray tube with approx. 400 W of power applied (33 kV, 13 mA). Spectroscopic ellipsometer Horiba Smart SE was used for the measurements of the optical constants of (Ga<sub>0.1</sub>In<sub>0.9</sub>)<sub>2</sub>Se<sub>3</sub> thin films. Measurements were carried out in the spectrum region from 440 nm to 1000

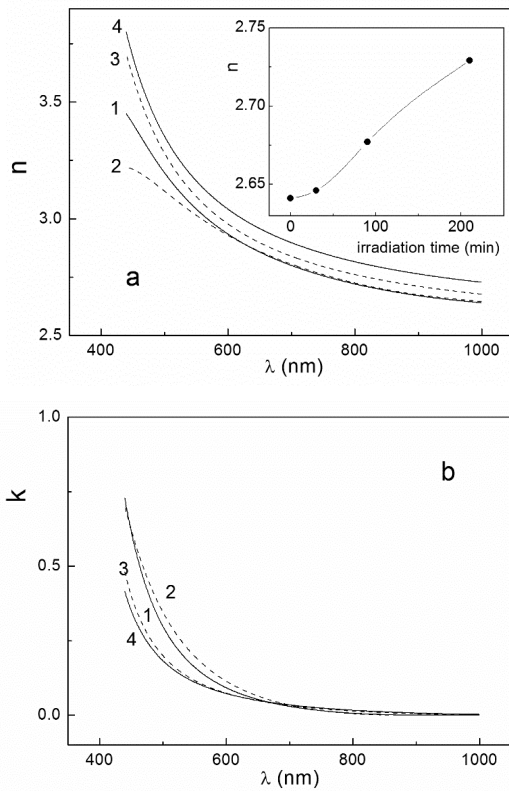


Fig. 1. Spectral dependences of refractive indices  $n$  (a) and extinction coefficients  $k$  (b) for as-deposited (1) and X-ray irradiated  $(\text{Ga}_{0.1}\text{In}_{0.9})_2\text{Se}_3$  thin films at various irradiation time: (2) 30, (3) 90 and (4) 210 min. The insert shows the dependence of refractive index on X-ray irradiation time.

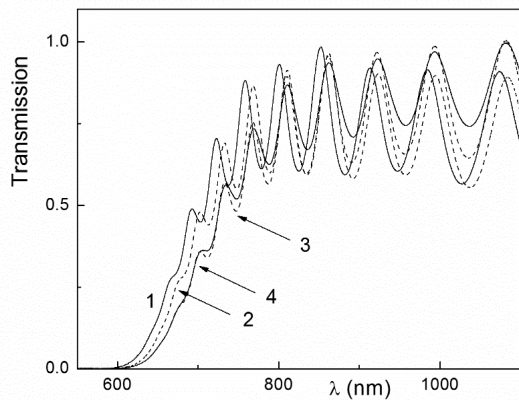


Fig. 2. Optical transmission spectra of as-deposited (1) and X-ray irradiated  $(\text{Ga}_{0.1}\text{In}_{0.9})_2\text{Se}_3$  thin films thin films at various irradiation time: (2) 30, (3) 90 and (4) 210 min.

Spectral dependences of absorption coefficient in the range of their exponential behavior and in Tauc region at various irradiation time for X-ray irradiated  $(\text{Ga}_{0.1}\text{In}_{0.9})_2\text{Se}_3$  thin films are shown in Fig.3. It is shown in Ref. [4] that the optical absorption edge for  $(\text{Ga}_{0.1}\text{In}_{0.9})_2\text{Se}_3$  thin films in the region of its exponential behaviour is described by Urbach rule

$$\alpha(h\nu, T) = \alpha_0 \cdot \exp\left[\frac{h\nu - E_0}{E_U(T)}\right], \quad (1)$$

where  $E_U(T)$  is the Urbach energy,  $\alpha_0$  and  $E_0$  are the coordinates of the convergence point of the Urbach bundle,  $h\nu$  and  $T$  are the photon energy and temperature, respectively. In the X-ray irradiated  $(\text{Ga}_{0.1}\text{In}_{0.9})_2\text{Se}_3$  thin films we also observed the Urbach shape of the optical absorption

edge (Fig. 3a). It should be noted that the optical absorption edge for X-ray irradiated  $(\text{Ga}_{0.1}\text{In}_{0.9})_2\text{Se}_3$  thin films is shifted to the long-wavelength region with irradiation time increase.

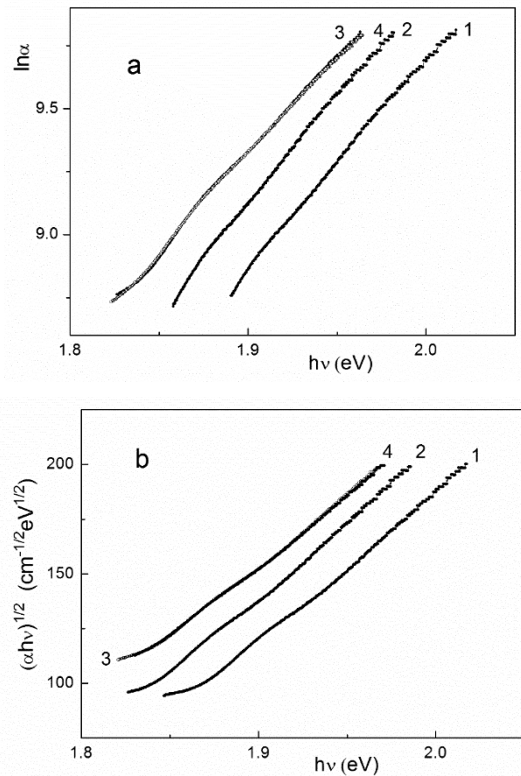


Fig.3. Spectral dependences of  $\ln \alpha$  (a) and  $(\alpha h\nu)^{1/2}$  (b) for as-deposited (1) and X-ray irradiated  $(\text{Ga}_{0.1}\text{In}_{0.9})_2\text{Se}_3$  thin films at various irradiation time: (2) 30, (3) 90 and (4) 210 min.

For the characterisation of the absorption edge spectral position such parameter as energy pseudogap  $E_g^\alpha$  ( $E_g^\alpha$  is the energy position of the exponential absorption edge) at a fixed absorption coefficient value  $\alpha$  was determined. We used the  $E_g^\alpha$  values taken at  $\alpha=10^4$  cm<sup>-1</sup> for thin films. The observed variation of the optical absorption edge leads to the  $E_g^\alpha$  value decrease and  $E_U$  value increase with irradiation time increase (from 1.940 to 1.883 eV and from 116 to 137 meV, respectively). The dependences of  $E_g^\alpha$  and  $E_U$  for X-ray irradiated  $(\text{Ga}_{0.1}\text{In}_{0.9})_2\text{Se}_3$  thin films on irradiation time are presented in Fig. 4.

In the Tauc region the  $E_g^T$  value can be determined from the Tauc relation [12]:

$$\alpha(h\nu) = \frac{B(h\nu - E_g^T)^2}{h\nu}, \quad (2)$$

which is valid within the range of high energies, when the absorption coefficient has values  $\alpha(h\nu) \geq 10^{-4}$  cm<sup>-1</sup>. In Eq. (2)  $B$  is the constant that depends on film material and characterizes the slope of the Tauc absorption edge. The  $E_g^T$  values for as-deposited and X-ray irradiated  $(\text{Ga}_{0.1}\text{In}_{0.9})_2\text{Se}_3$  thin films was determined by extrapolation of the dependences  $[\alpha(h\nu) \cdot h\nu]^{1/2} \sim f(h\nu)$  down to  $\alpha(h\nu) = 0$  (Fig.4). It is shown that the  $E_g^T$  value decreases with irradiation time increase from 1.750 to 1.680 eV.

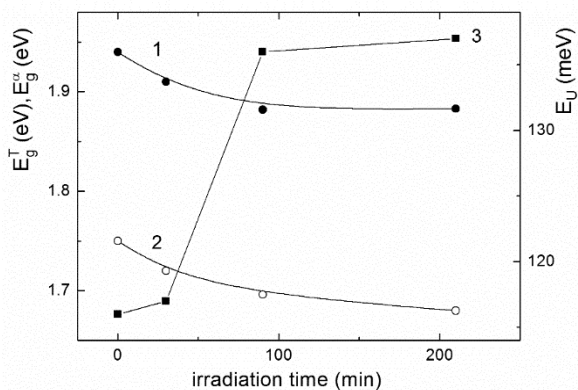


Fig. 4. Dependences of energy pseudogap  $E_g^T$  (1), Tauc energy  $E_g^T$  (2) and Urbach energy  $E_U$  (3) on X-ray irradiation time for  $(Ga_{0.1}In_{0.9})_2Se_3$  thin films.

It is well-known that Urbach energy  $E_U$  is characterised by the disordering level of investigated system and is described by the equation [13, 14]

$$E_U = (E_U)_T + (E_U)_X = (E_U)_T + (E_U)_{X,stat} + (E_U)_{X,dyn} \quad (3)$$

where  $(E_U)_T$  and  $(E_U)_X$  are the contributions of temperature-related and structural disordering to  $E_U$ , respectively;  $(E_U)_{X,stat}$  and  $(E_U)_{X,dyn}$  are the contributions of static structural disordering and dynamic structural disordering to  $(E_U)_X$ , respectively. The Urbach energy  $E_U$  increasing in X-ray irradiated  $(Ga_{0.1}In_{0.9})_2Se_3$  thin films is the evidence of the increase of the structural disordering due to the X-ray irradiation (Fig. 4). It should be noted that the most significant change of Urbach energy is revealed after 90 min of X-ray irradiation (Fig.4).

#### IV. CONCLUSION

$(Ga_{0.1}In_{0.9})_2Se_3$  films were deposited onto a quartz substrate by thermal evaporation technique. The spectral dependencies of the absorption coefficient were derived from the spectrometric studies of interference transmission spectra. The influence of X-ray irradiation on optical properties of  $(Ga_{0.1}In_{0.9})_2Se_3$  thin films has been investigated. With the irradiation time increase, the decrease of the energy pseudogap as well as the increase of the Urbach energy and refractive index have been observed. Besides, the increase of

Urbach energy is the evidence of increase in structural disordering contribution, which is caused by X-ray irradiation.

#### REFERENCES

- [1] S. Popović, B. Čelustka, Ž. Ružić-Toroš, D. Broz, "X-ray diffraction study and semiconducting properties of the system  $Ga_2Se_3-In_2Se_3$ ", Phys. Stat. Sol. (a), vol. 41, pp. 255-262, 1977.
- [2] J. Ye, T. Yoshida, Y. Nakamura, O. Nittono, "Realization of giant optical rotatory power for red and infrared light using  $III_2VI_3$  compound semiconductor  $(Ga_xIn_{1-x})_2Se_3$ ", Jap. J. Appl. Phys., vol. 35, pp. 4395-4400, 1996.
- [3] M. Kranjčec, B. Čelustka, B. Etlinger, D. Desnica, "The indirect allowed optical transition in  $(Ga_{0.3}In_{0.7})_2Se_3$ ", Phys. Stat. Sol. (a), vol. 109, pp. 329-336, 1988.
- [4] M. Kranjčec, D.I. Desnica, B. Čelustka, Gy.Sh. Kovacs, I.P. Studenyak, "Fundamental optical absorption edge and compositional disorder in  $\gamma_1-(Ga_xIn_{1-x})_2Se_3$  single crystals", Phys. Stat. Sol. (a), vol. 144, pp. 223-233, 1994.
- [5] M. Kranjčec, I.P. Studenyak, Yu.M. Azhniuk, "Photoluminescence and optical absorption edge in  $\gamma_1-(Ga_xIn_{1-x})_2Se_3$  mixed crystals", Phys. Stat. Sol. (b), vol.238, pp. 439-450, 2005.
- [6] J. Ye, T. Yoshida, Y. Nakamura, O. Nittono, "Optical activity in the vacancy ordered  $III_2VI_3$  compound semiconductor  $(Ga_{0.3}In_{0.7})_2Se_3$ ", Appl. Phys. Lett., vol. 67, pp. 3066-3068, 1995.
- [7] M. Kranjčec, I.D. Desnica, B. Čelustka, A.N. Borec, Gy.Sh. Kovacs, Z.P. Hadmashy, L.M. Suslikov, I.P. Studenyak, "On some crystal-optic properties of  $\gamma_1-(Ga_xIn_{1-x})_2Se_3$  single crystals", Phys. Stat. Sol. (a), vol. 153, pp. 539-546, 1996.
- [8] M. Kranjčec, I.P. Studenyak, L.M. Suslikov, Gy.Sh. Kovacs, "Cerovec E. Birefringence in  $\gamma_1-(Ga_xIn_{1-x})_2Se_3$  single crystals", Opt. Mat., vol. 25, pp.307-312, 2004
- [9] M. Kranjčec, I.D. Desnica, I.P. Studenyak, B. Čelustka, A.N. Borec, I.M. Yurkin, Gy.Sh. Kovacs, "Acousto-optic modulator with a  $(Ga_{0.4}In_{0.6})_2Se_3$  monocrystal as the active element", Applied Optics, vol. 36, pp. 490-493, 1997.
- [10] I.P. Studenyak, M. Kranjčec, V.Yu. Izai, V.I. Studenyak, M.M. Pop, L.M. Suslikov. "Ellipsometric and spectrometric studies of  $(Ga_{0.2}In_{0.8})_2Se_3$  thin film", Ukr. Fiz. Zhurn., vol. 65, No. 3., pp. 231-235, 2020
- [11] R. Swanepoel, "Determination of the thickness and optical constants of amorphous silicon", J. Phys. E: Sci. Instrum., vol. 16, No. 12, pp. 1214-1222, 1983.
- [12] J. Tauc, "States in the gap", J. Non-Cryst. Solids, vol. 8-10, pp. 569-585, 1972.
- [13] G.D. Cody, T. Tiedje, B. Abeles, B. Brooks, Y. Goldstein, "Disorder and the optical-absorption edge of hydrogenated amorphous silicon", Phys. Rev. Lett., vol. 47, pp. 1480-1483, 1981.
- [14] I.P. Studenyak, M. Kranjčec, M.V. Kurik, "Urbach rule and disordering processes in  $Cu_6P(S_{1-x}Se_x)_3Br_{1-y}I_y$  superionic conductors", J. Phys. Chem. Solids., vol. 67, pp. 807-817, April 2006.

# Effect of Annealing on the Surface Photoconductivity of Silicosillenite Crystals

Tatiana Panchenko\*, Ludmila Karpova<sup>+</sup>

\* Oles Honchar Dnipro National University, Department of Physics, Electronics and Computer Systems  
Gagarina av., 72 / 49010 / Dnipro / Ukraine / +380679835466 / panchtv141@gmail.com

<sup>+</sup> Ukrainian State University of Chemical Technology, Department of Mechanics  
Gagarina av., 8 / 49010 / Dnipro / Ukraine / +380503635545 / ludmila.karpova.ua@gmail.com

**Abstract** — The results of an experimental study of the effect of annealing in vacuum on the surface photoconductivity of undoped and chromium-doped silicosillenite crystals in the visible spectral range are presented. It is shown that varying the annealing conditions allows one to substantially modify the spectral distribution and quantitative characteristics of photoconductivity.

**Keywords** — surface photoconductivity, annealing, vacuum, oxygen, silicosillenite crystals, chromium impurity.

## I. INTRODUCTION

Crystals of the  $\text{Bi}_{12}\text{MO}_{20}$  family of sillenites (BMO, where  $M = \text{Si}, \text{Ge}, \text{Ti}$ ) have a unique set of practically useful properties (photorefractive, electro- and magneto-optical, piezoelectric and a number of other effects). They are successfully used in many areas of functional electronics [1]. Recently, designs of new functional devices in the sizes of nano- and micrometric scales are being developed. In this connection, interest in obtaining and studying the properties of surface layer [2], micro- and nanocrystals of BMO [3], and also crystals of BMO with nanoscale inclusions [4] is significantly increasing. Actual is the task of modifying the properties of sillenites in thin layers near the surface.

A feature of BMO crystals is high photosensitivity in the visible wavelength range ( $\sim 10^{-6}$  J/cm<sup>2</sup>). It is of interest to study the possibilities of a controlled modification of this sensitivity in the surface layers of samples of BMO crystals. This work presents the results of an experimental study of the effect of annealing on the surface photoconductivity of undoped and chromium-doped  $\text{Bi}_{12}\text{SiO}_{20}$  silicosillenite crystals (BSO and BSO:Cr, respectively).

## II. EXPERIMENT

Undoped BSO crystals of stoichiometric composition and with non-stoichiometric defects in the form of deficiency (BSO – Si) and excess silicon (BSO + Si), as well as BSO:Cr crystals with different concentrations of Cr impurities were grown by the Czochralski method. The content of Cr ions in BSO:Cr crystals was determined by the method of spectral emission analysis and amounted to  $\sim 10^{-4}$ ,  $10^{-3}$ ,  $10^{-2}$  and  $10^{-1}$  mass. %. Varying non-stoichiometry with respect to Si made it possible to vary the content of defects in the oxygen sublattice of tetrahedra, in the centers of which Si ions are located in BSO crystals.

The Cr impurity was chosen as the dopant due to its

strong influence on the optical absorption and photochromic effect in sillenites.

Surface photoconductivity was studied in the spectral range of the energy of light quanta  $h\nu = 0.4 - 3.4$  eV at room temperature. We used a prism monochromator SPM with a 600 Wt xenon lamp. The light beam was modulated at a frequency of 12 Hz. The measurements were carried out in a constant electric field, a stabilized voltage of 15 V was applied. The samples were prepared in the form of polished plates cut in the crystallographic plane (001). Ag electrodes with a gap between them of 1 mm were deposited on one of these planes. The useful signal was recorded using the synchronous detection technique. The dependences of the photocurrent  $I^{\text{ph}}(h\nu)$  were normalized with respect to the spectral distribution of the flux of light quanta. The light intensity in the studied spectral range was brought to the same value using a set of neutral filters. Annealing the samples in vacuum  $\sim 10^{-3}$  Pa was carried out at  $T \approx 830 - 850$  K for 2 hours.

The measurement results are presented in the form of spectral dependences of the relative photoconductivity  $\sigma^{\text{ph}} = (\sigma_1 - \sigma_0)/\sigma_0$ , where  $\sigma_1$  and  $\sigma_0$  are the surface conductivities during illumination and in the dark, respectively, on the energy of light quanta in the semi-logarithmic scale  $L_g \sigma^{\text{ph}}(h\nu)$ .

## III. EXPERIMENTAL RESULTS AND DISCUSSION

### A. Effect of annealing on the photoconductivity of BSO crystals with non-stoichiometric defects

BSO crystals are wide-gap semiconductors (band gap  $\Delta E_g \approx 3.3$  eV at room temperature). The forbidden zone has a complex structure of local levels [5]. It is due to the high concentration ( $\sim 10^{18}$  1/cm<sup>3</sup>) of intrinsic point defects. The most characteristic of them are non-stoichiometry defects. The stoichiometric composition contains 14.3 mol. %  $\text{SiO}_2$  and 85.7 mol%  $\text{Bi}_2\text{O}_3$ . We made a  $\text{SiO}_2$  deficit (10 mol. %) and an excess of  $\text{SiO}_2$  (17 mol. %) due to the corresponding excess or deficiency of  $\text{Bi}_2\text{O}_3$  in the charge. BSO crystals of stoichiometric composition were grown, as well as crystals with excess (BSO + Si) and silicon deficiency (BSO – Si).

The obtained dependences  $L_g \sigma^{\text{ph}}(h\nu)$  have the same character of the spectral distribution of photoconductivity with a wide intense weakly structured domed peak in the

region  $h\nu_1 = 2.1 - 3.1$  eV and a weak stepwise increase in

photoconductivity in the region  $h\nu_2 = 1.0 - 2.1$  eV (Fig. 1).

In this case, before annealing in vacuum, the photoconductivity in both spectral regions  $h\nu_1$  and  $h\nu_2$  exceeds (BSO + Si crystals) or less (BSO - Si crystals) than the photoconductivity of BSO samples with stoichiometric composition (Fig. 1, a).

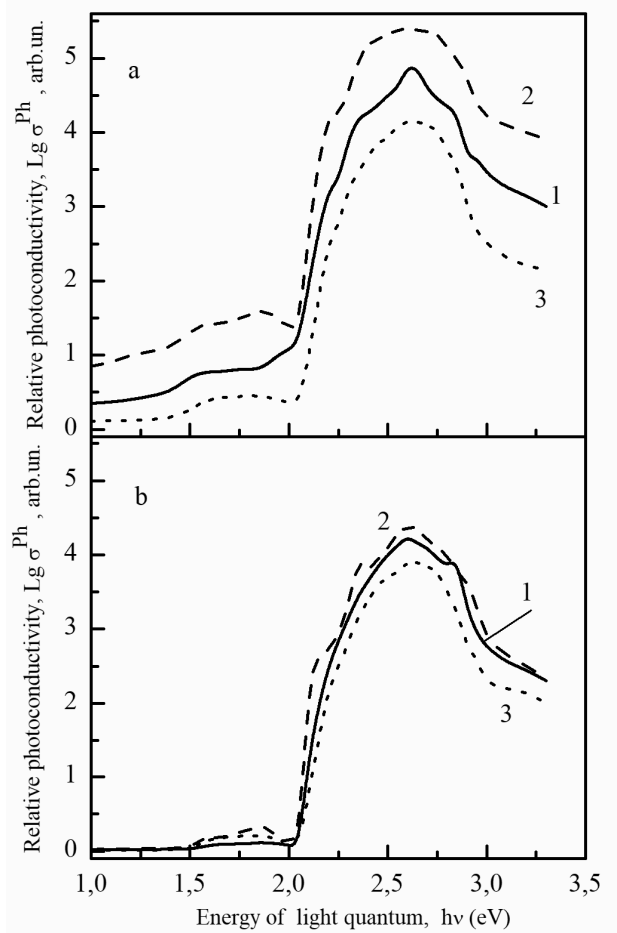


Fig. 1. The spectral dependences of photoconductivity of BSO (a, 1; b, 1), BSO + Si (a, 2; b, 2) and BSO - Si (a, 3; b, 3) crystals before (a) and after annealing in vacuum (b).

Thus, photoconductivity is associated with the defectiveness of the Si sublattice. It is known that in BSO crystals there are a number of vacancies (up to 10%) in  $Si^{4+}$  sites, which can be replaced by  $Bi^{3+}$  and  $Bi^{5+}$  ions. Such substitutions cause the appearance of acceptor and donor levels in the forbidden zone, respectively. To some extent, donor levels can be compensated. The filling of Si vacancies specified by nonstoichiometry in BSO + Si crystals leads to a decrease in the degree of compensation and, consequently, to an increase in photoconductivity. We have the opposite situation for BSO - Si crystals.

Annealing in vacuum causes a decrease in photoconductivity and eliminates the difference in its value for BSO and BSO  $\pm$  Si crystals (Fig. 1, b). This is partly explained as follows. The appearance of oxygen vacancies favors the formation of hole centers of  $O^-$  and nanosized complexes of the Si - O - Si type. They are characterized by intracenter absorption in the near UV region. Such absorption was observed in BSO crystals annealed in vacuum [6].

A possible reason for the extinction of photoconductivity may be the appearance of new recombination channels. 2-center recombination, for example, demonstrates itself in the phenomena of thermal activation and quenching of photoconductivity in BSO crystals [7].

### B. Effect of annealing on the photoconductivity of BSO crystals doped with chromium

The interest in studying the photoconductivity of BSO crystals doped with multiply charged chromium ions is due to the possibility of controlled control of their photoelectric properties and optical absorption due to the photochromic effect. This can be used, for example, in the development of planar optical waveguides with adjustable parameters.

The surface photoconductivity spectra  $Lg \sigma^{Ph}(h\nu)$  of BSO:Cr crystals containing different concentrations of Cr ions obtained before and after annealing in vacuum are shown in Fig. 2 a, b.

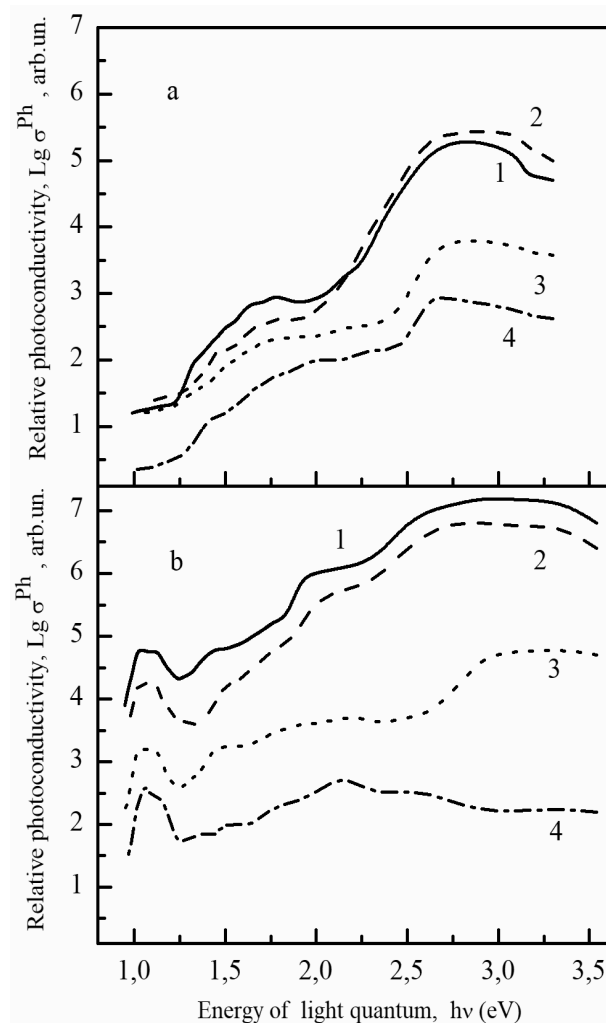


Fig. 2. The spectral dependences of photoconductivity of BSO:Cr crystals with a concentration of Cr  $10^{-4}$  (a, 1; b, 1),  $10^{-3}$  (a, 2; b, 2),  $10^{-2}$  (a, 3; b, 3) and  $10^{-1}$  mass. % (a, 4; b, 4) before (a) and after annealing in vacuum (b).

With an increase in the Cr content, a decrease in photosensitivity is observed in the entire studied spectral range. The nature of the spectral distribution of the photoresponse differs significantly from the photoresponse of undoped BSO with a more pronounced structure.

The effect of vacuum annealing is opposite to the effect on undoped BSO photoconductivity does not decrease, but

grows within the order of magnitude over the entire studied range.

In addition, an intense peak appears in the near infrared region with  $h\nu_{\max} = 1.12$  eV. Probably, a new broad peak also appears in the region  $h\nu \approx 1.8 - 2.5$  eV. It is hidden by the envelope of the  $I^{\text{ph}}(h\nu)$  spectrum curve for BSO:Cr crystals containing  $10^{-4}$ ,  $10^{-3}$ , and  $10^{-2}$  masses. % Cr, however, is recorded in crystals with  $10^{-1}$  mass. % Cr (Fig. 2, b).

Multiply charged (from +1 to +6) Cr ions in BSO crystals can replace  $\text{Bi}^{3+}$  ions in distorted oxygen octahedrons, as well as  $\text{Si}^{4+}$  ions in oxygen tetrahedrons. Many variants of the entry of Cr ions determine the appearance of new donors and acceptors. This substantially complicates the structure of the photoconductivity spectra of BSO:Cr crystals.

However, some of the local levels may play the role of recombination centers. If the concentration of recombination centers also increases with increasing chromium concentration, then the photoconductivity of un-annealed and vacuum-annealed BSO:Cr crystals decreases (Fig. 2, b).

#### IV. CONCLUSIONS

1. Varying the concentration of non-stoichiometry defects with respect to the Si:Bi ratio when growing BSO crystals allows one to vary the surface photoconductivity within one (range  $h\nu \approx 1 - 2$  eV) and two (range  $h\nu \approx 2 - 3.3$  eV) orders of magnitude. If it is necessary to reduce the spatial heterogeneity of the distribution of defects of non-stoichiometry with respect to the Si: Bi ratio and the related inhomogeneity of photoconductivity, the crystals should be annealed in vacuum.

2. Doping BSO crystals with Cr ions allows one to change the spectral distribution of photoconductivity and increase it within an order of magnitude in the region with  $h\nu < 2$  eV, however, with increasing concentration, the photoconductivity decreases.

Vacuum annealing provides an increase in photoconductivity in the entire spectral range with the appearance of a peak in the region  $h\nu \approx 0.9 - 1.4$  eV.

#### REFERENCES

- [1] P. Gunter, J. Huignard, "Photorefractive Materials and Their Applications", Part. 1. Springer Science+Business Media, New York, 2006.
- [2] Veber, S. Kunej, D. Suvorov, "Dielectric Properties of Sol-Gel-Derived  $\text{Bi}_{12}\text{SiO}_{20}$  Thin Films", in J. Am. Ceram. Soc., vol. 96 [1], pp. 157-160, 2013. DOI: 10.1111/j.1551-2916.2012.05438.x.
- [3] Zhen Wan & Gaoko Zhang, "Controlled synthesis and visible light photocatalytic activity of  $\text{Bi}_{12}\text{GeO}_{20}$  uniform microcrystals", in Scientific reports, vol. [4:6298], 2014. DOI: 10.1038/srep06298.
- [4] Filipic, A. Rlos, M. Gajc, D.A. Pawlac, J. Dolinsek, A. Levstic, "Dielectric relaxation in pure and Co-doped  $\text{Bi}_{12}\text{GeO}_{20}$  single crystals", in Journal of advanced dielectrics., vol. 5, №3, pp. 15500223-1 - 15500223-5, 2015. DOI:10.1142/S2010135X1550023X.
- [5] K. Malinovsky, O. A. Gudaev, S. I. Gusev, V.A. Demenko, "Photoinduced phenomena in sillenites". Ed. by. P. E. Tverdochlebov. Novosibirsk: Nauka, 1990. (In Russian).
- [6] S. Khudyakova, F. N. Grebenchukov. "The effect of annealing on the spectral dependences of the optical absorption in sillenite crystals", in Bulletin of the Samara Scientific Center of the Russian Academy of Sciences, vol. 15, No. 4, pp. 136K - 139K, 2013.
- [7] T. V. Panchenko, Z. Z. Yanchuk, "Photoelectric properties of  $\text{Bi}_{12}\text{SiO}_{20}$  crystals", in Phys. Stat. Sol., vol. 38, № 7, pp. 2018 -2028, 1996.

# CARBON NANOTUBES GROWN ON THE SURFACE OF TITANIUM ALLOY, FROM THE C<sub>2</sub>H<sub>2</sub> ATMOSPHERE, AT THE EQUIPMENT OF ION-PLASMA DEPOSITION

Valentine Panarin, Nikolay Svavilny

G.V. Kurdyumov's Institute for Metal Physics National Academy of Science of Ukraine  
03142, Kiev, Ukraine, 067-41-79-172, skywork@imp.kiev.ua

**Abstract** - The work is devoted to the creation and study of carbon nanostructures on the surface of a titanium strip, which is of interest to developers of a new generation of nanoscale electronic devices.

Experiments by CVD synthesis of carbon nanostructures on the surface of titanium alloy carried out on a modernized ion-plasma spraying equipment, created at the G.V. Kurdyumov's Institute for Metal Physics NAS of Ukraine. Carbon dioxide used as working gas, which dissociated in a vacuum chamber to form carbon atoms.

For the first time, a forest of carbon nanotubes grown on substrate in the form rolled and nitride strip made of titanium alloy. The structures of the obtained carbon nanoformations studied and their local chemical composition carried out. It was shown, that in absence of nickel catalytic centers, individual nanotubes and unstructured carbon formations of globular shape with a size of 20-40 nm are formed on the substrate. The surface of the rolled strip decorated by globular carbon particles, repeating traces of fatigue plastic deformation.

The presence of deposited nickel catalytic centers during the dissociation of acetylene, leads to the formation carbon nanotubes with a high density of distribution per unit surface of the centers. Carbon nanotubes mainly grow in colonies, the diameter which corresponds to the diameter of nickel catalytic centers. A comparison of the distribution density of the nanotubes and their length with the conditions of gas dissociation indicates an abnormally large diffusion coefficient of carbon atoms through the nickel catalytic center. Assumptions do about the quasi-liquid state of nickel catalytic centers, the abnormal mass transfer of carbon atoms through them, and the blurring concept of "surface" in nanoscale systems this type. The curvature of the initially rectilinear direction forest growth of nanotubes is due to the occurrence of internal stresses in them. The stresses are associated with a violation the uniform distribution of the carbon atoms streams through the catalytic center due to the formation of carbides or formation of graphene particles on the surface.

The structures of carbon nanotubes synthesized on a titanium substrate can use as cathodes for field emission or fundamentally new constructions of new generation micro-sized cooling radiators for electronic devices.

**Keywords** — synthesis, forest carbon nanotubes, titanium substrate, nickel catalytic centers, field emission.

## I. INTRODUCTION

In recent years, the attention of developers a nanoscale elements base of electronic circuits has been attracted by

carbon nanotubes (CNTs), due to a complex of unique physical properties [1,2]. However, most existing methods involve obtaining CNTs in the powder form of closely interconnected nanotube conglomerates, the separation of which is a complex and expensive technological operation. The using of CNTs in the powder form significantly limits the possibilities their application in radio engineering since a number of problems arise related to their necessary structure, spatial orientation, distribution, fixing in a given place of the electrical circuit, conductive substrate material, etc. Therefore, in technically developed countries, intensive searches are being made for technologies of synthesis of CNTs on conductive substrates of various compositions, with given structural states, on which their properties substantially depend.

At the G.V. Kurdyumov's Institute for Metal Physics National Academy of Science of Ukraine has developed a unique method for the synthesis of CNTs on the constructive materials surface, in particular titanium alloys [3,4], which opens up wide possibilities for creating nanoscale devices using CNTs. In this work, we obtained CNT colonies grown on a modernized installation of ion-plasma spraying, from the acetylene atmosphere dissociation products, on nitride strip of BT1-0 titanium alloy. The nitride layer use as a diffusion barrier, preventing the chemical interaction of the titanium substrate and metal - catalyst nickel.

## II. EXPERIMENTAL METHODS

All nanostructures obtained in the different regions of the strip, by covered in different ways opaque screens. The screening of the flow particles catalytic and work gas used to create various conditions for the condensation of the carbon atoms and nickel catalytic centers (CC), during the subsequent synthesis of CNTs due to C<sub>2</sub>H<sub>2</sub> dissociation. First, the tape sample covered to obscure half of its area from direct ingress of nickel particles from which the catalytic centers formed, and then, before the start of the synthesis process, this screen removed and placed perpendicular to the dividing line. This done to limit the direct hit of C<sub>2</sub>H<sub>2</sub> working gas on covered areas and the working gas "climbed" under a hot cover. Thus, the samples divided into 4 regions (Fig. 1).

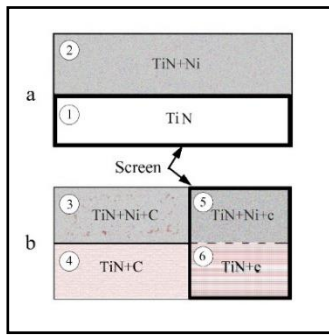


Fig. 1. Scheme of deposition of nickel catalytic centers on nitride titanium strip and the synthesis of carbon nanotubes in various areas covered by screens. Stage **a** (deposition catalytic): the screen covers region 1 - below it is the initial nitride substrate; region 2 - nickel CC on a nitride substrate. Stage **b** (synthesis CNT): a screen which covers the area 5,6, under which the flow of work gas  $C_2H_2$  is diffusion; 3 - region open for direct condensation of carbon with nickel CC; 4 - region open for direct carbon condensation without nickel CC. The size of the letters  $\underline{c}$  and  $\underline{c}$  meaning carbon with various concentrations.

Figure 2 shows the surface relief of the grain of the initial titanium strip caused by plastic deformation during its rolling. This relief decorated with condensed carbon particles obtained in the result dissociation of  $C_2H_2$ . It is interesting to note that the distribution of small carbon particles is heterogeneous and determined by the characteristic structure of fatigue due to exiting of the easy shear planes on the grain surface. The grains on the substrate are oriented differently; therefore, the distribution patterns of the surface relief, decorated by carbon, are different and, accordingly, the different distribution of carbon particles (see grains around the selected grain).

It can be assumed that, at the places where light shear planes emerge onto the surface (characteristic fatigue structures), the conditions for dissociation of  $C_2H_2$  gas are facilitated. Separate carbon atoms and their complexes released in this case condense, forming peculiar globular structures with a diameter of (20-40) nm that are not similar to carbon nanotubes (CNTs) (Fig. 3, a). Apparently, the condensation of carbon atoms in these areas is associated with their reduced surface energy, determined by the orientation of the atomic planes emerging on the grain surface.

Along with the indicated carbon formations associated with the shift of atomic planes, individual nanotubes of various thicknesses and lengths formed on the surface. These individual nanotubes, synthesized on uncontrolled, naturally occurring catalytic centers embedded in a substrate material, as will be shown later, are detached from the titanium substrate by a growing forest of oriented carbon nanotubes, which are synthesized at specially created nickel catalytic centers. As a result, these random CNTs, are located at the top of the CNT colonies (Fig.6).

The region of local X-ray spectral analysis (Fig. 4) shows that formed on the titanium substrate resulting globular structures contain carbon and oxygen (nickel is absent). These random catalytic centers can generate random CNTs.

#### IV. RESULTS AND DISCUSSION

In all subsequent experiments with the presence of nickel CCs, CNTs are formed both in the form of colonies and in the individual nanotube forms various diameters and lengths (Fig. 5). Mostly colonies formed with a large number of CNTs per unit surface area. Since the sizes of nickel CCs vary in the range (10-50 nm), the transverse sizes of the CNT colonies also fluctuate in approximately the same range. The high density of the distribution CNTs over the surface CCs suggests that there are a large number the centers in them that generate the nucleation and subsequent growth of CNTs.

It can be assumed that precisely in such a little size nickel CCs there are no carbides due to an almost liquid phase state [5], and graphene films are absent on their surface, which ensures a uniform distribution carbon's atom fluxes through them and, accordingly, a straight-line growth of CNT colonies.

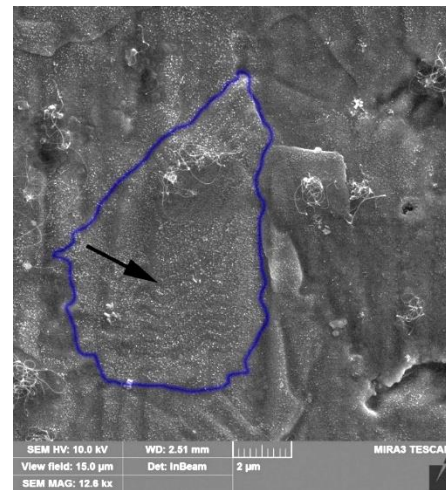


Fig. 2. Image of the surface a titanium substrate in the form of rolled strip after products condensation of dissociation  $C_2H_2$  gas on the region of substrate, marked by number 1 (without nickel), No1 on the Fig.1.

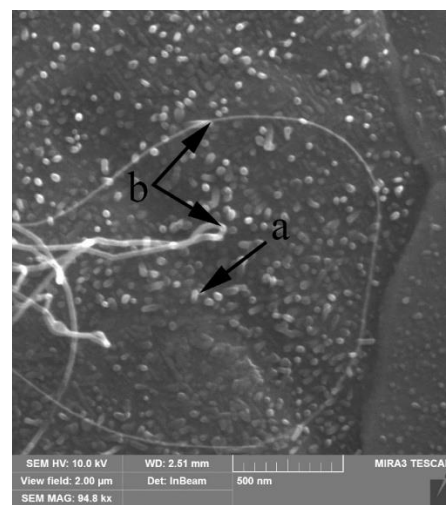
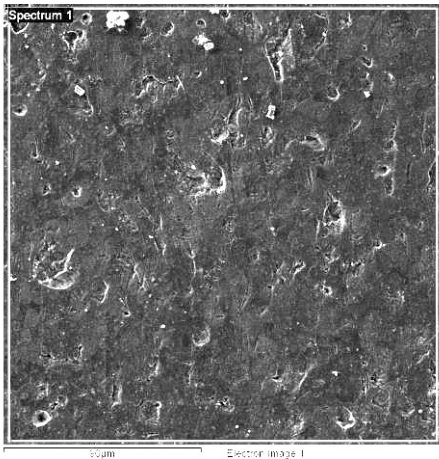


Fig. 3. The view of carbon nanostructures, formed on the substrate surface for rolled BT1-0 tape without the presence catalytic centers of nickel. a - arbitrary globular carbon nanostructures; b - random CNT on CCs, embedded in the substrate.

As was shown in [5], the bending of individual nanotubes and their colonies during growth determined by the uneven flow of carbon atoms dissolved in the CC to its surface. The fact that at first the CNT colonies grow coaxially and perpendicularly to the CC surface confirms the uniform distribution of the carbon atom flux in all directions inside the CC.

The bending of the colonies indicates a violation of the uniform distribution of atoms entering the growing nanotubes. The deficit atoms on the one side of nanotube causes the formation of defects and, as a result, the appearance of stresses leading to bending.



Spectrum	C	O	Al	Si	Ti
Spectrum 1	20.91	14.95	0.54	0.18	63.42
Mean	20.91	14.95	0.54	0.18	63.42
Std. deviation	0.00	0.00	0.00	0.00	0.00
Max.	20.91	14.95	0.54	0.18	63.42
Min.	20.91	14.95	0.54	0.18	63.42

Fig. 4. The local composition of the surface substrate after the dissociation  $C_2H_2$  in the absence a nickel catalytic centers.

If CNTs initially grow along the straight axis of the colony and then bend, this means a violation of the distribution of the carbon flux atoms inside the CC. Such a violation of the distribution of carbon atoms can be a consequence, for example, by the local formation of carbide insight them. It is also possible that the homogeneity of the catalytic reaction of  $C_2H_2$  on the CC surface is disturbed, for example, due to the formation of film-like graphene particles.

On the nitride surface of titanium, where there are no catalytic centers of nickel, on random, built-in catalytic centers due to the dissociation of  $C_2H_2$  gas, the formation of individual nanotubes randomly located over the entire surface of the substrate is also possible. (Fig. 3, b).

After deposition and annealing of nickel CCs, a CNT forest begins to form and grow intensively on their surface, which detaches previously formed single nanotubes from the substrate, leaving them at the vertices (Fig. 6)

The formation a forest of CNT colonies is possible only if the number of carbon atoms arriving per unit time per unit surface of the CC is greater or equal to the number of atoms

dissolved in it and diffusing to the surface for incorporation into CNTs. Otherwise, the concentration of carbon atoms in the CC will increase, which will lead to the formation of metal carbides. The occurrence of carbides, in turn, impedes the diffusion motion of carbon atoms through the body of the CC to its surface. As a result, the condition for the rapid growth of nanotubes are violated: the number of carbon atoms entering the surface of the CC should be equal to or less than the number of atoms entering the growing nanotubes. Since the time of formation nanotube forest is about 10 minutes, the atomic diffusion rate through the CC should be very high, with a high diffusion coefficient.

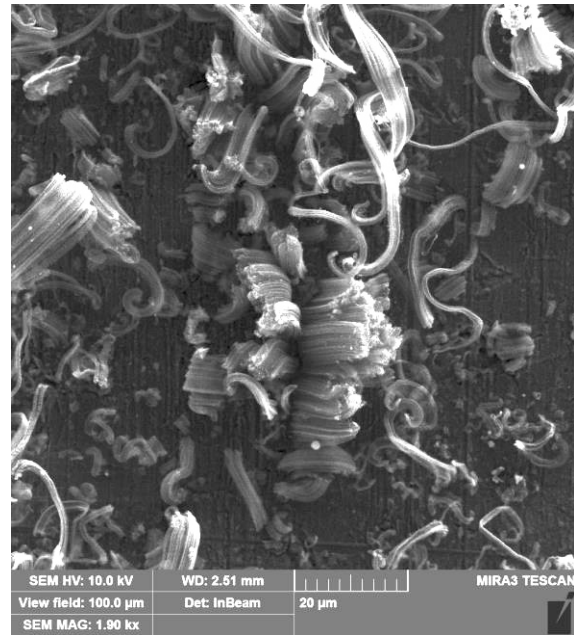


Fig. 5. CNTs grown on nickel CC deposited on a nitride titanium strip.

For the crystalline state of nickel, the diffusion coefficient of carbon atoms, even at temperatures over  $700^\circ C$ , will be insufficient to ensure the conditions for the rapid growth of nanotubes. Hence, it should be assumed that the allotropic state nickel in CC should be close to the liquid (quasi-liquid) state. The diffusion coefficient of carbon through nickel, which is in the liquid state, significantly exceeds the diffusion coefficient in the solid (crystalline) state.

The second assumption, explaining the unusually high speed of the diffusing flow of carbon atoms through the CC, is the possible realization of the anomalous mass transfer effect discovered by L.N. Larikov [6] for bulk material. In them, an abnormal mass transfer occurs under the influence of a strictly defined plastic deformation on the metal and at the same time maintaining the temperature in a narrow range of values. In our case, there is no plastic deformation of the catalytic centers and their temperature range is very wide. However, unlike the massive state of a solid crystalline body, we are dealing with nanoscale objects, the behavior and properties, which differ significantly [7].

As is well known, in thin films, the usual physical and chemical laws inherent in the massive state are violated.

Thin films are only part of a huge number of nanoscale systems, which are a separate world with their own laws that are different from massive bodies. The nanoscale sizes of CC, as in the case of thin films, do not allow one to accurately determine the allotropic state and even the very concept of the surface. Between their upper and lower parts there are several atomic layers, which erodes the concept of surface, and allows us to consider their allotropic state as liquid or quasi-liquid. In such a nanosystem, violation of Fick's laws, which are valid, as is known, for massive bodies, is possible.

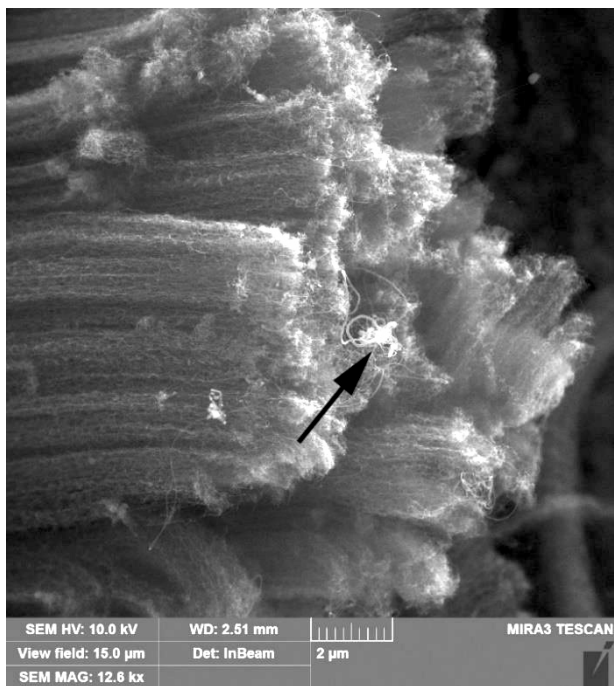


Fig. 6. The CNT forest growing from the CC surface detaches single nanotubes, holding them at its apex.

One should not discount the process of continuous bombardment of the CC surface by atoms, ions, excited atoms and electrons, dissociating working gas molecules. This bombardment causes complex oscillatory processes that can increase the speed of diffusion. We can assume the occurrence of resonance phenomena between the vibrating metal atoms of the CC and the carbon atoms dissolved in them. Carbon atoms move through internodes with the presence of long-range order in the case of a lattice, or randomly with the presence of short-range order in the case of a quasi-liquid state.

The predominantly oriented arrangement of the forest of CNT colonies creates the prerequisites for the creation of field emission cathodes in nanoscale designs of electrical circuit elements [8]. The work function of the electron exit from the ends of a CNT of small diameter and small radius

of curvature will be low, since it is in these places that the electric field strength will maximum.

The CNT forest structure can also use to create fundamentally new designs of small-sized cooling radiators for microelectronic devices due to their large heat dissipation surface area.

## V. CONCLUSIONS.

1. For the first time, carbon nanotubes from working gas  $C_2H_2$  atmosphere with a high density on the surface of nickel catalytic centers synthesized on the surface of BT1-0 titanium passivated alloy.

2. The change in the direction growth of carbon nanotube colonies is associated with a violation of the uniform distribution the flows of diffusing carbon atoms inside the different parts of the surface catalytic centers. The violation of the uniform distribution of carbon atoms is caused either by the formation of carbides inside the CC, or by the formation particles of graphene planes on their surface.

3. To explain the correspondence between the flux of carbon atoms entering to the surface of nickel catalytic centers and leaving it for the construction of carbon nanotubes, it suggested that the quasi-liquid allotropic state of nickel in the catalytic centers are exist.

4. An assumption about the possible occurrence of the effect of abnormal mass transfer of carbon atoms in the body of nickel catalytic centers during the synthesis of carbon nanotubes was done.

## RERERENCES

- [1] Углеродные нанотрубки: синтез, свойства и применение / [Харрис П.] Пер. с англ. – Новосибирск.: ИФП СО РАН. Офсет-ТМ - 2016. - 220 с.
- [2] Углеродные нанотрубки/ [В. Золотухин]. - *Соросовский образовательный журнал*, V.3, 1999. –р.р. 111–115.
- [3] An experimental study of the composite CNT/copper coating / [Panarin V.Ye., Svavilnyi N.Ye., Khominich A.I.]. - *Applied Nanoscience*. v.9 (5), 2019. - pp. 1111–1117. <https://doi.org/10.1007/s13204-018-0692-1>.
- [4] Carbon Nanotubes Synthesis on Titanium Substrate/ [Panarin V.Ye., Svavil'nyi N.Ye., Khominich A.I., Shkola A.A.]. // NAP-2018, 2018 IEEE 8<sup>th</sup> International Conference on "Nanomaterials: Applicatins & Properties": Zatoka, Ukraine Sept., 9-14. - 2018. - p.p.362-365.
- [5] On the analogy of physical and chemical processes of the directed grows of crystals and carbon nanotubes / [Panarin V.Ye., Svavil'nyi N.Ye., Khominich A.I., Shkola A.A.]. *Applied Nanoscience*, 2019. - <https://doi.org/10.1007/s13204-019-01168-1>.
- [6] Массоперенос при ударном нагружении кристаллов молибдена и молибдена, легированного рением/ [Белякова М.Н., Жолудь В.В., Лариков Л.Н., Мазанко В.Ф.]. - *Металлофизика*. Т. 14, № 2, 1992. - с.с. 96 -100.
- [7] Физика тонких пленок/ Под ред. Хасса Г. и Туна Р.Э. Т 1-8. –М.: «Мир» -1970-1976 г.г.
- [8] Холодные полевые эмиттеры на основе углеродных нанотрубок / [Елецкий А. В.] *Успехи физических наук*. No.180 (9), 2010. - с.897-930.

# The effect of vibration processing on the TiN electrospark coating on steel with nanostructured components

Zaitseva N.V., Zakharov S.M., S. Kedrovskiy, Shmatko O.A., Shmatko I.O.

G. V. Kurdyumov Institute for Metal Physics of the NAS of Ukraine,  
36 Academician Vernadsky Boulevard, / 03142 / Kyiv / Ukraine / Telephone number: +380975548275 /  
E-mail: sergeyv88001@gmail.com

**Abstract** — Using the methods of durometry, scanning electron microscopy with energy dispersive analysis, and X-ray phase analysis, we studied the changes in the structure and phase composition of steel-based surface layers with electric-spark titanium nitride coatings after highly cyclic (base 107 cycles) alternating loading. The systematization of experimental data about the layered structure of the doped layer were carried out. Structure refinement under the influence of vibration was detected. A scheme of the arrangement of phases in the coating layers is proposed.

**Keywords** — electric-spark coating, titanium nitride, vibration loads, layered structure, nanodimensional components.

## I. INTRODUCTION

The issues of reliability and strength are crucial in the operation of structures, machines and mechanisms, individual units and parts under conditions of high vibration loads and wear. To create materials with a high coefficient of resistance to such loads, it is necessary to understand the processes occurring in materials under the influence of vibrations, as well as determine the optimal structures that can best resist vibration fatigue and wear [1].

Coatings based on titanium nitride are interesting in aspects of protecting the surface of steel parts from corrosion and wear, as well as finishing decorative processing [2].

## II. RESEARCH PART

Electric-spark doping of the surface of medium-carbon steel 30XГСА with a ferrite-pearlite structure was carried out on industrial machine in the following mode:  $I_a = 16$  A,  $C = 1$   $\mu$ F,  $f = 66$  Hz,  $v = 100$  mm/min in increments of 50  $\mu$ m.

The alloying electrode for producing spark coatings was made in the form of a rod of pressed TiN powder and a binder. The composition of the binder included powdered aluminum nitride (AlN), electrolytic nickel and ПХВМ2 steel in a ratio of 75:5:20. Cyclic loading of parts with electric spark coatings based on titanium nitride was carried out on a vibration electrodynamic stand with a test base of 107 cycles.

The structure and phase composition of the doped layers were studied by methods of durometry, scanning electron microscopy with X-ray microanalysis, and X-ray

diffractometry using different wavelengths for layer-by-layer phase analysis.

As a result of electric-spark alloying of the surface of 30XГСА steel with titanium nitride surface layers were obtained, the hardness of which varies with the depth (Table 1).

Large melted areas make up about 70-80% of the total coating surface. Cracks are observed in these areas. Their length per unit area (density) is 0.22 cm<sup>-1</sup>. Regions with a fine relief of the surface usually don't contain cracks. In the transition zone, the structure mainly consists of dispersed elements on the background of a ferrite-pearlite structure (Fig. 1, c).

TABLE 1. SURFACE MICROHARDNESS OF THE SAMPLES MADE OF 30XГСА STEEL WITH ELECTROSPARK COATINGS BASED ON TITANIUM NITRIDE BEFORE AND AFTER ALTERNATING LOADING

1	Research plane	2 Microhardness values, GPa		
		Average	Maximum	Minimum
<b>Coating:</b>				
	before alt. loading	6.66	32.10	2.60
	after alt. loading	7.63	34.80	5.14
<b>Transition zone:</b>				
	before alt. loading	7.63	14.20	5.38
	after alt. loading	13.70	22.80	9.10
<b>Matrix:</b>				
	before alt. loading	4.10	4.60	3.60
	after alt. loading	5.48	6.60	4.60

Using layer-by-layer x-ray analysis, the phases forming the coating were determined. Figure 2 shows the arrangement of the preferential phases in depth. On the surface (up to 4  $\mu$ m) there are solution 2, TiC carbide and TiN nitride, at the depth of 4-8  $\mu$ m - intermetallic compound TiAl<sub>3</sub> and TiC<sub>0.64</sub>N<sub>0.33</sub> carbonitride, deeper, closer to the interface between the coating and the transition zone - bcc-solid solution 1, iron nitride Fe<sub>3</sub>N. In the middle of the transition zone  $\gamma$ -ferrum, TiAl<sub>3</sub>, CrMn<sub>3</sub>,  $\theta$ -Fe<sub>2</sub>Al<sub>8</sub>, Cr<sub>5</sub>Si<sub>3</sub> and SiC were detected.

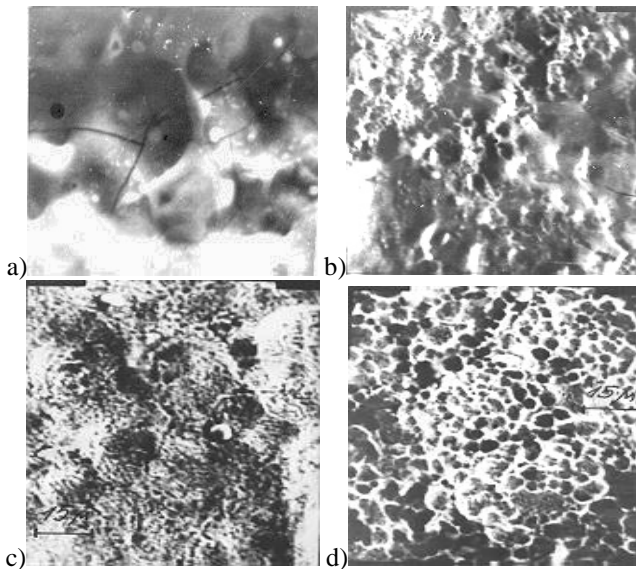


Fig.1- The electrospark titanium nitride coatings structure: a, b - coating surface structure; c, d - transition zone structure before (a, c) and after (b, d) alternating loading.

The area occupied by large melted regions (70%), after processing, decreases to 40-50% of the total area. The average size of these areas has decreased twice. Submicron particles (0.3-0.5 microns in size) of a fairly regular shape appear on the entire surface of the coating. Cracks on the surface of the coating disappear (Fig. 1, a, b). Partially, they apparently heal in the process of the appearance of dispersed particles of the newly formed phases. The transition layer acquires a pronounced dispersed structure (Fig. 1, d).

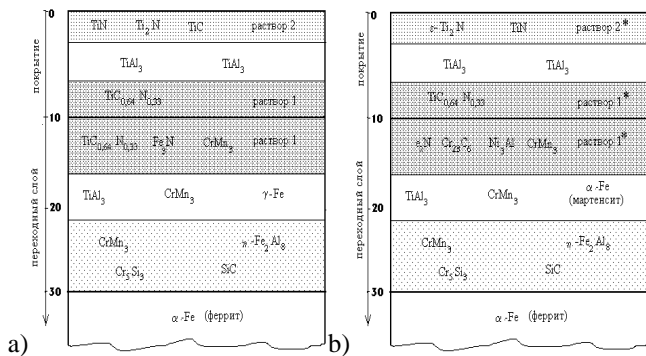


Fig. 2. The phases arrangement in depth of the electric-spark titanium nitride coating on 30X17CA steel before (a) and after (b) alternating loading.

The phases of the nitride, carbide, and carbonitride groups underwent the most significant changes. Both in the coating and in the transition layer the titanium carbide, titanium carbonitride and iron carbide disappeared, while

chromium carbide  $Cr_{23}C_6$  appeared. It is known [3], that under the action of deformation loads, partial dissociation of carbides occurs. The formation of chromium carbide is associated with the dissolution of  $Fe_3C$  and  $TiC$  and the enrichment of the coating and the transition layer with chromium, which diffuses from the steel substrate. The released iron and titanium atoms, in turn, form iron silicide  $FeSi_2$  and tetragonal titanium nitride  $\epsilon-Ti_2N$ .

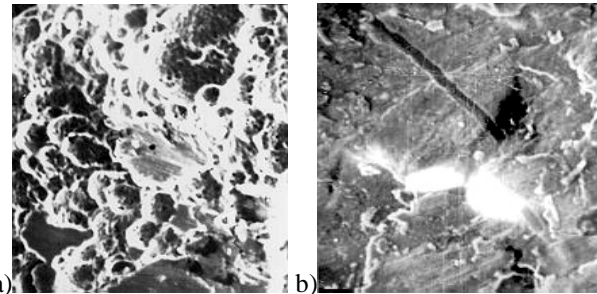


Fig. 3. The structure of the transition layer of the electric-spark titanium nitride coating after alternating loading: a - with signs of plastic deformation; b - fatigue microcrack.

Under the influence of alternating loading,  $TiC_{0.64}N_{0.33}$ ,  $TiN$  and  $Fe_3N$  disappeared in the transition layer, and  $Fe_2N$  appeared. Due to strain aging,  $Ni_3Al$  intermetallide was released, and high-alloyed austenite turned into strain martensite ( $c/a = 1.0028$ ).

### III. CONCLUSION

Vibration loading of steel samples with electric-spark coatings leads to dispersion of structural components up to submicron sizes and to a change in phase composition — dissolution of the hardening particles that arise during coating and the formation of new chemical compounds. Most of the phases that appear have a high, above  $1000^\circ C$ , temperature of synthesis and melting. Apparently, the alternating plastic deformation creates thermodynamic conditions similar to heating, without a noticeable increase in the average temperature of the sample.

### REFERENCES

- [1] Verkhoturov A.D., Osnovi materialologii, T.1, Vladivostok: Dalnauka, 2012.
- [2] Bezbah N.V., Dubovitskaya N.V., Snezhkov V.A. "The effect of surface plastic deformation of electrospark coatings on the fatigue strength of steel parts", Physics And Chemistry Of Materials Treatment.-1993, vol.3, pp.69-76.
- [3] Goldshtein M.I, Panfolova L.M., Sireyshchikova V.I. "Solubility of carbides of elements of groups IV-V in austenite of steels of various compositions", High temperature carbides.-"Naukova Dumka", Kiev, 1975, pp.119-121.

# The optical properties of the hyperbolic metamaterials with the whiskers

Andrii Korotun\*, Nazar Pavlishche\*, Vitalii Reva\*, Igor Titov<sup>+</sup>

\*National University "Zaporizhzhia Politechnic"  
Zhukovskogo Str. 64, 69063, Zaporizhzhya, Ukraine, E-mail: andko@zntu.edu.ua  
<sup>+</sup>UAD Systems

Alexandrovska Str. 84, 69002, Zaporizhzhya, Ukraine

**Abstract** — The optical properties of the nanocomposite materials with the cylinder inclusions (whiskers), which are the hyperbolic metamaterial, have been studied in the classical approximation. The analytic expressions for the real and imaginary parts of the diagonal elements of the dielectric permittivity tensor and for the absorbability of such material have been obtained. An influence of the type of the material of the whiskers and the parameters of the internal structure of the composite (radius of the whiskers and the distance between them) upon their optical characteristics has been analyzed.

**Keywords** — metamaterial, composite, whisker, dielectric tensor, coefficients of the absorption.

## I. INTRODUCTION

The generation of the materials with the optical properties, which are uncommon for the existing in nature materials, is one of the crucial tasks of the modern science. This problem can be solved with the help of the metamaterials – artificial composite structures, which consist of the small subwave particles, placed in the dielectric matrix or situated on the backup material. In the same way that the hard matters consist of the atoms which are placed in the lattice points, the metamaterials in general are the groups of the periodically placed macroscopic particles – “meta-atoms”.

The common matter consists of the particles (atoms, molecules, ions), which determine its properties. The electromagnetic characteristics of the metamaterials are determined by the “meta-atoms”. However, if the parameters and the structure of the atoms are constant, then the properties of their macroscopic analogs can be intentionally designed by the varying of its geometry, material and the period of the placing. It opens the great prospects for the obtaining the desired electromagnetic response. Among the other things, the advantage of the metamaterials is the possibility of the scaling of the dimensions of the “meta-atoms”, which lets to obtain this response in any part or the spectrum.

The variety of the implications of the metamaterials includes such directions as the realization of the negative refraction [1,2], masking of the objects [3], the control of the intensity of the interaction between the radiation and the matter in the hyperbolic metamaterials [4,5], the control of the polarization of the spontaneous radiation [6,7], the development of the superlens [8,9], the application of the metamaterials in medicine [10]. The development of the

nanofabrication methods gives the opportunity to create the different types of the metamaterials for the infrared and the optical ranges, including the multilayer structures, based on the alternating dielectric layers, and the materials of the “grid” type [11,12], the mediums with the plasmon and the dielectric rods [13,14], and also the three-dimensional structures with the particles of the different shape [15,16].

The non-conventional metamaterials, as to their design and the uncommon optical properties, are the metamaterials based on the mediums with the conductors including the hyperbolic metamaterials. These are the single axis mediums, in which the diagonal elements of the dielectric permittivity tensor have the opposite signs. That is why, the study of the optical properties of such materials is the crucial task.

## II. BASIC RELATIONS

Let us consider the composite based on the group of the parallel metal whiskers with the radius  $r$ , which are placed in the porous matrix with the permeability  $\epsilon_m$  and with the distance  $a$  from each other (fig. 1).

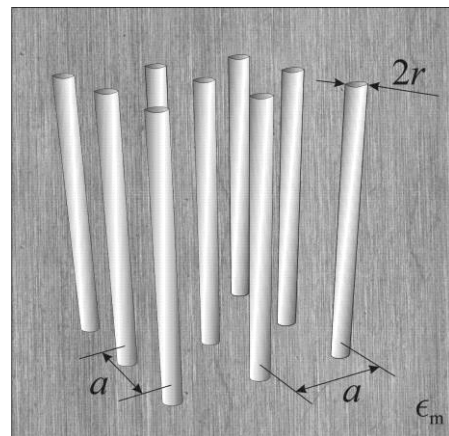


Fig. 1. Model of a composite with parallel metal whiskers

The groups of the nanowhiskers behave as the homogeneous effective medium. Its optical properties can be described in the terms of the complex permittivity tensor

$$\epsilon_{ij} = \begin{pmatrix} \epsilon_{\perp} & 0 & 0 \\ 0 & \epsilon_{\perp} & 0 \\ 0 & 0 & \epsilon_{\parallel} \end{pmatrix}, \quad (1)$$

where  $\epsilon_{\perp}$  and  $\epsilon_{\parallel}$  are the transverse and longitudinal components of the effective permittivity tensor.

The uncommon properties of such mediums are dictated by, from the first hand, the big length of the whiskers, which is considerably superior to the wavelength, and, from the other hand, the big aspect ratio. As the result, it ends in the significant optical anisotropy [4], strong dispersion of the optical anisotropy and strong spatial dispersion [12].

The composite with the nanowhiskers is the hyperbolic metamaterial, because its isofrequency surface is the hyperbola  $\text{Re}\epsilon_{\parallel} \text{Re}\epsilon_{\perp} < 0$  in all the treating frequency domain.

The expressions for the longitudinal and the transverse components of the dielectric tensor of the nanocomposite with the whiskers can be represented in the form

$$\epsilon_{\parallel} = p(\epsilon_1 + i\epsilon_2) + (1-p)\epsilon_m, \quad (2)$$

$$\epsilon_{\perp} = \epsilon_m \left[ 1 + p \frac{\epsilon - \epsilon_m}{\epsilon_m + (1-p)(\epsilon - \epsilon_m)\mathcal{L}} \right], \quad (3)$$

where  $p = \pi r^2/a^2$ ;

$$\mathcal{L} = \frac{1}{2} - \frac{(kr)^2}{3} - i \frac{2(kr)^3}{9} = \mathcal{L}_1 + i\mathcal{L}_2, \quad (4)$$

or

$$\mathcal{L}_1 = \frac{1}{2} - \frac{(kr)^2}{3}; \quad \mathcal{L}_2 = -\frac{2(kr)^3}{9}. \quad (5)$$

Suggesting that the dielectric permittivity of the metal whiskers is the complex-valued function of the wavevector

$$\epsilon(k) = \epsilon_1(k) + i\epsilon_2(k), \quad (6)$$

taking into account formulas (4) — (5) after some transformations we obtain the relations for the real and imaginary parts of the longitudinal and the transverse components of the dielectric tensor of the group of the whiskers

$$\text{Re}\epsilon_{\parallel} = p\epsilon_1 + (1-p)\epsilon_m, \quad \text{Im}\epsilon_{\parallel} = p\epsilon_2; \quad (7)$$

$$\text{Re}\epsilon_{\perp} = \epsilon_m \left( 1 + p \frac{\text{Re}\Lambda}{\Xi} \right), \quad \text{Im}\epsilon_{\perp} = p\epsilon_m \frac{\text{Im}\Lambda}{\Xi}, \quad (8)$$

with the following designation

$$\text{Re}\Lambda = (\epsilon_1 - \epsilon_m) \left[ \epsilon_m + (1-p)(\mathcal{L}_1(\epsilon_1 - \epsilon_m) - \mathcal{L}_2\epsilon_2) \right] + (1-p)\epsilon_2 \times (\mathcal{L}_1\epsilon_2 + \mathcal{L}_2(\epsilon_1 - \epsilon_m)); \quad (9)$$

$$\text{Re}\Lambda = (\epsilon_1 - \epsilon_m) \left[ \epsilon_m + (1-p)(\mathcal{L}_1(\epsilon_1 - \epsilon_m) - \mathcal{L}_2\epsilon_2) \right] + (1-p)\epsilon_2 \times (\mathcal{L}_1\epsilon_2 + \mathcal{L}_2(\epsilon_1 - \epsilon_m)); \quad (9)$$

$$\text{Im}\Lambda = \epsilon_2 \left[ \epsilon_m + (1-p)(\mathcal{L}_1(\epsilon_1 - \epsilon_m) - \mathcal{L}_2\epsilon_2) \right] - (1-p)(\epsilon_1 - \epsilon_m) \times (\mathcal{L}_1\epsilon_2 + \mathcal{L}_2(\epsilon_1 - \epsilon_m)); \quad (10)$$

$$\Xi = \left[ \epsilon_m + (1-p)(\mathcal{L}_1(\epsilon_1 - \epsilon_m) - \mathcal{L}_2\epsilon_2) \right]^2 + (1-p)^2 \times (\epsilon_1 - \epsilon_m) \left[ \mathcal{L}_1\epsilon_2 + \mathcal{L}_2(\epsilon_1 - \epsilon_m) \right]^2. \quad (11)$$

Let us use Drude expression for the dielectric function of the metal nanowhisker:

$$\epsilon(k) = \epsilon^{\infty} - \frac{k_p^2}{k(k + ik_{\tau})}, \quad (12)$$

where

$$k_p = \frac{\omega_p}{c}, \quad k_{\tau} = \frac{\omega_{\tau}}{c} = \frac{1}{\tau c}, \quad (13)$$

$\epsilon^{\infty}$  is the component, which describes the contribution of the ion core;  $\tau$  is the electron relaxation time;  $\omega_p$  is plasma frequency, for which

$$\omega_p^2 = \frac{e^2 n_e}{\epsilon_0 m^*}. \quad (14)$$

Here  $e$ ,  $n_e$  and  $m^*$  are the charge, the concentration and the effective mass of the electrons correspondingly,  $\epsilon_0$  is the electrical permittivity of vacuum.

Hence, the expressions for  $\epsilon_1(k)$  and  $\epsilon_2(k)$  are

$$\epsilon_1(k) = \epsilon^{\infty} - \frac{k_p^2}{k^2 + k_{\tau}^2}, \quad \epsilon_2(k) = \frac{k_p^2 k_{\tau}}{k(k^2 + k_{\tau}^2)}. \quad (15)$$

Due to the fact that the radius of the nanowhiskers is less than the free path, the surface dispersion is prevalent among the relaxation mechanisms. That is why, it is necessary to replace the value  $\tau$  in the relation (13) by  $\tau_{\text{eff}}$ , for which

$$\frac{1}{\tau_{\text{eff}}} = \frac{1}{\tau_{\text{bulk}}} + \frac{1}{\tau_s}, \quad (16)$$

where  $\tau_{\text{bulk}}$  is the electron relaxation time in 3D-metal;  $\tau_s$  is the relaxation time, which is connected with the dispersion of the electrons on the surface of the nanowhiskers.

The expression for the surface component of the relaxation time in the nanowire has been presented in the work [18]

$$\frac{1}{\tau_s} = \frac{9\pi}{64} (3\pi)^{\frac{1}{3}} \frac{v_F}{r}. \quad (17)$$

Here  $v_F$  is Fermi velocity.

After the substitution of the relation (13) into (15), taking into account (16) — (17), one has the expressions for the real and imaginary parts of the metal whisker

$$\epsilon_1(k) = \epsilon^\infty - \frac{k_p^2}{k^2 + \frac{1}{c^2 \tau_{\text{bulk}}^2} \left(1 + \frac{\tau_{\text{bulk}}}{\tau_s}\right)^2}. \quad (18)$$

$$\epsilon_2(k) = \frac{k_p^2}{ck \tau_{\text{bulk}} \left(k^2 + \frac{1}{c^2 \tau_{\text{bulk}}^2} \left(1 + \frac{\tau_{\text{bulk}}}{\tau_s}\right)^2\right)} \left(1 + \frac{\tau_{\text{bulk}}}{\tau_s}\right), \quad (19)$$

The relations for the longitudinal and transverse coefficients of the absorption have the form

$$\eta_{\parallel} = \frac{2\omega}{c\sqrt{\epsilon_m}} \text{Im}\sqrt{\epsilon_{\parallel}}, \quad \eta_{\perp} = \frac{2\omega}{c\sqrt{\epsilon_m}} \text{Im}\sqrt{\epsilon_{\perp}}. \quad (20)$$

Thereafter, one uses the expressions (7) — (8) together with (17) — (20) in order to obtain the real and imaginary parts of the longitudinal and the transverse components of the dielectric tensor and the absorptivity of the group of the nanowhiskers as a function of the wave number.

### III. THE RESULTS OF THE CALCULATIONS AND THE DISCUSSION

The calculations have been performed for the nanowhiskers Au, Al Cu, which are placed in the porous  $\text{Al}_2\text{O}_3$  ( $\epsilon_m = 2.4$ ). The parameters of the metal are given in the table 1.

TABLE 1. PARAMETERS OF METALS [18]

<sup>3</sup> alue	<sup>4</sup> Metals		
	Al	Cu	Au
$r_s / a_0$	2.07	2.11	3.01
$m^* / m_e$	1.06	1.49	0.99
$\epsilon^\infty$	0.7	12.03	9.84
$\tau_{\text{bulk}}, \text{fs}$	8	27	29

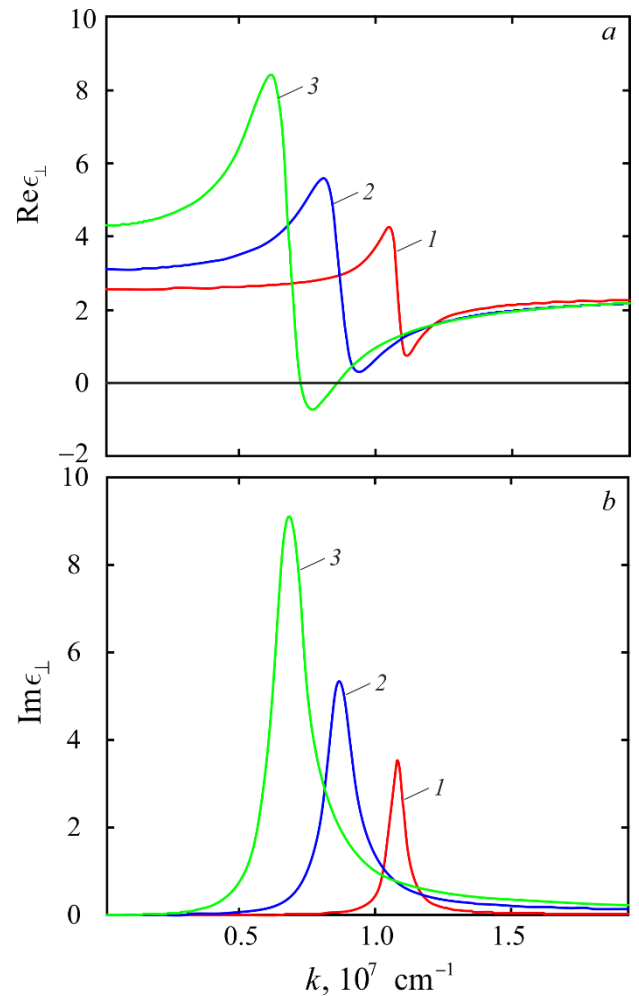


Fig. 2. Dependences of the real (a) and the imaginary (b) parts of the transverse dielectric function of the arrays of the whisker in the  $\text{Al}_2\text{O}_3$  with different radius ( $a=100 \text{ nm}$ ): 1 -  $r=10 \text{ nm}$ ; 2 -  $r=20 \text{ nm}$ ; 3 -  $r=30 \text{ nm}$ .

The figure 2 shows the relationship between the real and imaginary parts of the components of the dielectric tensor for the metamaterial based on the whiskers Al in the matrix  $\text{Al}_2\text{O}_3$  and the wave number. The distance between the whiskers is constant. The curves  $\text{Re}\epsilon_{\perp}(k)$  have one maximum and one minimum (fig. 2, a), and the curves  $\text{Im}\epsilon_{\perp}(k)$  – one maximum (fig. 2, b). It should be pointed out that if the radius of the metal nanowhiskers becomes greater than the maximums  $\text{Re}\epsilon_{\perp}$  and  $\text{Im}\epsilon_{\perp}$  and the minimums  $\text{Re}\epsilon_{\perp}$  become more noticeable due to the increase of the content of the metal fraction. These maximums and minimums are achieved at the smaller values of the wave number.

The figure 3 shows the relationships between the real and imaginary parts of the perpendicular component of the dielectric tensor for the same material and the wave number at the constant radius of the nanowhisker.

The greater is the distance between the whiskers, the less are the values  $\text{Re}\epsilon_{\perp}$  and  $\text{Im}\epsilon_{\perp}$ . At the same time the extremums become less noticeable. Hence, the properties of the rarefied composite with the whiskers are close to the properties of the dielectric matrix.

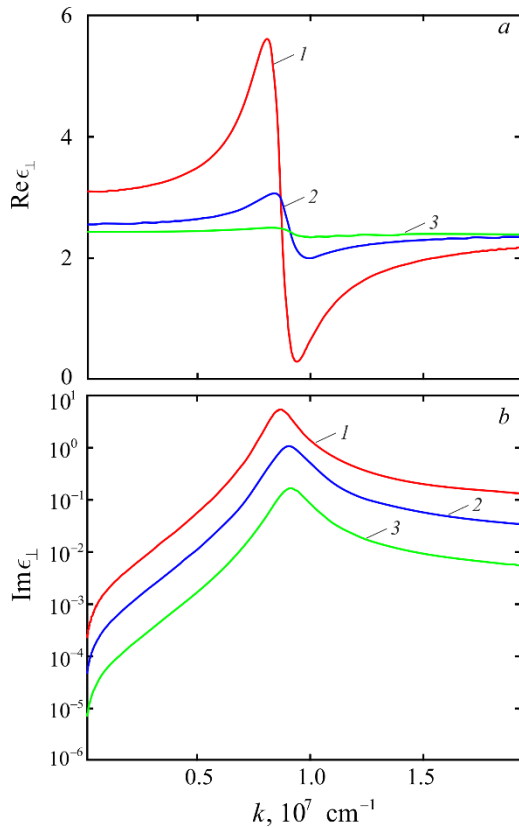


Fig. 3. Dependences of the real (a) and the imaginary (b) parts of the transverse dielectric function of the array of Al whisker in the  $\text{Al}_2\text{O}_3$  with the different distances between them ( $r=20 \text{ nm}$ ): 1 -  $a=100 \text{ nm}$ ; 2 -  $a=200 \text{ nm}$ ; 3 -  $a=500 \text{ nm}$ .

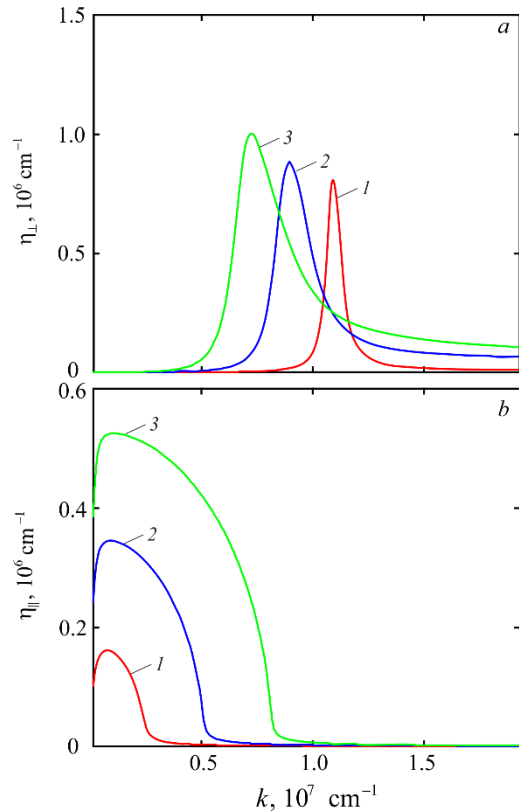


Fig. 4. Dependences of the transverse (a) and longitudinal (b) absorption coefficients of the array of Al whisker in the  $\text{Al}_2\text{O}_3$  with different radius ( $a=100 \text{ nm}$ ): 1 -  $r=10 \text{ nm}$ ; 2 -  $r=20 \text{ nm}$ ; 3 -  $r=30 \text{ nm}$ .

The figure 4 shows the relationships between the transverse and longitudinal coefficients of the absorption for the composite, which is under the investigation, and the wave number. The distance between the whiskers is constant.

It should be pointed out that the position of the maximums  $\eta_{\perp}(k)$  is the same as for the functions  $\text{Re}\epsilon_{\perp}$  and  $\text{Im}\epsilon_{\perp}$ , but the maximums for the composite with the whiskers with the smaller radius are more noticeable (fig 4, a). This is due to the good absorption of the electromagnetic emission by the matrix dielectric medium and due to the decrease of the volume part of the metal.

The position of the maximums  $\eta_{\parallel}(k)$  is the same as for  $\text{Im}\epsilon_{\parallel}$ , but the maximums for the composite with the whiskers with the smaller radius are more noticeable.

Let us compare the calculations of the real and imaginary parts of the transverse component of the dielectric tensor for the composite with  $r=30 \text{ nm}$  nanowhiskers of the different metal with the same radius at the medium  $\text{Al}_2\text{O}_3$  with the same distance between them.

Let us underline that the curves  $\text{Re}\epsilon_{\perp}(k)$  and  $\text{Im}\epsilon_{\perp}(k)$  in the case of the whiskers Cu have more noticeable extremums. As well, these extremums are placed closely in the case of the whiskers Cu and Au. The extremums  $\text{Re}\epsilon_{\perp}$  and  $\text{Im}\epsilon_{\perp}$  are reached at the significantly greater values of the wave number for the composite with the whiskers Al.

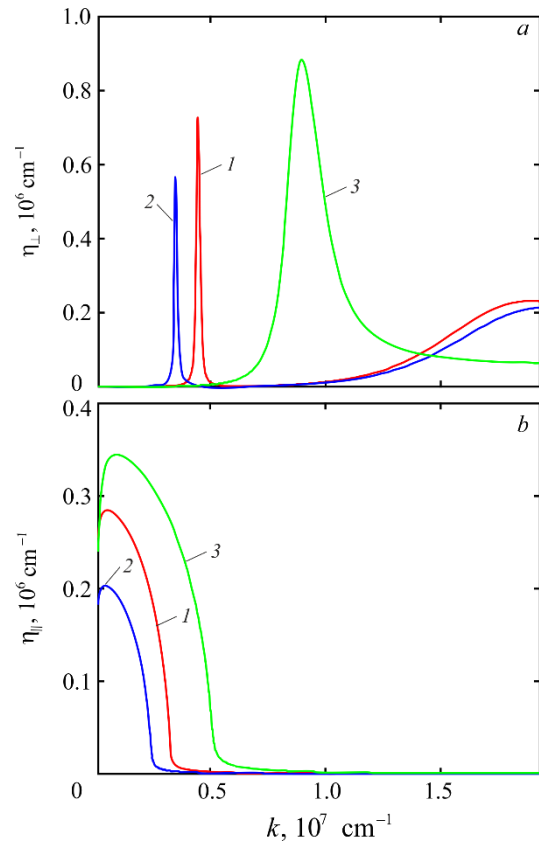


Fig. 5. Dependences of transverse (a) and longitudinal (b) absorption coefficients of the array of viscera of different metals in the  $\text{Al}_2\text{O}_3$ : 1 - Cu; 2 - Au; 3 - Al.

Such behavior of the curves  $\text{Re}\epsilon_{\perp}(k)$  and  $\text{Im}\epsilon_{\perp}(k)$  for the different metals can be explained exceptionally by the difference in the values of the volume concentration of the electrons in these metals, and correspondingly by the difference of the values of the plasma frequency.

The figure 5 shows the relationship between the longitudinal and transverse coefficients of the absorption and the wave number for the above-described composites. The curves for  $\eta_{\perp}(k)$  are qualitatively similarly to the corresponding curves  $\text{Im}\epsilon_{\perp}(k)$ , and quantitatively differ only in the fact that the maximum is more noticeable for the composite with Al (fig 5, a). The curves  $\eta_{\parallel}(k)$  have the extremums at the relatively small values of the wave number. The greater is the wave number the less is the longitudinal coefficient of the absorption (fig 5, b).

#### IV. CONCLUSIONS

The relationships between the wave number and the real and imaginary parts of the longitudinal and transverse components of the dielectric tensor and the relationships between the wave number and the coefficient of the absorption for the metamaterial with the nanowhiskers have been obtained.

The calculations for the cases when the whiskers are made of the different metals have the different radii and the distances between them are different have been performed.

It is established that the increase of the radius of the nanowhisker results in the increase of the extremal values of the real and imaginary parts of the transverse component of the dielectric permittivity and also in their shift into the long-wave region of the spectrum at the constant value of the wave parameter. It can be explained by the increase of the volume part of the metal fraction in the nanocomposite and also by the decrease of the absorption of the electromagnetic emission by the composite.

The bigger is the distance between the nanowhiskers, the closer are the properties of the composite to the properties of the dielectric matrix.

It has been shown that in the case of the whiskers of different metals the extremums of the real and imaginary parts of the transverse component of the dielectric tensor and the transverse coefficient of the absorption are situated close for Cu and Ag. These extremums are essentially shifted into the short-wave region for Al. It can be explained by the

greater values of the electron density in Al and, hence, the plasma frequency.

#### REFERENCES

- [1] G. V. Eleftheriades and K. G. Balmain, *Negative-Refractive Metamaterials: Fundamental Principles and Applications*. Wiley-VCH, 2005. 440 p.
- [2] V.M. Agranovich and Yu.N. Gartstein, "Spatial dispersion and negative refraction of light," *Phys. Usp.*, vol. 49, pp. 1029–1044, 2006.
- [3] A.V. Kildishev, V.M. Shalaev, "Enabling transformation optics through metamaterials," *Phys. Usp.*, vol. 54, pp. 53–63, 2011.
- [4] Poddubny, I. Iorsh, P. Belov, Y. Kivshar, "Hyperbolic metamaterials," *Nature Photonics*, vol. 7, pp. 958, 2013.
- [5] Y. Li-Mei, Y. Xiao-Jie, W. Tong-Biao, Z. Yong, Y. Tian-Bao, L. Qing-Hua, L. Nian-Hua, "Enhancement and modulation of spontaneous emission near graphene-based hyperbolic metamaterials," *Materials Research Express*, vol. 6, no. 12, id. 125803, 2019.
- [6] S. V. Lobanov, T. Weiss, N. A. Gippius et al., "Polarization control of quantum dot emission by chiral photonic crystal slabs, vol. 40, no. 7, *Opt. Lett.*, 2015, Pp. 1528–1531.
- [7] S. A. Dyakov, V. A. Semenenko, N. A. Gippius, S. G. Tikhodeev, "Magnetic field-free circularly polarized thermal emission from chiral metasurface," *Phys. Rev. B*, vol. 98, no. 23, id. 235416, 2018.
- [8] J. B. Pendry, "Negative Refraction Makes a Perfect Lens," *Phys. Rev. Lett.*, vol. 85, no. 18, pp. 3966–3969, 2000.
- [9] G. J. Chaplain, R. V. Craster, "Ultra-thin, entirely flat, Umklapp lenses," *Phys. Rev. B*, vol. 101, no. 15, id. 155430, 2020.
- [10] P. Slobozhanyuk, A. N. Poddubny, A. J. E. Raaijmakers et al., "Enhancement of magnetic resonance imaging with metasurfaces," *Adv. Mater.*, vol. 28, p. 1832, 2016.
- [11] S. V. Zhukovsky, A. Andryeuskii, O. Takayama et al., "Experimental demonstration of effective medium approximation breakdown in deeply subwavelength all-dielectric multilayers," *Phys. Rev. Lett.*, vol. 115, id. 177402, 2015.
- [12] S. S. Kruk, Z. J. Wong, E. Pshenay-Severin et al., "Magnetic hyperbolic optical metamaterials," *Nat. Commun.*, vol. 7, p. 11329, 2016.
- [13] V. Kabashin, P. Evans, S. Pastkovsky, A. V. Zayats, "Plasmonic nanorod metamaterials for biosensing," *Nat. Mater.*, vol. 8, no. 1, pp. 867–871, 2009.
- [14] A. Kolmychek, V. B. Novikov, I. V. Malysheva, A. P. Leontiev, K. S. Napolskii, T. V. Murzina, "Second-harmonic generation spectroscopy in gold nanorod-based epsilon-near-zero metamaterials," *Opt. Lett.*, vol. 45, no. 7, p. 1866, 2020.
- [15] N. Liu, H. Guo, L. Fu, M. Wegener, "Three-dimensional photonic metamaterials at optical frequencies," *Nat. Mater.*, vol. 7, no. 1, pp. 31–37, 2008.
- [16] W. Huang, R. Xu, Y.-S. Lin, Ch.-H. Chen, "Three-dimensional pyramid metamaterial with tunable broad absorption bandwidth," *AIP Advan.*, vol. 10, no. 3, id.035125, 2020.
- [17] W. A. Kraus, G. C. Schatz, "Plasmon resonance broadening in small metal particles," *J. Chem. Phys.*, vol. 79, pp. 6130–6139, 1983.
- [18] V. Korotun, A. A. Koval' and I. N. Titov, "Optical absorption of a composite based on bilayer metal–dielectric spherical nanoparticles," *J. Appl. Spectr.*, vol. 87, no. 2, pp. 240–248, May 2020.

# More on the size effects of polarizability of the single-wall achiral carbon nanotubes

Andrii Korotun, Yan Karandas

National University "Zaporizhzhia Politechnic"  
Zhukovskogo Str. 64, 69063, Zaporizhzhya, Ukraine, E-mail: andko@zntu.edu.ua

**Abstract**—The frequency dependences for the real and imaginary parts, for the module of the longitudinal and the transverse components of the polarizability tensor, for the absorption cross-section and the scattering cross-section and for the factor of the field amplitude gain have been obtained and studied. The fact of the occurrence of the dimensional oscillations of the transverse component of the polarizability tensor, the absorption cross-section, the scattering cross-section and the transversal factor of the field amplitude gain for the achiral CNT of both types has been established. The oscillation amplitude for the «armchair» type CNT is essentially greater than for the «zigzag» type CNT. The performed calculations indicate that there is no effect of the type of the nanotubes with the same radius upon the transverse component of the polarizability and the longitudinal factor of the field amplitude gain, and also indicate that the smoothing of the dimensional oscillations of the mentioned characteristics due to the neutralization of the quantum effect in the axial direction takes place.

**Keywords**— carbon nanotubes, polarizability, frequency dependences, cross-section

## I. INTRODUCTION

The single-wall carbon nanotubes (CNT) are the seamless cylinders with the open ends or with the closed ends, which are made of the graphene layer. Some CNT can be metallic or semiconductive. It depends on the chirality, in other words, on the orientation of the graphene lattice with respect to the axis of the tube. Due to this fact, CNT are the attractive blocks for the construction of the nanoelectronic and nanophotonic devices [1–8]. As well, the unique physical and chemical properties of CNT are used extensively in the biological visualization, the drug delivery and the thermal ablation [9–13]. It is known that, CNT, which are excited with the laser radiation in the biologically transparent near infrared band from 700 to 1100 nm, can cause the thermal destruction of the cancer cells both in vitro, and in vivo [10,12,14,15]. Such CNT have the advantage in comparison with the other nanomaterials, because they demand by a decade less radiation dose to achieve the effect of the thermal destruction of the growth [6].

The optical effects in the neighborhood of the plasmonic resonance, where the essential local increase of the electromagnetic fields takes place, are particularly attractive for the practical application. The work [16] deals with the hybridization of the plasmons in CNT with the metallic type of the conductivity. The dispersion relation for the surface plasmons with the consideration of the interaction between

the plasmonic modes of certain surfaces of the nanotube has been obtained. The dispersion relation for the surface plasmon-polaritons in the metal single-wall CNT has been obtained in [17] with the help of Maxwell set of the equations for the fields and with the help of the hydrodynamic linearized equations for 2D-electronic gas with the corresponding boundary conditions. The achiral single-wall carbon nanotubes (CNT) are the attractive objects for the above mentioned fields of the science and engineering due to the anisotropy of the electromagnetic response in this range [1–3].

An optical anisotropy of the achiral single-wall CNT, therefore, results from the great surface conductivity and the big value of the aspect ratio (the ratio of the length of the nanotube to its radius) [15]. The polarizability, the radiation absorption cross-section, the radiation scattering cross-section and also the factor of the local field gain in the neighborhood of CNT are the important value, which characterize the optical response of such structures. In this context, the study of the frequency and dimensional dependences between the optical characteristics of the achiral single-wall CNT is actual.

## II. BASIC RELATIONS

### A. The cross-sections for the absorption and the scattering of the radiation by the achiral CNT.

The study starts from the relations for the electromagnetic wave absorption cross-section and for the electromagnetic wave scattering cross-section by the carbon nanotubes

$$C_{\text{abs}} = \frac{4\pi\omega}{c} \sqrt{\epsilon_m} \text{Im} \left( \frac{2}{3} \alpha_{\perp} + \frac{1}{3} \alpha_{\parallel} \right),$$

$$C_{\text{sca}} = \frac{\omega^4 \epsilon_m^2}{6\pi c^4} \left( \frac{2}{3} |\alpha_{\perp}|^2 + \frac{1}{3} |\alpha_{\parallel}|^2 \right). \quad (1)$$

Here  $\epsilon_m$  – the dielectric permittivity of the medium, which surrounds the nanotube;  $\alpha_{\perp}$  and  $\alpha_{\parallel}$  – the transverse and the longitudinal components of the diagonal polarizability tensor of the single-wall CNT

$$\alpha = \begin{pmatrix} \alpha_{\perp} & 0 & 0 \\ 0 & \alpha_{\perp} & 0 \\ 0 & 0 & \alpha_{\parallel} \end{pmatrix}, \quad (2)$$

which have the form

$$\alpha_{\perp} = 2V \frac{\epsilon_{\perp}(\omega) - \epsilon_m}{\epsilon_{\perp}(\omega) + \epsilon_m}, \quad \alpha_{\parallel} = V \left( \frac{\epsilon_{\parallel}(\omega)}{\epsilon_m} - 1 \right), \quad (3)$$

where  $V$  – the volume of CNT, and the transverse and the longitudinal components of the dielectric tensor

$$\epsilon_{ij} = \begin{pmatrix} \epsilon_{\perp} & 0 & 0 \\ 0 & \epsilon_{\perp} & 0 \\ 0 & 0 & \epsilon_{\parallel} \end{pmatrix}, \quad (4)$$

are connected with the transverse and longitudinal surface conductivity of CNT by the following relations, correspondingly

$$\epsilon_{\perp}(\omega) = 1 + i \frac{\sigma_{\perp}(\omega)}{\epsilon_0 b \omega}, \quad \epsilon_{\parallel}(\omega) = 1 + i \frac{\sigma_{\parallel}(\omega)}{\epsilon_0 L \omega}. \quad (5)$$

Here  $b = 0.142$  nm and  $L$  – the thickness of the walls and the length of CNT, correspondingly.

The expression for the axial surface conductivity has the form [18]

$$\sigma_{\parallel}(\omega) = \frac{2e^2 v_F}{\pi^2 \hbar R_{(m,n)}} \frac{1}{i\omega + \nu}, \quad (6)$$

where  $R_{(m,n)} = (\sqrt{3}b\sqrt{m^2 + mn + n^2})/2\pi$  – the radius of the single-wall CNT with the indices of the chirality  $(m, n)$ ;  $\nu$  – the collision frequency;  $v_F$  – fermi velocity.

Using (6), the expression for the longitudinal component of the dielectric tensor can be represented in the form

$$\epsilon_{\parallel}(\omega) = 1 - \frac{R_{(m,n)}}{L} \frac{\omega_p^2}{\omega(\omega + i\nu)}, \quad (7)$$

taking into account the introduced square of the plasma frequency

$$\omega_p^2 \equiv \frac{2e^2 v_F}{\pi^2 \epsilon_0 \hbar R_{(m,n)}}. \quad (8)$$

Let us sort the real part out of the imaginary part in (7)

$$\text{Re} \epsilon_{\parallel} = 1 - \frac{R_{(m,n)}}{L} \frac{\omega_p^2}{\omega^2 + \nu^2}, \quad \text{Im} \epsilon_{\parallel} = \frac{R_{(m,n)}}{L} \frac{\omega_p^2 \nu}{\omega(\omega^2 + \nu^2)}. \quad (9)$$

The expressions for the real and imaginary parts of the transverse component of the dielectric tensor have the form [19]

$$\text{Re} \epsilon_{\perp} = 1 + \frac{e^2}{2\pi^2 \epsilon_0 \hbar R_{(m,n)} b} \left( \frac{1}{\omega^2 + \nu^2} \mathcal{J}_1 + \frac{2}{\hbar} \mathcal{J}_3 \right), \quad (10)$$

$$\text{Im} \epsilon_{\perp} = -\frac{e^2}{2\pi^2 \epsilon_0 \hbar R_{(m,n)} b} \frac{\nu}{\omega} \left( \frac{1}{\omega^2 + \nu^2} \mathcal{J}_1 + \frac{2\omega^2}{\hbar} \mathcal{J}_2 \right), \quad (11)$$

where the following designations have been introduced

$$\mathcal{J}_1 = \sum_{s=1}^m \int_{-a}^a \frac{\partial \epsilon_c}{\partial p} \frac{\partial}{\partial p} \left( \text{th} \left( \frac{\epsilon_c}{2k_B T} \right) \right) dp,$$

$$\mathcal{J}_2 = \sum_{s=1}^m \int_{-a}^a \frac{\omega_{cv} \mathcal{R}_{cv}^2}{(\omega_{cv}^2 - \omega^2 + \nu^2)^2 + 4\omega^2 \nu} \text{th} \left( \frac{\epsilon_c}{2k_B T} \right) dp, \quad (12)$$

$$\mathcal{J}_3 = \sum_{s=1}^m \int_{-a}^a \frac{[\omega_{cv}^2 - \omega^2 + \nu^2] \omega_{cv} \mathcal{R}_{cv}^2}{(\omega_{cv}^2 - \omega^2 + \nu^2)^2 + 4\omega^2 \nu} \text{th} \left( \frac{\epsilon_c}{2k_B T} \right) dp.$$

Here  $T$  – the temperature of the electronic subsystem of CNT;  $\omega_{cv} = 2\epsilon_c / \hbar$  – the frequency of the interband transitions;

$$\epsilon_c = \gamma_0 \sqrt{1 + 4 \cos \frac{3bp_x}{2\hbar} \cos \frac{\sqrt{3}bp_y}{2\hbar} + 4 \cos^2 \frac{\sqrt{3}bp_y}{2\hbar}}, \quad (13)$$

– the dispersion law of  $\pi$ -electrons in the conduction band;  $\gamma_0 = 2,7$  eV – overlap;

$$\mathcal{R}_{cv} = \frac{b\gamma_0^2}{2\epsilon_c^2} \left( 1 + \cos \frac{3bp_x}{2\hbar} \cos \frac{\sqrt{3}bp_y}{2\hbar} - 2 \cos^2 \frac{\sqrt{3}bp_y}{2\hbar} \right), \quad (14)$$

– the matrix element of the dipole moment operator of CNT.

The relations (12) – (14) can be defined concretely for CNT of zigzag type  $(m, 0)$  and armchair type  $(m, m)$ , using the substitution [19]:  $\{p_x \rightarrow p_z, p_y \rightarrow p_{\phi}\}$  and  $\{p_x \rightarrow p_{\phi}, p_y \rightarrow p_z\}$ , where

$$p_{\phi} = p_0 \frac{m}{s} = \frac{2\pi\hbar}{\sqrt{3}\beta_n b} \frac{m}{s}, \quad (15)$$

and the coefficient  $\beta_n = 1$  for CNT of the zigzag type and  $\sqrt{3}$  for CNT of the armchair type.

### B. The gain of the local electrical fields in the neighborhood of the single-wall CNT

The anisotropic Mie theory predicts the following expression for the factor of the amplitude gain in the case of LSP excitation on the surface of the individual CNT

$$\mathcal{G}_j = \left| \frac{\mathbf{E}_j}{\mathbf{E}_{inc}} \right|^2 = \left| 1 + (1 - \mathcal{L}_j) \frac{\epsilon_j(\omega) - \epsilon_m}{\epsilon_m + \mathcal{L}_j [\epsilon_j(\omega) - \epsilon_m]} \right|^2, \quad (16)$$

or

$$\mathcal{G}_j = \frac{(\text{Re} \epsilon_j)^2 + (\text{Im} \epsilon_j)^2}{|\mathcal{L}_j (\text{Re} \epsilon_j - \epsilon_m) + \epsilon_m|^2 + |\mathcal{L}_j \text{Im} \epsilon_j|^2}, \quad (17)$$

where  $\mathcal{L}_j$  – the geometrical factor, which depends on the shape of the particle.

According to (17), the relation between the real and imaginary parts of the dielectric permittivity plays the essential role.

Considering that the nanotube is the cylinder shell and taking into account that  $\mathcal{L}_\parallel = 0$  and  $\mathcal{L}_\perp = 1/2$ , the expression (17) falls into two relations for the longitudinal and transverse factors of the field gain

$$\mathcal{G}_\parallel = \frac{(\text{Re} \epsilon_\parallel)^2 + (\text{Im} \epsilon_\parallel)^2}{\epsilon_m^2} = \frac{|\epsilon_\parallel|^2}{\epsilon_m^2}, \quad (18)$$

$$\mathcal{G}_\perp = 4 \frac{(\text{Re} \epsilon_\perp)^2 + (\text{Im} \epsilon_\perp)^2}{(\text{Re} \epsilon_\perp + \epsilon_m)^2 + (\text{Im} \epsilon_\perp)^2}. \quad (19)$$

Thereafter, one uses the formulas (1), (3), (18) and (19) in order to obtain the numerical results.

### III. THE RESULTS OF THE CALCULATIONS AND THE DISCUSSION

The calculations have been performed for the achiral CNT of "armchair" (10, 10) and "zigzag" (18, 0) types which have the length  $L = 1 \mu\text{m}$ , the same radius and the metallic type of the conductivity.

The figure 1 shows the frequency dependences of the real and imaginary parts and the frequency dependences of the module of the transverse component of the polarizability tensor.

The results of the calculation show that the oscillations of  $\text{Re} \alpha_\perp(\omega)$ ,  $\text{Im} \alpha_\perp(\omega)$  and  $|\alpha_\perp(\omega)|$  have the bigger amplitude for CNT of «armchair» type, because of the stronger act of the quantum-size effects in such CNT. This effect can be explained by the smaller distances between the levels of the size quantization, and thus, the higher probability of the transitions between them.

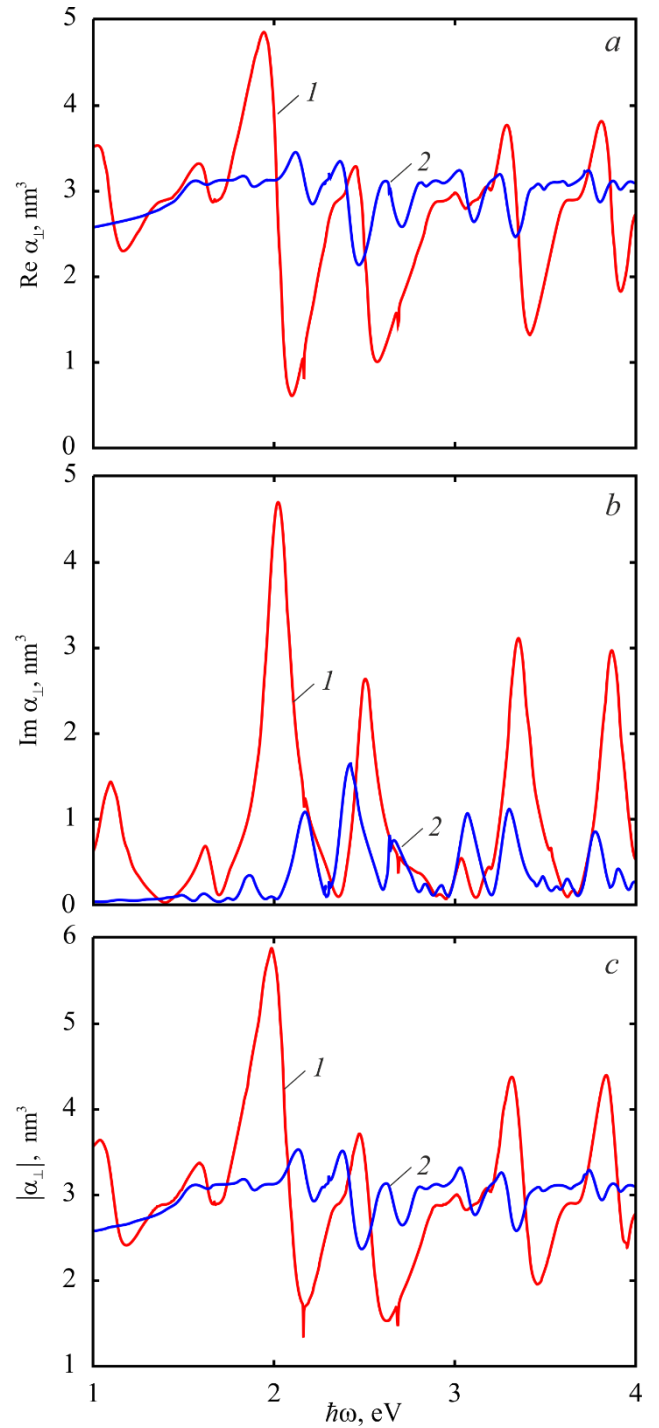


Fig. 1. The frequency dependences of the real (a) and imaginary (b) parts of the transverse polarizability and the frequency dependences of its module (c) for CNT of the different types: 1 – (10, 10); 2 – (18, 0).

The calculations of the absorption cross-section and the scattering cross-section (fig. 2) show that the absorption is essentially greater than the scattering for CNT which are under investigation. That is why the losses of the electromagnetic energy take place due to the absorption.

As well, by analogy with the polarizability, the absorption cross-section and the scattering cross-section of CNT of «armchair» type oscillate with essentially bigger amplitude, then in the case of CNT of «zigzag» type.

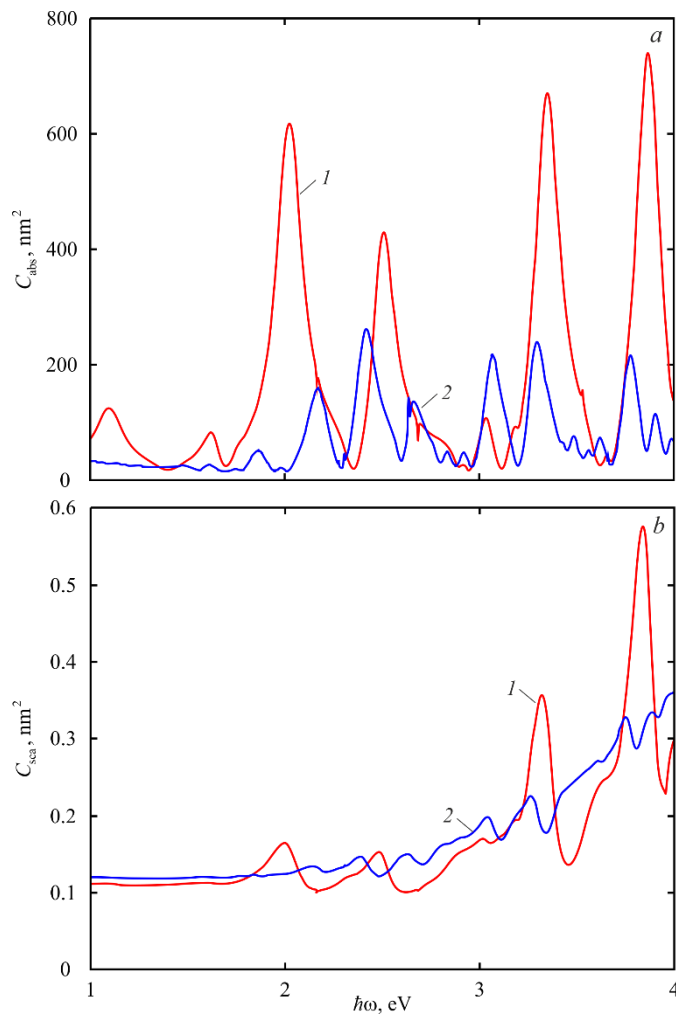


Fig. 2. The frequency dependences of the absorption cross-section (a) and the scattering cross-section (b) for CNT of the different types: 1 – (10, 10); 2 – (18, 0).

The figure 3 shows the frequency dependences of the transverse factor of the gain of the electric field amplitude in the neighborhood of the nanotube. Due to the fact that the behavior of the factor of the gain is determined by the polarizability module, the curves  $\mathcal{G}_\perp(\omega)$  are similar to the curves  $|\alpha_\perp(\omega)|$  and the oscillations  $\mathcal{G}_\perp(\omega)$  for CNT of «armchair» type are more noticeable, as in the previous cases.

Among the other things, it should be noted that the real and imaginary parts and the module of the longitudinal component of the polarizability tensor and the corresponding factor of the gain are essentially independent of the type of the nanotube and have no dimensional oscillations. These facts can be explained by the neutralization of the quantum-size effects in the axial direction.

#### IV. CONCLUSIONS

The frequency dependences for the real and imaginary parts, for the module of the diagonal components of the polarizability tensor, for the absorption cross-section and the scattering cross-section and for the factor of the gain of the field amplitude in the neighborhood of the achiral CNT with the metallic type of the conductivity have been obtained in the work.

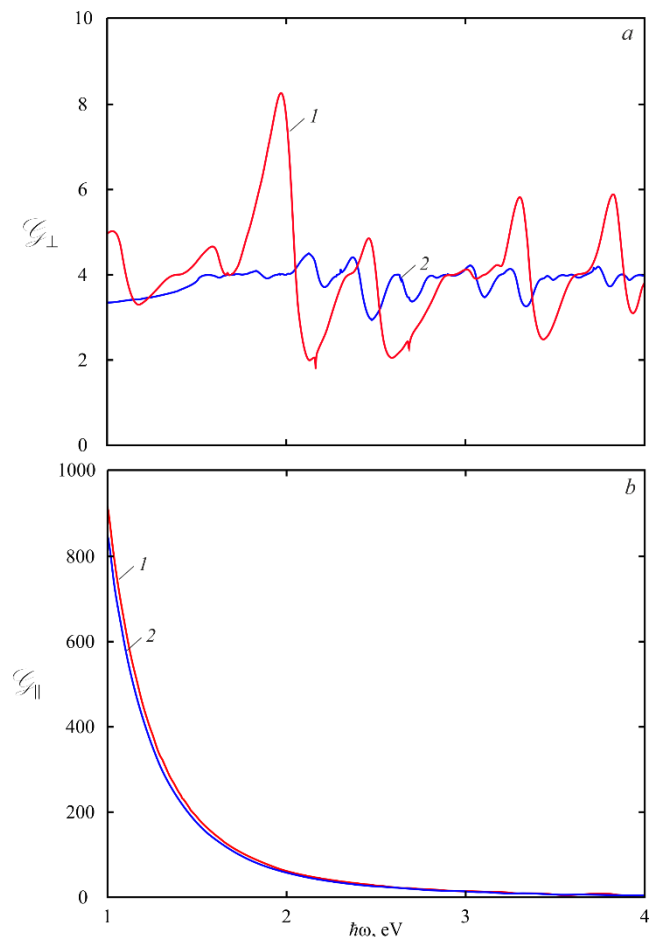


Fig. 3. The frequency dependences of the transverse (a) and the longitudinal (b) factors of the gain of the field amplitude for CNT of the different types: 1 – (10, 10); 2 – (18, 0).

The high probability of the transition between the levels of the size quantization for CNT of «armchair» type results in the major act of the quantum-size effects (the bigger amplitude of the oscillations for all above-mentioned values) for the nanotubes of the given type in comparison with CNT of «zigzag» type.

It has been shown that the absorption cross-section is essentially greater than the scattering cross-section for the considered CNT. That is why the losses of the energy take place mostly due to the absorption.

It has been established that the longitudinal components of the polarizability tensor and the factor of the gain of the field amplitude are essentially independent of the type of the nanotube and are the monotone decrease functions of the frequency due to the absence of the size quantization effects in the axial direction.

#### REFERENCES

- [1] S. A. Maksimenko and G. Ya. Slepyan, "Electrodynamics properties of carbon nanotubes," in: *Electromagnetic Fields in Unconventional Materials and Structures*, O. N. Singh and A. Lakhtakia, Eds. New York: John Wiley & Sons, 2000, pp. 217–255.
- [2] Ph. Avouris, M. Freitag and V. Perebeinos, "Carbon-nanotube photonics and optoelectronics," *Nat. Photonics*, vol. 2, pp. 341–350, June 2008.
- [3] J. Federici and L. Moeller, "Review of terahertz and subterahertz wireless communications," *J. Appl. Phys.*, vol. 107, p. 111101, 2010.
- [4] P. U. Jepsen, D. G. Cooke, and M. Koch, "Terahertz spectroscopy and imaging—Modern techniques and applications," *Laser Photon. Rev.*, vol. 5, no. 1, pp. 124–166, 2011.

- [5] S. Nanot, E. H. Haroz, J.-H. Kim, R. H. Hauge and J. Kono, "Optoelectronic Properties of Single-Wall Carbon Nanotubes," *Adv. Mater.*, vol. 24, pp. 4977–4994, 2012.
- [6] C. Rupasinghe, I. D. Rukhlenko and M. Premaratne, "Spaser Made of Graphene and Carbon Nanotubes," *ACS Nano*, vol. 8, pp. 2431–2438, February 2014.
- [7] X. Ma and H. Htoon, "Tailoring the photophysical properties of carbon nanotubes by photonic nanostructures," *Mod. Ph. Let. B*, vol. 29, p. 1530004, 2015.
- [8] Z. Li, B. Bai, C. Li and Q. Dai, "Efficient photo-thermionic emission from carbon nanotube arrays," *Carbon*, vol. 96, pp. 641–646, January 2016.
- [9] K. Welsher, Z. Liu, S. P. Sherlock, J. T. Robinson, Z. Chen, D. Daranciang and H. Dai, "A route to brightly fluorescent carbon nanotubes for near-infrared imaging in mice," *Nat. Nanotechnol.*, vol. 4, pp. 773–780, October 2009.
- [10] N. W. Kam, M. O'Connell, J. A. Wisdom and H. Dai, "Carbon nanotubes as multifunctional biological transporters and near-infrared agents for selective cancer cell destruction," *Proc. Natl. Acad. Sci. USA*, vol. 102, pp. 11600–11605, August 2005.
- [11] C. J. Gannon, P. Cherukuri, B. I. Yakobson, L. Cognet, J. S. Kanzius, C. Kittrell, R. B. Weisman, M. Pasquali, H. K. Schmidt, R. E. Smalley and S. A. Curley, "Carbon nanotube-enhanced thermal destruction of cancer cells in a noninvasive radiofrequency field," *Cancer*, vol. 110, pp. 2654–2665, December 2007.
- [12] P. Chakravarty, R. Marches, N. S. Zimmerman, A. D. Swafford, P. Bajaj, I. H. Musselman, P. Pantano, R. K. Draper and E. S. Vitetta, "Thermal ablation of tumor cells with antibody-functionalized single-walled carbon nanotubes," *Proc. Natl. Acad. Sci. USA*, vol. 105, pp. 8697–8702, July 2008.
- [13] Z. Liu, A. C. Fan, K. Rakhra, S. Sherlock, A. Goodwin, X. Chen, Q. Yang, D. W. Felsner and H. Dai, "Supramolecular stacking of doxorubicin on carbon nanotubes for in vivo cancer therapy," *Angew. Chem. Int. Ed. Engl.*, vol. 48, pp. 7668–7672, 2009.
- [14] J. T. Robinson, K. Welsher, S. M. Tabakman, S. P. Sherlock, H. Wang, R. Luong and H. Dai, "High performance in vivo near-IR (>1  $\mu\text{m}$ ) imaging and photothermal cancer therapy with carbon nanotubes," *Nano Res.*, vol. 3, pp. 779–793, October 2010.
- [15] H. Kosuge, S. P. Sherlock, T. Kitagawa, R. Dash, J. T. Robinson, H. Dai and M. V. McConnell, "Near Infrared Imaging and Photothermal Ablation of Vascular Inflammation Using Single-Walled Carbon Nanotubes," *J. Am. Heart. Assoc.*, vol. 1(6), p. e002568, December 2012.
- [16] A. Moradi, "Plasmon hybridization in metallic nanotubes," *J. Phys. & Chem. Sol.*, vol. 69, pp. 2936–2938, November 2008.
- [17] A. Moradi, "Surface plasmon-polariton modes of metallic single-walled carbon nanotubes," *Photon. & Nanostr. – Fundam. & Applicat.*, vol. 11, pp. 85–88, February 2013.
- [18] G. Y. Slepian, S. A. Maksimenko, A. Lakhtakia, O. Yevtushenko, and A. V. Gusakov, "Electrodynamics of carbon nanotubes: Dynamic conductivity, impedance boundary conditions, and surface wave propagation," *Phys. Rev. B*, vol. 60, pp. 17136–17149, December 1999.
- [19] A. V. Korotun and Ya. V. Karandas, "Infrared absorption by achiral carbon nanotubes," *Low Temp. Phys.*, vol. 46, pp. 64–70, January 2020.

# Luminescent solar concentrator: photon transport efficiency

Mykola Kulish\*, Vitaliy Kostylyov\*, Anatoly Sachenko\*, Igor Sokolovskiy\*, Anatoly Shkrebti†

\* V.E. Lashkaryov Institute of Semiconductor Physics NAS of Ukraine

41 pr. Nauki, 03028, Kiev, Ukraine E-mail: I.O.Sokolovskiy@gmail.com

+ Ontario Tech University, 2000 Simcoe St. N., Oshawa, ON, L1G 0C5, Canada

E-mail: Anatoli.Chkrebti@uoit.ca

**Abstract** — We develop an analytical model of light propagation in a square plate of a luminescent solar concentrator. The efficiency of the light transmission and its dependence on such parameters as quantum luminescence yield, absorption, the refractive index of the plate, and its size are analyzed.

**Keywords** — luminescent solar concentrator, photon transport, reabsorption, escape cone

## I. INTRODUCTION

Generally, photoconverter with a luminescent solar concentrator (LSC) consists of transparent for a sunlight plate, doped with luminophores and photovoltaic solar cells (SCs), attached to the plate ends (see Fig. 1) [1]. The luminophores absorb sunlight photons in a wide spectral range and then emit luminescent photons in a narrow spectral band. The luminophores emit photons in a random direction. Typically, the refractive index of the plate exceeds the refractive index of the surrounding medium. Therefore, most of the emitted photons are transported to the ends of the plate due to total internal reflection and enter into the solar cell, in which the energy of the luminescent photons is converted into electrical energy. The rest of the luminescent photons leaves the plate and therefore is lost. Since in the LSC plate the area of the end faces is much smaller than the area of the top face, and the cost of the plate is low, it is expected that the LSC photoconverters will generate less expensive electricity, as compared to that one produced by conventional solar cells [1, 2, 3, 4].

Photoconverters with a luminescent concentrator are also attractive since they are capable of converting into electricity not only the energy of the direct incident light but also the energy of the scattered light [5]. This implies that LSCs do not require systems that track Sun's position. The large concentrator area allows to effectively distribute the excess heat, resulting from the relaxation losses. As a result, the solar cells at the plate edges work at optimum temperature and no cooling systems are required. An additional advantage of LSCs is a possibility of placing them on facades and roofs of buildings, which allows consuming the electricity produced by LSC locally, while avoiding the various technical solution to integrate the photovoltaic systems into electrical networks [6].

The efficiency of solar energy conversion into electricity with the luminescent concentrator is less than 10% [7, 8]. One of the reasons for low LSC efficiency is the losses due to the reabsorption of the luminescent photons, caused by the overlap of luminescence and absorption spectra [2]. Among

the well-known luminophores (rare earth atoms and complexes, dyes, and semiconductor quantum dots (QDs)), only QDs can absorb solar photons in a wide spectral range and emit luminescent photons in a narrow spectral range. If the luminophores are embedded into the transparent dielectric matrix (e.g., of a parallelepiped shape), the luminescent photons are transferred through the total internal reflection to the matrix edges with attached solar cells, which convert the luminescence photon energy into electricity (see Fig. 1). During the transport of the luminescence photons toward the SCs, some of them are lost as a result of the reabsorption (as shown in Fig. 2). The amount of such losses depends on the bandgap of the bulk semiconductor, from which the QDs are made, the size of the quantum dots and their size dispersion [7, 9]. The purpose of this work is to determine the value of the aforementioned losses. Previous approaches were rather simplified or numerical (LightTools, Optical Research Associates, Monte-Carlo method application) [10].

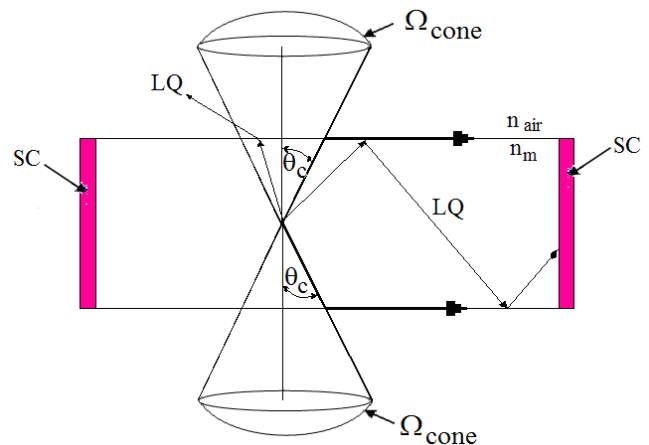


Fig.1 Typical geometry of the FLC matrix. The sunlight is absorbed by quantum dots (not shown in the figure). Luminescent quanta LQs can radiate in an arbitrary direction. When they fall to the matrix-space separation at angles  $\theta < \theta_c$ , they leave the matrix ( $\theta_c$  is the critical angle to which the refracted beam propagates along the matrix surface,  $\Omega_{cone}$  is the solid angle of the cone of leakage). When luminescent photons fall to the matrix-air separation boundary ( $n_m$  and  $n_{air}$  are respectively the refractive index of the matrix and air) at angles  $\theta \geq \theta_c$ , they are transported to the side face plate of the matrix through the full internal reflection and the photons fall to the entrance surface of the solar cell (SC), where their energy is converted into electrical energy.

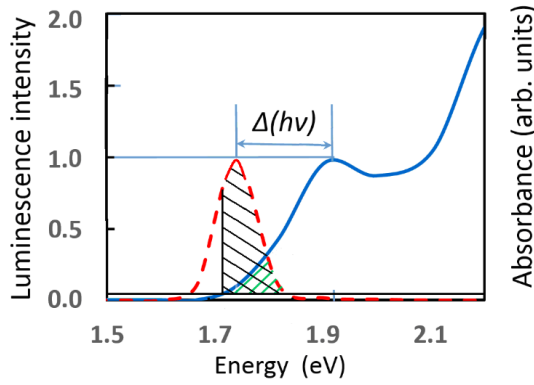


Fig.2 Reabsorption scheme. The overlap of luminescence and absorption spectra leads to the reabsorption.

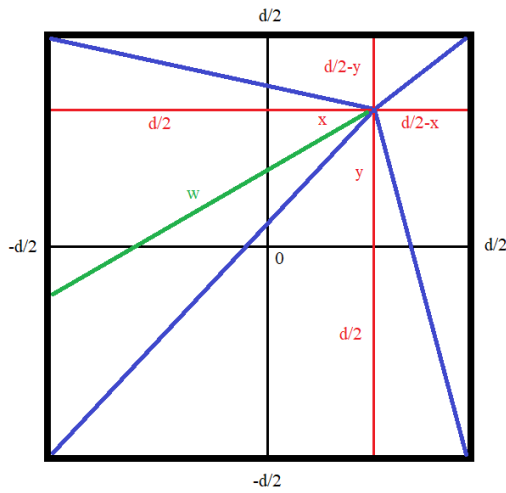


Fig.3 The geometry of the sample.

## II. REABSORPTION

The main advantage of QD as compared to other types of luminophores is the ability to precisely match the luminescence band with the maximum sensitivity of the solar cells by changing the QDs size, their diameter can vary from 1 to 20 nm [9]. A typical QD with a high quantum luminescence yield consists of a core surrounded by one or

$$\int_{\theta_c}^{\pi/2} \left[ \int_{-\arctan\left(\frac{d/2+y}{d/2-x}\right)}^{\arctan\left(\frac{d/2-y}{d/2-x}\right)} \exp\left(-\alpha \frac{d/2-x}{\sin(\theta) \cos(\beta)}\right) d\beta + \int_{-\arctan\left(\frac{d/2-x}{d/2-y}\right)}^{\arctan\left(\frac{d/2+x}{d/2-y}\right)} \exp\left(-\alpha \frac{d/2-y}{\sin(\theta) \cos(\beta)}\right) d\beta + \int_{-\arctan\left(\frac{d/2-y}{d/2+x}\right)}^{\arctan\left(\frac{d/2+y}{d/2+x}\right)} \exp\left(-\alpha \frac{d/2+x}{\sin(\theta) \cos(\beta)}\right) d\beta + \int_{-\arctan\left(\frac{d/2+x}{d/2+y}\right)}^{\arctan\left(\frac{d/2-x}{d/2+y}\right)} \exp\left(-\alpha \frac{d/2+y}{\sin(\theta) \cos(\beta)}\right) d\beta \right] d\theta \times \frac{k_\theta}{2\pi\left(\frac{\pi}{2} - \theta_c\right)}$$

Here  $k_\theta = 1 - (1 - 1/n_m^2)^{1/2}$  is the factor of losses due to escape cone,  $n_m$  is the refractive index of the matrix for the photon wavelength of QD emission. More accurate calculation requires to consider the light dispersion by integration through QD emission spectra. The first term in the equation corresponds to the photon paths from QD to the right side of the square, the second one to the top side, the third to the left side and the fourth to the bottom side.

more shells of semiconductor material and a shell of organic material. The core is made of a narrow-band semiconductor. It absorbs the solar photons in a wide spectral range and emits luminescent photons in a narrow luminescent band. The first shell is intended for passivation of the core surface dangling bonds. The bandgap of this shell exceeds the core bandgap. Each subsequent shell is different from the previous one by increasing bandgap. Their main purpose of the shells is to match semiconductor lattice parameters, necessary to reduce the appearance of dislocations. Organic shell consists of the set of organic molecules, deposited on the last inorganic shell. The primary purpose of the organic shell is to prevent QDs aggregation.

When QD is illuminated by sunlight, electrons gain the energy of absorbed photons and move from the quantum-dimensional levels of the valence band to the corresponding quantum-dimensional levels of the conduction band producing electron-hole pairs. Both electrons and holes quickly (for the picosecond time interval) relax from high energy levels to base quantized levels. Then, conduction band electrons lose energy and re-occupy their position on valence band level generating photons in the process of recombination.

Generally, the absorption spectrum in the region of the first absorption band (Fig. 2, solid curve) and the luminescence spectrum (Fig. 2, dashed curve, both are normalized to unity) overlap. Therefore, photons, emitted by QDs are partly reabsorbed by other QDs on the way through the matrix.

## III. PHOTON TRANSPORT

To estimate the losses of the light on its way from the luminophore to the solar cell, we calculate first the mean attenuation of the light on the way to the edge of the structure considered. The optical path is increased by a factor of  $1/\sin(\theta)$  due to deflection of the ray from the plane of the plate, where  $\theta$  is the angle to normal. Therefore, on the way to the plate edge the light intensity is attenuated by a factor of  $\exp(-\alpha w/\sin(\theta))$ . Here  $\alpha$  is light absorption coefficient and  $w$  is the distance the photon propagates to the edge. For every QD position  $(x, y)$  in the square plate with side  $d$ , the light attenuation should be averaged by four angles corresponding to four sides of the square plate (see Fig. 3):

Since the quadrants of the plate are equal, it is sufficient to average the attenuation by the one quadrant (see Fig. 3). Escape cone losses do not depend on the depth of the QD position, so there is no need to average QD emission by the depth. It should be noted, that the sunlight absorption by QDs is depth-dependent. Neglecting the reflection of the emitted light on the subcritical angles, we can define the light attenuation on the way to plate edge for QD emission as

$$k_w = \int_0^{d/2} \int_0^{d/2} \int_{\theta_c}^{\pi/2} \left[ \int_{-\arctan\left(\frac{d/2-x}{d/2-y}\right)}^{\arctan\left(\frac{d/2-y}{d/2-x}\right)} \exp\left(-\alpha \frac{d/2-x}{\sin(\theta) \cos(\beta)}\right) d\beta + \int_{-\arctan\left(\frac{d/2-x}{d/2-y}\right)}^{\arctan\left(\frac{d/2+y}{d/2-x}\right)} \exp\left(-\alpha \frac{d/2-y}{\sin(\theta) \cos(\beta)}\right) d\beta + \int_{-\arctan\left(\frac{d/2+y}{d/2-x}\right)}^{\arctan\left(\frac{d/2+x}{d/2+y}\right)} \exp\left(-\alpha \frac{d/2+x}{\sin(\theta) \cos(\beta)}\right) d\beta + \int_{-\arctan\left(\frac{d/2-y}{d/2+x}\right)}^{\arctan\left(\frac{d/2-x}{d/2+y}\right)} \exp\left(-\alpha \frac{d/2+y}{\sin(\theta) \cos(\beta)}\right) d\beta \right] d\theta dy dx \times \frac{k_\theta}{2\pi \left(\frac{\pi}{2} - \theta_c\right) \frac{d^2}{4}}$$

The absorption coefficient for the homogeneously doped plate can be set as  $\alpha = \alpha_m + \alpha_q$ , where  $\alpha_m$  is the absorption coefficient for the matrix material and  $\alpha_q$  is the absorption coefficient in the luminophore in its emission band, namely the reabsorption coefficient. Therefore, for QD luminescence quantum yield  $k_l$  the fraction of absorbed-emitted by the luminophore photons is

$$k_r = \frac{\alpha_q}{\alpha_m + \alpha_q} k_l (1 - k_w).$$

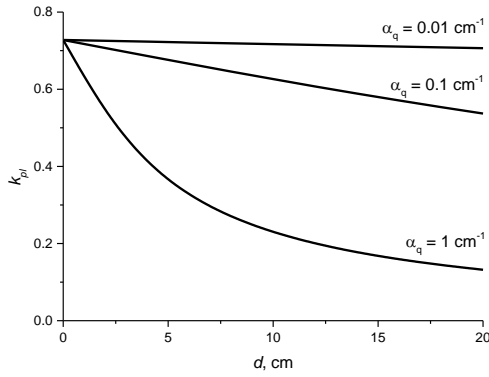


Fig.4 The transport efficiency  $k_{pt}$  vs. size of the plate  $d$ .

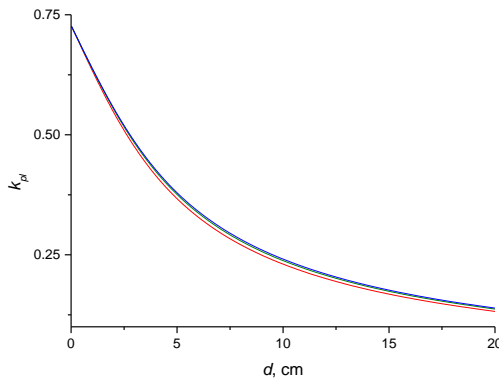


Fig.5 The transport efficiency  $k_{pt}$  vs. size of the plate for different matrix refractive indices. Red line is for 1.51, green for 2.0 and blue for 2.5.

This fraction of photons is also attenuated on the way to the plate's edge. Therefore, the final quantum efficiency can be set as the sum of infinite geometric progression (for the consideration of every reabsorption act with its losses) and equals to

$$k_{pl} = \frac{k_w}{1 - k_r}.$$

More accurate estimate the transport efficiency requires consideration of the same infinite (until the last photon) geometric progression of the reflections from the frontal and back surfaces on subcritical angles.

Fig. 4 shows the size dependence of the transport efficiency. As one can see, the efficiency drastically depends on the reabsorption effect. Fig. 5, in turn, demonstrates almost negligible dependence of the transport efficiency on the matrix refractive index.

#### IV. CONCLUSIONS

The analytical model for the propagation of QD-emitted light through the LSC plate is developed.

Reabsorption and LSC design strongly influence the light transport efficiency. Per contra, the refractive index of the plate only weakly influences the efficiency. Reabsorption is the main source of the losses.

#### REFERENCES

- [1] M.R. Kulish, V.P. Kostilyov, A.V. Sachenko, I.O. Sokolovskiy, A.I. Shkrebtii, "Photoconverter with luminescent concentrator. Matrix material," *Semiconductor Physics, Quantum Electronics & Optoelectronics*, 22 (1), 2019, pp. 80-87.
- [2] M.R. Kulish, V.P. Kostilyov, A.V. Sachenko, I.O. Sokolovskiy, A.I. Shkrebtii, "Influence of the quantum dots bandgap and their dispersion on the loss of luminescent quanta," *Semiconductor physics, quantum electronics and optoelectronics*, 23 (2), 2020, pp. 155-159.
- [3] Yun Seng Lim, Chin Kim Lo, Geok-Bee The, "Unsaturated polyester resin blended with MMA as potential host matrix for luminescent solar concentrator," *Renewable Energy* 45, 2012, pp. 156-162.
- [4] E.E. Bende, L.H. Slooff, A.R. Burgers, W.G.J.H.M. van Sark, M. Kennedy, "Cost & efficiency optimisation of the fluorescent solar-concentrator," in *The 23rd European photovoltaic solar energy conference*. Valencia, Spain; 1-5 September 2008.
- [5] A.F. Mansour, M.G. El-Shaarawy, S.M. El-Bashir, M.K. El-Mansy, M. Hammam, "A qualitative study and field performance for a fluorescent solar collector," *Polymer Testing* 21 (3), 2002, pp. 277-281.
- [6] Meinardi, F. Bruni, and S. Brovelli, "Luminescent solar concentrators for building-integrated photovoltaics," *Nature Reviews Materials* 2, 2017, 17072.
- [7] L.H. Slooff, E.E. Bende, A.R. Burgers, T. Budel, M. Pravettoni, R.P. Kenny, E.D. Dunlop, A. Büchtemann, "A luminescent solar concentrator with 7.1% power conversion efficiency," *Phys. status solidi (RRL)*, 2 (6), 2008, pp. 257-259.
- [8] M.R. Bergren, N.S. Makarov, K. Ramasamy, A. Jackson, R. Guglielmetti, H. McDaniel, "High-performance CuInS<sub>2</sub> quantum dot laminated glass luminescent solar concentrators for windows," *ACS Energy Lett.* 3, 2018, pp. 520-525.
- [9] Kitai, *Luminescent Materials and Applications*. John Wiley & Sons Ltd, 2008.
- [10] V.I. Klimov, T.A. Baker, J. Lim, K.A. Velizhanin, and H. McDaniel, "Quality Factor of Luminescent Solar Concentrators and Practical Concentration Limits Attainable with Semiconductor Quantum Dots," *ACS Photonics* 3, 2016, pp. 1138-1148.

# Dielectric Properties of Hexagonal Boron Nitride nanolayers

Ievgen Brytavskiy\*, Yaroslav Lepikh\*, Valentyn Smyntyna\*, Martin Heilmann<sup>+</sup>, João Marcelo Lopes<sup>+</sup>

\* Interdepartmental Scientific and Educational Physical-Technical Center  
of the MES and NAS of Ukraine at the Odessa I.I. Mechnikov National University,  
Odessa / 65028 / Ukraine / ndl\_lepikh@onu.edu.ua

<sup>+</sup> Paul-Drude-Institut für Festkörperelektronik  
Hausvogteiplatz 5-7 / 10117 / Berlin / Germany

**Abstract** — The dependence of h-BN nanolayers heterostack electronic properties on the morphology, number of used atomic layers and crystalline structure of epitaxially grown materials was studied in details by using the methods of Atomic force microscopy, Raman spectroscopy and comprehensive electrical characterization (current-voltage characteristics). The prospective methods of large-area fabrication of high-quality materials, which give the nanometer precision in layer thickness were used. Obtained results will be valuable for the implementation of new concepts of atomically thin grapheme-based electronic devices.

**Keywords** — hexagonal boron nitride, nanomaterials, electrical breakdown, AFM, molecular beam epitaxy

## I. INTRODUCTION

Heterosystems combining hexagonal boron nitride (h-BN) and graphene are one of the most promising, as they offer the potential advantages for electronic device industry, including high speeds, extremely low power consumption, and various novel functionalities.

For technological implementation, it is mandatory to synthesize these materials and heterostructures combining them with high precision in a scalable way [1]. Therefore, the direct synthesis of large-area graphene and h-BN through additive growth and subsequent comprehensive investigation of obtained heterostructure properties is ultimately required.

Performance and characterization of thin BN layers is of considerable fundamental interest [2-3] and has the potential for new applications, such as devices for flexible electronics, in particular if layer thickness will be controlled with atomic layer precision on a large area. The evaluation of h-BN nanolayers dielectric properties (permittivity, dielectric strength, tunneling effects) in order to obtain knowledge about the electronic parameters of this 2D material for usage in atomically thin multilayered heterostructures is needed.

Carrier mobility enhancement in graphene covered by h-BN has been studied in case of exfoliated and/or transferred material [4]. The influence of h-BN on the electronic properties of graphene for the case of large area, epitaxially grown systems is still unclear and indefinite. Therefore, the study of what is happening with graphene as an electronic material, in case if a few atomic layers thick h-BN film is deposited on top is obviously highly relevant for the future implementation of these materials in various applications. Hence, electrical characterization of h-BN films is valuable

for improving the synthesis of h-BN containing heterostructures with high electronic quality.

The well-established "flake" method [5] that consists of stacking  $\mu\text{m}$ -sized flakes of the two materials, which are obtained by mechanically exfoliation from bulk samples, is inherently unscalable. Additionally, any interface contamination introduced during the transfer process would adversely impact the properties of final devices. For technological implementation, it is mandatory to synthesize these materials and heterostructures combining them with high precision in a scalable way. Therefore, the direct synthesis of large-area graphene and h-BN through additive growth and subsequent comprehensive investigation of obtained heterostructure properties is ultimately required. New concepts of atomically thin devices, such as nanocapacitors [5] and tunnel transistors [6] can only be implemented in future technologies if large-area fabrication of high-quality material can be achieved, by using for instance the MBE h-BN / graphene fabrication approach. A crucial point on this way is the understanding of how the heterostack electronic properties depend on the morphology and crystalline structure of epitaxially grown materials.

## II. MATERIALS AND METHODS

Formation of capacitors was done by metallization, standard photolithography and lift-off process. h-BN layer played the role of insulator, while continuous Ni layer served as conductive bottom electrode and patterned Ni layer on h-BN served as top electrode.

The  $1 \times 1 \text{ cm}^2$  sapphire substrates with 400 nm Ni layer were used for h-BN deposition. The pattern of square Ni contacts was prepared by means of conventional optical lithography and standard metallization, Ni layer with 100 nm thickness was used for top electrical contacts. After the second photolithographic step the subsequent  $\text{SF}_6$  etching was performed for 1 min at 4 Pa pressure and a flux of 13 sccm in order to separate the mesa islands in continuous h-BN layer and to obtain individual Ni(top contact) / h-BN / Ni (substrate) capacitor structures.

Figure 1 shows the fabricated sample in polarized light, top Ni electrodes with different sizes can be seen. Around 20% of Ni square contacts were peeled off during lift-off procedure due to insufficient adhesion to h-BN.

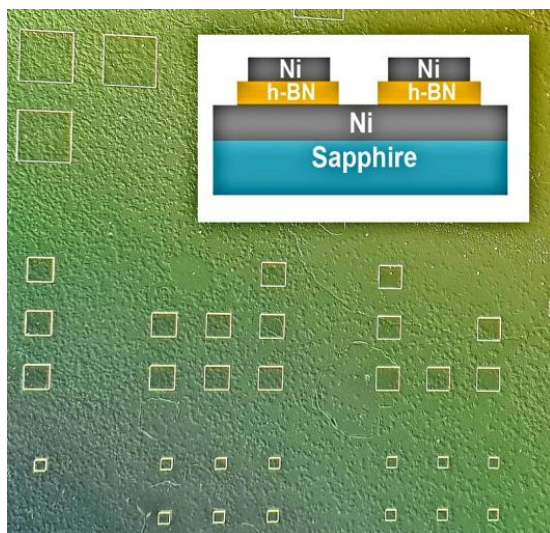


Fig. 1. The surface of fabricated sample, which contains top electrodes with different sizes: 200  $\mu\text{m}$ , 100  $\mu\text{m}$  and 50  $\mu\text{m}$  (lateral size of the squared electrode). Inset shows a layer schematic of the capacitor devices.

The dielectric breakdown of high-quality h-BN layers obtained by MBE method was investigated to reveal the breakdown behavior of studied 2D layered material. I-V measurements were performed using a semiconductor device parameter analyzer (Keithley 4200-SCS) assembled to the Probe station with the aim of study of the dielectric properties of h-BN: leakage current, tunneling process contribution, breakdown voltage.

Current-voltage characteristics (IVC) measurements for Ni / h-BN / Ni films were done by using tip probes with tip radius of 2  $\mu\text{m}$ . In order to get comparable results and due to convenient size, only 100  $\times$  100  $\mu\text{m}$  contacts were used for all IVC measurements and breakdown tests.

### III. RESULTS AND DISCUSSION

Figure 2 shows a typical behavior of I-V characteristic of a Ni/h-BN/Ni square capacitor device before the breakdown. The inset displays the logarithmic scale dependence of the current on applied voltage, showing three well-defined regions: current linearly increases with the voltage increment, which represents direct-tunneling related conduction ( $U < 0.9$  V), current exponentially increases with the voltage under moderate biases ( $\sim 0.9$  V  $< U < 2.6$  V) due to well-known Fowler-Nordheim tunneling process [7], and current sharply grows up to the limit level (100 mV) due to the dielectric breakdown at a bias of 2.66 V.

After the breakdown, I-V curves show a linear performance in repeated measurements (Fig. 2), indicating that conduction path with the conductivity of  $\sim 0.4$  S $\cdot\text{m}^{-1}$  had completely formed between probe tip and bottom Ni layer. A clear evidence of point breakdown and physical disruption of the layers can be seen on the microscopic images of tested devices.

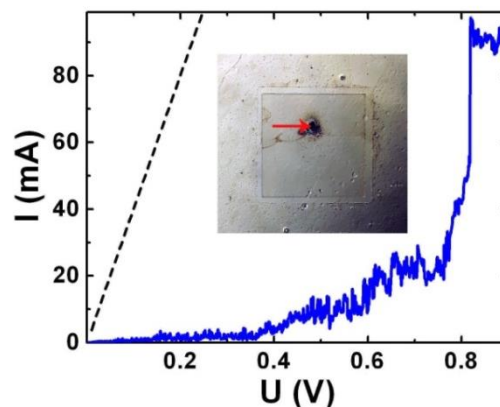


Fig. 2. IVC of Ni/h-BN/Ni capacitor measured until the breakdown at  $U=0.8$  V happened (solid line) and measured on the same spot after breakdown (dashed line). On the inset: the image of capacitor after breakdown test (fractured area marked by the arrow).

Electrical breakdown is a random process that always takes place at the weakest location of the insulating material. The grain boundaries, which are known to be defective paths with higher conductivity play the crucial role in case of breakdown in a bulk material and thin layers. Also a specific layer-by-layer breakdown in h-BN nanolayers was confirmed recently [8].

On the basis of detailed I-V measurements of Ni/h-BN/Ni capacitors the breakdown process of dielectric layer was confirmed. Statistical analysis of the breakdown voltages measured on capacitor array gave the mean value of voltage  $U_{BD} \sim 1 - 1.1$  V, where breakdown is most probable to happen .

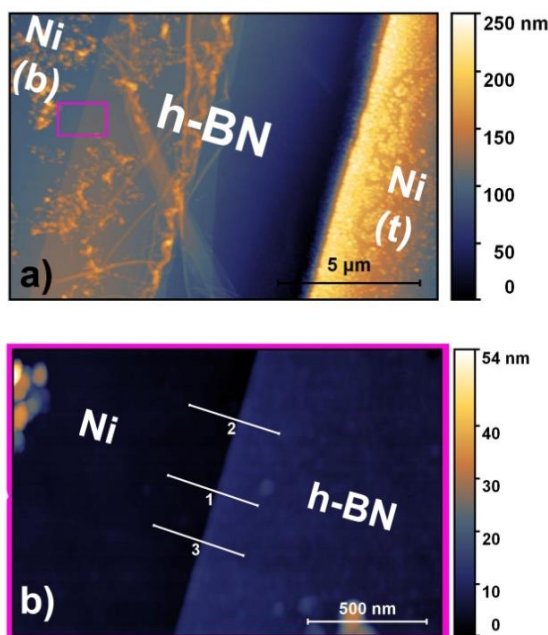


Fig. 3. (a) AFM image of h-BN region uncovered by Ni top contact. Ni (b) – Ni bottom layer where from h-BN was etched, Ni (t) – Ni top layer. Magenta colored rectangle mark the area from where a detailed AFM image was obtained and shown in (b). A clear step on the Ni / h-BN border was observed.

Additionally the AFM measurements were conducted in order to define the exact thickness of insulating h-BN layer. For this purpose, the sample after Ni top contacts deposition and h-BN etching was brought for AFM scanning. Due to selective etching by SF<sub>6</sub>, boron nitride is removed and bottom Ni layer remain untouched (Fig. 3 a). So the thickness of BN layer can be measured on Ni / BN border line (Fig. 3 b). Several AFM height profile measurements gave the h-BN film thickness h(BN) of 8 nm (Fig. 4 a). The applied electric field value can be calculated then as  $E = U / h(\text{BN})$ . The current density versus electric field dependence gives the value of dielectric strength of h-BN insulator layer, which turns to be up to  $3.3 \text{ MV}\cdot\text{cm}^{-1}$  (Fig 4. b).

- [5] Gang Shi et al., Nano Lett., 14, 1739–1744, (2014).
- [6] Zheng Liu, Lulu Ma, Gang Shi et al., Nature Nanotechnology, 8, 119–124 (2013).
- [7] Ji Y et al Appl. Phys. Lett. 108 012905 (2016).
- [8] Hattori, Yoshiaki et al. ACS nano 9 1 916-21 (2015).
- [9] Kim, S. M. et al. Nat. Commun. 6, 8662 (2015).
- [10] Lee, G.-H. et al. Appl. Phys. Lett. 99, 243114 (2011).
- [11] Vassilevski D.L., Vinogradov M.S., Borschak V.A.// Applied Surface Science.- Dec.1996.- 103(4).- P.383-389.

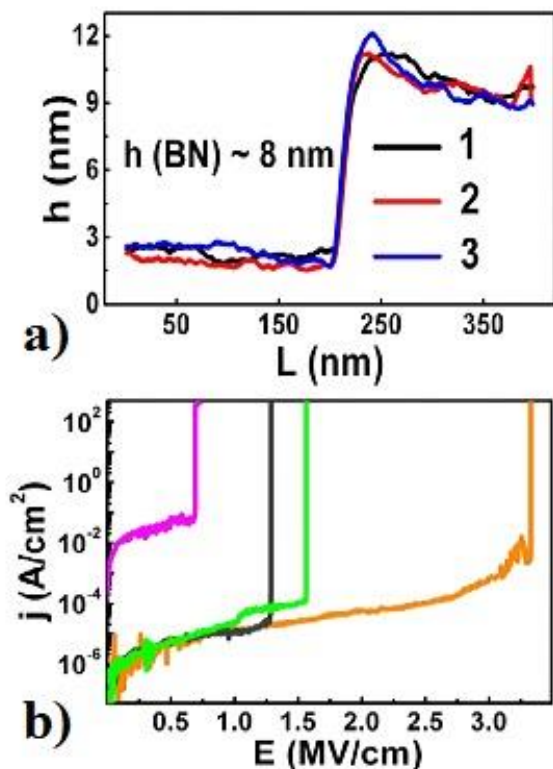


Fig. 4. (a) Height profiles measured from the marked lines in Fig 3 (b). 8 nm average thickness of h-BN layer was estimated. (b) The calculated current density versus electric field dependence of four capacitor devices of the same size.

The calculated breakdown electric field based on an h-BN thickness of 8 nm is  $0.7 - 3.3 \text{ MV}\cdot\text{cm}^{-1}$ , which is comparable with the observed values from devices with h-BN films grown by CVD [9] and exfoliated h-BN films [10]. Observed high electric field strength shows that MBE-grown h-BN is a reliable insulator for use in 2D electronic devices.

#### REFERENCES

- [1] J.A. Robinson, ACS Nano, 10, 42–5 (2016).
- [2] L. Britnell et al., Nano Lett. 12, 1707–10 (2012).
- [3] Q. Cai, D. Scullion, A. Falin, K. Watanabe, T. Taniguchi, Y. Chen, E.J.G. Santos and L. Li, Nanoscale 9, 3059–67 (2017).
- [4] W. Gannett, W. Regan, K. Watanabe, T. Taniguchi, M. F. Crommie, and A. Zettl, Appl. Phys. Lett. 98, 242105 (2011).

# Effect of the acid-base composition of the medium on the photoluminescence spectrum of CdS QDs

V.A. Smyntyna \*, V.M. Skobeeva <sup>§</sup>, K.A. Verheles <sup>+</sup>, N.V. Malushin <sup>@</sup>

\* Odesa I.I.Mechnikov National University

Pastera St. 27 / 65082/ Odessa / Ukraine / +380674806610/ smyntyna@onu.edu.ua

<sup>§</sup> Mechnikov Odessa National University Research Institute of Physics

Dvoryanskaya St. 2 / 65082/ Odessa / Ukraine / +380506367491/ v\_skobeeva@ukr.net

<sup>+</sup> Odesa I.I.Mechnikov National University

Pastera St. 27 / 65082/ Odessa / Ukraine / +380962837667 / klara2010@meta.ua

<sup>@</sup> Mechnikov Odessa National University Research Institute of Physics

Dvoryanskaya St. 2 / 65082/ Odessa / Ukraine / + 380949330702/ malushin@rambler.ru

**Abstract**— This article presents the results of the effect of pH on the luminescence of colloidal CdS quantum dots (QDs). A qualitative agreement was shown between the luminescence spectra of CdS QDs, both obtained at different pH values during synthesis, and CdS QDs subjected to treatment after synthesis. It was shown that the luminescence spectrum can be changed both by changing the synthesis conditions and by changing the acidity of colloidal CdS QDs.

**Keywords**— cadmium sulfide quantum dots, absorption, photoluminescence, nanomaterials.

## I. INTRODUCTION

Quantum dots are nanocrystals ranging from 2 to 10 nm in diameter, synthesized from semiconductor materials. Semiconductor CdS QDs have attracted considerable interest because of their unique properties that are absent in bulk materials due to the effect of quantum confinement of charge carriers. For a number of areas of science and technology, colloidal quantum dots are a promising material. They are of particular interest as an element base in optoelectronics, for medicine in the creation of biomedical markers and sensors, antimicrobial agents [1-4].

A necessary condition for the practical implementation of CdS QDs is the development of a technology for their production with controlled properties. One of the simplest and most technologically advanced methods for the synthesis of QDs is the colloidal chemical method. The colloidal method for the synthesis of quantum dots has attracted much attention, since it provides the ability to clearly control the size and surface properties of the resulting nanoparticles. The properties of QDs obtained by this method depend on such parameters as the concentration of starting materials, pH of the growth solution, etc. Colloidal synthesis in an aqueous medium [5] is attractive for its simplicity and safety: it does not require high temperatures, toxic and expensive reagents and solvents. Also, an important factor in controlling the optical characteristics of the obtained QDs was the acidity of the pH dispersion medium.

The results of studying the influence of various factors on the formation of the luminescence spectrum of CdS QDs are presented in [6-7].

This work presents the results of studies on the effect of pH on the luminescence of CdS QDs in order to clarify the possibility of transforming the luminescence spectrum of QDs, both during synthesis and after synthesis. It was shown that one of the important technological parameters is the pH of the initial solution

## II. DESCRIPTION OF OBJECTS AND METHODS OF RESEARCH

Nanocrystals of cadmium sulfide were obtained by the chemical method from solutions of cadmium and sulfur salts in a colloidal solution of gelatin. As a result of the exchange reaction:  $\text{Cd}(\text{NO}_3)_2 + \text{Na}_2\text{S} \Rightarrow \text{CdS} + 2\text{NaNO}_3$ , CdS quantum dots were formed.

To obtain a colloidal solution, 5% gelatin and equimolar concentrations of cadmium and sulfur salts were used. The volumes of the components introduced into the colloidal solution were the same.

The required pH values of solutions (2 ÷ 10) were changed by adding an aqueous solution of alkali or hydrochloric acid to an aqueous solution of gelatin with cadmium sulfide.

Optical absorption spectra were measured on an SF-26 spectrophotometer in the wavelength range from 320 nm to 600 nm. The measurement error did not exceed  $\pm 1\%$ . Luminescence was excited by a pulsed LCS-DTL-374QT laser with a light wavelength of 355 nm. Laser power - 35 mW.

## III. DESCRIPTIONS AND ANALYSIS OF RESULTS

Our earlier studies showed that the luminescence spectrum of CdS QDs depends on the pH of the initial solution [8]. It is known that hydrolysis of salts occurs in aqueous solutions, namely, at values up to pH = 8, the concentration of cadmium ions in the solution is dominant. At pH > 6, the concentration of cadmium ions decreases. At pH values > 8, cadmium hydroxide Cd(OH)<sub>2</sub> is formed. Sulfur salt hydrolysis occurs at pH > 6. In accordance with a change in pH, defects are formed, which are luminescence centers in QDs.

The results of these studies are illustrated in Fig. 1, which shows the luminescence spectra of CdS NC grown at different pH values. In the spectra of nanocrystals, both with

low pH (2 and 4) and with high pH (7 and 10), a short-wavelength luminescence band with  $\lambda_{\max} = 500$  nm is found. This band manifests itself in the photoluminescence spectra of CdS NCs obtained at pH = 7.10 in the form of an inflection and is leveled by the predominance of a long-wavelength band with  $\lambda_{\max} = 670$  nm in the spectrum.

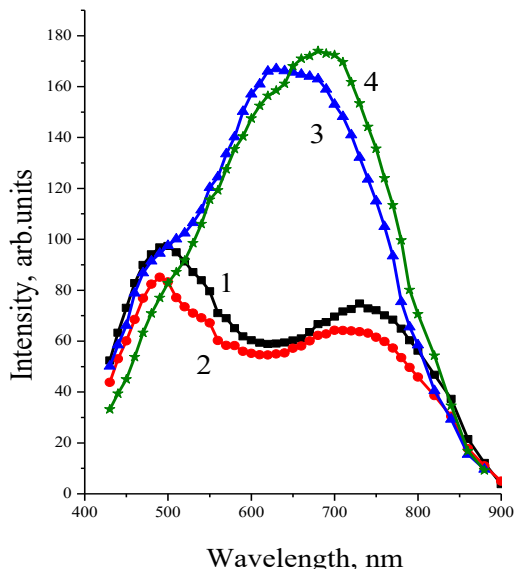


Fig.1 Luminescence spectra of CdS NC grown at different pH values of the solution: 2 (1), 4 (2), 7 (3), 10 (4).

It was of interest to study the sensitivity of the luminescence spectrum of grown CdS QDs to the acid-base composition of colloidal solutions in which they are located, to determine whether the process of defect formation as a result of a change in the solution pH is reversible, and how the pH value affects the change in the QD size.

The objects of study were CdS QDs obtained at a neutral pH = 6 (initial sample), with an equimolar ratio of cadmium and sulfur ions and having a wide luminescence band in the region ( $\lambda_{\max} = 667$  nm). Solutions of alkali or hydrochloric acid were added to the colloidal solution containing these QDs until pH was obtained (2, 4, 6, 8).

As a result, colloidal solutions of CdS QDs were obtained, the color of which changed from yellow to orange (Fig. 2). It can be seen that the color of solutions corresponding to pH = 2 and 4 is practically the same, which is confirmed by the data of the absorption spectra shown in Fig. 3.

Extrapolation of the absorption curves to the energy axis gives the values of the effective band gap of nanocrystals at different pH, which was used to determine the particle size, respectively, 2.9 nm (at pH 2 and 4), 3.5 nm (at pH 6), 4 nm (at pH 8).

The average particle radius was estimated from the optical absorption spectra. According to the theory of interband absorption [9], the effective width of the forbidden band of a nanocrystal  $E_g^*$  (the energy of the transition between the upper hole and lower electron levels) increases with decreasing particle radius according to the law:

$$\hbar\omega = E_g^* + E_{l,n}^{e,h}, \quad (1)$$

where  $E_g^*$  is the optical band gap of the bulk crystal;  $E_{l,n}^{e,h}$  is the dimensional quantization energy, inversely proportional to the square of the nanoparticle radius;  $l$  and  $n$  are the orbital and principal quantum number. Dimensional quantization energy is defined as the difference between the effective band gap of a nanocrystal and a single crystal. It can be calculated using the formula (1):

$$E_{l,n}^{e,h} = \hbar^2 \varphi_{l,n}^2 / 2 m_{e,h} r^2 \quad (2)$$

where  $m_{e,h}$  are effective masses of an electron and a hole;  $r$  is the average radius of a nanoparticle;  $\varphi_{l,n}$  are the roots of the Bessel function (for quantum numbers  $l = 0$  and  $n = 1$ ,  $\varphi_{01} = 3.142$ ).

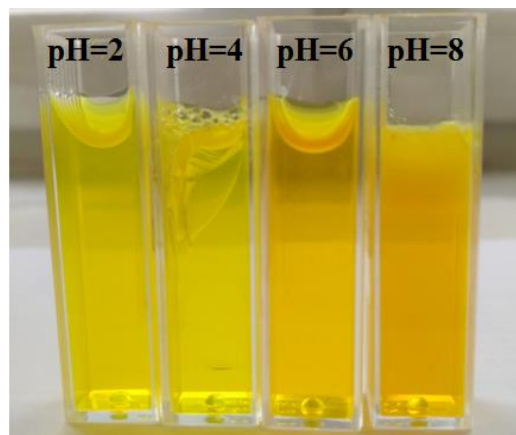


Fig.2 Samples of NC CdS obtained at different pH values.

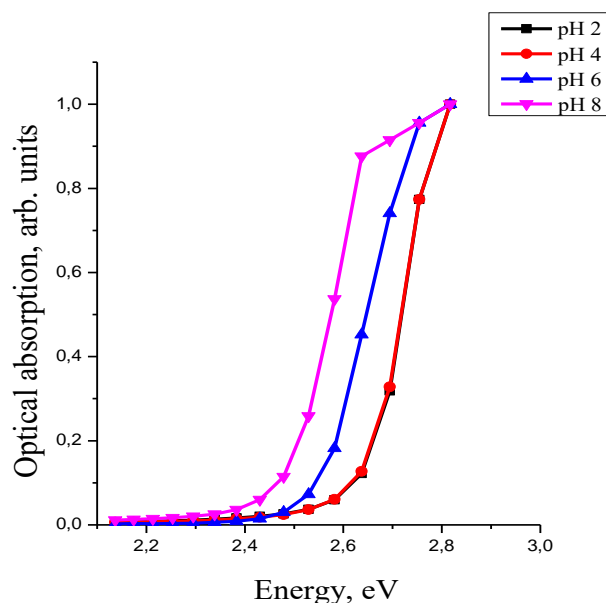


Fig. 3 Normalized absorption spectra of CdS NC grown at different pH values of the solution: 2 (1), 4 (2), 6 (3), 8 (4).

The observed results can be explained by the following phenomena. A decrease in the size of QDs upon addition of hydrochloric acid (pH = 2, 4) can occur due to their dissolution, while the size of QDs decreases from 3.5 nm to 2.9 nm. The increase in the size of QDs upon the addition of alkali may be due to either their coagulation or the formation of a cadmium hydroxide shell.

The luminescence spectra of the samples measured after acid-base treatment of already grown CdS QDs are shown in Fig. 4. The obtained spectra repeat the results of the experiment on the influence of the pH of the solution during the synthesis of nanocrystals [8]. In the spectra of nanocrystals with low pH (2 and 4), a short-wavelength luminescence band (570 nm) is found. At high pH values (6, 8), a long-wavelength band dominates, localized at the wavelength  $\lambda_{\max} = 690$  nm, the nature of which is associated with intrinsic defects in nanocrystals. The transformation of the contour of the luminescence bands of the whiskers under study is well illustrated by normalizing these spectra (Fig. 5). It was found that, both in an acidic medium (pH = 2, 4) and in an alkaline medium (pH = 8), the luminescence spectrum consists of two bands. The short-wavelength band ( $\lambda_{\max} = 580$  nm) dominates in an acidic medium, and the long-wavelength band - in an alkaline medium ( $\lambda_{\max} = 683$  nm).

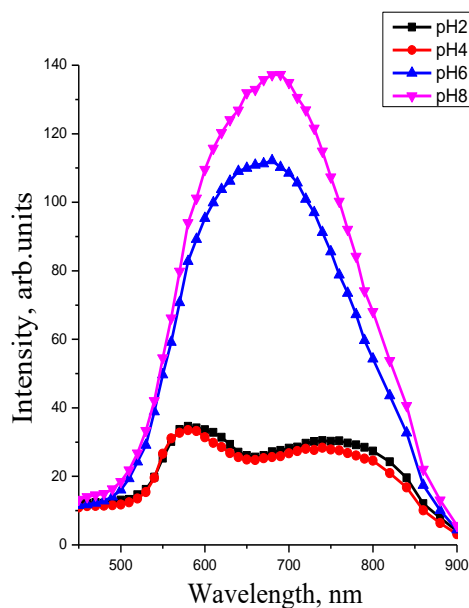


Fig.4 Luminescence spectra of CdS NC grown at different values of solution pH: 2 (1), 4 (2), 6 (3), 8 (4).

In earlier studies [8], when the acid-base balance of the solution changed during synthesis, a change in the spectrum was observed due to a change in the nature of surface defects. In this article, the acid-base balance of the already prepared solution with CT was changed. In this case, it was noticed that the change in the position of the emission spectrum correlates with the change in the size of the CdS QD.

Thus, in spite of the different experimental conditions on the effect of pH on the luminescence spectrum of CdSQDs, both obtained at different pH values during synthesis and treated after synthesis, there is a qualitative agreement between their luminescence spectra.

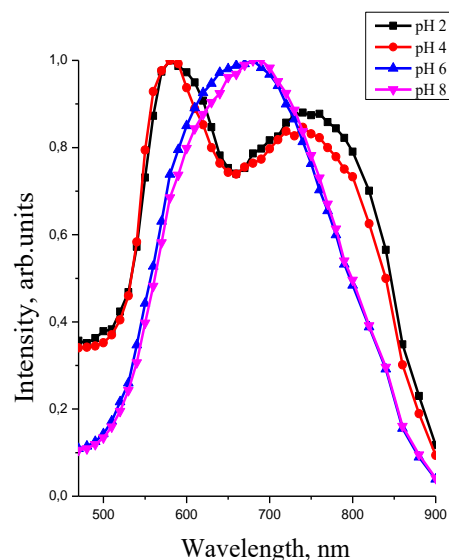


Fig.5 Normalized luminescence spectra of CdS NC grown at different pH values of the solution: 2 (1), 4 (2), 6 (3), 8 (4).

#### IV. CONCLUSIONS

The results of our studies have shown that the emission spectrum of CdS QDs depends on the acid-base composition of the medium. At low pH values, the bands localized in the region of 500-580 nm dominate, and at high pH values, in the region of 640-680 nm. It is shown that the luminescence spectrum can be changed both by changing the synthesis conditions and by changing the acidity of colloidal CdS QDs.

#### REFERENCES

- [1] S.F. Musikhin, O. A. Alexandrova, V.V. Luchinin, A.I. Maximov, V.A. Moshnikov. "Semiconductor colloidal nanoparticles in biology and medicine", *Biotechnosphere*, 2012 40-48.
- [2] AA Rempel, "Nanotechnologies. Properties and applications of nanostructured materials", *Russ chem rev*, 2007, 76 (5), 435-461 DOI: <https://doi.org/10.1070/RC2007v076n05ABEH003674>
- [3] Yu.A. Kolomiitseva, Yu.S. Kolomiitsev, B.G. Skuybin, S.A. Ambrozovich. "Investigation of the luminescence of CdSe / CdS quantum dots", *Bulletin of Science and Education No. 7 (43) 2018*. Vol. 2, 32-36
- [4] C.B. Rempel, A.A. Divorce, M.C. Hebogatikov, E.B. Shishkina, V. Ya. Schur, A.A. Rempel, "Dimensions and Fluorescence of Cadmium Sulfide Quantum Dots," *Physics of the Solid State*, 2013, vol. 55, no. 3, 567-571.
- [5] RR Shamilov, RR Garaishina, Yu. G. Galyametdinov, "Synthesis and luminescent properties of hybrid CdSe / CdS quantum dots in aqueous-organic media", *Bulletin of Kazan Technological University*, 2014, 60-63
- [6] Deepika and Rakesh Dhar, "Study of variation of band gap with the size of CdSe quantum dots", *The Pharma Innovation Journal* 2018, 7 (3): 41-43
- [7] Yilin Wang, Jian Ping Lu & Zhang Fa Tong, "Rapid synthesis of CdSe nanocrystals in aqueous solution at room temperature," *Bulletin of Materials Science* volume 33, pages 543-546 (2010).
- [8] A. Smyntyna, V. M. Skobeveva, K. A. Verheles, N. V. Malushin. "Influence of technology on the formation of luminescence centers in QDs CdS", *Journal of nano- and electronic physics. Sumy State University*, 2019, Vol. 11 No 3, 05031 (4pp) (2019).
- [9] Efros Al. L., Efros A. L. "Interband absorption of light in a semiconductor ball", *Fiz. and tech. semiconductors*. - 1982. - T.16. AT 7. - S. 1209-1214.

# The effect of dielectric on the polarizability of the two-layer metal-dielectric semisphere on the substrate

Andrii Korotun

National University "Zaporizhzhia Politechnic"  
Zhukovskogo Str. 64, 69063, Zaporizhzhya, Ukraine, E-mail: andko@zntu.edu.ua

**Abstract**—The expression for the polarizability for the two-layer metal-dielectric semisphere on the substrate has been obtained to the quadrupole approximation. The calculations have been performed for the semispheres  $\text{Cu}@\text{Cu}_2\text{O}$  and  $\text{Al}@\text{Al}_2\text{O}_3$  on the glass substrate. It has been established the presence of the red shift of the plasmonic resonance under the increase of the fraction of metal in the semispheres  $\text{Al}@\text{Al}_2\text{O}_3$  in contrast to  $\text{Cu}@\text{Cu}_2\text{O}$ , in the case of which only the increase of the maximum value of the imaginary part of the polarizability takes place.

**Keywords**— metal-dielectric semispheres, polarizability, quadrupole approximation, plasmonic resonance.

## I. INTRODUCTION

The rapid development of the nanotechnologies in the recent decades stimulates an active use of the micro- and nanostructures, in which the optical resonances of the different kinds are manifested. One distinguishes the plasmonic and spatial resonances depending on the material of which the structures have been formed.

The essential amplification of the local electric fields [1] takes place under the excitation of the plasmonic resonances. It causes the application of the nanostructures in sensorics [2], nonlinear optics [3], Riemann spectroscopy [4], laser technologies [5], for the increase of the effectiveness of the photocatalysis [6]. The location of the resonance depends essentially both on the morphology of the structure [7] and the environment [8], and on the presence of the other particles in the neighborhood of the nanoparticle. One of the wide spread types of the self-assembled nanostructures is such type as the island metallic films. An interest to the study of the properties of such systems results from, in particular, the possibilities of their use in the different applications of optics and photonics. The surface plasmonic resonance in the metallic nanoparticles opens up the space for the construction of the spectrally-selective lossy coatings [10], based on such films, and also provides the amplification of the fluorescence signal [11], infrared spectroscopy [12], and Riemann scattering [13]. Moreover, the island films of metals can be effectively used in photovoltaics and in the solar cells [14] and in the catalysis [15]. The amplification of the signal of Riemann scattering is possible by the value up to 8-9 orders [13], which gives an opportunity to use such films for the registration of the signal from the isolated molecules.

It should be pointed out that, as a rule, the shape of the islands in the film is close to the semispherical. Hence, it is not unreasonable to construct the theoretical models for the semispherical metallic nanoislands. Such nanoparticles on the surface can be oxidized and ruined with time. The silver nanoparticles are particularly sensible to these processes [16]. In order to protect them from the environment one can use the dielectric coating of the films, in particular  $\text{TiO}_2$ . The presence of the external layer shifts the location of the plasmonic resonance, hence, its influence should be taken into account under the calculation of the spectral characteristics of the island films. That is why the calculation of the polarizability and location of the surface plasmonic resonance of the metallic semisphere with the dielectric coating is actual task.

## II. BASIC RELATIONS

Let the metallic nanoisland with the dielectric permittivity  $\epsilon(\omega)$  has the shape of the semisphere with the radius  $R_c$  (domain 1), which is situated on the dielectric substrate (fig. 1) with the dielectric permittivity  $\epsilon_s$  (domain 2). The dielectric permittivity of the environment is  $\epsilon_m$  (domain 3). The dielectric permittivity of the complementary domain, which has the shape of the semisphere, in the substrate is  $\epsilon_s$  (domain 4). The nanoparticle is covered with the dielectric layer with the thickness  $t$  and the dielectric permittivity  $\epsilon_d$  (domain 5). The dielectric permittivity of the symmetrical semispherical layer in the substrate is  $\epsilon_s$  (domain 6).

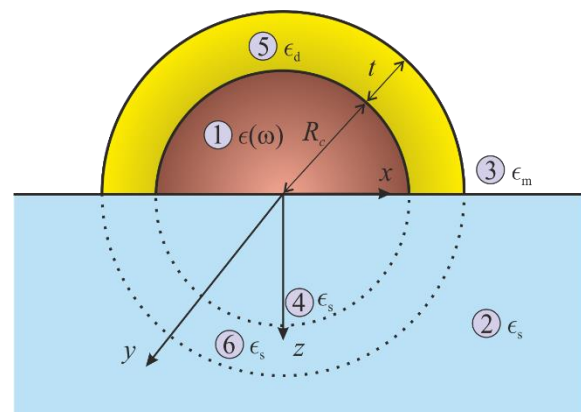


Fig.1 The schematic illustration of the two-layer particle on the substrate.

The two-layer semisphere is exposed to the planar monochromatic wave, which is polarized along the surface of the substrate, with the amplitude  $\xi_0$ . The work deals with the case of the longitudinal polarization of the external field, because the transverse component of the electric field is always small under the close to the normal grazing angles, which are the most commonly encountered in the plasmonic experiments.

Let us assume that the size of the nanoparticle is much less than the wave length. In this case in order to solve the posed problem, one can use the quasi-static approximation. In this approximation, the potential, which is generated by the two-layer semispherical nanoisland in the whole space, is determined by the solution of Laplace equation

$$\Delta\varphi = 0, \quad (1)$$

by the boundary conditions between the metal and the shell when  $r = R_c$ :

$$\begin{aligned} \varphi_1|_{r=R_c} = \varphi_5|_{r=R_c}, \quad \varphi_4|_{r=R_c} = \varphi_6|_{r=R_c}, \\ \epsilon(\omega) \frac{\partial\varphi_1}{\partial r}\Big|_{r=R_c} = \epsilon_d \frac{\partial\varphi_5}{\partial r}\Big|_{r=R_c}, \quad \frac{\partial\varphi_4}{\partial r}\Big|_{r=R} = \frac{\partial\varphi_6}{\partial r}\Big|_{r=R_c}, \end{aligned} \quad (2)$$

by the boundary conditions between the shell and the environment when  $r = R$  (where  $R = R_c + t$  is the total radius of the semisphere:

$$\begin{aligned} \varphi_2|_{r=R} = \varphi_6|_{r=R}, \quad \varphi_3|_{r=R} = \varphi_5|_{r=R}; \\ \frac{\partial\varphi_2}{\partial r}\Big|_{r=R} = \frac{\partial\varphi_6}{\partial r}\Big|_{r=R}, \quad \epsilon_m \frac{\partial\varphi_3}{\partial r}\Big|_{r=R} = \epsilon_d \frac{\partial\varphi_5}{\partial r}\Big|_{r=R}. \end{aligned} \quad (3)$$

and by the boundary conditions under  $\theta = \pi/2$ :

$$\begin{aligned} \varphi_1|_{\theta=\pi/2} = \varphi_4|_{\theta=\pi/2}, \quad \varphi_2|_{\theta=\pi/2} = \varphi_3|_{\theta=\pi/2}, \\ \varphi_5|_{\theta=\pi/2} = \varphi_6|_{\theta=\pi/2}; \quad \epsilon(\omega) \frac{\partial\varphi_1}{\partial\theta}\Big|_{\theta=\pi/2} = \epsilon_s \frac{\partial\varphi_4}{\partial\theta}\Big|_{\theta=\pi/2}, \quad (4) \\ \epsilon_s \frac{\partial\varphi_2}{\partial\theta}\Big|_{\theta=\pi/2} = \epsilon_m \frac{\partial\varphi_3}{\partial\theta}\Big|_{\theta=\pi/2}, \quad \epsilon_d \frac{\partial\varphi_5}{\partial\theta}\Big|_{\theta=\pi/2} = \epsilon_s \frac{\partial\varphi_6}{\partial\theta}\Big|_{\theta=\pi/2}. \end{aligned}$$

It should be pointed out that the polarizability of the two-layer semisphere coincides with the polarizability of the metal-oxide nanoparticle in the medium with the dielectric permittivity  $\epsilon_m$  to the dipole approximation. That is why let us find the polarizability to the quadrupole approximation. The solution of the problem (1) – (4) in the domains 1 – 6 to this approximation has the form

$$\begin{aligned} \varphi_1 = [A_1 r P_1^1(\cos\theta) + A_2 r^2 P_2^1(\cos\theta)] \cos\phi; \\ \varphi_2 = \left[ \frac{B_1}{r^2} P_1^1(\cos\theta) + \frac{B_2}{r^3} P_2^1(\cos\theta) - \xi_0 r P_1^1(\cos\theta) \right] \cos\phi; \end{aligned}$$

$$\begin{aligned} \varphi_3 = \left[ \frac{C_1}{r^2} P_1^1(\cos\theta) + \frac{C_2}{r^3} P_2^1(\cos\theta) - \xi_0 r P_1^1(\cos\theta) \right] \cos\phi; \\ \varphi_4 = [D_1 r P_1^1(\cos\theta) + D_2 r^2 P_2^1(\cos\theta)] \cos\phi; \\ \varphi_5 = \left[ E_1 r P_1^1(\cos\theta) + E_2 r^2 P_2^1(\cos\theta) + \frac{F_1}{r^2} P_1^1(\cos\theta) + \right. \\ \left. + \frac{F_2}{r^3} P_2^1(\cos\theta) \right] \cos\phi; \quad (5) \\ \varphi_6 = \left[ G_1 r P_1^1(\cos\theta) + G_2 r^2 P_2^1(\cos\theta) + \frac{H_1}{r^2} P_1^1(\cos\theta) + \right. \\ \left. + \frac{H_2}{r^3} P_2^1(\cos\theta) \right] \cos\phi, \end{aligned}$$

where  $P_1^1(\cos\theta) = \sin\theta$  and  $P_2^1(\cos\theta) = 3\sin\theta\cos\theta$  – Legendre polynomials.

The relation for the dipole polarizability of the metal-dielectric nanoisland can be obtained to the quadrupole approximation after the substituting of the solution (5) into the boundary conditions (2) – (4) and performing the tedious transformations. It has the form

$$\alpha = \frac{C}{\xi_0 R^3} = \frac{b_1 a_{22} - b_2 a_{12}}{a_{11} a_{22} - a_{12} a_{21}}, \quad (6)$$

with the designations

$$\begin{aligned} a_{11} = \frac{5}{12R^4} \left\{ -(\epsilon_d - \epsilon_m) + \frac{\epsilon_d - \epsilon_m}{\beta_c^{5/3}} \frac{\epsilon(\omega)(5\epsilon_d + \epsilon_s) + 4\epsilon_d\epsilon_s}{\epsilon_s(\epsilon(\omega) - \epsilon_d)} + \right. \\ \left. + \frac{5}{2\beta_c^{4/3}} \frac{\epsilon_d(\epsilon(\omega) + \epsilon_s)(\epsilon_d + 3\epsilon_s + 2\epsilon_m)}{\epsilon_s(\epsilon(\omega) - \epsilon_d)} \right\}; \\ a_{12} = \frac{1}{R^5} \left\{ -(\epsilon_d - \epsilon_m) - \frac{1}{3\beta_c^{5/3}} \frac{\epsilon(\omega)(5\epsilon_d + \epsilon_s) + 4\epsilon_d\epsilon_s}{\epsilon_s(\epsilon(\omega) - \epsilon_d)} \times \right. \\ \left. \times \frac{\epsilon_d(2\epsilon_s + 5\epsilon_m) + 3\epsilon_s\epsilon_m + 5(\epsilon_d - \epsilon_m)\epsilon_d(\epsilon(\omega) + \epsilon_s)}{\epsilon_s \beta_c^{4/3} \epsilon_s(\epsilon(\omega) - \epsilon_d)} \right\}; \\ a_{21} = \frac{1}{R^3} \left\{ \epsilon_d - \epsilon_m + \frac{3(\epsilon_d - \epsilon_m)\epsilon(\omega) + \epsilon_s}{\beta_c^{4/3} \epsilon(\omega) - \epsilon_d} + \right. \\ \left. + \frac{\epsilon_d + 3\epsilon_s + 2\epsilon_m}{\beta_c} \frac{2\epsilon(\omega) + \epsilon_d + 3\epsilon_s}{\epsilon(\omega) - \epsilon_d} \right\}; \\ a_{22} = \frac{8}{5R^4} \left\{ \epsilon_d - \epsilon_m - \frac{3}{2\beta_c^{4/3}} \frac{\epsilon_d(2\epsilon_s + 5\epsilon_m) + 3\epsilon_s\epsilon_m}{\epsilon_s} \times \right. \\ \left. \times \frac{\epsilon(\omega) + \epsilon_s}{\epsilon(\omega) - \epsilon_d} + \frac{\epsilon_d - \epsilon_m}{\beta_c} \frac{2\epsilon(\omega) + \epsilon_d + 3\epsilon_s}{\epsilon(\omega) - \epsilon_d} \right\}; \\ b_1 = \frac{5(\epsilon_d - \epsilon_m)}{24R} \xi_0 \left\{ 1 + \frac{5}{\beta_c^{4/3}} \frac{\epsilon_d(\epsilon(\omega) + \epsilon_s)}{\epsilon_s(\epsilon(\omega) - \epsilon_d)} - \right. \\ \left. - \frac{1}{\beta_c^{1/3}} \frac{\epsilon(\omega)(5\epsilon_d + \epsilon_s) + 4\epsilon_d\epsilon_s}{\epsilon_s(\epsilon(\omega) - \epsilon_d)} \right\}; \quad (7) \end{aligned}$$

$$b_2 = \frac{\epsilon^\infty}{\epsilon_0} \left\{ \frac{2\epsilon_d + 3\epsilon_s + \epsilon_m}{2} + \frac{3(\epsilon_d - \epsilon_m)}{\beta_c} \frac{\epsilon_s + \epsilon_d}{\epsilon(\omega) - \epsilon_d} - \frac{\epsilon_d - \epsilon_m}{2} \frac{-\epsilon(\omega) + 4\epsilon_d + 3\epsilon_s}{\epsilon(\omega) - \epsilon_d} \right\}.$$

Here  $\beta_c = (R_c/R)^3$  is the volume "fraction" of the material of core of the metallic semisphere.

In the following, we restrict ourselves to the case of the dielectric function of the metals taking into account the attenuation:

$$\epsilon(\omega) = \epsilon^\infty - \frac{\omega_p^2}{\omega^2 + \gamma^2} + i \frac{\omega_p^2 \gamma}{\omega(\omega^2 + \gamma^2)}, \quad (8)$$

where  $\epsilon^\infty$  is the contribution of the ion core into the dielectric function of the metal,  $\omega_p$  is the frequency of the volume plasmons,  $\gamma$  is the relaxation rate.

### III. THE RESULTS OF THE CALCULATIONS AND THE DISCUSSION

The calculations have been performed for the two-layer semispheres  $\text{Cu@Cu}_2\text{O}$  and  $\text{Al@Al}_2\text{O}_3$  on the glass substrate. The environment is the air ( $\epsilon_m=1$ ). The parameters of these materials are given in the tables I and II.

TABLE 1. PARAMETERS OF METALS [17]

5	Value	6 Metals	
		Al	Cu
	$r_s/a_0$	2.07	2.11
	$m^*/m_e$	1.06	1.49
	$\epsilon^\infty$	0.7	12.03
	$\gamma_{\text{bulk}}, 10^{14} \text{ s}^{-1}$	1.25	0.37

TABLE 2. PARAMETERS OF OXIDES ( $\epsilon_d$ ) AND SUBSTRATE ( $\epsilon_s$ ) [17]

7 Oxides		8 Substrate
$\text{Al}_2\text{O}_3$	$\text{Cu}_2\text{O}$	Glass
3.13	3.7	2.25

The graphs of the frequency dependences of the real part of the polarizability for the semispheres  $\text{Cu@Cu}_2\text{O}$  and  $\text{Al@Al}_2\text{O}_3$  are given in the figures 2, *a* and 3, *a*. These figures show that function  $\text{Re}\alpha(\hbar\omega)$  is alternating in sign and has one maximum and one minimum. The greater is the volume of the metallic fraction, the more expressed are these maximum and minimum.

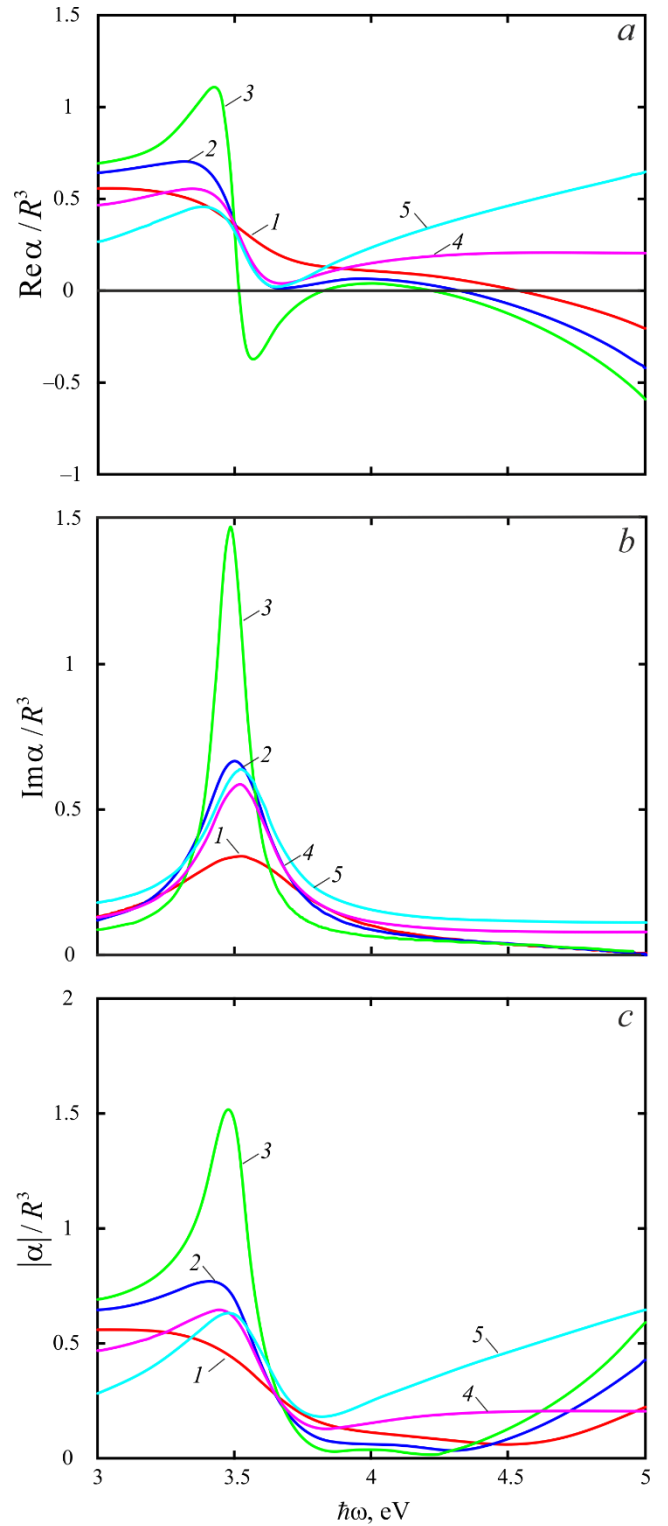


Fig. 2 Frequency dependences of the real (a) and imaginary (b) parts of the transverse polarizability component and its modulus (c) of  $\text{Cu@Cu}_2\text{O}$  nanoislands on glass: 1 –  $R=10$  nm,  $t=1$  nm; 2 –  $R=20$  nm,  $t=1$  nm; 3 –  $R=50$  nm,  $t=1$  nm; 4 –  $R=20$  nm,  $t=5$  nm; 5 –  $R=20$  nm,  $t=10$  nm

The similar dependences for the imaginary part of the polarizability are given in the figures 2, *b* and 3, *b*. The function  $\text{Im}\alpha(\hbar\omega) > 0$  in the spectral band which is under the study in contrast to  $\text{Re}\alpha(\hbar\omega)$ . It should be pointed out that the behavior of the frequency dependences for the given systems under the variation of the radius of the metallic core

and the thickness of the oxide shell are quite different. In the case of the semispheres  $\text{Cu@Cu}_2\text{O}$ , the greater is the volume of the metallic fraction (due to the increase of the radius of the metallic core or due to the decrease of the thickness of the oxide shell), the greater is the maximum value  $\text{Im}\alpha$  under the factual loss of the shifts of the resonance location. In the case of the semispheres  $\text{Al@Al}_2\text{O}_3$ , the "red" shift and the increase of the maximum  $\text{Im}\alpha(\hbar\omega)$  under the increase of the radius of the metallic core (the curves in sequence  $1 \rightarrow 2 \rightarrow 3$  in the figure 3, b) take place, and the increase of the thickness of the oxide layer results in the "violet" shift under the almost invariant maximum value (the curves in sequence  $2 \rightarrow 4 \rightarrow 5$  in the figure 3, b).

The frequency dependences for the module of the polarizability for the considered above compositions have been given in the figures 2, c and 3, c. In the case of the semispheres  $\text{Cu@Cu}_2\text{O}$  the inequality  $\text{Im}\alpha(\hbar\omega) > \text{Re}\alpha(\hbar\omega)$  is true only in the domain  $\text{Im}\alpha_{\text{max}}(\hbar\omega)$ . Hence,  $|\alpha_{\text{max}}(\hbar\omega)|$  are situated in this frequency domain. The graphs  $|\alpha(\hbar\omega)|$  and  $\text{Im}\alpha(\hbar\omega)$  are qualitatively similar and the numerical values are quantitatively close due to the fact that  $\text{Im}\alpha(\hbar\omega) \gg \text{Re}\alpha(\hbar\omega)$  in the considered frequency domain.

#### IV. CONCLUSIONS

The relation for the polarizability has been obtained to the quadrupole approximation for the two-layer metal-oxide semispherical nanoparticles on the dielectric substrate. The numerical results have been given for the nanoparticles  $\text{Cu@Cu}_2\text{O}$  and  $\text{Al@Al}_2\text{O}_3$ .

It has been established that the real part of the polarizability is the alternating in sign function of the frequency, and the imaginary part is always positive.

It has been demonstrates that the increase of the volume of the metallic fraction due to the increase of the radius of the core, results in the increase of the maximum value of the imaginary part of the polarizability for the semispheres  $\text{Cu@Cu}_2\text{O}$  and  $\text{Al@Al}_2\text{O}_3$ , and in the presence of the "red" shift of these maximums for the semispheres  $\text{Al@Al}_2\text{O}_3$ .

It has been shown that the presence of the oxide coating gives an opportunity to control the properties of the plasmonic semispherical nanoparticles. The increase of the thickness of the oxide layer results in the presence of the "violet" shift of the location of the plasmonic resonance for the semispheres  $\text{Al@Al}_2\text{O}_3$  under the almost equal maximum value of the imaginary part of the polarizability.

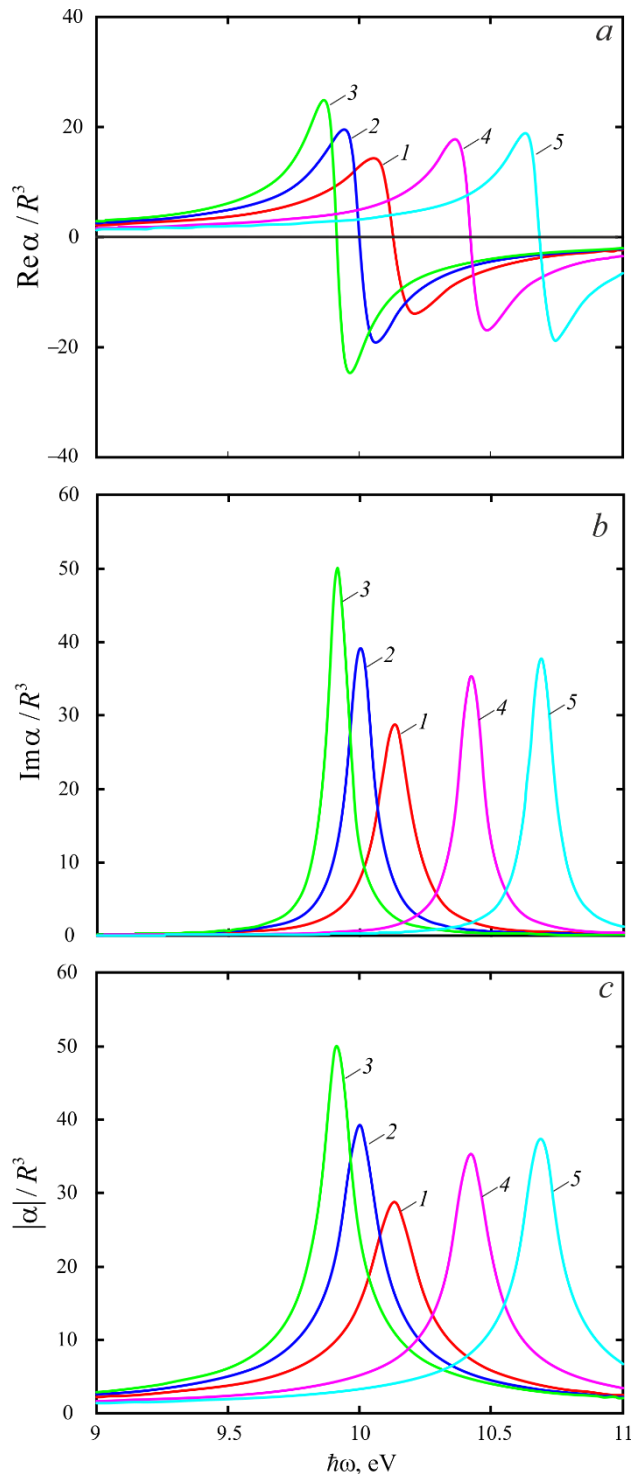


Fig.3 Frequency dependences of the real (a) and imaginary (b) parts of the transverse polarizability component and its modulus (c) of  $\text{Al@Al}_2\text{O}_3$  nanoislands on glass: 1 –  $R=10$  nm,  $t=1$  nm; 2 –  $R=20$  nm,  $t=1$  nm; 3 –  $R=50$  nm,  $t=1$  nm; 4 –  $R=20$  nm,  $t=5$  nm; 5 –  $R=20$  nm,  $t=10$  nm

#### REFERENCES

- [1] E. Hao, G. C. Schatz, "Electromagnetic fields around silver nanoparticles and dimers," J. Chem. Phys., vol. 120, pp. 357–366, January 2004.
- [2] B. Prabowo, A. Purwidyantri, K.-C. Liu, "Surface Plasmon Resonance Optical Sensor: A Review on Light Source Technology," Bios., vol. 8, pp. 80–107, August 2018.
- [3] M. Kauranen, A. V. Zayats, "Nonlinear plasmonics," Nat. phot., vol. 6, pp. 737–748, November 2012.

- [4] K. A. Willets, R. P. Van Duyne, "Localized Surface Plasmon Resonance Spectroscopy and Sensing," *Annu. Rev. Phys. Chem.*, vol. 58, pp. 267–297, October 2006.
- [5] M. A. Noginov, G. Zhu, A. M. Belgrave, R. Bakker, V. M. Shalaev, E. E. Narimanov, S. Stout, E. Herz, T. Suteewong, U. Wiesner, "Demonstration of a spaser-based nanolaser," *Nature*, vol. 460, pp. 1110–1112, August 2009.
- [6] S. Linic, P. Christopher, D. B. Ingram, "Plasmonic-metal nanostructures for efficient conversion of solar to chemical energy," *Nature Mater.*, vol. 10, pp. 911–921, November 2011.
- [7] Amendola, R. Pilot, M. Frascioni, O. M. Maragò, M. Antonia Iati, "Surface plasmon resonance in gold nanoparticles: a review," *J. Phys.: Condens Matter.*, vol. 29, pp. 1–48, May 2017.
- [8] Noguez, "Surface Plasmons on Metal Nanoparticles: The Influence of Shape and Physical Environment," *J. Phys. Chem. C*, vol. 111, pp. 3806–3819, January 2007.
- [9] W. Rechberger, A. Hohenau, A. Leitner, J. R. Krenn, B. Lamprecht, F. R. Aussenegg, "Optical properties of two interacting gold nanoparticles," *Opt. Comm.*, vol. 220, pp. 137–141, May 2003.
- [10] M. Held, O. Stenzel, S. Wilbrandt, N. Kaiser, A. Tünnermann, "Manufacture and characterization of optical coatings with incorporated copper island films," *Appl. Optics*, vol. 51, pp. 4436–4447, July 2012.
- [11] K. Aslan, S. N. Malyn, C. D. Geddes, "Angular-dependent metal-enhanced fluorescence from silver island films," *Chem. Phys. Lett.*, vol. 453, pp. 222–228, April 2008.
- [12] T. R. Jensen, R. P. Van Duyne, S. A. Johnson, V. A. Maroni, "Surface-enhanced infrared spectroscopy: a comparison of metal island films with discrete and nondiscrete surface plasmons," *Appl. Spectrosc.*, vol. 54, pp. 371–377, March 2000.
- [13] L. Haynes, R. P. van Duyne, "Plasmon-sampled surface-enhanced Raman excitation spectroscopy," *J. Phys. Chem. B*, vol. 107, pp. 7426–7433, March 2003.
- [14] R. Santbergen, T. L. Temple, R. Liang, A. H. M. Smets, R.A.C.M.M. van Swaaij, M. Zeman Maroni, "Application of plasmonic silver island films in thin-film silicon solar cells," *J. Optics.*, vol. 14, id. 024010, January 2012.
- [15] R. Narayanan, M. A. El-Sayed, "Catalysis with transition metal nanoparticles in colloidal solution: nanoparticle shape dependence and stability," *J. Phys. Chem. B*, vol. 109, pp. 12663–12676, July 2005.
- [16] T. W. H. Oates, M. Losurdo, S. Noda, K. Hinrichs, "The effect of atmospheric tarnishing on the optical and structural properties of silver nanoparticles," *J. Phys. D: Appl. Phys.*, vol. 46, id. 145308, March 2013.
- [17] V. Korotun, A. A. Koval', "Optical Properties of Spherical Metal Nanoparticles Coated with an Oxide Layer," *Opt and Spectr.*, vol. 127, no. 6, pp. 1161–1168, December 2019.

# The HF-LF minilab for analysing dielectric and semiconductor matter with the tunnel diodes and Corbino-electrodes in resonator

I.N. Bondarenko\*, V.A. Nikolaenko<sup>+</sup>

\*Kharkiv National University of Radio Engineering and Electronics  
14 Nauka Ave / 61166 / Kharkiv / Ukraine

<sup>+</sup>B. Verkin Institute for Low Temperature Physics and Engineering, National Academy of Sciences of Ukraine  
47 Nauka Ave. / 61103 / Kharkiv / Ukraine / 0962065756 / nikolaenko@ilt.kharkov.ua

**Abstract**— Study the quantum-size structures of matter is important in order to coupling nanotechnologies and use of the nanomaterials. The high frequency (HF) resonant method in research of semiconductors and dielectrics at low temperature is sensitive and exact in row others. This is due to high quality of resonance at low signal-to-noise ratio and at small energy loss in tested matter. The concept of "giga - nano" takes a place here. The use of compact tunnel diodes as the generator and detector coupled with resonator considered in this work is attractive for low-temperature studies of nanostructures. The feature of work is also that the bottom of resonator is coaxial system of rings - Corbino geometry. The Corbino system serves, on the one hand, as analyzer of matter properties of at low frequencies (LF), on other one, serves as a modulator of HF field in resonator. Filling the vacuumed cavity by various gases additionally can serve by the specific theme of researches. So, proposed HF-LF mini-analyzer of matter for the low- temperature investigation. The main composition of device on resonator basis is given.

**Keywords**—nanomaterials, dielectrics and semiconductors; HF cavity; superfluid helium; nanowires

## I. INTRODUCTION

Study of the structural characteristics of dielectrics and semiconductors, in particular, quantum-electron formations in them, is necessary for applications. The chips with quantum-size structures play a crucial role in modern devices. At commensurable of structure with the electron wavelength, its quantum-mechanical nature, described by the Schrödinger equation with the corresponding boundary conditions, is clearly expressed. These structures include quantum wells, quantum wires, quantum dots, and superlattices. The practice interest is effects such as size quantization, resonant tunneling, superposition, and entanglement of quantum states. One of concepts the quantum interaction of electrons with matter was considered in [1].

Devices using nanostructured chips take place in many areas: receivers and transmitters of irradiation, information and computer systems, etc. At creating of artificial nanostructures with given kinetic and spectral properties use the methods of "zone engineering" and "engineering of wave functions". Both the low temperatures and the high carrier's mobility are necessary for the qualitative

realization systems with quantum wells. The quantized energy levels of carrier in the Heisenberg uncertainty relation,  $\Delta\varepsilon \cdot \Delta\tau \leq h$ , (the values  $\Delta\varepsilon$  and  $\Delta\tau$  are uncertainties in energy and relaxation time, respectively,  $h$  - Planck's constant) should be clearly resolved against the background of thermodynamic energy  $k \cdot T$  ( $k$  is Boltzmann constant). The quantum-size effects at relatively high temperatures take place in semiconductors with an electron mobility of at least  $1000 \text{ cm}^2 / \text{V} \cdot \text{s}$  at structures up to 100 nm. The coherence of the particle states at boundary should be enough and the roughness lateral size should not exceed de Broglie wavelength. Modern nanotechnologies allow obtaining samples with the atomic- smooth surfaces, and the use of the separation layers (spacers) essential shields the charged defects.

Many methods and tools is used for a detailed study of both the bulk and the surface features of matter, namely: EPR (electro-paramagnetic resonance) and NMR (nuclear-magnetic resonance); Raman spectroscopy; x-ray spectroscopy; tunnel and atomic force scanning microscopy. Modernized methods for study the microstructures of matter can be applied in study of the nanostructures. The method of high frequency (HF) resonance at low temperatures is sensitive and exact at studying the subtle effects in dielectrics and semiconductors [2-6]. At low temperatures the quality factor,  $Q$  of microwave resonator reaches high value (especially the superconducting resonator), and the "scanning" resonance line is extremely narrow. In such conditions the power of thermal noise in matter does not exceed the quantum limit, and the external fields are shielded by the conducting shell of resonator. The  $Q$ - factor of resonator reaches values more  $10^{10}$  at helium temperatures and the measurement resolution, determined by width of the resonance line  $\Delta f$ , is less than 1 Hz at frequency of  $\sim 10$  GHz.

Notable is study of dielectrics and semiconductors under pulses of heat, light, or irradiation. Such parameters as Fermi level, the carrier recombination time, the energy ionization of traps, the carrier free path, the effective capture cross section and the effective carrier masses can be determined. In the microwave range at a magnetic field it is possible to study the EPR of matter. The topological

dielectrics and the weakly conducting materials have special attention in modern studies. One of the goals here is search for Majorana quasiparticles and creation of a quantum bits of quantum computer on their basis.

HF resonance method as usually complicated because large composition of HF devices: generator, receiver, attenuators, circulator etc. In this work for the improvement of situation proposed the combination of an HF resonator with tunnel diodes as a generator and detector.

The coplanar system of ring electrodes (Corbino system) takes place here too. On the one hand the system serves as a analyzer of the matter properties at low frequencies (LF) and, on other one, serves as a modulator of HF field in resonator. Need to be notice the filling vacuumed cavity by gases or condensed matters additionally is specific theme of researches.

## II. THE DEVICE DESIGN.

### A. CAVITY.

High-frequency electrical oscillation  $H_{011}$  -type in the cylindrical resonator is most acceptable mode in the experimental studies of semiconductors and dielectrics. The matter interacts weakly with electric field near walls of resonator [2, 3]. The conductivity,  $\sigma$  is determined by the losses of HF energy in the matter relative to an accumulated energy in the cavity volume.

$$\frac{1}{Q} - \frac{1}{Q_0} = \frac{4\pi n e \mu}{\omega} \frac{\int E^2 dS}{\int E^2 dV} \quad (1)$$

here  $n$  is the electron density,  $\mu$  is the electron mobility of charge  $e$  and  $\omega$  is frequency. The value of azimuthally component of the electric field  $E_\varphi$  along both the axe ( $z$ ) and the radial ( $r$ ) coordinate is the relation  $E_\varphi(z, r) = E_0 \cdot \sin(\pi z/l) \cdot J_1(3.83 r/a)$  (here  $J_1$  is the Bessel function,  $a$  is resonator radius,  $l$  is resonator height). The conductivity of a disk-shaped insert with thickness  $d$  near bottom is expressed as

$$\sigma = \Delta(1/Q) \cdot \omega \cdot l \cdot \left[ 8 \sin^2(\pi \cdot d/l) \right] \quad (2)$$

The  $Q$ -factor can be calculated by the decrement method:  $Q = \omega_0 \cdot \tau / 2 \cdot \ln(V1/V2)$ , where  $\tau$  is time of change of the output HF pulse from value of  $V1$  to  $V2$ . The magnitude of voltage is measured exactly enough by the comparator method. At the power changes in  $e$ - time, the  $Q$ -factor is determined by simplest expression as  $\omega_0 \cdot \tau$ . The relative change in resonance frequency, given by the dielectric constant  $\epsilon$ , for thin insert ( $d/l \ll 1$ ) is

$$\Delta f/f_0 = \left( \pi^2/3 \right) \cdot (\epsilon - 1) \cdot (d/l)^3 \quad (3)$$

The promise of this method was noted at studying of surface electrons above helium film on dielectric substrate in resonator [6]. With  $Q$ -factor of a superconducting resonator about  $10^7$  the electron mobility was determined as  $\sim 1 \text{ cm}^2 / \text{V} \cdot \text{s}$ , and with higher of  $Q$ -factor this value was significantly lower.

From the expressions for  $\Delta f$  and  $\sigma$ , the values of both the losses,  $\text{tg } \delta$ , and the polarization of helium determined as  $1,8 \cdot 10^{-9}$  and  $\sim 10^{-9}$  respectively.

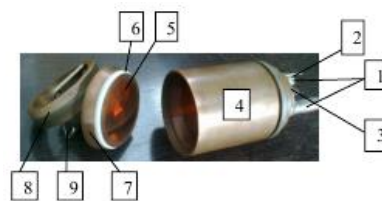


Fig. 1. Cylindrical microwave resonator with Corbino system (photo): 1 – the tubes for coupling the microwave resonator with the generator and the detector; 2 – the capillary of filling the cavity with gaseous or liquids; 3 – the heat line connecting the resonator with the refrigerator; 4 – the resonator housing; 5 – the coplanar system of ring measuring electrodes - Corbino system; 6 – the insulating ring- high mode choke; 7 – the conical flange of the vacuum seal; 8 – the clamping ring; 9 – the power supply connector (DC and AC).

The combined design of microwave resonator is shown in Figure 1. It is a copper cylinder (resonator) with internal diameter and height of 42 mm for  $H_{011}$  mode. Resonator has two tubes for placing tunnel diode modules. The Corbino electrode system was situated on the resonator bottom. Structural elements of the resonator are shown in items to Fig. 1. The internal surface of resonator, for specific research tasks, can be covered with a layer of superconducting material (usually lead or tin) with thickness exceeding the skin- layer.

### B. TUNNEL DIODE MODULE

It was noted above that the complex composition of HF devices in traditional measurements limits the use of resonance method. Tunnel diodes are used to simplify of apparatus at low-temperature measurement. The tunnel diode coupled with the resonator can operate either in the HF generator regime or in the HF detector one. The regime is set by the operating point on the N-shaped current-voltage characteristic.



Fig. 2. The tunnel diode module in coaxial line: 1 is the piston with adjusting wheel; 2 is the section of short-circuit coaxial line; 3 is binding loop of the tunnel diode with cavity.

An image (photo) of the tunnel diode module with the tuning piston on coaxial line and with the coupling loop to resonator is shown in Fig.2. The tunnel diode operates at relatively low potential of  $\sim 0.2\text{V}$  and here need high stability bias source. The frequency- pulling regime leads to an increase the resolution HF resonance method [7]. The frequency tuning of generator by the electric potential on tunnel diode reaches 250 MHz. The relative frequency instability during measurement time is estimated to be less than  $\sim 10^{-14}$ .

### C. CORBINO SYSTEM.

A coplanar combination of rings (Corbino's geometry) located on resonator bottom (Fig. 3. The Fig. 1, p. 5 shows this Corbino's geometry system in composition of HF-LF minilab on resonator basis).



Fig. 3. The coplanar system of ring measuring electrodes - Corbino system. It consist the (in radial direction): inner disc is electrode to LF amplifier (or bridge), the separating ring at the ground potential, outer measurement ring - to LF generator signal, guard ring for forming the surface electron spot, the insulated ring

It added as low-frequency system for analyzing conductivity of matter up to 50 MHz in minilab. The components Corbino system in this device have following dimensions: internal disk the diameter 15 mm, rings with external diameters of 17 mm, 36 mm and 39 mm, respectively. The gap between components is smaller 0.1 mm. In this system, the LF- impedance of matter are determined by the Sommer-Tanner method [8]. The capacitive coupling of the substrate with ring electrodes connected to a sensitive device (for example, to a capacitive bridge or to a two-phase closed amplifier - lock-in-amplifier) is considered.

The long line model for calculating the characteristics of a substance is considered in [9]. The phase shift of the signal relative to the electrodes of the generator and amplifier depends on the specific resistance of the substrate  $\rho$ , the capacitive coupling of the substrate to the electrodes  $C$ , and the geometric factor  $G$ , determined by the ratio of the diameter of the rings,  $\Delta\varphi \sim \rho \cdot C \cdot G$ . The magnetoresistance of electrons localized above liquid helium using Corbino systems are measured in [10]. The study of magnetoresistance was considered for both the Drude mode and the ultra-quantum limit mode.

The system with Corbino electrodes, in addition to low-frequency study of substance, makes it possible to modulate the HF field in the resonator. The sensitivity of measurement increases. The Corbino system is housed in a cone-shaped flange, vacuum sealed using vacuum grease (Fig. 1, p. 7). The vacuumized cavity can be filled with the corresponding gas during complex studies of semiconductors and dielectrics. A sample of a disk-shaped substance is placed near the bottom of the resonator (for ease of calculation).

### III. EXAMPLE OF RESERCHE.

Modern nanotechnologies have led to creation of, for example, one-dimensional (1D) or quasi-one-dimensional (Q1D) conducting systems. The charges move freely in one direction, while the other movements of the charge are quantized. Study of 1D system in semiconductors motivated the creation of this system based on surface electrons over helium - SE. The Q1D system of electrons over helium in the grooves of a profiled substrate with a clamping field,  $E_{\perp}$ , was first realized by Kovdrya and

Nikolaenko [11]. The advantages of SE are high plasma homogeneity, wide range of variation of electron density and width of conductive lines in separate experiment.

Figure 4 demonstrates the result on study by Sommer-Tanner method the conductivity of Q1D- surface electrons on a negatively charged profiled substrate. The experiments on this question were carried out with subsequent analysis (the analysis is not given here). The procedure arrangement of this system was follows. Electrons are emitted from a free source onto a substrate to form charge bands. Then the electrons are directed by the field into the grooves with helium to form lines from the surface electrons. The depth of the potential well for SE is estimated as  $\varphi \sim e \cdot E_{\perp} \cdot \delta$  ( $\delta$  is the deviation of the fluid surface in the groove with a radius of curvature of about 40 microns), with a quantization of the spectrum  $\sim 0.1$  K. The charged bands of the dielectric substrate shift the spectrum of surface electrons as  $\omega^2 \sim \pi^2 \cdot e^2 \cdot n_x / m \cdot a^2$  (here  $n_x$  is the density of the linear charge of the substrate,  $a$  is the distance between the charges). The temperature dependence of the conductivity  $\sigma$  at the substrate charge potentials and surface electrons of about 15 V has a stepwise behavior at temperatures below 1.4 K. The observed feature is not described by SE scattering on helium atoms in a gas or on rplons. Dependence shows the behavior of the Q1D system. The energy interval  $\hbar \cdot \omega$  in this case corresponds to the distance between the peaks. The parameters of the steps in different experiments were different.

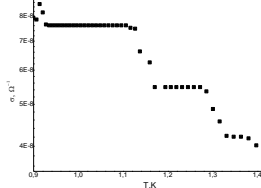


Fig. 4. The conductivity vs temperature of quasi-one-dimensional surface electrons over superfluid helium at charged profiled substrate. The measuring is performed by Sommer-Tanner method.

### IV. CONCLUSION

Thus, the universal mini-system for high-frequency studies of dielectrics and semiconductors using tunnel diodes as the generator and the detector was proposed on the basis of a microwave resonator. For low-frequency studies of matter, the coplanar combination of coaxially arranged rings (Corbino geometry) at the bottom of resonator was used. The compact tunnel diodes near resonator provide a simple design and that at low temperatures lead to decrease in noise potential. Modulation of the microwave signal by a low-frequency signal through the Corbino system increases the sensitivity and accuracy of measurements. Filling the evacuated cavity with gases or other condensed substances allows analyzing their influence on the properties of semiconductors and dielectrics.

### ACKNOWLEDGMENT

The number of researches takes a part in this work and we thank them for that.

The authors hope that this work will be stimulating for further research semiconductors, dielectrics and surface

electrons over helium. The results must use in nano-electronic considering the quantum features matter.

## REFERENCES

- [1] A. Gritsunov, I. Bondarenko, A. Pashchenko, O. Babichenko, "Theory of Natural Oscillatory Systems and Advance in Nanoelectronics", Proc. of the 14-th International Conference "Modern problems of radio engineering, telecommunications and computer science" (TCSET 2018), Ukraine. Lviv-Slavske, Feb. 23-26, pp. 92-97, 2018
- [2] A.A. Brandt, "Study of dielectrics at microwave frequencies", M. : Fizmatgiz, 403 p., 1963.
- [3] I.N. Bondarenko, F.F. Mende, "Investigation properties both the dielectrics and the semiconductors use cooled and super conducting cavity", Kharkov , 72 p., 1980 (in Russian).
- [4] I.N. Bondarenko, "Examination of dielectrics by means of the cooled microstrip resonators", Telecommunications and Radio Engineering, V53, № 7-8, 1999, pp. 171-175, DOI: 10.1615/TelecomRadEng.v53.i7-8.260.
- [5] I.N. Bondarenko, A.V. Galich, "The resonant sensors". Proc. of 24<sup>th</sup> International Crimean Conference Microwave & Telecommunication Technology (CriMiCo'2014), pp. 984-985.
- [6] Yu.Z. Kovdrya, F.F. Mende, and V.A. Nikolaenko, "High-frequency conductivity of electrons above helium film in the regime of localization on substrate potential inhomogeneities", Phys. Nizk. Temp., V.10, №11, pp. 1129-1140, 1984 (in Russian).
- [7] J. Jimenez, J. Benard, P. Sudraud, A. Septier, //Proc. IEEE, v.61, p.121, 1973.
- [8] W.I. Sommer, and D.J. Tanner, "Mobility of Electrons on the Liquid <sup>4</sup>He", Phys. Rev. Lett., V.27, №20, pp.1345-9, 1971.
- [9] R. Mehrotra, Q.J. Guo, Y.Z. Ruan, D.B. Mast, and A.J. Dham, "Density-dependent mobility of a two-dimensional electron fluid", Phys. Rev. B 29, pp 5239-5242, 1984.
- [10] Yu.Z. Kovdrya, V.A. Nikolaenko, O.I. Kirichek, and V.N. Grigor'ev, "Magnetoresistance of electrons localized above liquid helium", Phys. Nizk. Temp., **18** (7), pp. 673 – 678, 1992, (in Russian); Sov.J Low Temp. Phys. 18 (7), pp. 477-480, 1992.
- [11] Yu.Z. Kovdrya, V.A. Nikolaenko, "Quasi-one-dimensional electron system over liquid helium", Fiz. Nizk. Temp. , **18**, pp.1278-80, 1992 (in Russian).

# Transformation of defects in the near-surface layers of semiconductor structures caused by electroresonance and magnetic resonance phenomena

Grigorii Milenin\*, Roman Redko\*<sup>+,</sup>

\*V. Lashkaryov Institute of Semiconductor Physics, National Academy of Sciences of Ukraine  
45 Nauky Pr./ 03028 / Kyiv / Ukraine / +380445256182 / milenin.gv@gmail.com, redko.rom@gmail.com

<sup>+</sup>State University of Telecommunications  
7 Solomenska street / 03680 / Kyiv / Ukraine / +380442492595 / redko.rom@gmail.com

**Abstract**—The present work is devoted to the analysis of the mechanisms of defect transformation in the near-surface layers of semiconductor structures due to weak magnetic fields and the non-thermal action of microwave electromagnetic radiation. The movement of dislocations and ions stimulated by these influences results, in particular, to long-term non-monotonous changes of the intensity of photoluminescence bands, which were observed in semiconductor materials.

**Keywords**— microwave radiation, non-thermal action, weak magnetic field, resonance phenomena

## I. INTRODUCTION

The influence of both weak magnetic fields ( $\mu B \ll kT$ ) and non-thermal effect of electromagnetic radiation of the microwave (MW) range on the state of defects in semiconductor crystals refer to the number of experimentally confirmed phenomena [1–4]. At the same time, this fact is nontrivial, since the energies of interaction of particles and defects in crystals under these fields are negligible as compared to the energy barriers that they need to overcome during their movement. It is reasonable to assume that these fields cause resonant phenomena in the system of crystal defects.

## II. POSSIBLE RESONANCE PHENOMENA AT MICROWAVE IRRADIATION OF SEMICONDUCTOR MATERIALS

Let's consider possible resonance processes which can take place at noted external actions on III-V semiconductor compounds.

### A. Electroresonant detached of dislocations in semiconductor crystals

Electrically charged dislocations, fixed at the ends, have their own (main) angular vibration frequency  $\omega_1$  equal to [5]:

$$\omega_1 = \frac{\pi}{L} \left( \frac{G}{\rho} \right)^{\frac{1}{2}}, \quad (1)$$

where  $G$  is the Poisson module,  $\rho$  – bulk density of material,  $L$  – dislocation length. If the frequency of electromagnetic radiation coincides with that of own dislocation oscillations, then the action of electrical component of the electromagnetic wave causes resonance phenomena. At the

resonant frequency, the amplitude and, hence, the energy of oscillations at small damping increase sharply. As soon as the oscillation energy exceeds the binding energy of the dislocations with the stoppers, then they become detached and begin to move under the action of internal mechanical stresses in the semiconductor crystal.

### B. Electroresonant destruct of impurity complexes in semiconductors

In crystals which containing background impurities (e.g. copper, iron), donor-acceptor complexes (impurity or impurity-defect complexes) are formed. The donor is donor cations, and the acceptor is impurity anions (copper in case of III-V compounds). When these complexes are combined into an electrically neutral cluster, then such a cluster in the near-surface region of the semiconductor, where depleting band bending takes place, is a nanostructural similarity to an ionic crystal. The ion-plasma oscillation frequency is [5]:

$$\omega_2 = \left( \frac{e^2 N}{\varepsilon \varepsilon_0 \mu} \right)^{\frac{1}{2}}, \quad (2)$$

where  $N$  is the concentration of impurity ions;  $e$  – elementary electric charge;  $\varepsilon$  – dielectric constant of semiconductor material;  $\varepsilon_0$  – electric constant of vacuum; where  $\mu$  – is the reduced mass of a pair of ions. The coincidence of the frequency of an electromagnetic wave with an ion-plasma frequency will be accompanied by a resonant increase in the amplitude of oscillations of ions and by destruction of impurity complexes and, consequently, of clusters consisting of them with subsequent diffusion of decomposition products.

## III. POSSIBLE RESONANCE PHENOMENA AT WEAK MAGNETIC FIELDS TREATMENT OF SEMICONDUCTOR MATERIALS

### A. Electrical-resonance transformation of defects

The angular velocity of rotation of electron, in uniformity magnetic field  $B$ , is equal to [5, 6]:

$$\omega_B = \frac{eB}{m_n}, \quad (3)$$

where  $m_n$  is the effective mass of electron in a semiconductor crystal. While the power of electromagnetic waves  $W$  radiated by electrons of a semiconductor crystal is equal to [5, 7]:

$$W = \frac{ne^2 \omega_B^2 v_T^2}{12\pi\epsilon\epsilon_0 c^3}, \quad (4)$$

where  $n$  is the concentration of free electrons in a semiconductor;  $v_T = \sqrt{3kT/m_n}$  – mean square thermal velocity of electrons;  $c$  – speed of light.

When creating a pulsed magnetic field (alternating magnetic field) electromagnetic waves of a wide frequency range will be generated. Thus, the mechanisms of transformation of the defect structure in semiconductor materials which have been exposed to pulsed magnetic fields could be the same as under the non-thermal effect of electromagnetic radiation of a wide frequency range. As noted above, transformation of the subsystem of defects under the influence of electromagnetic radiation is caused by the detachment of dislocations, as well as destruction of impurity-defect complexes due to resonance phenomena.

#### B. Magnetic-resonance effects

On the one hand, in semiconductor materials, paramagnetic centers are dangling bonds carrying unpaired electrons in the cores of dislocations. On the other hand, the atoms of the stoppers, which can be oxygen, donor and acceptor ions, have magnetically sensitive activity. The magnetic field transforms the paramagnetic defect-stopper pair from singlet to triplet, which results in dislocation detachment and it acquires the ability to move under the action of a mosaic of internal stresses of the crystal. The combined action of perpendicular constant magnetic and microwave fields on the crystal under the condition of paramagnetic resonance induces magnetic resonance transitions between levels split by the Zeeman interaction [1-4]. The latter circumstance is the reason for an additional increase in the probability of dislocation detachment. In semiconductor crystals, the dynamics of the subsystem of free charge carriers in a magnetic field can be the reason that magnetic resonance effects will be observed in the absence of an external field, since conduction electrons are a source of electromagnetic waves at the cyclotron frequency. The spectral lines of the cyclotron emission of electrons in a semiconductor crystal are not

infinitely narrow, since charged carriers, when moving under the action of a magnetic field, experience acts of scattering by defects and phonons. This results in broadening of the cyclotron radiation line and, consequently, to the presence in the spectrum of the latter of frequencies that satisfy the condition of electron paramagnetic resonance [5].

#### IV. CONCLUSIONS

Thus, the evolution of the defect subsystem of semiconductor structures under the non-thermal action of electromagnetic radiation of the microwave range is based on electric resonance phenomena could be caused by the coincidence of the frequencies of the latter with the natural and ion-plasma frequencies of vibrations of dislocations and clusters of impurity-defect complexes. The transformation of the defect structure in semiconductor materials under the action of pulsed magnetic fields is based on the idea of the identity of the effect of magnetic and electromagnetic fields on a semiconductor crystal.

Presented approaches were applied to the analysis of long-term transformations of photoluminescence bands, which were observed at room temperature in typical III-V compounds (GaAs:Te, GaN:Si, InP:Te, GaP:Te). Our calculations result to next values:  $\omega_2 \sim 10^9$ - $10^{10}$  Hz,  $W \sim 60$ - $70 \text{ W} \cdot \text{m}^{-3}$  [7].

#### REFERENCES

- [1] R.B. Morgunov, "Spin micromechanics in the physics of plasticity," *Phys. Usp.*, vol. 47, pp. 125-147, [2004].
- [2] Yu.I. Golovin, "Magnetoplastic effect in solids (Review)," *Physics of the Solid State*, vol. 46, pp. 789-824, [2004].
- [3] A.L. Buchachenko, "Magnetoplasticity of diamagnetic crystals in microwave fields," *Journal of Experimental and Theoretical Physics*, vol. 105, pp. 593-598 [2007].
- [4] A.L. Buchachenko, "Effect of magnetic field on mechanics of non-magnetic crystals: The nature of magnetoplasticity," *Journal of Experimental and Theoretical Physics*, vol. 102, pp. 795-798 [2006].
- [5] G.V. Milenin, R.A. Redko, "Transformation of structural defects in semiconductors under action of electromagnetic and magnetic fields causing resonant phenomena," *SPQEO*, vol. 22, pp. 39-46, [2019].
- [6] G. Bekefi *Radiation Processes in Plasmas*. Wiley, New York-London-Sydney, 1966.
- [7] G.V. Milenin, R.A. Redko, "Radiative recombination in III-V semiconductors compounds and their surface morphology transformations due to treatments in weak magnetic fields," *Journal of Luminescence*, vol. 216, pp. 116678, [2019].

**MATHEMATICAL MODELING AND  
TECHNOLOGIES IN NANOELECTRONICS**

# Numerical simulation of the field distribution of a resonator coaxial probe for scanning microwave microscopy

<sup>+</sup>Yu.Ye. Gordienko, <sup>\*</sup>M.I. Slipchenko, <sup>+</sup>I.M. Shcherban

<sup>+</sup>Kharkiv National University of Radio Electronics

61166, Kharkiv National University of Radio Electronics, tel. (057) 702-13-62 E-mail: ihor.shcherban@nure.ua

<sup>\*</sup> Institute for Scintillation Materials NAS of Ukraine

Naukovets ave. 60, 61072, Kharkiv, Ukraine, E-mail: naukovets.big@gmail.com,

**Abstract** — The report presents the results of a study of the electrodynamic properties of resonator probes with a coaxial aperture, developed for local microwave diagnostics of various objects. In particular, the influence of the gap in the probe-object system, the size and shape of the tip on the field distribution of a classical quarter-wave resonator measuring transducer is analyzed. The results of a study of the field distribution of a probe with a tunable sensitivity by changing the position of the tip end relative to the plane of the aperture are presented. The dependence of the field distribution on the displacement of the tip in such a probe has been established. The prospects for organizing scanning over the depth of layered objects by a sensor with tunable sensitivity are discussed.

**Keywords** — electrodynamic properties, local microwave diagnostics, tunable sensitivity, quarter-wave resonator, field distribution, resonator probes, near-field, evanescent electromagnetic field.

## I. INTRODUCTION

Scanning microwave microscopy (SMM) is gaining wider interest in the technology and study of functional devices in nanoelectronics. Its development requires a detailed, including theoretical study of the electrodynamic processes that form the scanning signals. The resolution and contrast in the SMM are primarily determined by the field distribution of the scanning probe. The main feature of local microwave diagnostics in general and scanning microwave microscopy (SMM) in particular is the near-field nature of the interaction of a microwave sensor with an object [1]. The electromagnetic field arising in the resonator and exiting through the subwavelength aperture is usually called evanescent. Evanescent electromagnetic fields are rapidly decaying or exponentially decaying electromagnetic fields. The study of the distribution of the electromagnetic field, as well as its changes under the influence of various factors, is the main task in the analysis of the electrodynamic properties of resonator measuring transducers (RMT). And they, in turn, determine the type of conversion characteristics of resonator probes (RP). The study of the distribution of the evanescent field is theoretical, since in practice we are already dealing with signals that are determined both by the properties of the object and the electrodynamic properties of the RMT. At the moment, field distributions are mainly obtained by modeling the probe-object system in software packages based on solving the Maxwell system of equations by the finite element or finite difference method [2]. At the dawn of the formation of SMM, analytical models were

mainly used to model the processes of interaction between the probe and the object [3, 4]. However, it should be noted that the existing theoretical models, despite the cumbersome nature of their analytical description, as well as the complexity of the calculation, are extremely imprecise and idealized. Therefore, the field distribution in a quantitative representation has not been practically investigated.

The aim of this work is to study the electrodynamic properties of resonator probes by establishing theoretical dependences of the field distribution in their aperture part.

## II. MAIN PART

The main physical and technical element in local microwave diagnostics and SMM is the probe. Our research is based on the use of a resonator probe with a coaxial measuring aperture (RPCA). It is shown schematically in Fig. 1 in interaction with an object.

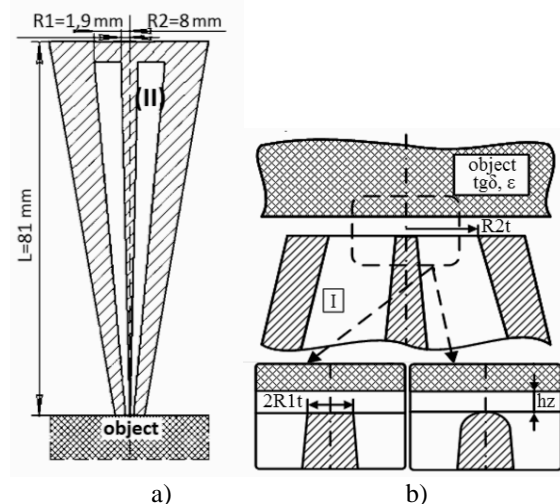


Fig. 1 – a) Schematic representation of a classic quarter-wave RPCA; b) schematic representation of the aperture assembly

Based on the results of numerous studies, it can be concluded that the geometry of the aperture-forming region (I) is practically independent of the electrodynamic properties of the storage region (II), which almost unambiguously determines the spatial distribution of the probe microwave field in the object. As shown in a number of works, the evanescent field penetrates into the object to a depth approximately equal to the radius of the probe tip [4]. The electrodynamic

properties and structure of the object affect the sounding depth practically only within the limits of the existence of the evanescence of the field distribution. This is clearly demonstrated by the dependences shown in Fig. 2.

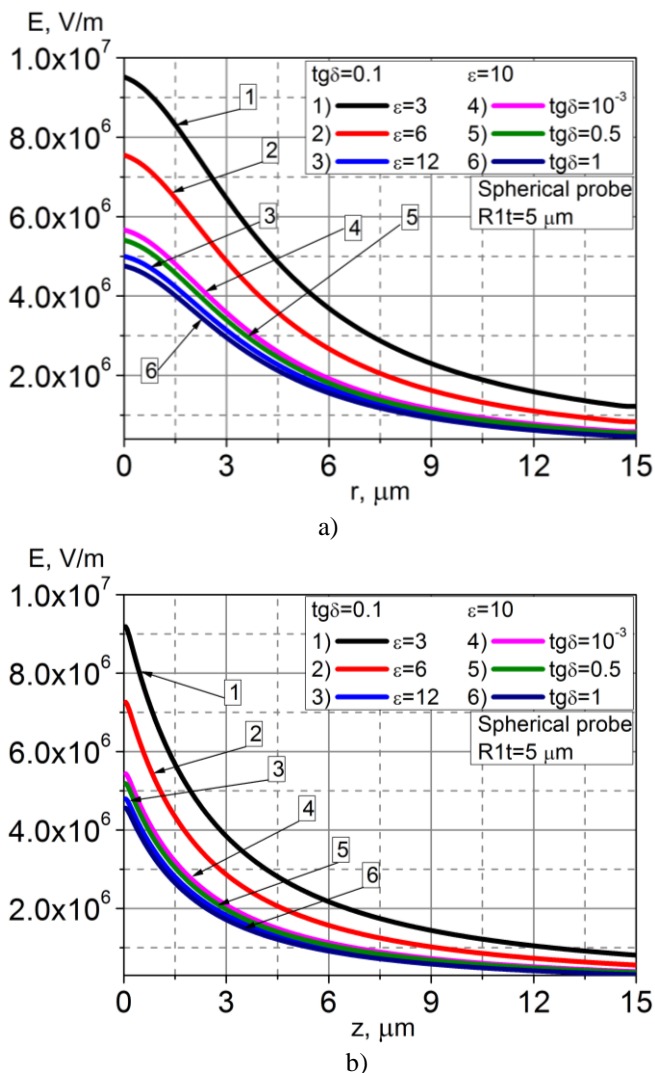


Fig. 2 – Distribution of the field over the surface (a) and over depth (b) depending on the electrodynamic parameters of the object

Also, as shown in our works, the field distribution strongly depends on the size and shape of the probe tip and the air gap between the tip and the object [5, 6]. Thus, it can be concluded that only the geometry of the aperture unit affects the distribution of the evanescent field. And various changes in the geometry of the aperture unit have a significant effect on the field distribution. Therefore, further we focus on the study of the geometry of the aperture-forming region of the probe.

Fig. 3 shows the field distribution, depending on the size and shape of the tip, obtained by solving the system of Maxwell's equations by the finite element method. The indicated solutions were found using standard packages based on the finite element method [7]. All studies were carried out for an operating frequency of 10 GHz and an object with  $\text{tg}\delta=0.1$ ,  $\epsilon=20$ .

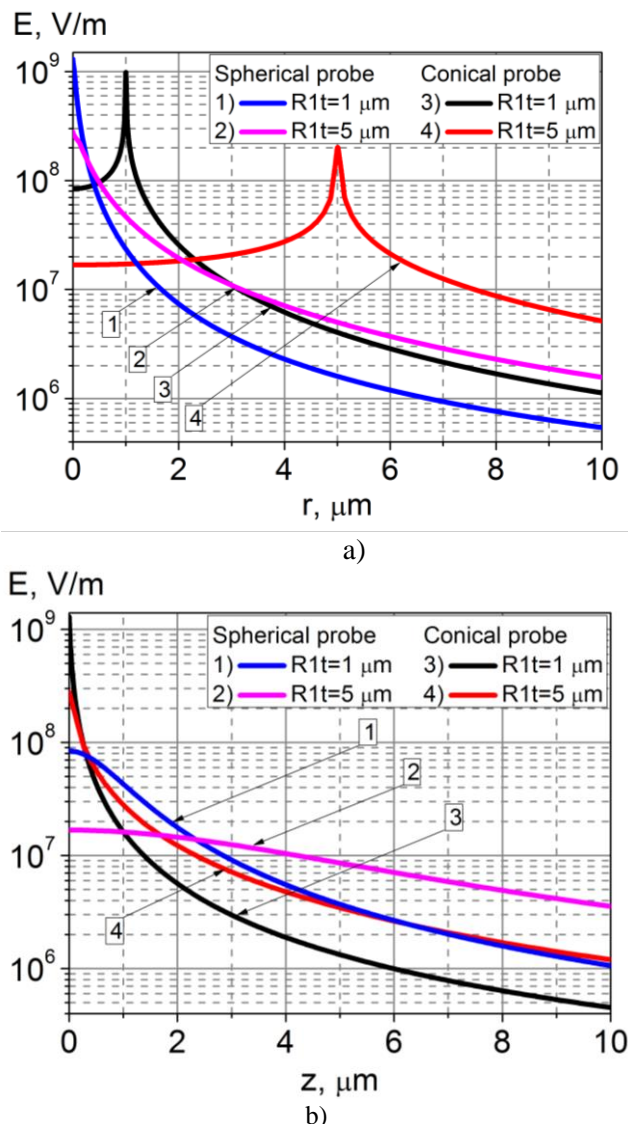


Fig. 3 – Distribution of the field over the surface (a) and over the depth (b) at different R1t for the spherical and conical shape of the tip

It can be seen from the given dependences that when a spherical tip is used, the field strength is maximum at the point closest to the tip. When using a truncated cone tip, there are two extrema, with their maxima located at the periphery. The so-called tubularity of the field takes place. It is characteristic of the studied tip shapes that with a decrease in the tip radius, the field strength increases, the so-called lightning rod effect. However, upon a detailed examination of the presented dependences, one can see that with an increase in the radius of the tip, the steepness of the decay of the field strength becomes not so strong, and the character of the decay smoothly changes from exponential to quasi-linear.

Also, the air gap in the probe-object system should be attributed to the factors influencing the geometry of the aperture assembly. The influence of the gap between the tip and the object on the response of measuring signals has been shown in many works on the SMM. However, the influence of the gap on the field distribution was not considered in full, but only fragmentarily in a few works [3, 4]. Fig. 4 shows the field distribution of an aperture coaxial probe with a spherical tip as a function of the gap size.

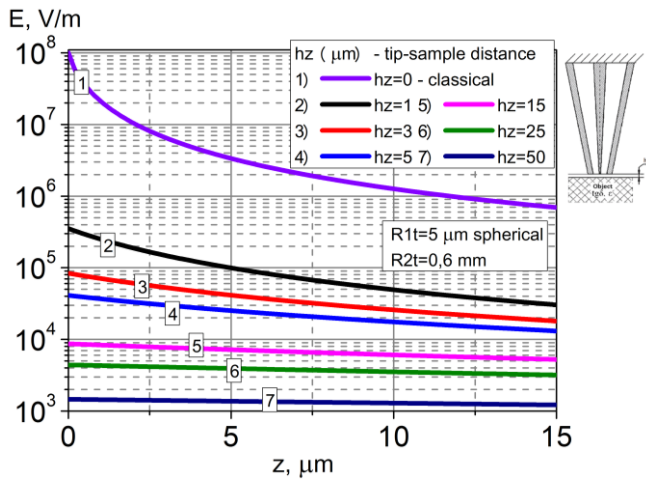


Fig. 4 – Depth distribution of the field at different values of the gap

From the presented dependences, it is primarily seen that the presence of an air gap significantly reduces the field strength in the object. This leads to a decrease in the sensitivity of the sensor and a decrease in the amplitude of the measurement information signals. As mentioned in our work [6] the gap can be used as a tool for changing the sensitivity of the sensor. But, since its value is often determined by rather approximate methods, the results obtained turn out to be very poorly reproducible. An alternative to such a tool for expanding the sensitivity of the probe, as shown in our works, can be a resonator with a displaceable tip relative to the aperture plane [6, 8]. The measurement range of the electrophysical parameters of objects of the classical quarter-wave RP is in the range  $\epsilon$ : 1-15,  $\text{tg}\delta$ : 0.001-0.1. The use of a RMT with a retractable probe-forming central conductor makes it possible to measure  $\epsilon$  in the range 1-60, and  $\text{tg}\delta$  from 0.0001 to 2. A schematic representation of such a probe with possible operating modes is shown in Fig. 5. As shown in our works [6, 8] the most effective range of change in the position of the needle is limited, first of all, by the sensitivity of the sensor and is on the order of several values of the radius of the needle, both when moving out of the resonator and when immersed in it. However, as shown in [9], when the probe tip extends beyond the plane of the aperture by a value exceeding ten times or more the value of  $R1t$ , the sensor starts to emit and goes into monopole antenna mode.

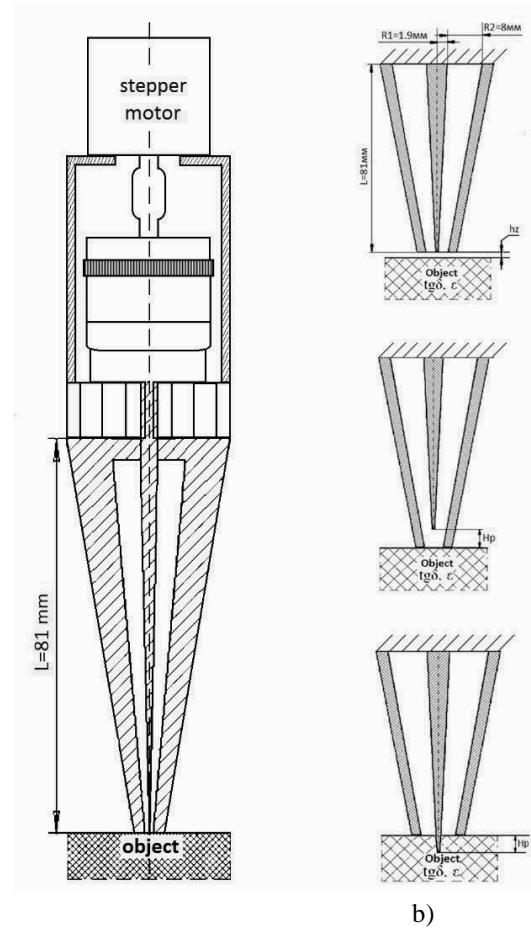


Fig. 5 – a) Schematic representation of a RMT with a retractable tip; b) main operating modes of a RP

Fig.6 shows the distribution of the field over the depth of such a RP at different positions of the tip relative to the aperture.

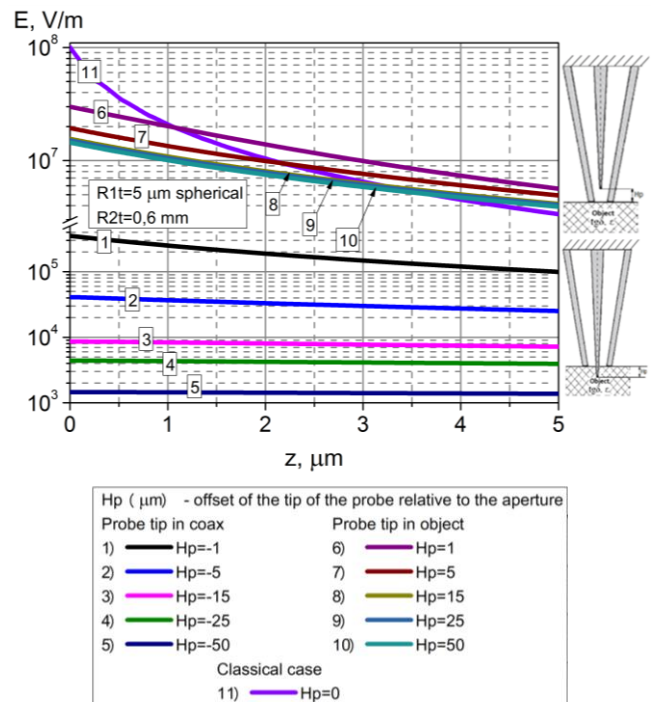


Fig. 6 – Distribution of the field over the depth of the tunable RP at different positions of the tip relative to the aperture

It can be seen from the presented dependences that the maximum achievable field strength for a spherical tip is retained below the center and strongly depends on the position of the tip. As expected, the field strength increases when the tip moves into the object under study, and decreases when immersed in the resonator. However, as you can see, the field strength with the classical coplanar position of the tip is still higher than with other variations in the displacement, but only on the surface of the object. A similar picture is observed with a decrease in the radius of the tip of the probe. Apparently, the evanescence of the field worsens not only with an increase in the radius of the tip, but also with a departure from coplanarity in such a probe.

Thus, the presented dependences convince of the possibility of organizing microscanning of objects in depth, using a resonator probe with an adjustable sensitivity.

### III. CONCLUSIONS

As a result of the numerical studies of the field distribution in the aperture part of the coaxial resonator probes, the following provisions were established:

- With an increase in the radius of the probe tip, a slight violation of the evanescence of the field is observed. This is expressed, first of all, by the fact that the steepness of the decrease in the field strength with depth becomes smoother, and the form of the dependence itself smoothly passes from exponential to quasilinear.

- The gap between the probe and the object not only significantly reduces the energy of the field in the object, but also the locality.

- Using a coaxial resonator with a moving center conductor as a sensitivity control tool is preferable to a gap when using classic quarter-wave RMT.

- The dependence of the field energy on the position of the probe tip relative to the aperture can be used as a key aspect when scanning objects inhomogeneous in depth.

### REFERENCES

- [1] T. Mitch Wallis and Pavel Kabos, "Measurement Techniques for Radio Frequency Nanoelectronics", Cambridge University Press, 2017, 314 p.
- [2] B.-Y. Wu, X.-Q. Sheng, R. Fabregas, and Y. Hao, "Full-wave modeling of broadband near field scanning microwave microscopy", *Sci. Rep.*, vol. 7, no. 1, 2017, pp.1-10.
- [3] Gao and X.-D. Xiang, "Quantitative microwave near-field microscopy of dielectric properties", *Rev. Sci. Instrum.*, Vol. 69, No. 11, 1998, pp. 3846-3851.
- [4] Imtiaz and S. M. Anlage, "Effect of tip geometry on contrast and spatial resolution of the near-field microwave microscope", *Journal of Applied Physics*, Vol. 100., 2006, pp. 1-8.
- [5] Yu.E. Gordienko, S.U. Larkin and A.M. Prokaza, "Quantitative estimation of physical processes at a contactless scanning microwave microscopy", *Telecommunications and Radio Engineering*, Vol.71, №12, 2012, pp.1115-1123.
- [6] Gordienko Yu.Ye., Shcherban I.M. and Levchenko A.V. "Principles of universalization of microwave facilities for diagnostics of small-scale objects", *Telecommunication and Radio Engineering*, Vol. 75, № 14, 2016, pp. 1313-1320.
- [7] Bate K.-Yu., "Finite element methods", M.: Fizmatlit, 2010, 1024 p.
- [8] Gordienko Yu.Ye., Shcherban I.M., "Diapason properties of resonant aperture sensors for microwave diagnostics of small objects", *Telecommunication and Radio Engineering*, Vol. 79, № 9, 2020, pp. 793-801.
- [9] L.F. Chen, C.K. Ong, C.P. Neo, V.V. Varadan, V.k. Varadan, "Microwave Electronics: Measurement and Materials Characterization", John Willy & Sons, Ltd, 2004. - 537 p.

# Simulation of Parameters of Frequency Selective Surface in Microwave Band

Mayboroda D.V.\*, Pogarsky S.A. \*

\*V.N. Karazin Kharkiv National University  
 4, sq. Svobody, 61022, Kharkiv, Ukraine  
 +38(057)707-52-78, shfmayboroda@gmail.com

**Abstract** — The paper presents the results of numerical simulations of the electrodynamic characteristics of a cell of an infinite 2D frequency-selective surface (FSS) with the topology of the structural element of the  $\Psi$  form. The simulation was performed as part of the Finite Element Method (FEM) using the ANSOFT HFSS software product. The results obtained make it possible to predict the possibility of creating highly efficient frequency-selective surfaces using the proposed key element topology.

**Keywords**—frequency-selective surface, cell, patch, topology

## I. INTRODUCTION

The operation of frequency selection is one of the most important in any microwave radio system. A relatively new way of performing frequency selection is the spatial selection method. It is carried out using the so-called frequency-selective surfaces (FSS), also called spatial filters. Such elements have dispersive transmission and / or reflection characteristics. In the microwave range, FSSs are periodic arrays of the same type of metal elements located on a dielectric substrate. Depending on the assigned technical tasks and methods for their implementation, both 1D and 2D arrangement of elements on the substrate can be used.

FSS have a number of significant advantages in comparison with the well-known classical elements of frequency selection. Among them, one can indicate low profile, the ability to use structures with a limited number in periodic sequences of elements, the ability to work with arbitrary polarization of signals, angular stability, multi-frequency sufficiently high attenuation outside the working bands, and the possibility of using lithography methods, which greatly simplifies and reduces the cost of production.

Because of their advantages, FSSs are quite widely used in practical applications: reflector antennas [1], dichroic sub-reflectors [2], radio identification systems (RFID) [3], lenses antennas [4], systems protection from electromagnetic interference [5].

In this paper, we present the results of modeling the basic electrodynamic characteristics of a cell of an infinite 2D FSS with the topology of the structural element of the  $\Psi$  form.

## II. STRUCTURE UNDER STUDY

We will consider the electrodynamic structure, which is a cell of an infinitely 2D structure of the  $\Psi$  shape. A view of the structural element with the notations is shown in Fig. 1.

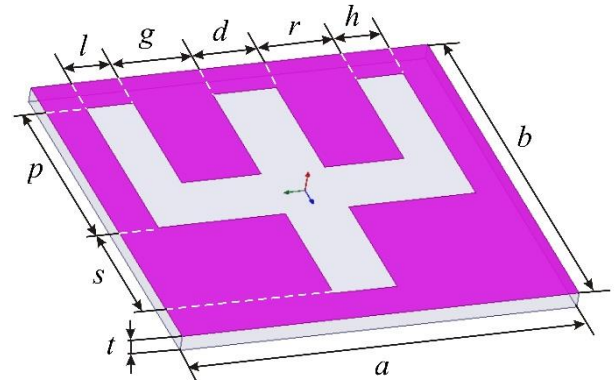


Fig.1. The view of the structure.

Table 1 presents the geometric dimensions of the topological elements of the structure.

TABLE 1. SIZES OF STRUCTURAL ELEMENTS

Parameter	Value	Parameter	Value
a	12.5 mm	g	2.5 mm
b	12.5 mm	d	2 mm
p	6 mm	r	2.5 mm
s	4 mm	h	1.5 mm
l	1.5 mm	t	var

Two structural parameters, namely, the thickness of the substrate  $t$  and the relative dielectric constant of the substrate  $\epsilon_r$ , are variable.

It should be noted that the topology of the basic element of the structure itself is quite complex, and all functional dependencies are multi-parameter. For this reason, the development of a rigorous electrodynamic solution that would allow us to analyze the dependences on all parameters is practically impossible. Simulation of parameters was performed numerically using the finite element method (FEM) implemented in the ANSOFT HFSS software.

### III. THE RESULTS OF SIMULATIONS

The structure under consideration is complex compositional, and the dependencies describing its properties are complex parametric. One of the most important parameters in this sense is the thickness of the dielectric substrate and the value of relative permittivity.

In Fig. 2 the curves show the dependences of the modulus of the reflection coefficient  $|S_{11}|$  via frequency at the fixed value  $\epsilon_r = 2.2$  and variations in the thickness of the substrate from 0.4 mm to 0.7 mm.

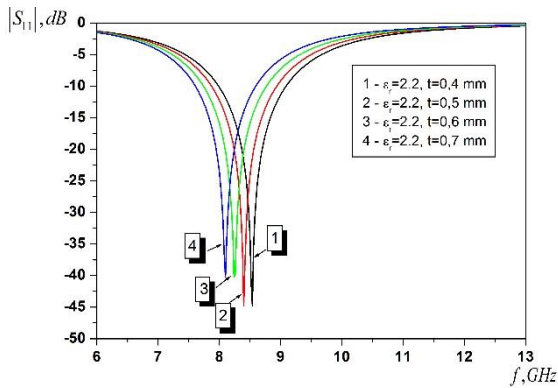


Fig. 2. The dependences of  $|S_{11}|$  via frequency with variation of  $t$ .

A change in thickness in this interval leads to a shift in the resonance absorption frequency towards lower frequencies by  $\Delta F \approx 500 \text{ MHz}$ . All curves are smooth with a fairly high level of steepness. If one concentrates on the magnitude of the return loss of -10 dB (at the level of  $\text{VSWR} \approx 2$ ), the matching bandwidth is 900 MHz. For all the dependencies, the steepness level is approximately the same and reaches a value of 0.038 dB / MHz.

The dependences  $|S_{11}|$  for a fixed value  $t = 0.5 \text{ mm}$  and for a variation in the values of relative permittivity  $\epsilon_r$  as a function of frequency are quite predictable (Fig. 3). With increasing  $\epsilon_r$  values, the peaks of the resonance curves shift to a lower frequency region. The magnitude of the maximum displacement is  $\Delta F \approx 1.93 \text{ GHz}$ . In this case, the curves remain smooth, the steepness of the fronts does not fundamentally change. However, with increasing  $\epsilon_r$  values, the level of return losses decreases.

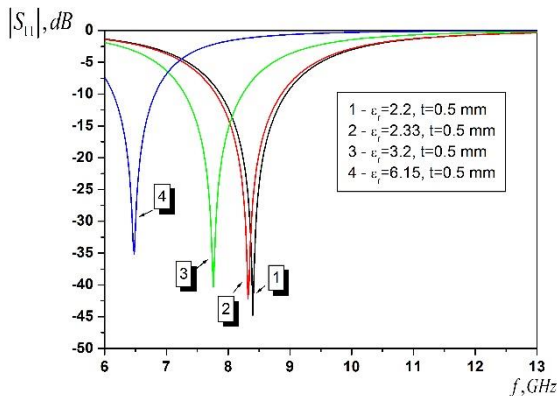


Fig. 3. The dependences of  $|S_{11}|$  via frequency with variation  $\epsilon_r$ .

Another important characteristic of any frequency-selective surface is the degree of its transparency (or transmission coefficient  $|S_{21}|$ ). In Fig. 4 one can find the cell dependences of  $|S_{21}|$  at the fixed value  $\epsilon_r = 2.2$  and variation of the substrate thickness  $t$  in the frequency range under consideration.

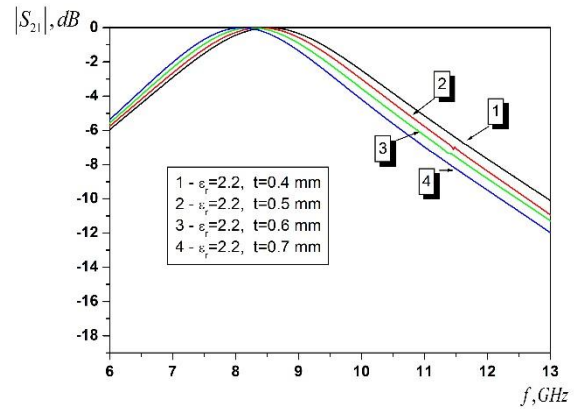


Fig. 4. The dependences of  $|S_{21}|$  via frequency with variation  $t$ .

When comparing the dependences for the reflection coefficients  $|S_{11}|$  in Fig. 2,3 and transmission coefficients  $|S_{21}|$  in Fig. 4, it is necessary to note the following features. The dependences for  $|S_{11}|$  are of a pronounced resonance character with rather high values of the return losses at the resonance frequencies. Dependencies  $|S_{21}|$  have a completely "blurry" look. So, the bandwidth within which the surface transparency does not fall below the value -3 dB is more than 2.89 GHz. With increasing frequency, the transparency of the surface decreases significantly. Near the end of the frequency range, it does not exceed -12 dB.

With a symmetrical patch placement with the same topology on the back (free) side of the substrate, significant changes occur during the interaction of the incident wave and the element of the frequency-selective surface. In Fig. 5 the dependences of  $|S_{11}|$  via the frequency for a fixed thickness of the substrate  $t$  and the variation of  $\epsilon_r$  values are shown.

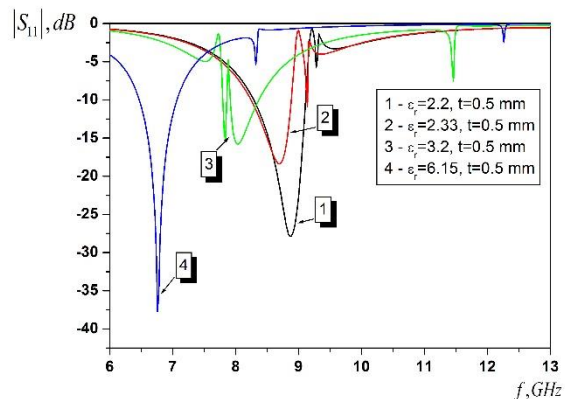


Fig.5. The dependences of  $|S_{11}|$  via frequency with variation  $\epsilon_r$ .

It is evident that frequency dependencies with variations of relative dielectric constants are more complex and ambiguous.

For small values of the relative permittivity  $\epsilon_r = 2.2$ , there is no additional parasitic resonances in the structure (or they are very insignificant). As the values increase to 2.33 ... 3.2, the resonance phenomena increase significantly. At the value  $\epsilon_r = 3.2$ , significant resonance phenomena appear immediately in two frequency ranges. Moreover, in the frequency range from 7.45 to 8.73 GHz, they turn out to be significant. In this case, the return loss is significantly reduced. At the same time, the level of matching remains at an acceptable level (with the exception of single frequencies). With a further increase in the value of  $\epsilon_r$ , noticeable changes in the characteristic occur. Firstly, the maximum is significantly shifted to the low-frequency region (more than 2 GHz). Secondly, the level of return losses increases significantly (from -15 ... -20 to -37 dB). And finally, the observed level of parasitic resonances does not exceed -3 dB.

Bilateral placement of structural elements leads to significant changes in the dependences  $|S_{21}|$  via frequency when the values  $\epsilon_r$  vary. The corresponding dependences are shown in Fig. 6.

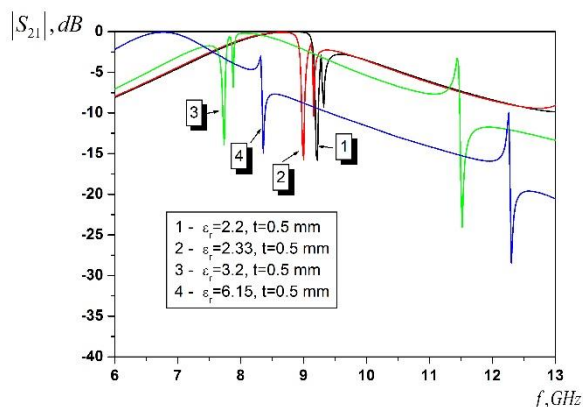


Fig.6. The dependences of  $|S_{21}|$  via frequency with variation  $\epsilon_r$ .

Comparison of dependencies in Fig. 4 and Fig. 6 indicates the appearance of additional resonances in the structure due to both resonances between the topological elements and the presence of two-sided shielding. This is evidenced by abrupt changes in the amplitude  $|S_{21}|$  near certain frequencies. At the same frequencies, an abrupt change in the phases of oscillations occurs. With small changes in the values of  $\epsilon_r$ , a relatively small shift of the minima of the transmission coefficients to the low-frequency region occurs. The offset does not exceed the value  $\Delta F \approx 210$  MHz. With increasing values of  $\epsilon_r$  in the characteristics, resonances associated with two-sided

shielding prevail. One group is in the low-frequency region, and the second group is in the high-frequency region. At the same time, with increasing frequency, a significant decrease in the transparency of the structure is observed (the coefficient  $|S_{21}|$  reaches values of -23.86 ... -28.36 dB). The transparency bands of the structure turn out to be substantially offset from each other, and they turn out to be substantially narrower. At the same time, in the characteristics (with values of  $\epsilon_r = 3.2$  and  $\epsilon_r = 6.15$ ), quite wide frequency ranges are observed, within which the value  $|S_{21}|$  varies quite smoothly (in the band from 8.56 GHz to 11.98 GHz, the coefficient varies in the range from -7.4 dB to -16 dB).

#### IV. CONCLUSIONS

Thus, the presented results of numerical simulation of the electrodynamic characteristics of a cell of an infinite 2D FSS with the  $\Psi$  topology of the structural element of the species showed the possibility of spatial frequency selection. It has been established that two types of resonances can occur in the structure, associated both with the ratio of the geometric dimensions of the structural element and with the presence of two-sided shielding. The influence of the thickness of the dielectric substrate and the dielectric constant on the reflection and transmission coefficients is studied. The totality of the results allows us to predict the creation of sufficiently technologically advanced and highly efficient frequency-selective surfaces in the microwave range.

#### ACKNOWLEDGMENT

This work was supported by Ministry of Education and Science of Ukraine (grants 0219U003518, 0118U002038).

#### REFERENCES

- [1] J.Arnaud, and F.Pelow, "Resonant-grid quasi-optical diplexers", Bell Syst. Tech. J., 1975, vol. 54, pp. 263–283.
- [2] S.Agahi, and R.Mitra, "Design of a cascaded frequency selective surface as a dichroic subreflector", In Proceedings of the Antennas and Propagation Society International Symposium: AP-S Merging Technologies for the 90' (Digest), Dallas, TX, USA, 7–11 May 1990; pp. 88–91.
- [3] F.Costa, S.Genovesi, A.Monorchio, and G.Manara, "A robust differential-amplitude codification for chipless RFID". IEEE Microw. Wirel. Compon. Lett., 2015, vol. 25, pp. 832–834.
- [4] Pozar, "Flat lens antenna concept using aperture coupled microstrip patches", Electron. Lett., 1996, vol. 32, pp. 2109–2111.
- [5] D.Li, T.-W.Li, E.-P.Li, and Y.-J.Zhang, "A 2.5-D Angularly Stable Frequency Selective Surface Using Via-Based Structure for 5G EMI Shielding", IEEE Trans. Electromagn. Compat., 2018, vol. 60, pp. 768–775.

# Problems of solar cell simulation

Aleksandr Galat\*, Aleksandr Sliusarenko\*

\* Kharkiv National University of Radio Electronics, Department of Microelectronics, Electronic Devices and Appliances

Kharkiv, Nauky ave. 14 / 61166/ Kharkiv / Ukraine /(+38) 057-702-13-62 / oleksandr.galat@nure.ua

**Abstract** — The present work is devoted to comparing various approaches to simulation the solar photovoltaic modules characteristics in order to determine the adequacy of a particular method in solving the problem of optimizing the structure and configuration of multilayer solar cell. As options, analytical methods for modeling the absorption capacity of multilayer structures of photovoltaic modules are considered, which allow one to evaluate the efficiency of absorption of sunlight, analytical models of current-voltage characteristics, complex programs for calculating the parameters of photovoltaic modules, combining analytical and numerical methods. The calculation results for the ZnO / CdS /  $\text{CuIn}_x\text{Ga}_{1-x}\text{Se}_2$  structure are presented, which make it possible to judge the possibilities and disadvantages of certain methods.

**Keywords** — solar cells, multilayer structure, characteristics, analytical methods, configuration

## I. INTRODUCTION

Recent years in the study of solar cells showed a significant increase in the number of experimental works, which presents mainly the results of the evaluation of the efficiency of solar photovoltaics [1]. Reducing the cost of production of different types of solar panels have led to increased interest in the devices of the second, third and fourth generations, including multi-layer, tandem, with a complex structure. However, for such configurations, the problem of optimizing the design is especially important, and the number of parameters determining the efficiency increase.

On the other hand significant progress in the development of mathematical modeling of characteristics of the solar inverters embodied in the emergence of powerful software tools to calculate the optical and electrical parameters of a wide range of configurations of such structures. These include software AMPS-1D [2], SCAPS [3], gpvdm [4]. This is because experiments in the field of the formation of structures of solar cells require more accurate predictions about the composition of materials, thickness of active layers, the design of contact pads formed structures [5, 6].

As for the materials of solar cells, the main focus of the developers is on perovskite-based structures [6, 7], although interest in  $\text{CuIn}_x\text{Ga}_{1-x}\text{Se}_2$ , CdTe, polymer is not reduced [4, 5]. The developers have achieved a significant increase of performance efficiency. The structure on the basis of perovskite is quite simple to manufacture. In their tandem construction with Si the structure and layers technology is particularly important. The version with four contacts is actually two individual elements arranged one above the other. Every element is optimized in a specific spectral range, but draining the current require conductive layers,

which leads to an increase in the number of boundaries between layers and, consequently, growth of the reflected radiation flux. If you use the minimum number of contacts, the number of interlayer boundaries, and the reflection will be minimal. In this case, it is necessary to accurately calculate the structure of the active layers so that the current flowing through each layer is the same. Otherwise, we have the inevitable losses.

At the same time, software tools, despite the wide possibilities of realization of mathematical models have their limitations. These limitations are revealed when comparing with experimental data, which is also not always possible to unambiguously interpret. You must take into account the difference of the levels of technology, conditions for the formation of active layers of solar cells, the quality of the materials, and means of measurement and more. An assessment of the adequacy of the modeling may be performed by comparing the results of calculations using analytical and numerical methods implemented in different software tools.

## II. THE MAIN GOALS AND OBJECTIVES

The present work is devoted to comparing various approaches in modeling the characteristics of solar photovoltaic modules. The main goal is to determine the convenience and universality of a particular method in solving the problem of optimizing the structure and configuration of multilayer solar cells. Analytical methods for modeling the absorption capacity of multilayer photovoltaic structures are considered and used. They allow us to evaluate the efficiency of absorption of sunlight, to obtain the maximum theoretical efficiency Analytical models of current-voltage characteristics, complex programs for calculating the parameters of photovoltaic modules, combining analytical and numerical methods (for example gpvdm [4]) are also considered.

Calculations of the absorption capacity of the structure make it possible to determine the maximum theoretical efficiency of the photovoltaic module structure. According to the classical definition maximum theoretical efficiency is the ratio of the net power (in this case absorbed) to the incident power on the photoconverter (light input). Of course, not all absorbed power is converted into electrical power, part will go into losses (thermal, radiative, etc.). However, at the first stage, it is necessary to achieve the maximum (ideally 100%) absorption of solar radiation by the material of the photoconverter. And here, analytical calculations of the absorption capacity can help in the synthesis of the optimal sequence and layer thickness of the active part of the solar cell [5]. And only after that it is

worth solving the problem of determining the power of losses and its minimization.

### III. CALCULATIONS OF THE ULTIMATE THEORETICAL EFFICIENCY OF A SOLAR CELL

In the calculations below, it was taken into account that the total spectral absorption range of the above materials lies in the range 300 ... 1400 nm. The lower limit is determined by the "cutoff" of the standard spectrum of AM1.5, the upper one is determined by the sensitivity of the CIGS layer. The spectrum of the incident radiation was taken into account in the range 300 ... 2500 nm. It was this range that was the basis for determining the power of the solar radiation flux (more than 99% of the AM1.5 spectrum). The range was divided into  $n$  subbands (to ensure sufficient calculation accuracy  $n > 30$ , the width of the spectral subband  $\Delta\lambda$  varied depending on the smoothness of the power density distribution functions and the optical absorption coefficients of the structure layers.

Below are the calculation results for the ZnO / CdS / CIGS structure. The composition of the CIGS layer was selected according to the recommendations [3 ... 5], based on the presented calculations of efficiency. The ratio of the material components is chosen so that the band gap is 1.2 eV..

Figure 1 shows the dependence of the absorbing ability of the investigated structure (A3) on the CIGS layer thickness ( $x$ ) in the range 1 ... 10000 nm. Layer thickness: ZnO - 20 nm, CdS - 50 nm (d21) and 100 nm (d22). As can be seen from the graphs up to a thickness of 10 nm, the main absorption is due to the buffer layer of CdS - about 6%. With an increase in the CIGS thickness from 10 to 1000 nm, the absorption rapidly increases to 63%, and then the growth slows down sharply.

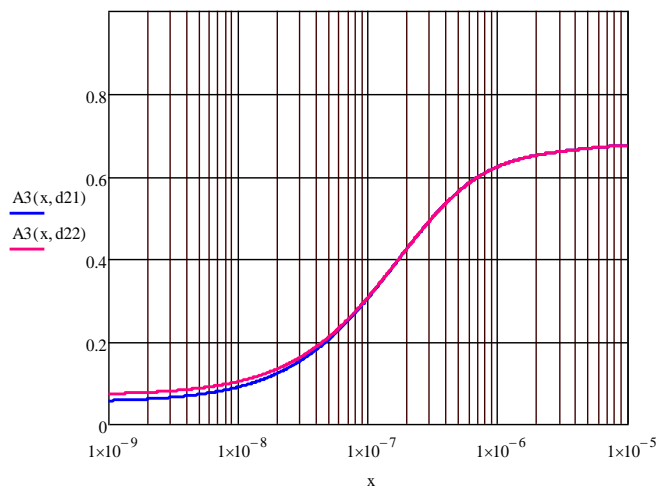


Fig. 1. The dependence of the structure absorbing ability on the CIGS layer thickness

Figure 2 shows the dependence of the absorbing ability of the investigated structure (A3) on the CdS layer thickness ( $x$ ) in the range 1 ... 10000 nm. Layer thickness: ZnO - 20 nm, CIGS - 1 nm (d11), 10 nm (d12), 100 nm (d13), 1000 nm (d14), 10000 nm (d15). As can be seen from the graphs up to a thickness of 10 nm of the CIGS layer we have a strong influence of CdS layer thickness on absorption. With an increase in the CIGS thickness above 100 nm, the role of the CdS layer in absorption decreases to zero.

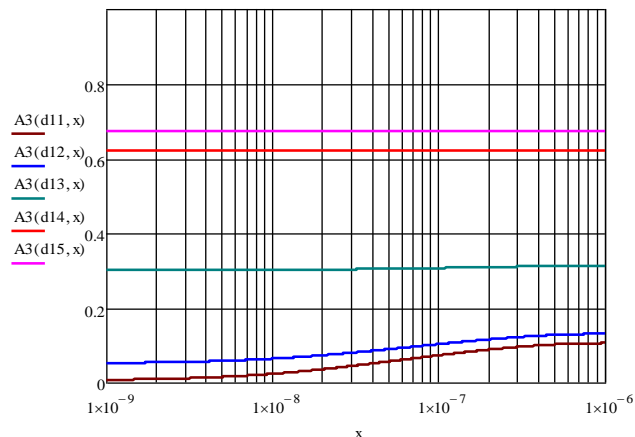


Fig. 2 The dependence of the absorbing ability of structure on the CdS layer thickness

Thus, the calculation of the total absorption of this structure allows us to draw the following conclusions: the most effective increase in the thickness of the CIGS layer is up to 1  $\mu\text{m}$  (maximum up to 4  $\mu\text{m}$ ), in the range of 4 ... 10  $\mu\text{m}$ , the increase in absorption (1 ... 2%) does not justify a multiple increase in the layer thickness. As for the CdS layer, it is not suitable for the role of an active absorber, capturing no more than 10% of sunlight even at a thickness of 10  $\mu\text{m}$ .

### IV. USING UNIVERSAL SOLAR CELL CALCULATION PROGRAMS

Working with universal programs for calculating solar cells (AMPS-1D [2], SCAPS [3], gpvdm [4]) requires a deep acquaintance with the features of preliminary preparation of these programs for calculating a specific structure, the correct choice of elements of the calculation method, and correct input of the initial data. Universal programs usually include ready-made examples for the simplest cases. However, the reliability of the results obtained strongly depends on the depth of understanding of the program, knowledge of its applicability limits, and correct assessment of the results.

As an example, let us cite the results of modeling the structure of the solar photoconverter considered above and using the gpvdm program [4], which is currently in the public domain. For the convenience of comparing the results of the simulation, the configuration of the photoconverter was selected, similar to that described in Section 3. The size and material of the structure layers: the upper contact layer — Al (grid) — 10 nm, the ZnO window — 20 nm, the CdS buffer layer — 50 nm, and the main active CIGS layer with  $W_g = 1.2 \text{ eV} - 62 \dots 4000 \text{ nm}$ , the lower contact layer - Al - 10nm.

The calculation results for thin active layers are shown in Table 1. The dynamics of the change in the results generally corresponds to the results of the analytical calculation of the absorption capacity (Fig. 1). But there are differences. For example, according to Table 1, with an increase in the thickness of the CIGS layer from 125 to 250 nm, the structural efficiency ( $\eta$ ) increased 5-fold (from 0.28 to 1.53%), although according to the results of analytical calculations, the radiation absorption increased from about 35% to 45%, that is, 30%.

TABLE 1. THE MAIN STRUCTURAL PARAMETERS CALCULATED BY GPVDM FOR A SMALL THICKNESS OF THE CIGS LAYER

Parameter	Example		
	1	2	3
d1, nm	62	125	250
FF	0.051988	0.124946	0.616374
$\eta$ , %	0.016181	0.283891	1.532246
Pmax, W/m <sup>2</sup>	0.161812	2.838913	15.322462
Voc, V	1.239383	1.192098	1.134410
Jsc, A/m <sup>2</sup>	-2.511313e+000	-1.905979e+001	-2.191362e+001
Jpmax, A/m <sup>2</sup>	-8.103744e-001	-1.462218e+001	-1.934010e+001
Vpmax, V	1.996759e-001	1.941511e-001	7.922640e-001

The calculation results for thicker active layers are shown in table 2. Here we see a decrease in efficiency structures with increasing thickness, which obviously reflects a sharp decrease in the number of current carriers reaching the contacts. Maximum efficiency corresponds to a CIGS layer thickness of about 250 – 500 nm. The calculation data are far from the best experimental results of measuring the effectiveness of such structures. This may be the result of, for example, inaccurate input of initial data, setting mathematical calculation parameters, and other factors.

TABLE 2. THE MAIN STRUCTURAL PARAMETERS CALCULATED BY GPVDM FOR LARGE CIGS LAYER THICKNESS

Parameter	Example		
	4	5	6
d1, nm	500	1000	2000
FF	0.795168	0.617908	0.260506
$\eta$ , %	1.009523	0.855279	0.287788
Pmax, W/m <sup>2</sup>	10.095234	8.552794	2.877877
Voc, V	1.034291	0.816699	0.594887
Jsc, A/m <sup>2</sup>	-1.227481e+001	-1.694815e+001	-1.857038e+001
Jpmax, A/m <sup>2</sup>	-1.127341e+001	-1.230480e+001	-1.482920e+001
Vpmax, V	8.954906e-001	6.950781e-001	1.940683e-001

In fig. Figure 3 shows the current-voltage characteristic of the photoconverter for the case with maximum efficiency (Example 4). Judging by the figure, the form of the characteristic really indicates a high filling factor (0.795), but the calculated efficiency is too low (1%). For example 3, it is higher (1.5%), although the filling factor is 0.616. It is also necessary to note the insufficient smoothness of the characteristic, which is obviously connected with a large step of the voltage change during the calculation.

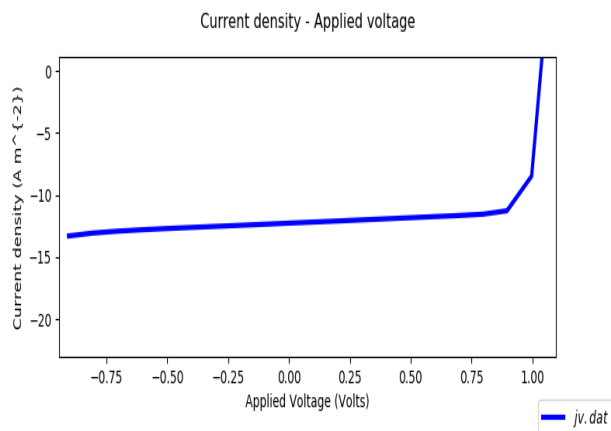


Fig. 3 The dependence of the photoconverter current density on the applied voltage for the structure with maximum efficiency

## V. CONCLUSIONS

Comparison of the calculation results with the known data made using the AMPS-1D program [4] for a similar configuration of the solar converter indicates that the results differ, sometimes quite significantly. It should be borne in mind that various values of the same electrophysical parameter of materials used in the structure of solar converters are given in the literature. The values of the parameters differ due to the difference in the technology of obtaining samples, and also because of the difference in the means of measuring these parameters.

Thus, all of the above suggests the need for a more in-depth study of the capabilities of known programs, their application features in the calculation of specific devices.

We would like to acknowledge the use of gpvdm program that was developed by Dr. Roderick C.I. MacKenzie, The University of Nottingham, Nottingham, UK.

## REFERENCES

- [1] Novikov G F, Gapanovich M V "Third generation Cu-In-Ga-(S,-Se) based solar inverters", Phys. Usp. 60, pp.161–178 (2017); Новиков Г Ф, Гапанович М В "Солнечные преобразователи третьего поколения на основе Cu-In-Ga-(S, Se)" УФН, 187, 173–191 (2017)
- [2] J.R. Ray, C.J. Panchal, M.S. Desai, U.B. Trivedi "Simulation Of Cigs Thin Film Solar Cells Using AMPS-1D", J. Nano- Electron. Phys., 2011, vol.3, № 1, pp. 747-754.
- [3] H. Heriche, Z. Rouabah, N. Bouarissa "High-efficiency CIGS solar cells with optimization of layers thickness and doping" Optik, 2016, vol. 127, №24, pp. 11751-11757.
- [4] R.C.I. MacKenzie, V. S. Balderrama, S. Schmeisser, R. Stoof, S. Greedy, J. Pallarès, L. F. Marsal, A. Chanaewa, E. von Hauff, "Loss mechanisms in high efficiency polymer solar cells", Adv. Energ. Mat., 10.1002/aenm.201501742, 2015.
- [5] A.B. Galat "Calculation of the absorbing capacity of a solar CuIn1-XGaXSe2 photovoltaic converter" Telecomm. Radio Eng., 2018, vol. 77, № 1, pp. 61-67
- [6] K. Zhang, Z. Wang, G.Wang, J. Wang, Y. Li, W. Qian, S. Zheng, S. Xiao, S. Yang "A prenucleation strategy for ambient fabrication of perovskite solar cells with high device performance uniformity". Nat Commun., 2020, vol. 11, № 1006.
- [7] M. H. Elshorbagy, E. López-Fraguas, F. A. Chaudhry, J. M. Sánchez-Pena, R. Vergaz, B. García-Cámara "A monolithic nanostructured-perovskite/silicon tandem solar cell: feasibility of light management through geometry and materials selection" / Sci. Reports, 2020, vol. 10, № 2271.

# Model of the Growth Mechanism of Whisker Nanocrystals with the Participation of Hot Adatoms

Denis Grankin\*, Viktor Grankin<sup>+</sup>

\*Pryazovskyi State Technical University, Computer Science Dept.  
Universytetska St., 7 / 87555 / Mariupol / Ukraine / +380629446511 / pstu511a@gmail.com

<sup>+</sup>Pryazovskyi State Technical University, Computer Science Dept.  
Universytetska St., 7 / 87555 / Mariupol / Ukraine / +380629446156 / victor.grankin@gmail.com

**Abstract** — A kinetic model has been developed for the growth of semiconductor whisker nanocrystals due to adsorption from the gas phase, taking into account the diffusion of excited ("hot") atoms formed in adsorption events and the accommodation of their excitation energy via the electron channel on metal droplets of catalysts. Surface processes were simulated using the probabilistic Monte Carlo method. It was shown that the relaxation processes of hot adatoms can determine the growth rate of whisker nanocrystals.

**Keywords** — *nanomaterials, nanowires, whisker nanocrystals, filamentary nanocrystals*

## I. INTRODUCTION

Nanostructures with one-dimensional, two-dimensional or three-dimensional restriction of charge carriers have a quantum spectrum of energy states. This determines their unique electrical, optical and adsorption properties. Recently, considerable interest has been shown in semiconductor nanostructures perpendicular to the surface of the substrate (they are called filamentary nanocrystals (FNC) or nanowhiskers). This is explained by the possible applications of FNCs in various fields, including micro- and optoelectronics. Based on the FNCs, experimental samples of field-effect transistors, diodes, and light-emitting devices are constructed.

The key issue is the creation of FNCs with desired properties, obtaining p-n junctions in nanowhiskers and filamentary heterostructures. Studies of growth processes and properties of FNCs are currently of great interest. Interesting results were achieved in the study and description of the processes of FNCs formation [1]. However, the existing models do not consider the features of the state of adatoms and surfaces in the processes of surface transport and crystal formation. Therefore, the mechanisms of FNCs growth are not fully developed.

Semiconductor FNCs in most cases are grown on pre-prepared surfaces. The surface is activated by metal drops, i.e. growth catalysts (most often it is Au nanodroplets). Depending on the conditions of deposition and the radius of the droplet, there may be different modes of whisker growth. Nanowhiskers are formed either by the vapor-liquid-crystal (VLC) mechanism [2], or by the diffusion mechanism, i.e. as a result of surface diffusion and incorporation of component atoms at the interface between the catalyst droplet and the FNC [1]. For the diffusion mechanism, the diffusion flux of adatoms to the top of the nanowhisker consists of atoms adsorbed directly on the side faces of the whisker, as well as

of atoms that come to the side walls from the surface of the substrate. In diffusion models of FNC growth, it is assumed that the diffusion of adatoms on the surface is equilibrium, i.e., it is determined by the parameters of the gas-surface system.

The explanation of the directional crystal growth according to the VLC mechanism in the modern presentation is as follows [2]. Let the solution have a simple phase diagram and in the solid state the substances do not mix at all, but in the liquid state it forms a homogeneous solution with the equilibrium concentration of the semiconductor material, depending on the temperature. At the initial instant of time, liquid droplets of a saturated solution in equilibrium with the substrate are located on the surface. As a result of deposition, part of the semiconductor material falls into the droplet. The entry into the droplet occurs by direct ingress of a substance from the gaseous phase (vapor). It was suggested in [1] that this can also occur as a result of diffusion of adatoms deposited on the lateral surface to the top of the FNC, as well as diffusion of adatoms from the surface of the substrate through the side walls to the top of the FNC. In both mechanisms, the material transitions from vapor to liquid, and as a result, the solution becomes supersaturated and crystallizes on the surface under the drop. Growth occurs as a result of two-dimensional nucleation of crystalline islands from a supersaturated solution. As a result, a crystalline column grows under the droplet with a lateral size approximately equal to the diameter of the droplet, and the droplet itself moves upward at a speed equal to the growth rate of the FNC.

A higher growth rate of nanowhiskers from a droplet compared to an inactivated surface is explained by two factors:

- 1) an increase in the rate of a chemical reaction at the surface of a droplet [2] and
- 2) "collection" of material from the side walls and from the surface of the substrate due to diffusion flows directed into the droplet [1].

In the first case, a droplet plays the role of a chemical, and in the second, a physical catalyst for growth.

Currently, studies have appeared that indicate that the system cannot always be described as quasi-equilibrium and it is necessary to take into account the reactivity of the so-called hot atoms [3], which are formed on the surface in exothermic reactions and have excess energy for a given temperature. Such an atom dissipates its energy in the process of moving parallel to the surface by the mean free

path  $L_d$  and remains in a highly excited vibrational state before accommodation in the free adsorption site. Since hot atoms have excess energy, their surface diffusion can be considered as non-activation – nonequilibrium diffusion. It is assumed that excited atoms can play a key role in exothermic heterogeneous chemical reactions. Similar processes should occur during the epitaxial growth of a semiconductor, since the capture of atomic particles by a surface is accompanied by the formation of new bonds and proceeds with a large energy release. However, the processes of the formation of hot adatoms in the adsorption acts and their participation in the formation of nanowhiskers are not considered in existing models of FNC growth.

The aim of this work is to construct a nanowhisker growth mechanism that takes into account the formation of hot adatoms and their relaxation on nanodroplets of catalysts.

## II. A MODEL OF THE MECHANISM OF NANOWHISKER GROWTH WITH PARTICIPATION OF HOT ADATOMS

At a high heat of the adsorption reaction, a long-lived (in the life scale of single-phonon excitations) non-equilibrium vibrational state is formed on the surface, namely, hot atoms with a lifetime of  $\tau \gg 10^{-13}$  s. The vibrational state interacts with both the atomic and electronic subsystems of the crystal transferring the corresponding subsystems to excited states. Electronic accommodation manifests itself experimentally; heterogeneous surface chemiluminescence is excited. In [4], a new phenomenon of high-efficiency electronic accommodation (HEA) of the energy of vibrationally excited states generated in a reaction on the surface of electronically excited semiconductors is introduced. An even greater efficiency of accommodation via the electronic channel is observed on metals, because there is no band gap in the metal and the electron can take any portion of energy from a vibrationally excited molecule or atom (resonant vibrational-electronic transition).

If a nanodot of metal (a droplet of catalyst) is placed on the surface of a semiconductor or dielectric, and then epitaxial growth of the semiconductor is performed, then, according to the HEA phenomenon, the vibrationally excited states arising in the reaction on the surface of the semiconductor will relax on the catalyst droplets through the electron channel at a rate of several orders of magnitude greater than the phonon channel on the substrate. The catalysis of epitaxial growth by a droplet of a catalyst in this case may be due to the fact that there will be an effective relaxation of hot atoms on the surface of a droplet of a catalyst as a result of a resonant vibrational-electronic transition. A concentration gradient of hot atoms arises, directed from the nanodot, which leads to the flow of matter toward the nanodot. The mechanism of epitaxial growth, taking into account the accommodation of the reaction energy through the electronic channel, includes: the stage of exothermic adsorption with the formation of a hot atom  $R^vL$ , relaxation of  $R^vL$  via the phonon channel, nonequilibrium diffusion of hot atoms over the surface and relaxation of  $R^vL$  via the electronic channel. The kinetic mechanism of FNC growth on the surface of an elementary semiconductor with deposited catalyst drops, taking into account the possibility of formation of hot atoms and their relaxation, includes the following stages:

- I.  $R + L \xrightarrow{\nu_1} R^vL$  – exothermic atomic adsorption;
- II.  $R^vL \xrightarrow{\mu} R + L$  – nonequilibrium atomic desorption;
- III.  $R^vL + L_0 \xrightarrow{\Gamma_1} RL + L_0 + Ph$  – multi-phonon relaxation;
- IV.  $R^vL + L \xrightarrow{\Gamma_2} L + R^vL$  – nonequilibrium diffusion of a hot atom;
- V.  $R^vL + M \xrightarrow{k_1} RL + M$  – high-efficiency electronic accommodation;
- VI.  $RL + L \xrightarrow{\Gamma_3} L + RL$  – equilibrium diffusion of an adatom;
- VII.  $RL + M \xrightarrow{\Gamma_4} RL_m + M$  – diffusion of adatoms from the perimeter of a catalyst droplet along the lateral crystal-liquid interface;
- VIII.  $RL_m \xrightarrow{\nu_m} L_m$  – incorporation of an atom into the lattice under a droplet of catalyst.

Here  $\nu_1$ ,  $\mu$ ,  $k_1$  and  $\Gamma_i$  are probabilities and rate constants of the corresponding reactions.  $L$  and  $M$  are a surface center on a semiconductor substrate and on a catalyst droplet, respectively,  $RL$  and  $RL_m$  are adsorbed atoms,  $L_m$  is an atom embedded in the FNC's lattice under a droplet of catalyst.

Designations for concentrations at a moment of time  $t$ :  $[RL] \rightarrow N_1$ ,  $[L] \rightarrow N$ ,  $[R^vL] \rightarrow N_1^v$ ,  $[M] \rightarrow N_m$ ,  $[RM] \rightarrow N_{1m}$ ,  $[RL_m] \rightarrow N_{1M}$ . In its turn,  $\nu_1$ ,  $\nu_{1m} = \sigma_{1,1m}j$ , where  $j$  is the atomic flux density toward the surface,  $\sigma_{1,1m}$  is the cross section for the adsorption of atoms on the surface of a semiconductor and a nanodroplet, respectively.

The value of  $\Gamma_3 = \Gamma_{30} \exp(-E_3 / kT)$  is determined by the activation energy  $E_3$  of atomic diffusion over the surface of the semiconductor, whereas nonequilibrium diffusion of hot atoms is non-activational and  $\Gamma_2$  does not depend on  $T$ .

## III. RESULTS AND DISCUSSION

Under different conditions, various growth mechanisms of nanowhiskers are possible. Several possible cases are considered.

1) If the rate of multiphonon relaxation is much higher than the rate of nonequilibrium desorption ( $\Gamma_1 N_0 \gg \mu$ ), then relaxation processes do not affect the rate of epitaxial growth on the substrate and it is determined only by activation processes. For this reason, under these conditions, the nonequilibrium diffusion of hot atoms to the droplet catalyst will be negligible compared to equilibrium diffusion due to the low concentration of hot atoms on the surface, since they relax by the effective, under the given conditions, phonon channel of accommodation of energy of the adsorption reaction. Under these conditions, FNC growth will be determined by the equilibrium diffusion of adatoms according to the mechanism described in [1].

2) In the case when the multi-phonon channel of accommodation of the energy of the exothermic reaction is ineffective, hot atoms with large  $\tau$  arise on the surface. These atoms over time  $\tau$  can travel large distances over the surface

as a result of nonequilibrium diffusion. The matter and reaction energy are transferred from the substrate to the catalyst droplet and the surface can no longer be considered as spatially homogeneous. As a result of this, it is necessary to solve the system of differential kinetic equations in partial derivatives, resulting from the general kinetic model. An analytical solution to the system of partial differential equations for this model is impossible. To calculate in time the quantities of  $N(t,x,y,z)$ ,  $N_1(t,x,y,z)$ ,  $N_1^v(t,x,y,z)$ ,  $N_m(t,x,y,z)$ ,  $N_{1m}(t,x,y,z)$ ,  $N_1M(t,x,y,z)$  for different parts of a spatially inhomogeneous surface, it is necessary to use stochastic solution methods. A program has been created for Monte Carlo probabilistic modeling of processes on the surface of semiconductors with FNCs described by the kinetic model. The epitaxial growth rate was calculated both on the substrate and on the nanowhisker depending on the distance between the catalyst droplets and their diameter, and on the conditions of the processes.

For large  $\Gamma_1'$ , the mean free path along the surface is much shorter than the length of the FNC and hot atoms do not participate in the formation of the FNC. In this case, FNC growth occurs by the equilibrium diffusion mechanism. When  $\Gamma_1' \leq \mu$ , the growth rate of the epitaxial layer on the substrate is determined mainly by relaxation processes. For small  $\Gamma_1'$ , the value of  $L_d$  increases by several orders of magnitude (up to hundreds of nanometers). This value of  $L_d$  of a hot atom is larger than the diameter of the FNC and is comparable with the distance between the catalyst droplets and the length of the FNC. Under these conditions, nonequilibrium diffusion towards the droplet catalyst and accommodation of R'L energy via the electronic channel on it will mainly determine the growth rate of FNC, rather than activation processes.

The relaxation rate of R'L due to accommodation of energy via the electronic channel at the perimeter of the droplet catalyst increases with increasing  $d$  and is accompanied by a decrease in  $L_d$ . The resulting transfer of reaction energy and substance to the droplet catalyst decreases the relaxation rate of R'L and their concentration on the substrate, which reduces the growth rate of the epitaxial layer on the substrate. The growth rate of FNC, when nonequilibrium diffusion of hot atoms predominates in comparison with equilibrium diffusion of adatoms, is higher on substrates with small values of  $\Gamma_1'$ , where  $L_d$  is large.

Under these conditions, the transfer of the substance to the droplet catalyst has a stronger effect on the growth rate of the epitaxial layer on the substrate itself. In the calculations, the probability of relaxation of a hot atom on a droplet catalyst was taken equal to 1 due to the high efficiency of accommodation of the reaction energy via the electronic channel on metals.

The concentrations of all the reagents described in the model were determined, and the mean free paths of hot atoms along the surface of the substrate and FNCs under conditions of epitaxial growth were obtained.

#### IV. CONCLUSION

The hot adatoms relaxation processes can determine the growth rate of FNCs. This occurs due to the entrainment of the substance and the heat of reaction to the droplet catalyst by hot adatoms. In the case of a high accommodation rate of atomic adsorption energy over the phonon channel, the process of equilibrium diffusion of adatoms to the droplet catalyst according to the mechanism proposed in [1] is decisive, and in the case when the probability of multiphonon relaxation of hot atoms is small and less than the probability of nonequilibrium desorption of atoms, the determining factor in the growth of FNCs is the nonequilibrium diffusion of hot atoms toward a drop. According to the proposed mechanism, the nanowhisker growth rate depends on the diameter  $d$  of the nanodroplets of the catalyst (grows proportionally to  $1/d$ ), as well as on the distance between the droplets and the mean free path of hot atoms.

#### REFERENCES

- [1] G. Dubrovskii, G. E. Cirlin, I. P. Soshnikov, A. A. Tonkikh, N. V. Sibirev et al., "Diffusion-induced growth of GaAs nanowhiskers during molecular beam epitaxy: Theory and experiment," *Phys. Rev. B*, vol. 71, 205325, May 2005.
- [2] Е. И. Гиваргизов, Рост нитевидных и пластинчатых кристаллов из пара, М.: Наука, 1977.
- [3] T. Zambelli, J. V. Barth, J. Winterlin and G. Ertl, "Complex pathways in dissociative adsorption of oxygen on platinum," *Nature*, vol. 390, pp. 495–497, December 1997.
- [4] P. Grankin, V. Yu. Shalamov and N. K. Uzunoglu, "High-efficiency electronic accommodation of energy of heterogeneous recombination of hydrogen atoms on the surface of the monocrystal ZnS," *Chem. Phys. Lett.*, vol. 328, pp. 10–16, September 2000.

# Mechanism of the Dye "Self-Desensitization" Effect upon Excitation of Its Aggregated States

Aleksandr Tyurin\*, Sergei Zhukov<sup>+</sup>, Aleksandr Bekshaev<sup>@</sup>

\*I.I. Mechnikov Odessa National University

Dvorianska 2, 65082, Odessa, Ukraine, +380 723-80-36, tyurin@onu.edu.ua

<sup>+</sup>I.I. Mechnikov Odessa National University, Research Institute of Physics

Dvorianska 2, 65082, Odessa, Ukraine, +380 723-80-36, zhukov@onu.edu.ua

<sup>@</sup>I.I. Mechnikov Odessa National University, Research Institute of Physics

Dvorianska 2, 65082, Odessa, Ukraine, +380 723-80-36, bekshaev@onu.edu.ua

**Abstract** — We study the processes of interaction between molecules and H-aggregates of a dye adsorbed at the surface of AgBr and AgBrI emulsion microcrystals (EMC). Methods of the low-temperature (T = 4.2 K) luminescence enable to associate the "self-desensitization" with the mechanism conditioned by the interaction of H- and J-aggregates of the dye with its molecules, which results in the decay of the spectral sensitivity of emulsions employing organic dyes. Methods of low temperature (T = 77 K) luminescence show the interaction of the first excited state of the H-aggregates with the triplet state of the molecular dye, which indicates the process of the excited H-aggregates' energy dissipation through the triplet state of its molecules.

**Keywords** — microcrystal, spectral sensitization, molecular dye, aggregated dye, self-desensitization, luminescence, anomalously slowed-down fluorescence

## I. INTRODUCTION

The property of dyes to selectively and efficiently absorb light of certain spectral ranges is used in spectral sensitization of the silver-halide emulsions [1], in photoelectric transformers based on nanoparticles and nanotubes (organic dye-sensitized solar cells) [2], as well as in laser techniques [3–5].

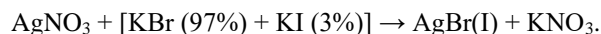
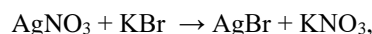
During the adsorption of dyes on the EMC surface, in addition to interaction with the surface, there exists a predominant interaction between individual dye molecules, which leads to the appearance of ordered pairs of dye molecules – dimers (H-aggregates) and polymolecular structures, the so-called J-aggregates, which absorb light in the spectral ranges shifted with respect to the absorption spectrum of the molecular dye [6]. The interaction of molecules with the H- and J-aggregates of the dye ultimately leads to the appearance of dye luminescence, which may be one of the mechanisms of the "self-desensitization" even at low dye concentrations.

## II. EXPERIMENTAL APPROACH

One of the methods for studying the dissipation of the photoexcitation energy of a dye is the luminescence method with time-resolved spectra [7]. The experimental setup, in which low-temperature (T = 4.2 and 77 K) luminescent studies were performed, allows one to measure the spectral characteristics during continuous irradiation of samples with exciting light (a "fluorescence mode"), as well as to perform

intermittent (modulated) excitation by  $\Pi$ -shaped light pulses. Time period of the sample excitation and the time of registration of its luminescence are equal and amount to  $0.1 \cdot 10^{-4}$  s, and the time interval between the end of irradiation and the luminescence registration (dark interval) is  $1.1 \cdot 10^{-3}$  s – a "phosphorescence mode".

The studies were carried out on emulsion microcrystals AgBr and AgBr(I) with cubic crystal structure and an average size  $d \approx 0.25$   $\mu\text{m}$ , obtained by the two-jet emulsification via the double-exchange reaction in various binders: in gelatin and in water (sol),



The content of silver ions in the emulsion was controlled by measurement of pBr. Spectral sensitization of the EMC was performed by two J-aggregating dyes:

anionic dye – piridinium salt of 3,3'-di- $\gamma$ -sulfopropyl-9-ethyl-4,5,4',5'-dibenzothiacarbocyaninebetaine, further referred to as Dye1;

and the cationic dye – 3,3',9-triethyl-5,5'-diphenyloxcarbo-cyaninenitrate, further referred to as Dye2.

## III. RESULTS OF EXPERIMENTS

Sensitometric tests of the AgBr EMC in gelatin were performed with the spectrophotometer SF-4 according to a standard method. The sensitivity curves of the exposed and developed emulsions depending on the concentrations of the dyes introduced and the wavelength of the exposing light are presented in Figs. 1 and 2.

The reflection spectra of the AgBr EMC samples in gelatin depending on the introduced dye concentration are presented in Figs. 3 and 4.

For wavelengths corresponding to the molecular Dye1, there is no shift to the long-wavelength part of the spectrum, and for the region corresponding to the J-aggregated Dye1, a shift from 680 to 685 nm occurs (Fig. 3, curves 1 – 5). It should be noted that at a concentration higher than  $5 \cdot 10^{-5}$  (mol Dye1 / mol AgBr), the minimum, corresponding to the molecular dye reflection, transforms into the "shoulder" (curve 3 in Fig. 3), and for the Dye1 J-aggregates, the reflection minimum occurs (Fig. 3, curve 5).

The work is supported by the Ministry of Education and Science of Ukraine, project No 582/18 (State Registration Number 0118U000198).

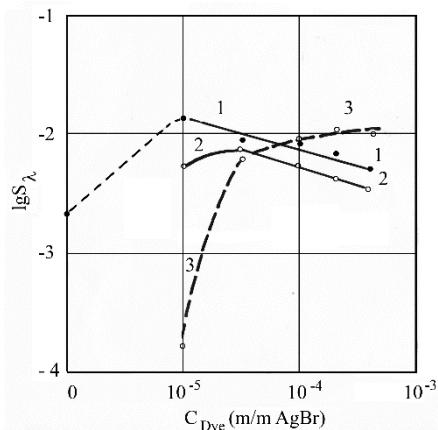


Fig. 1. Sensitivities of the cubic AgBr EMC ( $d \approx 0.25 \mu\text{m}$ ) in gelatin, depending on the concentration of Dye1 at illumination by monochromatic light of the wavelength  $\lambda$ , nm: 1 – 425 (range of intrinsic absorption of AgBr); 2 – 630 (range of molecular Dye1 absorption); 3 – 690 (absorption range of Dye1 J-aggregates)

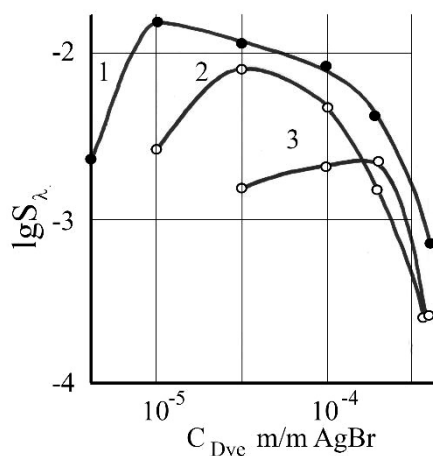


Fig. 2. Sensitivities of the cubic AgBr EMC ( $d \approx 0.25 \mu\text{m}$ ) in gelatin, depending on the concentration of Dye2 at monochromatic light illumination of the wavelength  $\lambda$ , nm: 1 – 425 (intrinsic absorption range of AgBr); 2 – 580 (molecular Dye2 absorption); 3 – 635 (J-aggregate of Dye2 absorption)

For wavelengths corresponding to the molecular Dye2, a shift from 570 to 580 nm occurs, and for the J-aggregated Dye2, the shift from 630 to 650 nm is seen (Fig. 4, curves 1 and 5). It should be noted that even at a concentration of  $5 \cdot 10^{-5}$  (mol Dye2 / mol AgBr), the reflection decreases in the region corresponding to molecular Dye2 (Fig. 4 curve 2); this process is even more intense for the Dye2 J-aggregates (Fig. 4, curves 3 – 5).

As follows from Fig. 5a, in the spectrum of low-temperature ( $T = 4.2 \text{ K}$ ) luminescence of AgBr EMC in the dye-free gelatin, two bands with  $\lambda_{\text{max}} \approx 495 \text{ nm}$  and  $595 \text{ nm}$  are observed (Fig. 5a). The short-wavelength luminescence with  $\lambda_{\text{max}} \approx 495 \text{ nm}$  is due to the residual homological impurity of  $\Gamma$  iodine ions located in the nodes of the AgBr crystal lattice [8], which is recorded at  $T \leq 50 \text{ K}$ . The luminescence excitation spectrum of single iodine ions has two maxima  $\lambda = 310 \text{ nm}$  and  $430 \text{ nm}$ , associated with the adsorption of light by iodine ions [9].

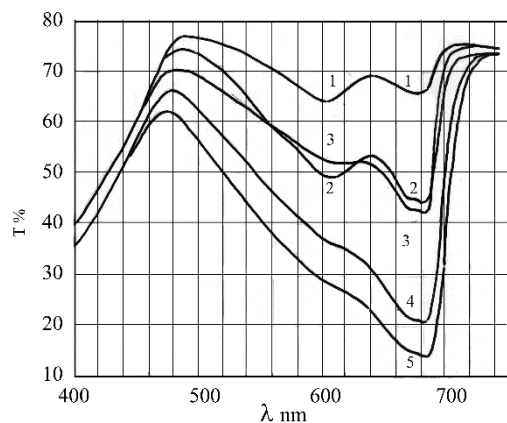


Fig. 3. Reflection spectra of cubic EMC AgBr ( $d \approx 0.25 \mu\text{m}$ ) vs the Dye1 concentration (mol Dye1 / mol AgBr): 1 –  $10^{-5}$ ; 2 –  $5 \cdot 10^{-5}$ ; 3 –  $10^{-4}$ ; 4 –  $3 \cdot 10^{-4}$ ; 5 –  $6 \cdot 10^{-4}$ .

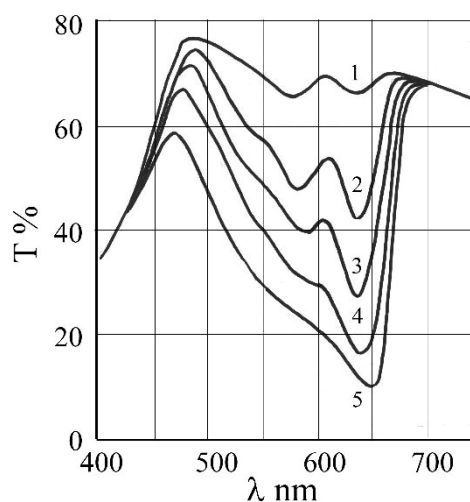


Fig. 4. Reflection spectra of cubic EMC AgBr ( $d \approx 0.25 \mu\text{m}$ ) vs the Dye2 concentration (mol Dye2 / mol AgBr): 1 –  $10^{-5}$ ; 2 –  $5 \cdot 10^{-5}$ ; 3 –  $10^{-4}$ ; 4 –  $3 \cdot 10^{-4}$ ; 5 –  $6 \cdot 10^{-4}$ .

In the region of the intense exciton absorption peak near  $300 \text{ nm}$  ( $4.17 \text{ eV}$ ) at  $4.2 \text{ K}$  [8], a sharp excitation minimum of the  $495 \text{ nm}$  band is observed (Fig. 5b). Obviously, in this case, the mean free path of the exciton is less than the average distance between the centers determining the luminescence in this band. In the region  $T \geq 77 \text{ K}$ , the thermal ionization of excitons occurs and intensity of the exciton excitation band decreases, and all processes in AgBr EMCs are determined by the electron-hole energy migration mechanism.

The band with  $\lambda_{\text{max}} \approx 595 \text{ nm}$  corresponds to the luminance of pair centers of the mixed hetero-halide composition  $\text{Br}^0\Gamma^-$  [10].

The luminescence of AgBr EMCs containing Dye1 ( $10^{-4}$  mol Dye1 / mol AgBr) at  $T \approx 4.2 \text{ K}$ , excited by monochromatic light at  $\lambda \approx 360 \text{ nm}$  in the "fluorescence mode", is characterized by luminescence of  $\Gamma$  iodine ions with a maximum of  $\lambda_{\text{max}} \approx 495 \text{ nm}$  (Fig. 6, curve 1). When excited by light from the absorption region of Dye1 molecules ( $\lambda \approx 630 \text{ nm}$ ), it is characterized by the presence of four fluorescence bands (Fig. 6, curve 2), for which the following factors are responsible: single iodine ions  $\Gamma$  at the sites of the AgBr crystal lattice ( $\lambda_{\text{max}} \approx 495 \text{ nm}$ ), H-

aggregates of Dye1 ( $\lambda_{\max} \approx 545$  nm), centers  $\text{Br}^0\text{I}^-$  ( $\lambda_{\max} \approx 595$  nm) and, finally, J-aggregates of Dye1 ( $\lambda_{\max} \approx 670$  nm) [11].

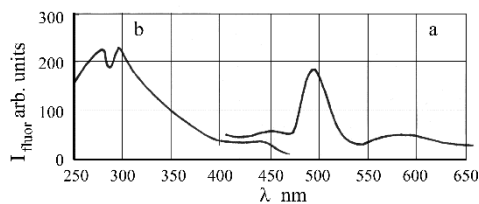


Fig. 5. (a) Spectrum of luminescence of EMC AgBr at  $T \approx 4.2$  K without dye at continuous excitation by monochromatic light with  $\lambda \approx 360$  nm; (b) Excitation spectrum of luminescence with  $\lambda_{\max} \approx 495$  nm.

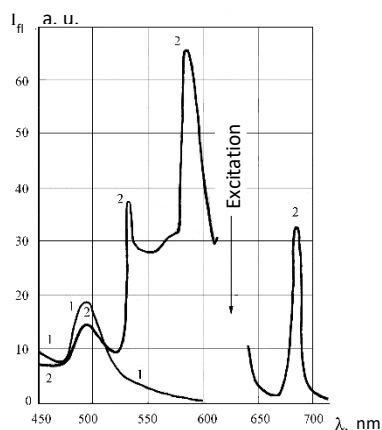


Fig. 6. Fluorescence spectra of AgBr EMCs the Dye1 concentration ( $10^{-4}$  mol Dye1 / mol AgBr) at  $T \approx 4.2$  K. The spectra are registered at excitation by monochromatic light with  $\lambda \approx 360$  nm (curve 1) and  $\lambda \approx 630$  nm (curve 2).

It should be specially noted that the luminescence of single iodine ions, Dye1 H-aggregates, and the intense luminescence of mixed heterohaloid  $\text{Br}^0\text{I}^-$  centers are observed at the anti-Stokes form of excitation, and while the anti-Stokes luminescence of  $\text{I}^-$  and  $\text{Br}^0\text{I}^-$  was observed earlier [12], the anti-Stokes luminescence of the Dye1 H-aggregates upon excitation from the absorption region of Dye1 molecules is observed for the first time.

So, in the "fluorescent mode", when the light is excited from the absorption band of the Dye1 molecules, two of four luminescence bands are associated with presence of an uncontrolled impurity of iodine ions in AgBr EMC, and two bands arise as a result of the excitation transfer from Dye1 molecules to its H- and J-aggregates. Such a transfer of photoexcitation from H-aggregates to Dye1 molecules is not observed, and there is no luminescence of Dye1 molecules upon excitation by light from the absorption region of the Dye1 H-aggregates in the "fluorescence mode".

To clarify the mechanism of photoexcitation transfer between the molecular and polymolecular forms of dyes, which would include long-term phosphorescence processes, we performed luminescent studies at  $T \approx 77$  K under the photoexcitation conditions described in the methodological part of the work.

To elucidate the mechanism of "self-desensitization" in the case of a controlled homologous iodine impurity in EMC, we consider the low-temperature ( $T = 77$  K) luminescence of

the AgBr(I) EMC in water (sol) at a Dye2 concentration  $5 \cdot 10^{-5}$  (mol Dye2 / mol AgBr).

When the luminescence is continuously excited by monochromatic light from the Dye2 absorption region ( $\lambda = 500$  nm) (Fig. 7a, curve 2), the molecular Dye2 fluorescence arises with  $\lambda_{\max} = 680$  nm, which is effectively excited from the molecular Dye2 absorption region,  $\lambda_{\max} = 600$  nm (Fig. 7b, curve 2').

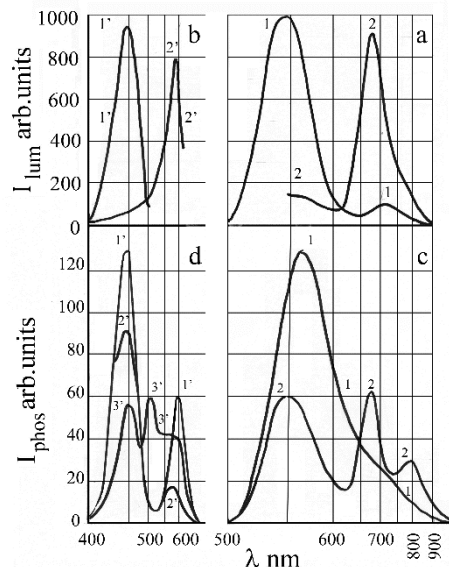


Fig. 7. Luminescence of the AgBr(I) EMC in water (sol) (Dye2 concentration is  $5 \cdot 10^{-5}$  mol Dye2 / mol AgBr): (a) continuous excitation, luminescence spectra excited by monochromatic light with  $\lambda$ : 1 – 450 nm; 2 – 500 nm; (b) continuous excitation, excitation spectra of luminescence with  $\lambda_{\max}$ : 1' – 550 nm; 2' – 800 nm; (c) excitation by the  $\Pi$ -shaped light pulses, luminescence spectra excited by monochromatic light with  $\lambda$ : 1 – 450 nm; 2 – 600 nm; (d) excitation by the  $\Pi$ -shaped light pulses, excitation spectra of luminescence with  $\lambda_{\max}$ : 1' – 550 nm; 2' – 650 nm; 3' – 800 nm.

In case of excitation by the  $\Pi$ -shaped pulses of monochromatic light from the molecular Dye2 absorption region ( $\lambda = 600$  nm), in the "phosphorescent mode", the emission spectrum is characterized by maxima at  $\lambda = 550$  nm, 680 nm and 800 nm, which in AgBr(I) EMCs are anti-Stokes luminescence of paired iodine centers [13], anomalously slowed down fluorescence and phosphorescence of the molecular Dye2, respectively (Fig. 7c, curve 2). In the excitation spectrum, for the luminescence of the paired iodine centers of AgBr(I) EMCs, two maxima,  $\lambda = 450$  nm and 600 nm, are recorded, which relate to the AgBr(I) EMC absorption region and to the anti-Stokes absorption region of the molecular Dye2, respectively (Fig. 7d, curve 1'). The abnormally slowed-down fluorescence of molecular Dye2 in the excitation spectrum corresponds to two peaks,  $\lambda = 450$  nm and 580 – 600 nm, which relate to the intrinsic absorption of the AgBr(I) EMC and molecular Dye2 (Fig. 7d, curve 2').

As for the molecular Dye2 phosphorescence with  $\lambda_{\max} = 800$  nm, its correspondence in the excitation spectrum is represented by two maxima  $\lambda = 450$  nm, 510 nm, and by the "shoulder" at 550 – 600 nm, which belong to the AgBr(I) EMC absorption region, to the dimer absorption region (H-aggregates of Dye2), and to the molecular Dye2 absorption band (Fig. 7d, curve 3').

#### IV. DISCUSSION

As the studies have shown, the interaction processes between photoexcited molecular and polymolecular forms of the dye responsible for "self-desensitization" are controlled in detail by the proposed luminescent technique, which allows using the obtained data to establish the nature of the dye adsorption on the AgHal EMC surface. Thus, the absence of fluorescence of the paired  $\text{Br}^0\text{I}^-$  and  $\text{I}^0\text{I}^-$  EMC centers, excited by light from the AgBr EMC absorption band ( $\lambda = 360$  nm), at  $T = 4.2$  K (Fig. 6, curve 1), and intense emission of these bands upon excitation from the absorption region of Dye1 molecules (Fig. 6, curve 2), means that the Dye1 molecules are adsorbed in a direct "optical" contact with these centers, which ensures the efficient transfer of photoexcitation from Dye1 to these centers in the "fluorescence mode". Adsorbed Dye1 molecules are in the same close optical contact with H- and J-aggregates, which ensures the luminescence of these aggregates upon excitation of Dye1 molecules. It should also be noted that the anti-Stokes emission band of the H-aggregates is very narrow. In our opinion, this indicates that the luminescence occurs due to excitons localized on the H-aggregate.

As is known from [6], photoexcited charge-carriers from H-aggregates of dyes are not transferred to AgBr EMCs, i.e. when we observe a process of photoexcitation transfer from Dye1 molecules to AgBr microcrystals, then photoexcitation transfer from the molecules to Dye1 H-aggregates acts as a process of the dye "self-desensitization". The self-desensitization mechanism of H-aggregates depends entirely on the mechanism of the anti-Stokes H-aggregates' emission upon excitation by light from the absorption region of Dye1 molecules. If the mechanism of the anti-Stokes luminescence in this case is the same as that considered by us earlier in [13], then it can be assumed that the "self-desensitization" also takes place, but, since this luminescence is described here for the first time, its mechanism requires a separate study. As for the Dye1 J-aggregates, the photoexcitation is transmitted to them from the Dye1 molecules in the Stokes manner.

In case of excitation by  $\Pi$ -shaped light pulses and measurement of the AgBr(I) EMCs' luminescence with the Dye2 adsorbed on their surface ( $10^{-5}$  mol Dye2 / mol AgBr) upon excitation by light from the AgBr(I) EMC intrinsic absorption region of  $\lambda = 460$  nm, the luminescence of Dye2 molecules is observed. Based on their luminescence excitation spectra, we can conclude that at such a concentration of the Dye2, its J-aggregates are not yet formed and their luminescence is absent. The photoexcitation of Dye2 molecules leads to the anti-Stokes luminescence of paired  $\text{I}^0\text{I}^-$  centers, providing also the anomalously slowed-down Stokes fluorescence and phosphorescence of the molecular Dye2. Since the phosphorescence excitation of the molecular Dye2 is possible from the absorption region of the Dye2 H-aggregates, it should be interpreted as the "self-desensitization" of the dye even at minimal concentrations upon excitation from the absorption region of the Dye2 H-aggregates.

It is currently not possible to establish the "self-desensitization" mechanism for the case of phosphorescence of the Dye2 molecules, since the phosphorescence of Dye2 molecules upon excitation from the absorption region of the Dye2 H-aggregates has been observed here for the first time, and the mechanism of its luminescence needs to be clarified.

#### V. CONCLUSION

A comparison of the luminescent data obtained at temperatures of liquid helium and liquid nitrogen showed the existence of mechanisms of interaction of photoexcited molecular and aggregated dye structures. Regardless of the concentrations used, the interaction of molecular and aggregated forms (in our case, H- and J-aggregates) occurs, which enables to associate the "self-desensitization" effect with the mechanisms of energy dissipation during photoexcitation transfer between molecular and aggregated states of the dye.

#### REFERENCES

- [1] T.H. James, *The Theory of the Photographic Process*. New York, NY: Macmillan Pub Co, 1977.
- [2] B. O'Regan and M. Grätzel, "A low-cost, high-efficiency solar cell based on dye-sensitized colloidal  $\text{TiO}_2$  films", *Nature*, vol. 353, pp. 737–740, 1991.
- [3] M. Bass, T. F. Deutsch, and M. J. Weber, *Dye Lasers*, Technical Report R-69, Raytheon Company, Waltham, Massachusetts, November 20, 1969, 108 pp.
- [4] V.I. Bezrodnyi, N.A. Derevyanko, A.A. Ishchenko, and L.V. Karabanova, "A dye laser with a polyurethane matrix", *Technical Physics*, vol. 46, pp. 858–863, 2001.
- [5] H.R. Aldag, S.M. Dolotov, M.F. Koldunov et al., "Microporous glass-polymer composite as a new material for solid-state dye lasers: I. Material properties", *Quantum Electronics*, vol. 30, pp. 954–958, 2000.
- [6] Dietz, *Current state of the spectral sensitization theory*, *J. fur Signalfzeichnungsmaterialien*, vol. 6, No 4, pp. 245–266; No 5, pp. 341–361, 1978 (in German).
- [7] S.A. Zhukov, *Photo-Induced Physico-Chemical Processes and their Sensitization in the "Core – Silver-halide Shell" Microsystems*. DSci Thesis, I.I. Mechnikov National University, Odessa, 2018.
- [8] V.M. Belous, N.G. Barda, E.A. Dolbinova, I.L. Kuusmann, C.B. Luschik, and N.S. Roose "Electronic excitation, luminescence and hidden image formation in silver halogenides" *Zhurn. nauchn. i prikl. fotogr. i kinematogr.*, vol. 23, No 6, pp. 460–472, 1978 (in Russian).
- [9] V.M. Belous, E.A. Dolbinova, and V.P. Churashov, "Determination of energy levels of iodine centers in emulsion microcrystals", *Zhurn. nauchn. i prikl. fotogr. i kinematogr.*, vol. 23, No 3, pp. 211–213, 1978 (in Russian).
- [10] V.M. Belous, S.A. Zhukov, E.A. Dolbinova, A.Yu. Akhmerov, N.A. Orlovskaya, and V.P. Churashov, "Luminescent investigations of the formation mechanism of the hidden photographic image centers in silver halogenides", *Zhurn. nauchn. i prikl. fotogr. i kinematogr.*, vol. 37, No 2, pp. 99–108, 1992 (in Russian).
- [11] A.V. Tyurin, V.P. Churashov, S.A. Zhukov, et al. "Interaction of molecular and polymolecular forms of a dye", *Optics and Spectroscopy*, vol. 104, No 1, pp. 88–94, 2008.
- [12] A.V. Tyurin and S.A. Zhukov, *Photoinduced Processes in AgHal microcrystals with dye*. LAP LAMBERT Academic Publishing, 2018, 129 pp.
- [13] A.V. Tyurin, V.P. Churashov, S.A. Zhukov., et al., "A mechanism of the anti-stokes luminescence of a dye-sensitization silver halide emulsion", *Optics and Spectroscopy*, vol. 104, No 2, pp. 203–209, 2008.

# The size effects in Van der Waals interaction between the spherical metallic nanoparticles

Nina Smirnova\*, Andrii Korotun\*, Valentina Tretiak\*, Igor Titov<sup>+</sup>

\*National University "Zaporizhzhia Politechnic"

Zhukovskogo Str. 64, 69063, Zaporizhzhya, Ukraine, E-mail: andko@zntu.edu.ua

<sup>+</sup>UAD Systems

Alexandrovska Str. 84, 69002, Zaporizhzhya, Ukraine

**Abstract** — The size dependences of such characteristics of van der Waals interaction between the spherical metallic nanoparticles as the free energy and Hamaker constant have been studied in the work with the help of the classical approach. The dimensionally-corrected Drude dielectric function, which takes into account the electron scattering in the bulk and on the surface of the nanoparticle, has been used for the calculations. The calculations have been performed for the particles of the different metals and for the different distances between the nanoparticles. (*Abstract*)

**Keywords** — nanoparticles, size effects, Van der Waals interaction, Hamaker constant

## I. INTRODUCTION

The metallic nanoparticles attract such a great attention because of their interesting optical and electronic properties, which are not shared by their three-dimensional analogs [1—3]. The size effects cause such differences when the sizes drop to the nanoscale level.

The available at the moment methods of the obtaining of the nanoparticle such as the photo lithography and the electron-beam lithography are laborious and costly. The bottom-up self-assembly of the nanoparticles is the powerful and economically-effective alternative [1, 3]. This, along with the majority of the other possible methods of the construction, would demand the more fundamental understanding of the interactions between the particles on the nanoscale level, including the far-ranging interaction.

The full explanation of the interaction between the metallic nanoparticles is impossible without taking into the consideration van der Waals interaction, despite the fact that it is weak. An exact computation of the corresponding force of the interaction depends on Hamaker constant in the equations which govern van der Waals interaction. The knowledge of this constant is necessary, for example, for the describing of the interfacial phenomena and the aggregation prediction or the disperse behavior of the colloids. The theoretical magnitude of Hamaker constant can be calculated with the help of Lifshitz theory, which takes into account the dielectric and spectral properties of the nanoobjects in the foregoing broad frequency interval [3—6]. The certain difficulties emerge under the obtaining of the spectral data for the majority of the materials and under the exact determination of the related parameters (for example, the dielectric permittivity and the polarizability). These difficulties complicate the obtaining of the estimate of Hamaker constant. The surface force apparatus (SFA) [7]

and the atomic force microscope (AFM) [8—10] are the powerful instruments for the experimental determination of Hamaker constant, but the fact that the results are sensitive to the impurities [11] requires the complicated preparation of the samples.

That is why the determination of the size dependence of Hamaker constant for the case of van der Waals interaction between the spherical nanoparticles is the actual task.

The size dependence of Hamaker constant naturally follows from the expression for the free energy of the interaction between the spherical nanoparticles taking into account the known spectrum of the electromagnetic fluctuations.

## II. BASIC RELATIONS

Let us consider van der Waals interaction of two spherical metallic nanoparticles. For the sake of simplicity let us assume that the particles have the same radius, they are of the same material and the distance between the centers of the nanoparticles is equal to  $d$  (fig. 1). The dielectric properties of the material are described by the function  $\epsilon(\omega)$ .

Let us introduce the spherical coordinate systems  $(r_1, \phi_1, \theta_1)$  and  $(r_2, \phi_2, \theta_2)$  for each particle. Since the phenomena in the system do not depend on the azimuth angles, then one has the Helmholtz equation for Fourier components of the scalar potential in the nanoparticles (the domains 1 and 2) and in the surrounding (the domain 3) with the dielectric permittivity  $\epsilon_m$

$$\begin{aligned} \left[ \frac{1}{r_1^2} \frac{\partial}{\partial r_1} \left( r_1^2 \frac{\partial}{\partial r_1} \right) + \frac{1}{r_1^2} \frac{\partial^2}{\partial \phi_1^2} \right] \varphi_{1\omega}(\omega, r_1, \phi_1) &= \\ &= k^2 \varphi_{1\omega}(\omega, r_1, \phi_1), \\ \left[ \frac{1}{r_2^2} \frac{\partial}{\partial r_2} \left( r_2^2 \frac{\partial}{\partial r_2} \right) + \frac{1}{r_2^2} \frac{\partial^2}{\partial \phi_2^2} \right] \varphi_{2\omega}(\omega, r_2, \phi_2) &= \\ &= k^2 \varphi_{2\omega}(\omega, r_2, \phi_2). \end{aligned} \quad (1)$$

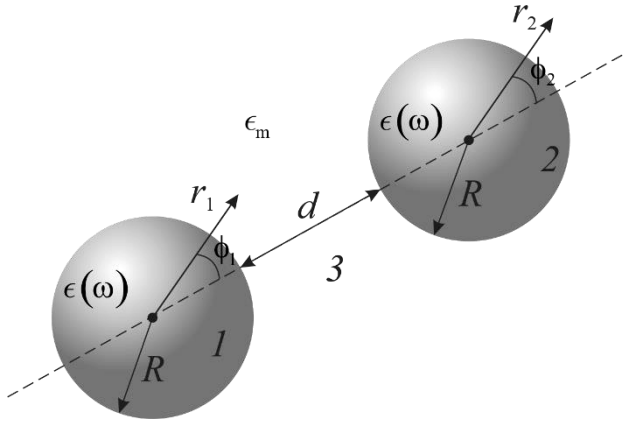


Fig. 1. The geometry of the problem.

The solutions of the equations (1) for the domains 1 and 2 have the form

$$\begin{aligned}\varphi_{1\omega}(\omega, r_1, \phi_1) &= \sqrt{\frac{\pi}{2kr_1}} \sum_{m=-\infty}^{+\infty} C_{1m} I_{m+\frac{1}{2}}(kr_1) e^{im\phi_1}, \\ \varphi_{2\omega}(\omega, r_2, \phi_2) &= \sqrt{\frac{\pi}{2kr_2}} \sum_{m=-\infty}^{+\infty} C_{2m} I_{m+\frac{1}{2}}(kr_2) e^{im\phi_2},\end{aligned}\quad (2)$$

and for the domain 3

$$\begin{aligned}\varphi_{3\omega}(\omega, r_1, \phi_1, r_2, \phi_2) &= \sqrt{\frac{\pi}{2k}} \times \\ &\times \sum_{m=-\infty}^{+\infty} \left( \frac{A_{1m}}{\sqrt{r_1}} K_{m+\frac{1}{2}}(kr_1) e^{im\phi_1} + \right. \\ &\left. + \frac{A_{2m}}{\sqrt{r_2}} K_{m+\frac{1}{2}}(kr_2) e^{im\phi_2} \right),\end{aligned}\quad (3)$$

where  $k$  — the wave number, and the coefficients  $A_{1m}$ ,  $A_{2m}$ ,  $C_{1m}$  and  $C_{2m}$  can be determined from the boundary conditions for the continuity of the potential and of the normal component of the electric displacement vector

$$\begin{aligned}\varphi_{1\omega}|_{r_1=R} &= \varphi_{3\omega}|_{r_1=R}, & \varphi_{2\omega}|_{r_2=R} &= \varphi_{3\omega}|_{r_2=R}; \\ \epsilon(\omega) \frac{\partial \varphi_{1\omega}}{\partial r_1} \Big|_{r_1=R} &= \epsilon_m \frac{\partial \varphi_{3\omega}}{\partial r_1} \Big|_{r_1=R}; \\ \epsilon(\omega) \frac{\partial \varphi_{2\omega}}{\partial r_2} \Big|_{r_2=R} &= \epsilon_m \frac{\partial \varphi_{3\omega}}{\partial r_2} \Big|_{r_2=R}.\end{aligned}\quad (4)$$

Let us use Graf theorem in order to obtain the relation between  $\varphi_{3\omega}$  and one group of the coordinates

$$\begin{aligned}\frac{1}{\sqrt{r_1}} K_{n+\frac{1}{2}}(kr_1) e^{in\phi_1} &= \frac{1}{\sqrt{r_2}} \sum_{m=-\infty}^{+\infty} K_{n+m+1}(kd) I_{m+\frac{1}{2}}(kr_2) e^{im\phi_2}; \\ \frac{1}{\sqrt{r_2}} K_{n+\frac{1}{2}}(kr_2) e^{in\phi_2} &= \frac{1}{\sqrt{r_1}} \sum_{m=-\infty}^{+\infty} K_{n+m+1}(kd) I_{m+\frac{1}{2}}(kr_1) e^{im\phi_1},\end{aligned}\quad (5)$$

and substituting (5) into (2) — (4), we obtain

$$\begin{aligned}C_{1m} I_{m+\frac{1}{2}}(kR) &= A_{1m} K_{m+\frac{1}{2}}(kR) + \\ &+ \sum_{p=-\infty}^{+\infty} A_{2p} K_{p+m+1}(kd) I_{m+\frac{1}{2}}(kR); \\ C_{2m} I_{m+\frac{1}{2}}(kR) &= A_{2m} K_{m+\frac{1}{2}}(kR) + \\ &+ \sum_{p=-\infty}^{+\infty} A_{1p} K_{p+m+1}(kd) I_{m+\frac{1}{2}}(kR);\end{aligned}\quad (6)$$

$$\begin{aligned}\epsilon(\omega) C_{1m} f(kR) &= \\ &= \left\{ A_{1m} g(kR) + f(kR) \sum_{p=-\infty}^{+\infty} A_{2p} K_{p+m+1}(kd) \right\} \epsilon_m; \\ \epsilon(\omega) C_{2m} f(kR) &= \\ &= \left\{ A_{2m} g(kR) + f(kR) \sum_{p=-\infty}^{+\infty} A_{1p} K_{p+m+1}(kd) \right\} \epsilon_m,\end{aligned}$$

where the following designations have been introduced

$$\begin{aligned}f(kR) &= -I_{m+\frac{1}{2}}(kR) + kR \left( I_{m-\frac{1}{2}}(kR) + I_{m+\frac{3}{2}}(kR) \right); \\ g(kR) &= -K_{m+\frac{1}{2}}(kR) - kR \left( K_{m-\frac{1}{2}}(kR) + K_{m+\frac{3}{2}}(kR) \right).\end{aligned}$$

Then we get rid of  $C_{1m}$  and  $C_{2m}$  in the relations (6) and obtain the system of the equations

$$\begin{aligned}A_{1m} + \Delta_{1m} \sum_{p=-\infty}^{+\infty} A_{2p} K_{m+p+1}(kR) &= 0; \\ A_{2m} + \Delta_{2m} \sum_{p=-\infty}^{+\infty} A_{1p} K_{m+p+1}(kR) &= 0,\end{aligned}$$

and the expressions for  $\Delta_{1m} = \Delta_{2m} = \Delta_m$  can be obtained from the system of the equations (6):

$$\begin{aligned}\Delta_m &= (\epsilon(\omega) - \epsilon_m) I_{m+\frac{1}{2}}(kR) f(kR) \times \\ &\times \left\{ \epsilon(\omega) f(kR) K_{m+\frac{1}{2}}(kR) - \epsilon_m g(kR) I_{m+\frac{1}{2}}(kR) \right\}^{-1}.\end{aligned}\quad (7)$$

The expression for the free energy of van der Waals interaction between the spherical nanoparticles can be represented in the form

$$F(d) = k_B T V \sum'_{n=0}^{\infty} \int \frac{d\mathbf{k}}{(2\pi)^3} \ln \det(\hat{\mathbf{I}} - \hat{\mathbf{L}}(i\omega_n, k)), \quad (8)$$

where the integration is performed over the whole spherical  $\mathbf{k}$ -space;  $k_B$  — Boltzmann constant,  $T$  — the temperature,  $V$  — the system volume,  $\hat{\mathbf{I}}$  — the unity operator, and the matrix of the operator  $\hat{\mathbf{L}}$  has the form

$$L_{lm} = \sum_{p=-\infty}^{+\infty} \Delta_{1m}(k, i\omega_n) \Delta_{2p}(k, i\omega_n) K_{m+p+1}(kd) K_{l+p+1}(kd). \quad (9)$$

In order to simplify formula (8) let us use the fact that the distance between the nanoparticles is essentially greater than their radius  $R/d \ll 1$ . As well, the contribution of the domain  $kR \ll 1$  into the integral in the formula (8) is the main. Taking into account the known expressions for the spherical Infeld and Macdonald functions in terms of the elementary functions

$$I_{m-\frac{1}{2}}(z) = \sqrt{\frac{2}{\pi z}} z^m \left( \frac{1}{z} \frac{d}{dz} \right)^m \text{ch } z,$$

$$K_{m-\frac{1}{2}}(z) = \sqrt{\frac{\pi}{2z}} z^m \left( -\frac{1}{z} \frac{d}{dz} \right)^m e^{-z},$$

one can make the conclusion that all terms in the sum (9) except  $L_{00}$  can be neglected, and in the expression

$$\ln \det(\hat{\mathbf{I}} - \hat{\mathbf{L}}) = -\text{Sp} \hat{\mathbf{L}} - \frac{1}{2} \text{Sp}(\hat{\mathbf{L}}^2) - \frac{1}{3} \text{Sp}(\hat{\mathbf{L}}^3) - \dots$$

only the first term is used. In this case from (8) we obtain

$$F(d) = -\frac{k_B TV}{2\pi^2} \sum'_{n=0}^{+\infty} \int dk k^2 \text{Sp} \hat{\mathbf{L}} =$$

$$= -\frac{k_B TV}{2\pi^2} \sum'_{n=0}^{+\infty} \int dk k^2 \Delta_0^2(k, i\omega_n) K_1^2(kd), \quad (10)$$

where in the same approximation

$$\Delta_0(k, i\omega_n) = \frac{(kR)^3 (\epsilon(i\omega_n) - \epsilon_m)}{3\pi (\epsilon(i\omega_n) \frac{(kR)^2}{6} + \epsilon_m (2 + kR))} \quad (11)$$

By substituting (11) into (10), we obtain

$$F(d) = -\frac{k_B TV R^6}{9\pi^4} \sum'_{n=0}^{+\infty} (\epsilon(i\omega_n) - \epsilon_m)^2 \times$$

$$\times \int_0^{+\infty} dk \frac{k^8 K_1^2(kd)}{\left[ \frac{(kR)^2}{6} \epsilon(i\omega_n) + (2 + kR) \epsilon_m \right]^2}. \quad (12)$$

The expression for  $\epsilon(i\omega_n)$  follows from Drude formula, taking into account the substitution  $\omega \rightarrow i\omega_n$ , and has the form

$$\epsilon(\omega_n) = \epsilon(i\omega_n) = \epsilon^\infty + \frac{\omega_p^2}{\omega_n (\omega_n + \gamma_{\text{eff}})}, \quad (13)$$

where  $\omega_p$  – the plasma frequency;  $\gamma_{\text{eff}}$  – an effective relaxation velocity, which takes into account the scattering in the bulk and on the surface of the nanoparticles [12]

$$\gamma_{\text{eff}} = \gamma_{\text{bulk}} + \gamma_s = \gamma_{\text{bulk}} + \mathcal{A} \frac{v_F}{R}, \quad (14)$$

and the effective parameter, which describes the degree of the coherence loss for the spherical nanoparticles, can be represented in the form [13]

$$\mathcal{A} = \frac{1}{4} \left( \frac{\omega_p}{\omega} \right)^2. \quad (15)$$

Since the condition  $k_B T \ll \hbar\omega \ll \hbar c/d$  is satisfied, then the summation in (12) can be replaced by the integration with respect to  $\omega$ . Taking into account the substitution  $k_B T \rightarrow \hbar\omega_p$  and the relations (13) – (15), after the interchange of the integrations we obtain

$$F(d) = -\frac{\hbar\omega_p V R^6}{9\pi^4} \int_0^{+\infty} dk k^8 K_1^2(kd) \times$$

$$\times \int_0^{\omega_p} \frac{d\omega}{\omega} \left[ \frac{(\epsilon(\omega) - \epsilon_m)}{\frac{1}{6} (kR)^2 \epsilon(\omega) + \epsilon_m (2 + kR)} \right]^2. \quad (16)$$

Introducing the new variables of the integration  $x = kd$  and  $y = \omega_p/\omega$ , we obtain the following expression for the free energy of van der Waals interaction

$$F(d) = -\frac{\hbar\omega_p V R^6}{9\pi^4 d^9} \int_0^{+\infty} dx x^8 K_1^2(x) \times$$

$$\times \int_0^{\infty} \frac{dy}{y} \left( \frac{a_3 y^3 + a_2 y^2 + a_1 y + a_0}{b_3 y^3 + b_2 y^2 + b_1 y + b_0} \right)^2, \quad (17)$$

with the following designations

$$a_3 = \frac{1}{4} \frac{v_F}{R} (\epsilon^\infty - \epsilon_m); \quad a_2 = \omega_p;$$

$$a_1 = \gamma_{\text{bulk}} (\epsilon^\infty - \epsilon_m); \quad a_0 = \omega_p (\epsilon^\infty - \epsilon_m);$$

$$b_3 = \frac{1}{4} \frac{v_F}{R} \left[ \frac{1}{6} \frac{R^2}{d^2} x^2 + \epsilon_m \left( 2 + \frac{R}{d} x \right) \right];$$

$$b_2 = \frac{1}{6} \frac{R^2}{d^2} \omega_p x^2; \quad b_1 = \gamma_{\text{bulk}} \left[ \frac{1}{6} \frac{R^2}{d^2} x^2 + \epsilon_m \left( 2 + \frac{R}{d} x \right) \right];$$

$$b_0 = \omega_p \left[ \frac{1}{6} \frac{R^2}{d^2} x^2 + \epsilon_m \left( 2 + \frac{R}{d} x \right) \right].$$

Taking into account the relation between Hamaker constant and the free energy of van der Waals interaction for the spherical bodies [14]

$$F(d) = -\frac{16}{9} \mathcal{A} \frac{R^6}{d^9} V,$$

we obtain the size dependence for this characteristics

$$\mathcal{A}_{\text{H}} = -\frac{\hbar\omega_p}{16\pi^2} \int_0^{+\infty} dx x^8 K_1^2(x) \times \int_0^{\infty} \frac{dy}{y} \left( \frac{a_3 y^3 + a_2 y^2 + a_1 y + a_0}{b_3 y^3 + b_2 y^2 + b_1 y + b_0} \right)^2 \quad (18)$$

Thereafter, the relations (17) and (18) are used for the calculation of the size dependence for the free energy and Hamaker constant in the case when the nanoparticles are of the different metals and the distances between the nanoparticles are different.

### III. THE RESULTS OF THE CALCULATIONS AND THE DISCUSSION

The calculations have been performed for gold nanoparticles, copper nanoparticles and aluminum nanoparticles, which are situated in the air ( $\epsilon_m = 1$ ). The parameters of these materials are given in the table 1.

TABLE 1. PARAMETERS OF METALS [15]

10	Value	11 Metals		
		Al	Cu	Au
	$r_s / a_0$	2.07	2.11	3.01
	$m^* / m_e$	1.06	1.49	0.99
	$\epsilon^\infty$	0.7	12.03	9.84
	$\gamma_{\text{bulk}}, 10^{14} \text{ s}^{-1}$	1.25	0.37	0.35

Before starting the discussion let us make the remark which refers to the integration in the expressions (17) and (18). The inner integrals in these expressions are the improper integrals of the second kind and hence these integrals are divergent if  $y \rightarrow 0$  ("ultraviolet" catastrophe). However, the frequency range  $\omega \in [0, 0.1\omega_p; 10\omega_p]$ , and correspondingly,  $y \in [0, 1; 100]$  is of the physical interest. That is why the integration has been performed in this frequency domain.

The figure 2 shows the size dependences for the free energy of van der Waals interaction and for Hamaker constant in the case of the gold nanoparticles. The distances between the nanoparticles are different. It should be pointed out that the increase of the sizes of the nanoparticle results in the decrease of the value of Hamaker constant due to the increase of the system volume. Moreover, the bigger is the distance between the nanoparticles the more essential is the decrease (fig. 2, a). The energy of the interaction decreases essentially when the distances between the particles are relatively small. When the distances increase, the energy is essentially independent of the size of the particles (fig. 2, b), because the size of the particle is minor in comparison with the distance between them.

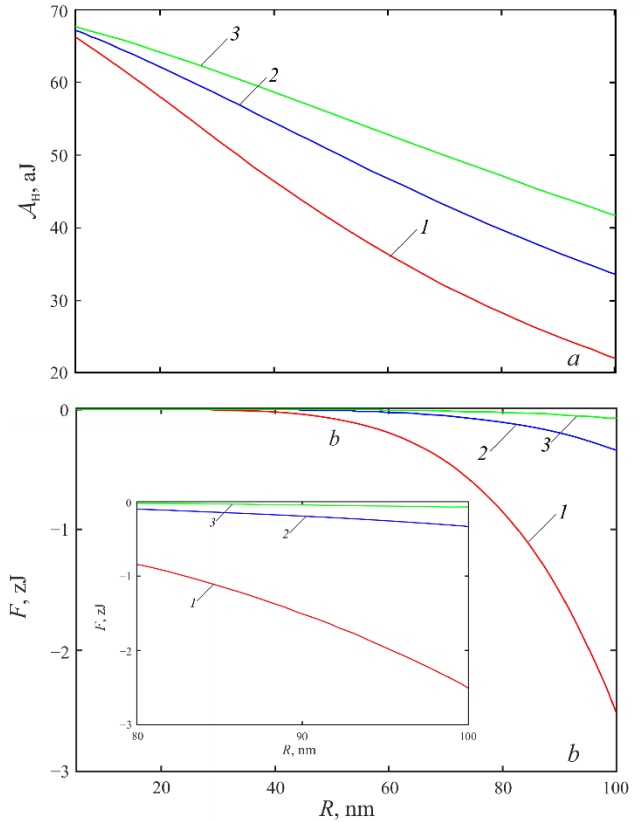


Fig. 2. The size dependences for Hamaker constant (a) and the free energy (b) of the interacting gold nanoparticles the distances between which are different: 1 –  $d = 500$  nm; 2 –  $d = 750$  nm; 3 –  $d = 1000$  nm.

The figure 3 shows the comparison of the calculation results for the different metals in the case when the distance between the nanoparticles is equal to 500 nm. The increase of the sizes of the particles results in the decrease of Hamaker constant and in the decrease of the free energy for all metals (for Au at the  $R > 30$  nm). However, this decrease is minor for all metals except gold. The curves of the size dependences for Hamaker constant for all metals are qualitatively similar (at the  $R > 30$  nm), but the value of Hamaker constant is the greatest for copper nanoparticles in the considered frequency range. Such behavior of the mentioned dependences is connected with the essential differences between the values  $\omega_p$  and  $\gamma_{\text{bulk}}$  for the given metals.

### IV. CONCLUSIONS

The size dependences for Hamaker constant and the free energy of van der Waals interaction between the spherical metallic nanoparticles with regard for two mechanisms of the electron scattering have been obtained. The calculations have been performed in the frequency domain which is of the practical interest.

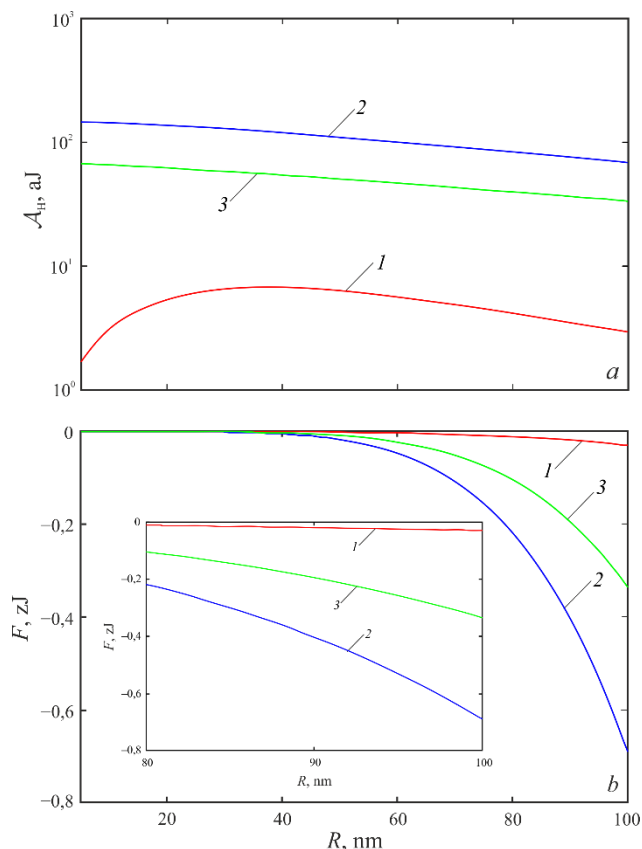


Fig. 3. The size dependences for Hamaker constant (a) and the free energy (b) for the nanoparticles of different metals the distances between which are 500 nm: 1 – Au ; 2 – Cu ; 3– Al .

It is established that the increase of the sizes of the nanoparticle results in the decrease of the value of Hamaker constant due to the increase of the system volume. Besides, the bigger is the distance between the nanoparticles the more essential is the decrease. The free energy decreases essentially when the distances between the interacting gold particles are relatively small. When the distance becomes bigger, the free energy is essentially independent of the size of the particles due to the attenuation of the interaction under the increase of the distance between the nanoparticles.

The increase of the sizes of the particle results in the increase of Hamaker constant and in the decrease of the free energy. This is true for all considered metals. However, this decrease of van der Waals energy is minor for all metals except gold. The value of Hamaker constant is the greatest

for copper nanoparticles in the considered frequency range in the case when the sizes of the interacting nanoparticles are equal. This fact can be explained by the differences in the concentration of the electrons and by the differences in the values of the volume relaxation rate.

#### REFERENCES

- [1] M. Kuno, Introductory Nanoscience: Physical and Chemical Concepts ed S Scholl. New York: Garland Science, Taylor and Francis Group, 2012.
- [2] C. F. Bohren and D. R. Huffman "Absorption and Scattering of Light by Small Particles," Weinheim: Wiley, 2004
- [3] A. O. Pinchuk, G. C. Schatz, A. Reinholdt, and U. Kreibig, Nanotechnol. Res. J. 1 229, 2009.
- [4] B. Faure, G. Salazar-Alvarez, and L. Bergström, "Hamaker constants of iron oxide nanoparticles," Langmuir, 2011, vol. 27, pp. 8659–8664.
- [5] A. O. Pinchuk, "Size-dependent Hamaker constant for silver nanoparticles," J. Phys. Chem. C, 2012, vol. 116, pp. 20099–20102.
- [6] Luo Yaxue, Gao Xiaodan, Tian Rui, and Li J. Hang, "Approach to Estimation of Hamaker Constant as Taking Hofmeister Effects into Account," Phys. Chem. C, Just Accepted Manuscript, April 2018.
- [7] J. N. Israelachvili, and G. E. Adams, "Measurement of forces between two mica surfaces in aqueous electrolyte solutions in the range," pp. 0–1000, nm. J. Chem. Soc., Faraday Trans, 1978, vol. 74, pp. 975–1001.
- [8] S. Das, P. A. Sreeram, and A. K. Raychaudhuri, "A method to quantitatively evaluate the Hamaker constant using the jump-into-contact effect in atomic force microscopy," Nanotechnology, 2007, vol. 18, 035501.
- [9] R. G. Horn, D. R. Clarke, and M. T. Clarkson, "Direct measurement of surface forces between sapphire crystals in aqueous solutions," J. Mater. Res, 1988, vol. 3, pp. 413–416.
- [10] R. D. Rodriguez, E. Lacaze, and J. Jupille, "Probing the probe: AFM tip-profiling via nanotemplates to determine Hamaker constants from phase-distance curves," Ultramicroscopy, 2012, vol. 121, pp. 25–30.
- [11] A. I. Gómez-Merino, F. J. Rubio-Hernández, J. F. Velázquez-Navarro, F. J. Galindo-Rosales, and P. Fortes-Quesada, "The Hamaker constant of anatase aqueous suspensions," J. Colloid Interface Sci, 2007, vol. 316, pp. 451–456.
- [12] U. Kreibig, and M. Volmer, "Optical properties of metal clusters," Berlin: Springer, 1995.
- [13] N. I. Grigorichuk, and P. M. Tomchuk "Optical and transport properties of spheroidal metal nanoparticles with account for the surface effect," Phys. Rev. B 84, 085448, 2011.
- [14] Y. S. Barash, "Van der Waals Forces," Moscow: Nauka, 1988.
- [15] A. V. Korotun, A. A. Koval' and I. N. Titov, "Optical absorption of a composite based on bilayer metal–dielectric spherical nanoparticles," J. Appl. Spectr., vol. 87, no. 2, pp. 240–248, May 2020.

# Modeling of the key characteristics of high-efficiency silicon solar cells with planar surfaces

Anatoly Sachenko\*, Vitaliy Kostylyov\*, Viktor Vlasiuk\*, Igor Sokolovskiy\*, Anatoly Shkrebtiy<sup>†</sup>, Mykhaylo Evstigneev<sup>@</sup>

\* V.E. Lashkaryov Institute of Semiconductor Physics NAS of Ukraine  
41 pr. Nauki, 03028, Kiev, Ukraine E-mail: I.O.Sokolovskiy@gmail.com

<sup>†</sup>Ontario Tech University, 2000 Simcoe St. N., Oshawa, ON, L1G 0C5, Canada  
E-mail: Anatoli.Chkrebtiy@uoit.ca

<sup>@</sup> Department of Physics and Physical Oceanography, Memorial University of Newfoundland  
St. John's, NL, A1B 3X7, Canada E-mail: mevstigneev@mun.ca

**Abstract**—Short-circuit current, open-circuit voltage, and photoconversion efficiency of silicon high-efficiency solar cells (SCs) with all back contact (BCSC) with planar surfaces are calculated theoretically. In addition to the recombination channels usually considered in this kind of modeling, namely, radiative, Auger, Shockley-Read-Hall, and surface recombination, the model also takes into account the nonradiative trap-assisted exciton Auger recombination and recombination in the space-charge region. It is established that these two recombination mechanisms are essential in the SCs-RM in the maximum power regime of operation. The model results are in good agreement with the experimental results from the literature.

**Keywords**— modeling, solar cells, silicon, space-charge region recombination, quantum efficiency

## I. INTRODUCTION

The vast majority of silicon solar cells, used currently, have one or two textured surfaces [1]. This significantly reduces the reflection of light at the air-semiconductor interface. At the same time, non-textured silicon-based SCs are used, in which the reduction of light reflection is achieved by applying antireflection coatings. A special niche is now occupied by silicon SCs with back contact (BCSC). Although they are also mostly textured, the physical basis of

$$\tau_{\text{eff}}(n) = \left[ \frac{1}{\tau_{\text{SRH}}(n)} + \frac{1}{\tau_{\text{exc-Auger}}(n)} + \frac{S_{\text{S0}}}{d} \left( 1 + \frac{\Delta n}{n_0} \right) + \frac{1}{\tau_r(n)} + \frac{1}{\tau_{\text{Auger}}(n)} + \frac{S_{\text{SC}}(n)}{d} \right]^{-1}, \quad (1)$$

where  $n = n_0 + \Delta n$  is the total majority carrier concentration, a sum of the equilibrium,  $n_0$ , and excess,  $\Delta n$ , contributions;  $\tau_{\text{SRH}}$  is Shockley-Read-Hall (SRH) lifetime;  $S_{\text{S0}} \propto n_0$  is the net recombination velocity at the front and rear surfaces at the low injection level;  $\tau_{\text{exc-Auger}}(n) = \tau_{\text{SRH}} n_x / n$  is the exciton Auger recombination time with  $n_x = 8.2 \cdot 10^{15} \text{ cm}^{-3}$  [4];  $\tau_r$  is radiative recombination time, and  $\tau_{\text{Auger}}$  is band-to-band Auger recombination time [5].

SRH lifetime in an n-type base is given by

$$\tau_{\text{SRH}}(n) \cong \frac{\tau_{p0}(n_0 + \Delta n + n_1) + \tau_{n0}(p_1 + \Delta n)}{n_0 + \Delta n}, \quad (2)$$

where  $\tau_{p0} = (C_p N_t)^{-1}$  and  $\tau_{n0} = (C_n N_t)^{-1}$  are electron and hole lifetimes,  $n_1$  and  $p_1$  are the equilibrium electron and hole concentrations in the case when Fermi level coincides with

their operation is somewhat different from those of the traditional SC design [2]. In particular, these SCs must have long lifetimes of nonequilibrium charge carriers ( $\sim 1 \text{ ms}$ ), which brings them closer to traditional highly efficient textured silicon SCs with two-sided contacts. Second, the rate of surface recombination on the illuminated surface in these SCs should be low enough, which also brings them closer to highly efficient textured silicon SCs. A separate issue for these SCs is to describe the intrinsic quantum efficiency of the photocurrent in the long-wavelength absorption region. To date, it has not been studied thoroughly enough.

In this work, a theoretical modeling of the key characteristics of these BCSC is performed, taking into account all known components of the effective lifetime in silicon and the peculiarities of the internal quantum efficiency of photocurrent in the long-wavelength absorption region. The obtained theoretical curves are compared to the experimental work [3], and a good agreement between the theory and the experiment is achieved.

## II. EFFECTIVE RECOMBINATION TIME IN SILICON

The general expression for the effective recombination lifetime in Si with the n-type base has the form

the deep-impurity energy. Depending on the value of the impurity energy, as well as the electron and hole capture cross-sections, SRH lifetime as a function of excess concentration may change between two extreme values and may increase, decrease, or remain constant with  $\Delta n$ . In the following, we will assume that  $\tau_{\text{SRH}} = \text{const}$ .

It is worthwhile to focus on the question why most today's simulations do not take into account non-radiative exciton recombination. In our opinion, the answer is that it is masked by the SRH and surface recombination. Indeed, redefinition of the SRH time as  $\tau_{\text{SRH}}^* = \tau_{\text{SRH}} / (1 + n_0/n_x)$  and the surface recombination velocity as  $S^* = S_0 + (S_0 + dn_0 / (\tau_{\text{SRH}} n_x)) \Delta n / n_0$  renders introduction of the non-radiative exciton Auger recombination unnecessary. Note that for  $n_0 = 4.9 \cdot 10^{15} \text{ cm}^{-3}$ , the value of  $\tau_{\text{SRH}}^*$  is smaller than  $\tau_{\text{SRH}}$  by about 60%. It should also be noted that

an expression for the effective lifetime in Si similar to the formula for  $\tau_{SRH}^*$  was used in some previous work [6] with  $n_x = 7.1 \cdot 10^{15} \text{ cm}^{-3}$ .

The inverse radiative lifetime at  $T = 300 \text{ K}$  is  $1/\tau_r(n) = A(n_0 + \Delta n)$  with the radiative recombination parameter

$$A = \int_0^\infty A(E_{ph}) dE_{ph},$$

$$A(E_{ph}) = \alpha(E_{ph}) \left( \frac{n_r(E_{ph}) E_{ph}}{\pi c \hbar^3 n_i(T)} \right)^2 \exp\left(-\frac{E_{ph}}{kT}\right), \quad (3)$$

where both the absorption coefficient  $\alpha$  and refractive index  $n_r$  depend on the photon energy  $E_{ph}$  as tabulated in [7]. In order to approximately take into account the bandgap narrowing effect [8] by the amount  $\Delta E_g$ , the argument of the absorption coefficient was shifted by the size of bandgap narrowing energy (see [9]), i.e.  $\alpha(E_{ph}) = \alpha_0(E_{ph} + \Delta E_g)$ , where  $\alpha_0$  is the absorption coefficient from [7] at zero bandgap narrowing size.

The space charge region (SCR) recombination velocity is obtained under the assumption that it is due to the recombination centers, uniformly distributed inside a layer of thickness  $w_R$ . They are characterized by the hole capture time  $\tau_R$ , electron-to-hole capture time ratio  $b_R$ , and energy close to the middle of the bandgap. Hence, the SCR recombination velocity is written as

$$S_{SC} = \frac{n_0 + \Delta n}{\tau_R} \int_0^{w_R} \frac{dx}{(n_0 + \Delta n)e^{y(x)} + b_r \Delta n e^{-y(x)}}. \quad (4)$$

Note that we neglected the terms proportional to  $p_0$  and  $n_i$  in the denominator of this expression. The function  $y(x)$  is the electric potential in the semiconductor divided by the thermal voltage  $kT/q$ . The behaviour of the electrostatic potential  $y(x)$  in (4) is determined from the Poisson's equation,  $\frac{d^2 y}{dx^2} = -\frac{q^2}{\epsilon_0 \epsilon_{Si} kT} (\Delta n e^{-y(x)} + n_0 - (n_0 + \Delta n) e^{y(x)})$ , in which  $\epsilon_0$  and  $\epsilon_{Si}$  are vacuum permittivity and relative dielectric constant of Si, respectively. Its solution reads

$$x = \frac{L_D}{\sqrt{2}} \int_{y_0}^y \frac{dz}{\sqrt{(1 + \Delta n/n_0)(e^z - 1) - z + (e^{-z} - 1)p_0/n_0}}, \quad (5)$$

where  $y_0 = y(x=0)$  is the value of the normalized potential on the boundary of the  $p^+$ - and  $n$ -regions and where  $L_D = \frac{1}{q} \sqrt{\frac{\epsilon_0 \epsilon_{Si} kT}{n_0}}$  is Debye screening length in the absence of injection.

To find  $y_0$ , we treat the  $p^+$ -side of the junction within the depletion approximation. Namely, the ionized acceptors on the  $p^+$ -side form a thin space-charge layer of thickness

$$w_p = \frac{1}{q} \sqrt{\frac{2\epsilon_0 \epsilon_{Si} kT}{N_a} \left( \ln \frac{N_a}{p_0 + \Delta n} + y_0 \right)} \quad (6)$$

with the surface charge density  $-qN_a w_p$ , where  $N_a$  is the acceptor concentration in the  $p^+$ -Si. The  $n$ -side of the junction has the positive surface charge density of the same

magnitude. Hence, the electric field in the junction plane is

$$-\frac{qN_a w_p}{\epsilon_0 \epsilon_{Si}} = -\frac{kT}{q} \frac{dy}{dx} \Big|_{x=0}, \text{ allowing us to relate } N_a \text{ to } y_0 \text{ as}$$

$$N_a \left( \ln \frac{N_a}{p_0 + \Delta n} + y_0 \right) = (n_0 + \Delta n)(e^{y_0} - 1) - n_0 y_0 + \Delta n(e^{-y_0} - 1) \quad (7)$$

or, more compactly,  $e^{y_0}(y_0 + b) = \frac{p_0 + \Delta n}{n_0 + N_a}$ ,

$$b = \frac{1}{n_0 + N_a} \left( N_a \ln \frac{N_a}{\Delta n} + (n_0 + \Delta n)(1 - e^{y_0}) + \Delta n \right).$$

This can be re-written in terms of Lambert's function  $W_L(x)$ , defined as a solution of a transcendental equation  $W_L(x)e^{W_L(x)} = x$  as

$$y_0 = W_L \left( \frac{\Delta n}{n_0 + N_a} e^b \right) - b.$$

In the practically relevant case  $N_a \gg n_0$ ,  $\Delta n$ , we have  $y_0 < -1$ , and thus

$$b = \ln \frac{N_a}{\Delta n} + O \left( \frac{n_0 + \Delta n}{N_a} \right).$$

Substitution of this approximation gives a simple expression for the surface potential:

$$y_0 \cong \Omega - b = 0.5671 - \ln(N_a / \Delta n), \quad (8)$$

where  $\Omega = W_L(1) = 0.56714\dots$  is the so-called Omega-constant. The accuracy of the analytic approximation (8) is better than 0.1% for the doping and excess carrier concentration values used in this work. Coming back to the integral (4), it is more convenient to change the integration variables from  $x$  to  $y$  according to (5):

$$S_{SC} = \frac{L_D}{\tau_R \sqrt{2}} \int_{y_0}^{y_R} \frac{dy}{\left( e^y + b_r \frac{\Delta n}{n_0 + \Delta n} e^{-y} \right) \sqrt{\left( 1 + \frac{\Delta n}{n_0} \right) (e^y - 1) - y + \frac{\Delta n}{n_0} (e^{-y} - 1)}} \quad (9)$$

where the upper integration limit  $y_R$  is the solution of (5) at  $x = w_R$ . Calculations of  $S_{SC}$  according to (9) show that in the relevant parameter range, the result practically does not depend on  $N_a$ , as long as for  $N_a \gg \Delta n$ ; hence, the lower integration limit in (9) can be set to  $-\infty$  for all practical purposes.

In the high-efficiency Si SCs, in particular, BCSC, the bulk SRH lifetime can be of the order of, or even exceed, 1 ms. If one assumes that  $\tau_R \sim \tau_{SRH}$ , then (9) predicts  $S_{SC} < 10^{-2} \text{ cm/s}$ , allowing one to neglect surface recombination relative to the remaining recombination mechanisms. However,  $\tau_R$  may be several orders of magnitude smaller than  $\tau_{SRH}$  and have a value of about 1  $\mu\text{s}$ . This suggests, first of all, that the concentration of deep levels in the SCR significantly exceeds the concentration of deep energy levels in the neutral bulk. The reasons may be related to the gettering effect during the high-temperature diffusion stage of the junction production, the presence of boron complexes that increase the concentration of deep levels, high electric field strength in SCR, etc. But as a result, there is a situation when the recombination rate in the SCR of the highly efficient silicon SCs in the maximum power regime becomes comparable with other recombination channels, which leads to the need to take into account recombination in the SCR in SC modeling.

### III. PHOTOCOVERSION PARAMETERS OF BCSC

If the minority carriers' diffusion length  $L_d = \sqrt{D_p \tau_{eff}}$  is much bigger than one-quarter of the base thickness  $d/4$ , and if the combined surface and SCR recombination velocity  $S_{SC} + S_{S0} \ll 2D_p/d$ , then the excess concentration profile is practically uniform in the base region. In that case, one can employ the narrow-base approximation and express the illuminated I-V relation as [8]

$$I(V) = I_L - \frac{qA_{SC}d \Delta n}{\tau_{eff}} + \frac{V - IR_s}{R_{SH}}, \quad (10)$$

where the first term is the light-generated current, the second term is the recombination current,  $A_{SC}$  is the SC area, and  $R_s$  and  $R_{SH}$  are the series and shunt resistance. The excess carrier concentration is related to the applied voltage by a modified acting mass law,

$$(n_0 + \Delta n)(p_0 + \Delta n) = n_i^2 \exp\left(\frac{\Delta E_g + q(V - IR_s)}{kT}\right) \quad (11)$$

where  $n_i$  is the intrinsic concentration at low injection [10], and  $\Delta E_g(n_0, \Delta n)$  is the magnitude of bandgap narrowing in Si [9]. Eq. (11) can be solved for the excess concentration

$$\Delta n = -\frac{n_0}{2} + \sqrt{\frac{n_0^2}{4} + n_i^2 e^{\Delta E_g/kT} \left( e^{q(V-IR_s)/kT} - 1 \right)}. \quad (12)$$

Equations (10)-(12) need to be solved numerically. The photoconversion efficiency  $\eta$ , the voltage,  $V_m$ , current,  $I_m$ , and output power,  $P_m$ , in the maximum-power operation regime are found by setting the derivative of  $P = IV$  with respect to voltage to zero. The open-circuit voltage and the short-circuit current are obtained by setting in (10)  $I$  and  $V$  to zero, respectively.

$$IQE(\lambda) = \frac{\alpha L}{1 - \alpha^2 L^2} \frac{-(S_0 L / D) \left[ (1 - R_d e^{-2\alpha d}) - e^{-\alpha d - d/L} (1 + R_d) \right] + \alpha L (1 - R_d e^{-2\alpha d}) + e^{-\alpha d - d/L} (1 + R_d)}{\cosh(d/L) + (S_0 L / D) \sinh(d/L)} + \frac{\alpha L}{1 - \alpha^2 L^2} \left[ (1 + R_d) + \alpha L (1 - R_d) e^{-\alpha d} \right]. \quad (17)$$

Shown in Fig. 1 is the spectral dependence of  $IQE$  according to (15) (curve 1) and (17) (curves 2-6) for the special case  $R_d = 1$ . As seen in this figure, when  $L = 1$  cm and  $S_0 = 0$ , (15) and (17) yield identical results. Upon decreasing  $L$ , the maximal  $IQE$ -values get smaller (see curves 3 and 6). Likewise, increasing  $S_0$  also results in the smaller  $IQE$  maxima (curves 4 and 5).

Fig. 2 shows the experimental  $EQE(\lambda)$  and  $R(\lambda)$  curves for BCSC from [3], as well as the theoretical approximations (14), (17) for  $d = 300 \mu\text{m}$ ,  $L = 0.17$  cm, and  $S_0 = 3$  cm/s. The value of  $R_d$  was also slightly varied from 0.8 to 1. As seen in the figure, the theoretical  $EQE(\lambda)$  curve agrees with the experimental one very well.

Once  $EQE(\lambda)$  is known, the dependence of the light-generated current on the base thickness  $d$  follows immediately, see (13), allowing us to optimize the SC with respect to the base thickness.

### IV. RESULTS AND DISCUSSION

We first analyze the results obtained in [3] for a BCSC with the photoconversion efficiency of 19.2%. To model its key parameters, it is necessary to determine the

In this approximation, the light-generated current is a fit parameter. On the other hand, it can be found by integrating the incident radiation spectral irradiance  $I(\lambda)$  as

$$J_L = \frac{q}{hc} \int d\lambda \lambda I(\lambda) EQE(\lambda), \quad (13)$$

where  $EQE(\lambda)$  is external quantum efficiency, related to the internal quantum efficiency  $IQE(\lambda)$  and reflection coefficient  $R(\lambda)$  by

$$EQE(\lambda) = f \cdot IQE(\lambda) (1 - R(\lambda)), \quad (14)$$

where the numerical coefficient  $f < 1$  has to do with the fact that part of the incident radiation is absorbed by a coating layer outside of the semiconductor. The simple limit approximation for IQE of SC with specular flat surfaces is

$$IQE(\lambda) = 1 - \exp(-2\alpha(\lambda)d). \quad (15)$$

A more accurate expression can be obtained by solving the stationary diffusion equation for the excess carrier concentration with the boundary conditions

$$j(x=0) = -S_0 \Delta n(x=0), \quad \Delta p(x=d) = 0, \quad (16)$$

where  $S_0$  is the net recombination velocity on the front surface. The solution of this equation is

$$\Delta n = C_1 e^{-\frac{x}{L}} + C_2 e^{\frac{x}{L}} + \frac{\alpha L I_0 / D_p}{1 - (\alpha L)^2} \left[ e^{-\alpha x} + R_d \left( e^{-\alpha x} + e^{\alpha(-2d+x)} \right) \right],$$

where  $R_d$  is the reflection coefficient of the rear surface, and the integration constants  $C_{1,2}$  are to be found from (16). The internal quantum efficiency  $IQE(\lambda) = j(x=d)$  then becomes

recombination parameters  $\tau_R$  and  $b_r$  from the measurements of dark I-V curves. In addition, it is necessary to find the SRH lifetime and surface recombination velocity. Fig. 3 shows the experimental dependences of the dark current density for the SCs studied on the applied voltage at a temperature of 25 °C, while Fig. 4 shows the experimental dependences for the illuminated current density as a function of the applied voltage under the AM1.5 conditions. Finally, Fig. 5 shows the experimental effective and bulk lifetimes on the excess concentration of charge carriers for the freshly formed SCs (before metallization).

The SRH lifetime  $\tau_{SRH}$  can be extracted from the fit of the experimental bulk lifetime vs. excess concentration  $\tau_b(\Delta n)$  curve shown in Fig. 5. Given that its maximum is at  $\Delta n = 10^{15} \text{ cm}^{-3}$ ,  $\tau_{SRH}$  can be found from (18) to be  $2.4 \cdot 10^{-3}$  s. The values of  $\tau_R$  and  $b_r$  are found from fitting the experimental dependences of the dark current vs. voltage curve, whereas  $S_{S0}$  can be found by fitting the I-V curve in the presence of illumination. A good fit is achieved by using the following parameters:  $\tau_R = 6 \cdot 10^{-6}$  s,  $b_r = 0.1$ ,  $S_{S0} = 22$  cm / s. As can be seen from Figs 3 and 4, the theoretical dark and illuminated current-voltage curves agree well with the experimental ones.

With the above parameters, one can also build the theoretical curve of effective life time as a function of  $\Delta n$ ,

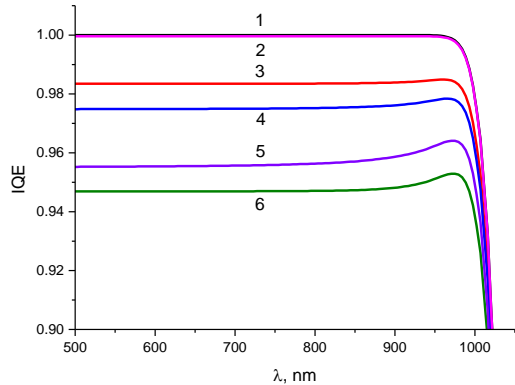


Fig.1. Theoretical spectral dependence of internal quantum efficiency for  $d=300 \mu\text{m}$ ,  $R_s=1$ .  $L$  (in  $\mu\text{m}$ ) and  $S_0$  (in  $\text{cm/s}$ ): 2 -  $10^4$ , 0; 3 - 1640, 0; 4 - 1640, 3; 5 - 1640, 10; 6 - 900, 0.

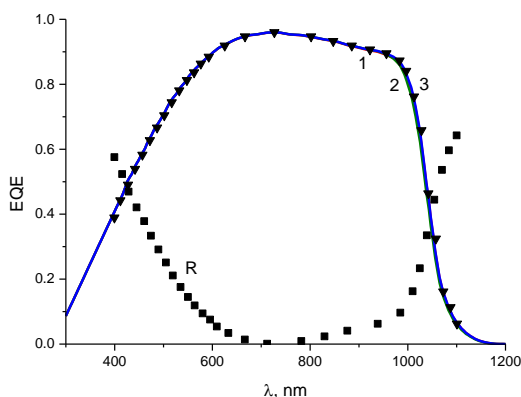


Fig. 2. Experimental spectral dependence of EQE and R (squares).

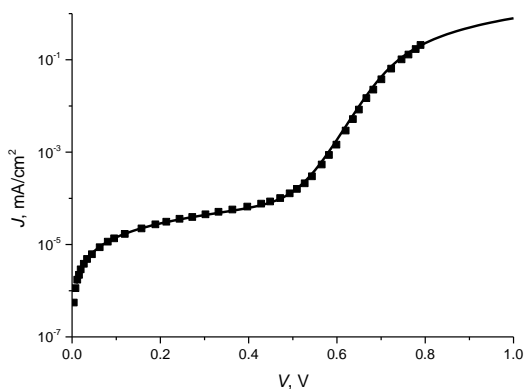


Fig. 3. Experimental (squares) and theoretical (solid line) dark I-V curves.  $R_s$ : 1 for 0.8, 2 for 0.9 and 3 for 1.

shown in Fig. 5. As can be seen from this figure, in the region  $\Delta n < 10^{15} \text{ cm}^{-3}$ , the effective lifetime decreases with decreasing  $\Delta n$ . This decrease is associated with the recombination in SCR. Incidentally, the point of maximum power in this case happens to be  $1.85 \cdot 10^{14} \text{ cm}^{-3}$ , and the effective lifetime at this point is  $5 \cdot 10^{-4} \text{ s}$ .

With the above parameters, the open circuit voltage calculated using the experimental value of the short-circuit current density of  $35 \text{ mA/cm}^2$ , is  $682 \text{ mV}$ , which is completely identical to the experimental value. The calculation of the photoconversion efficiency using the approach described above with the above parameters and the value of the series resistance of  $0.6 \Omega \cdot \text{cm}^2$ , gives a value of

$19.2\%$ , which also coincides with the experimental value. With the theoretical values of  $V_m$  and  $J_m$ , the fill factor equals  $0.804$ , while its experimental value in [3] is  $0.805$ .

In the same way, the key parameters of the other three SCs can be calculated. A comparison of the experimental (see Table 1 of [3]) and theoretical parameter values is given in Table 1.

TABLE 1

NN	1	2	3	4
$V_{OC \text{ exp}}$ , mV	683.2	681.4	682.5	682.0
$V_{OC \text{ theor}}$ , mV	683.2	681.4	682.5	682.0
$FF_{\text{exp}}$ , %	78.2	80.4	79.4	80.5
$FF_{\text{theor}}$ , %	78.2	80.3	79.4	80.4
$\eta_{\text{exp}}$ , %	18.7	19.1	18.9	19.2
$\eta_{\text{theor}}$ , %	18.7	19.1	18.9	19.2
$S_{S0}$ , cm/s	20.2	22.9	21.1	22
$R_{S \text{ exp}}$ , $\Omega \cdot \text{cm}^2$	1.3	0.9	1.1	0.8
$R_{S \text{ theor}}$ , $\Omega \cdot \text{cm}^2$	1.12	0.71	0.73	0.65
$R_{S1 \text{ theor}}$ , $\Omega \cdot \text{cm}^2$	1.02	0.69	0.7	0.63

In addition to the key parameters of SCs, Table 1 shows the value of  $S_{S0}$  and of the series resistance calculated in two approximations. In the first approximation, the  $R_S$  was obtained from fitting the experimental and theoretical photoconversion efficiency curves (see the penultimate column in Table 1). In the second approach (the last column in Table 1), the values of the series resistance were calculated as

$$R_{s1} = \left( 1 - \frac{\eta}{\eta(R_s = 0)} \right) \frac{V_m}{J_m} \equiv \left( 1 - \frac{FF}{FF(R_s = 0)} \right) \frac{V_m}{J_m} . \quad (18)$$

As seen from Table 1, the theoretical values of the key parameters agree with the experimental ones with accuracy of better than  $0.1\%$ , which significantly exceeds the experimental error. With respect to the experimental and calculated series resistance values, the differences are much larger. The smallest discrepancy between the two theoretical methods above is about  $3\%$ . The biggest difference between the theoretical and experimental  $R_S$ -values from Table 1 is about  $40\%$ .

In [3], the method of measuring the series resistance is not explained. Usually, the method of two intensities is used for this purpose. This method does not take into account the corrections associated with the bandgap narrowing, which should lead to an increase in the series resistance value. Note also that expression (21) is approximate, whereas the most accurate value of  $R_S$  is found by fitting the experimental photoconversion efficiency results.

Table 1 also shows the low-signal values of surface recombination velocity  $S_{S0}$  in different SCs. As can be seen from the table, there is a clear correlation between the open-circuit voltage and the values of  $S_{S0}$ : namely, the smaller  $S_{S0}$ , the greater the value of the open-circuit voltage.

Shown in Fig. 6 solid line is the theoretical photoconversion efficiency vs. the base doping level curve for the SCs with an efficiency of  $19.2\%$ . As can be seen from

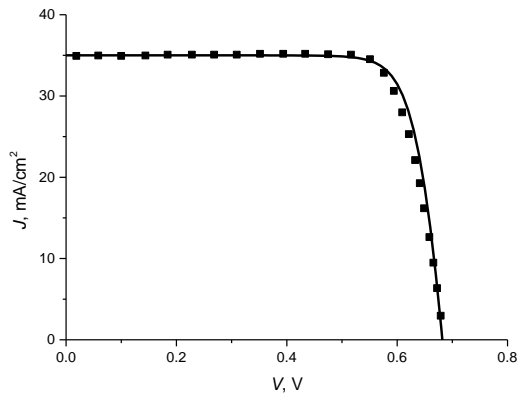


Fig. 4. Experimental (symbols) and theoretical (solid line) illuminated I-V curve.

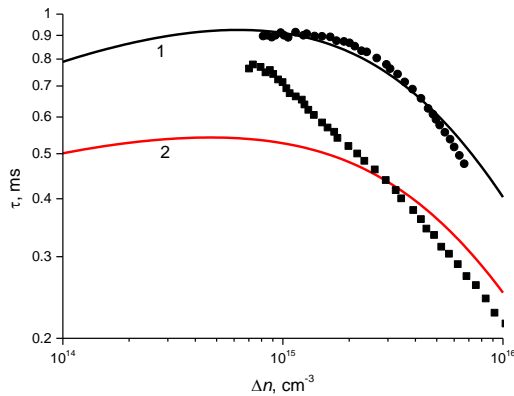


Fig. 5. Experimental (symbols) and theoretical (solid lines) bulk (curve 1) and effective (curve 2) lifetimes vs. excess concentration.

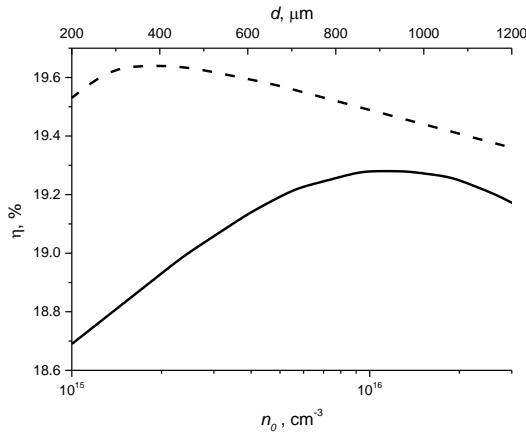


Fig. 6. Theoretical photoconversion efficiency vs. doping level (solid) and base thickness (dash).

the figure, the maximum the photoconversion efficiency of 19.3% is realized at the level of base doping, which is  $1.2 \cdot 10^{16} \text{ cm}^{-3}$ . The efficiency value at  $n_0 = 4.9 \cdot 10^{15} \text{ cm}^{-3}$  is smaller than the maximum efficiency by 1%-rel.

Figure 6 shows also the theoretical dependence of the photoconversion efficiency for SC with  $\eta_{exp} = 19.2\%$  as a function the base thickness (dashed line). As can be seen from the figure, the maximum efficiency occurs at the base thickness of 570  $\mu\text{m}$ . The relative difference between the maximal value and the value at the base thickness of 300  $\mu\text{m}$  is 0.5%.

As the result, the approach developed here, allows both to theoretically describe the key parameters of the high-performance silicon SCs with flat surfaces, and to obtain optimal values of their thickness and doping level.

## V. CONCLUSIONS

The performance of silicon SCs with a flat surface [3] is analyzed within the thin base approximation. It is shown that near the absorption edge, its internal quantum efficiency is described as  $1 - e^{-2\alpha(\lambda)d}$ . The calculations take into account all known recombination mechanisms in silicon, namely, Shockley-Read-Hall recombination, surface recombination, radiative recombination, nonradiative excitonic trap-assisted Auger recombination, and band-to-band Auger recombination. An important parameter is determined: the recombination lifetime in the SCR. It is shown that including the nonradiative exciton recombination into consideration is equivalent to the renormalization of the SRH lifetime. The difference between the true and the effective SRH lifetimes increases with the doping concentration. The proposed approach allowed calculating the key photovoltaic parameters: short-circuit current density, open-circuit voltage, and the fill factor and photoconversion efficiency. A comparison of the theoretical results with the experimental curves for the four SC samples from [1] showed almost perfect agreement and allowed calculating optimal values of the doping level and thicknesses for those SCs.

## REFERENCES

- [1] M.A. Green. Third generation photovoltaics. Advanced solar energy conversion. Springer (2006)
- [2] V. Sachenko, A. P. Gorban, V. P. Kostylyov, A. A. Serba, I. O. Sokolovskyi. Comparative analysis of photoconversion efficiency in the Si solar cells under concentrated illumination for the standard and rear geometries of arrangement of contacts// Semiconductors. - 2007.- Vol.41, No.10.-P. 1214-1223.
- [3] Ngwe Zin, Andrew Blakers, Keith McIntosh, Evan Franklin, Teng Kho, Johnson Wong, Thomas Mueller, Armin G. Aberle, Zhiqiang Feng, and Qiang Huang. 19% Efficient N-Type All-Back-Contact Silicon Wafer Solar Cells With Planar Front Surface. Solar2011, the 49th AuSES Annual Conference 30th November -2nd December 2011.
- [4] Sachenko A.V., Kostylyov V.P., Vlasyuk V.M., Sokolovskyi I.O., and Evstigneev M. The influence of the exciton nonradiative recombination in silicon on the photoconversion efficiency. Proceedings 32 European Photovoltaic Solar Energy Conf. and Exhib., Germany, (20 - 24 June 2016. Munich, Germany) Munich. 2016. P.141-147.
- [5] Richter, S. Glunz, F. Werner, J. Schmidt, and A. Cuevas. Improved quantitative description of Auger recombination in crystalline silicon. Phys. Rev. B 86, 165202:1-14 (2012).
- [6] J.G. Fossum, Solid St. Electron., Computer-aided numerical analysis of silicon solar cells, 19 (4) (1976), pp.269- 277.
- [7] M.A. Green, "Self-consistent optical parameters of intrinsic silicon at 300 K including temperature coefficients. Sol. Energy Mater. Sol. Cells", Sol. Energy Mater. Sol. Cells, vol. 92, pp. 1305-1310 , 2008.
- [8] Sachenko, V. Kostylyov, I. Sokolovskyi, and M. Evstigneev. Effect of Temperature on Limit Photoconversion Efficiency in Silicon Solar Cells.IEEE. Journal of Photovoltaics, 10, 63-69 (2020)
- [9] Schenk, "Finite-temperature full random-phase approximation mode of band gap narrowing for silicon device simulation", J. Appl. Phys., vol. 84, pp. 3684-3695, 1998.
- [10] T. Trupke, M.A. Green, P. Würfel, P. P. Altermatt, A. Wang, J. Zhao, and R. Corkish. Temperature dependence of the radiative recombination coefficient of intrinsic crystalline silicon. J. Appl. Phys. 94, 4930 (2003).

# Modeling of Photovoltaic Converters Based on Nanocrystalline Materials in the Comsol Multiphysics Program

N.N. Chernyshov<sup>1</sup>, A.V. Belousov<sup>2</sup>, A.V. Razinka<sup>2</sup>

<sup>1</sup>Kharkov National University of Radio Electronics. 14 Prospect of Science, Kharkov, 61166, Ukraine.

<sup>2</sup>The Federal State Budget Educational Institution of Higher Education "Belgorod State Technological University named after V.G. Shukhov". 46 Kostyukova Street, Belgorod, 308012, Russian Federation.  
e-mail: nc.chernyshov@gmail.com

**Abstract** - The scientific article demonstrates a computer model of solar cells based on nanocrystalline materials. Calculations of the spectral sensitivity characteristics of various nanocrystalline materials show that the elements made of Si and Ge have a wider sensitivity, since they cover a wide frequency range. Therefore, these materials are used to improve the efficiency and output characteristics of the PVC. When used together, a wide total spectrum of solar radiation is used.

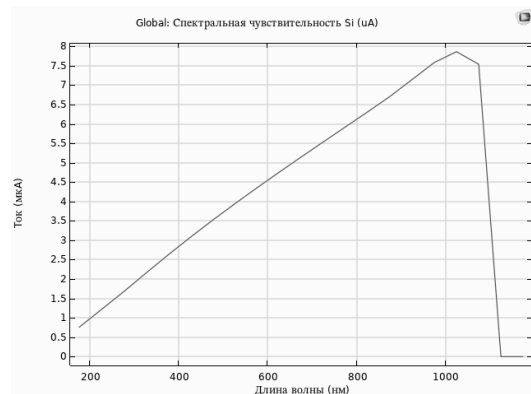
**Keywords** – computer model, nanocrystal line materials, heterostructure, semiconductor photovoltaic converters, spectral sensitivity, solar radiation, charge carrier generation

## I. INTRODUCTION

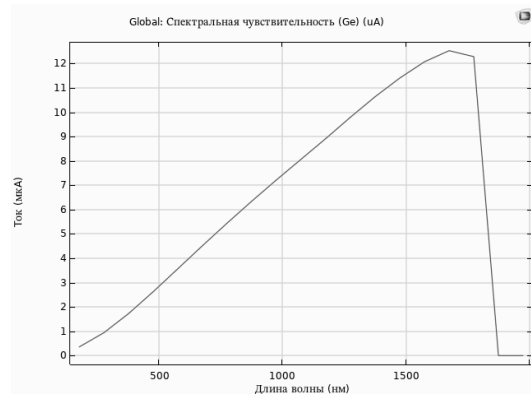
Solar energy is a promising area for research. According to forecasts, by 2020 it will amount to 500-540 GW [1]. The best type of solar energy conversion today is the photovoltaic effect in semiconductor photovoltaic converters (PVC). The theoretical efficiency of solar energy conversion based on a system of heterostructures with a large number of p-n junctions can reach 86%. In a system with three p-n junctions, today it is realistic to achieve an efficiency of 46%; with large-scale production this figure will be 40%. Most often today the silicon PVCs are used, which have the efficiency of 25% in the laboratory and 18% in production [2]. In this regard, it is necessary to pay attention to developing new designs of a generating facility operating on the basis of using renewable energy sources. For this, the criteria and procedure for qualifying power plants operating on the basis of the use of renewable energy sources have been established [3]. COMSOL Multiphysics is a versatile environment for the numerical simulation of systems, devices, and processes for all areas of design, manufacturing and research. In addition to using multiphysics simulation tools for their own projects, the user can turn the developed models into applications for further use by teams of engineers in production departments and test laboratories, as well as by customers. The basic software can be used alone or in any combination with expansion modules for PVC simulation that complement its functionality.

## II. SPECTRAL SENSITIVITY CHARACTERISTICS

This model demonstrates how to use the semiconductor optoelectronics interface in the frequency domain. This interface combines a semiconductor interface with an electromagnetic wave interface, and is suitable for simulating semiconductor devices. This example simulates a simple photodiode [4]. As a result of the simulation, the characteristics of the spectral sensitivity of photocells were constructed (Fig. 1).



a



b

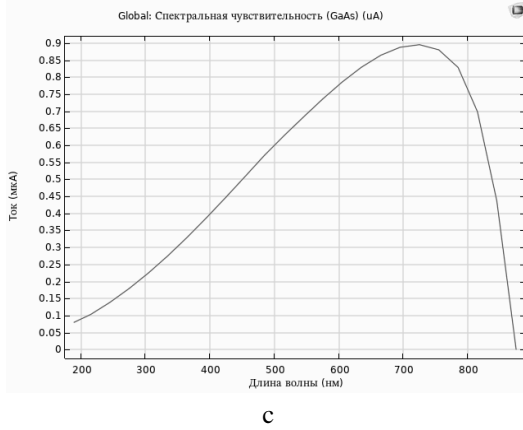


Fig. 1 Spectral sensitivity of the PVC: a-Si, b-Ge, c-GaAs

### III. CALCULATION OF OUTPUT CHARACTERISTICS

Simulation was carried out in the application Si Solar Cell with Ray Optics. This application combines the Ray Optics Module and the Semiconductor Module to illustrate the operation of Si PV cells for a specific date and location. Ray Optics calculates the average illuminance for the date and location selected by the application user. The Semiconductor Module then calculates the rated output with user-specified design parameters. The normalized output is multiplied by the calculated average illumination to obtain the cell output at the specified date and location, assuming a simple linear relationship between output and illumination. The user can then calculate the efficiency of the PVC and the amount of electricity generated during the day. The basic model consists of a 1D silicon PN junction with carrier generation and Shockley-Reed-Hall recombination. The grounded anode is modeled as a thin ohmic contact deposited on the emitter (n-doped region). In the same way, the cathode is modeled as an ideal contact deposited on the side of the base (p-doped region) and connected to an external circuit [5]. An equivalent circuit is shown in Fig. 2.

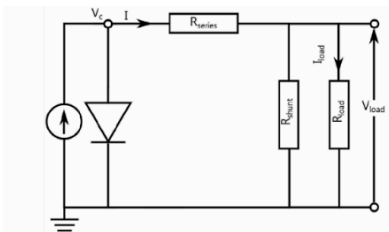


Fig. 2. PVC equivalent circuit

Models of the Sun and FEP are shown in Figure 3-4.

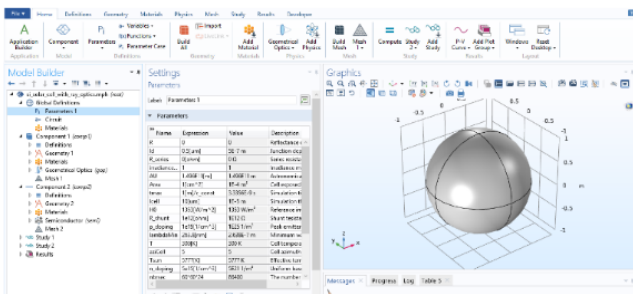


Fig. 3. Model of the Sun in Comsol

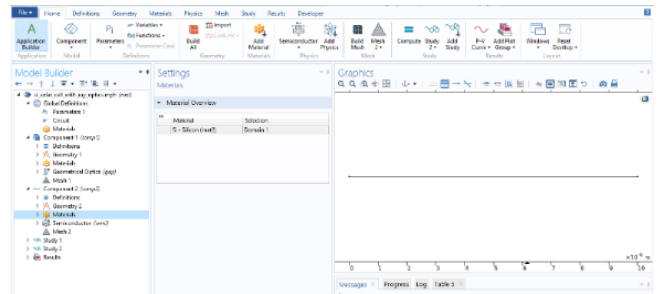


Fig. 4. 1D PVC model in Comsol

### Mathematical model used

The cathode voltage is obtained by solving the circuit equation

$$V_c = IR_{eq}, \quad (1)$$

where  $R_{eq}$  – is the equivalent resistance

$$R_{eq} = \left( \frac{1}{R_{load}} + \frac{1}{R_{shunt}} \right)^{-1} + R_{series}. \quad (2)$$

It is assumed that the transparent anode (emitter side) has an ideal antireflection coating, that is, the reflection coefficient  $R(\lambda)$  is equal to 1.

$$G(z) = \int_0^{\infty} \alpha(\lambda)(1 - R(\lambda))\phi(\lambda) \exp(-i\alpha)z) d\lambda, \quad (3)$$

where  $\alpha(\lambda)$  – is the absorption coefficient, defined as

$$\alpha(\lambda) = \frac{4\pi k(\lambda)}{\lambda}, \quad (4)$$

where  $k(\lambda)$  – is the imaginary part of the refractive index, and  $\phi(\lambda)$  – is the rate of photon generation, defined as

$$\phi(\lambda) = \frac{\lambda}{hc} F(\lambda), \quad (5)$$

where  $F(\lambda)$  – is the spectral radiation (here it is approximated by the spectrum of the Sun's black body at a temperature  $T_{Sun} = 5777K$ )

$$F(\lambda) = \frac{2\pi hc^2}{\lambda^5 \left( \exp\left(\frac{hc}{k_B \lambda T_{Sun}}\right) - 1 \right)}. \quad (6)$$

The absorption of light in the device is modeled using tabular data of the refractive index for silicon as a function of incident wavelength and cell temperature (uniform cell structure). It is assumed here that the characteristic output of the cell is proportional to the power density of the incident light (illumination). Accordingly, we solve the one-dimensional problem only once, using the reference radiation  $H_0 = 1353W/m^2$ . Then we multiply [6] output (current and power) obtained by the model by a multiplication factor, which depends on the orientation of the cell and the position of the Sun at a given location and time of day.

### IV. SIMULATION RESULTS

The position of the Sun is calculated using the Ray Optics module. Sunlight direction is automatically calculated based on latitude, longitude, time zone and time.

The zenith angle  $\theta$  and azimuth angle  $\varphi$  of the Sun are converted to a direction vector in Cartesian coordinates, assuming the north, west, and vertical directions correspond to the  $x, y, z$  directions in the model.

Atmospheric mass. It is the length of the path that light travels through the atmosphere, normalized to the shortest possible path length. Given the curvature of the Earth, atmospheric mass is defined as [7]

$$AM = \frac{1}{\cos(\theta) + 0.50572(96.07995 - \theta)^{-1.6364}}, \quad (7)$$

where  $\theta$  is the zenith angle, defined in the range  $(-\pi/2; +\pi/2)$ .

The angle of incidence is defined as the projection of the cell normal vector onto the direction of the solar unit vector, that is

$$\theta_i = a \cos(n_c n_s), \quad (8)$$

where  $n_c$  is the cell vector and  $n_s$  is the direction of the solar unit vector. The components of these vectors can be expressed in terms of the zenith and azimuth angles. For example, the vector of the solar unit is expressed as a component

$$\begin{cases} n_{sx} = -\cos(\varphi) \sin(\theta); \\ n_{sy} = \sin(\varphi) \cos(\theta); \\ n_{sz} = -\cos(\theta). \end{cases} \quad (9)$$

Direct radiation the intensity of the direct component of sunlight during each day can be determined using two different models:

- Outside the Earth's atmosphere (depending on the distance to the Sun);
- On the Earth's surface from the air mass model.

In the distance model, the Sun is modeled as a spherical black body at a temperature  $T_{Sun} = 5777 K$ . Solar radiation at a distance  $D$  from a spherical source of radius  $R_{Sun}$  is calculated using the surface ratio

$$H_d = \frac{R_{Sun}^2}{D^2} H_{Sun} \cos(\theta_i), \quad (10)$$

where  $H_{Sun}$  is obtained from the Stefan-Boltzmann black body equation, that is

$$H_{Sun} = \sigma T_{Sun}^4, \quad (11)$$

where  $\sigma = 5.6703 \cdot 10^{-8} \frac{W}{m^2 K^4}$  is the Stefan-Boltzmann constant.

For the air mass model, the direct intensity as a function of air mass is obtained from the experimentally determined equation [8]

$$H_d = H_0 \left( (1 - 0.14h) 0.7^{AM^{0.678}} + 0.14h \right) \cos(\theta_i), \quad (12)$$

where  $h$  is the height above sea level, m. Curves I-V and P-V. These curves are obtained by changing the  $R_{load}$  from very low values (repeating short circuit conditions) to very high values (repeating open circuit conditions).  $I_{sc}, V_{oc}, P_{max}, I_{mp}, V_{mp}$

The efficiency of a PVC is defined as the fraction of incident energy that is converted into electricity and is defined as

$$\eta = \frac{I_{sc} V_{oc} FF}{P_{in} V_{oc}}, \quad (13)$$

where  $P_{in}$  is defined as

$$P_{in} = H_0 A, \quad (14)$$

where  $A$  is the area of the PVC.

Generation per item in one day. This value is obtained by integrating the product of the efficiency and the incident power over the 24-hour period of a given day. Result in units of W [8].

The location field contains the geographical coordinates of Kharkov. The date of June 21, 2020 is chosen as the day on which the Sun rises above all over the horizon. The orientation of the PVC is chosen so that the angle of incidence of the sun's rays relative to its surface when the Sun is at its zenith is  $90^\circ$ . Since the Sun rises on this day about  $60^\circ$  above the horizon [9], the angle of inclination of the PVC will be equal to  $30^\circ$ , based on the conditions described above. Any astronomical object culminates in the south, including the Sun, so the azimuthal angle of the PVC is  $180^\circ$ . All of the above parameters are shown in Fig. 5.

Fig. 5. Model Parameters in Si PVC with Ray Optics

Sunlight Properties	Cell Properties
Cell's azimuth angle:	180 °
Cell's tilt angle:	30 °
Simulation thickness:	10 um
Junction depth:	0.5 um
Cell exposed surface area:	1 cm <sup>2</sup>
Cell temperature:	300 K
Series resistance:	0 ohm
Shunt resistance:	1e12 ohm
Uniform base doping, n-type:	5e15 1/cm <sup>3</sup>
Peak emitter doping, p-type:	1e19 1/cm <sup>3</sup>

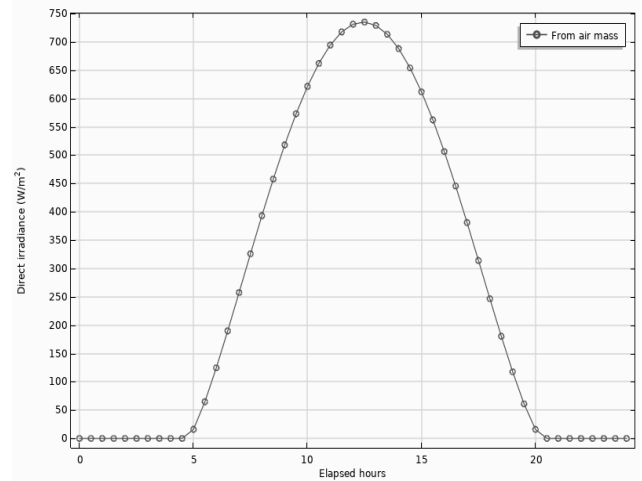


Fig. 8. Direct solar radiation

The calculation results are shown in Fig. 6-9.

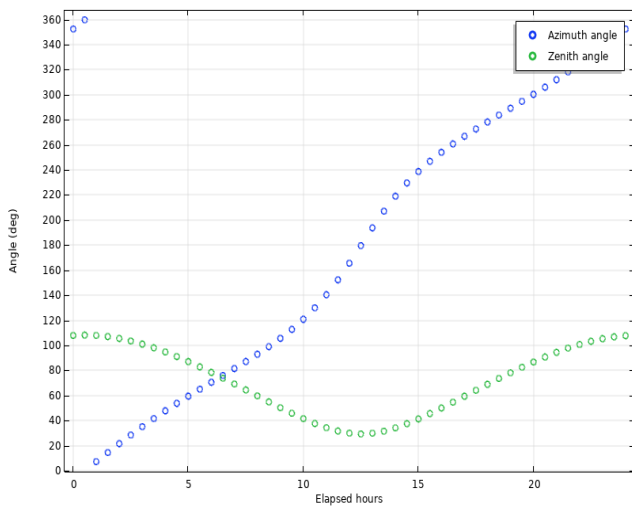


Fig. 6. Sun position during the day

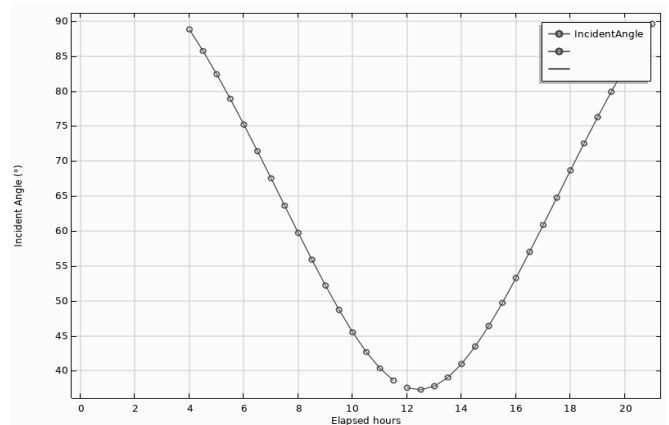


Fig. 9. The angle of incidence of sun rays

The calculation results for Si PVC are shown in Fig. 10-12.

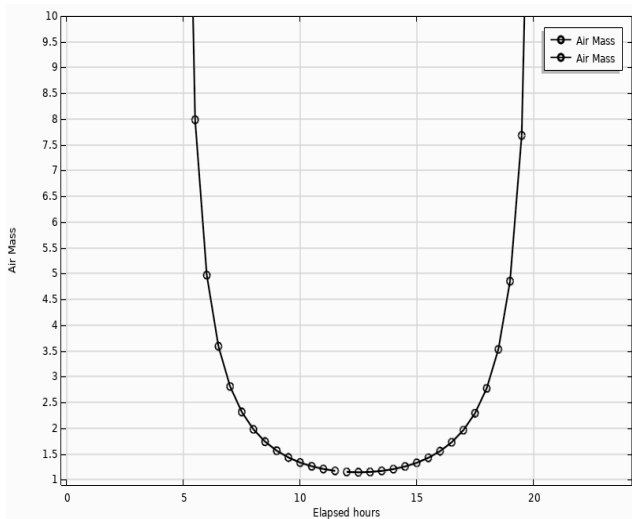


Fig. 7. The indicator of atmospheric influence on the intensity of solar radiation reaching the Earth's surface (atmospheric mass, AM)

Sunlight related results:		
Day of the year:	173	day
Air mass at noon:	1.14	1
Irradiance at noon:	925.9	W/m <sup>2</sup>
Cell related results:		
Generation per cell for the Day:	50.41	mW-h
Fill factor	0.8676	1
Efficiency	6.911	%
Select Hour of the Day:	0:00 AM	
Isc	0	mA
Voc	0	V

Fig. 10. Results of calculations of Si PVC

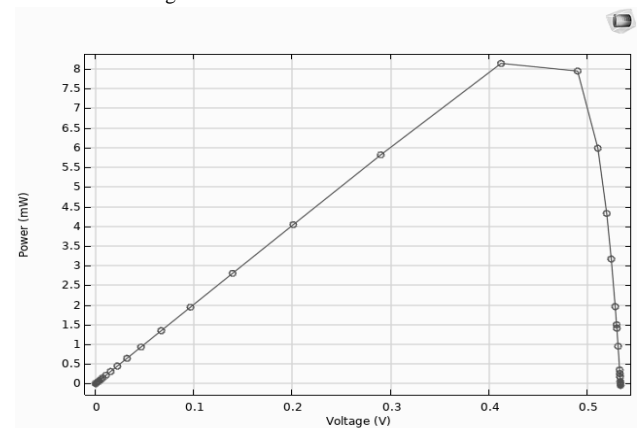


Fig. 11. Volt-watt characteristics of Si PVC

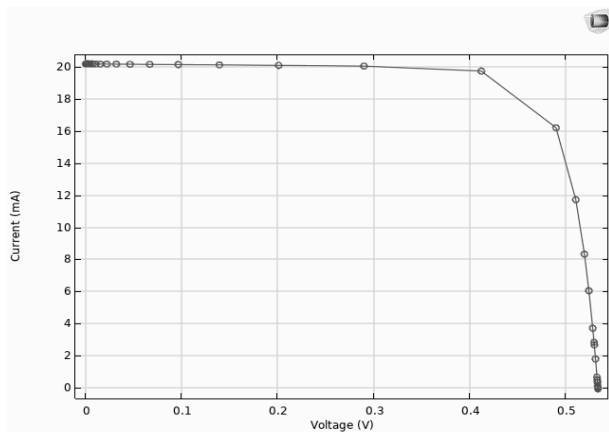


Fig. 12. Current-voltage characteristics of Si PVC

### V. CONCLUSIONS

From the calculations of the spectral sensitivity characteristics, it can be seen that the Si and Ge elements have a wider sensitivity, since they cover a wider frequency range; therefore they are used to calculate the efficiency and output characteristics of the PVC. It can be seen that the GaAs element has a larger bias towards the mid-frequency range, the InP element towards the ultraviolet range, and the

Ge element towards the infrared range. Therefore, they have found a narrower application in PVCs, as the components that absorb the individual spectra of solar radiation. When used together, they allow the use of a wide total spectrum of solar radiation.

### REFERENCES

- [1] Joar Johansaon. Modelling and simulation of CIGS solar cell modules. Master thesis. 2007.
- [2] GaAs PIN Photodiode.: [www.comsol.ru](http://www.comsol.ru).URL: [https://www.comsol.ru/model/download/662261/models.semicond.gaas\\_pin\\_photodiode.pdf](https://www.comsol.ru/model/download/662261/models.semicond.gaas_pin_photodiode.pdf).
- [3] Si Solar Cell with Ray Optics.: [www.comsol.ru](http://www.comsol.ru).URL:[https://www.comsol.ru/model/download/558491/applications.si\\_solar\\_cell\\_with\\_ray\\_optics.pdf](https://www.comsol.ru/model/download/558491/applications.si_solar_cell_with_ray_optics.pdf).
- [4] Stellarium: [www.stellarium-web.org](http://www.stellarium-web.org).URL: <https://stellarium-web.org>.
- [5] Performances improvement of maximum power point tracking perturb and observe method: [www.actapress.com](http://www.actapress.com). URL: <http://www.actapress.com>.
- [6] Evaluation of Micro Controller Based Maximum Power Point Tracking Methods Using dspace Platform: [www.itee.uq.edu.au](http://www.itee.uq.edu.au) / URL: <http://www.itee.uq.edu.au/~aupec/aupec06/htdocs/content/pdf/165.pdf>.
- [7] MPPT algorithms: [www.powerelectronics.com](http://www.powerelectronics.com) / URL: <http://www.powerelectronics.com/discrete-power-semis>.
- [8] Efram, Comparison of Photovoltaic Array Maximum Power Point Tracking Techniques: Efram, Trishan; P.L. Chapman – 2007 – pp. 437.
- [9] Chernyshov N.N., Belousov A.V., Alkhaldeh M., Rogozin I.V. Using physical processes in semiconductor material for photoelectric energy conversion in the educational process of electric power specialties // International Scientific – Practical Conference / Information innovative technologies. Prague (CH), 2018. – pp.210-214.

## TABLE OF CONTENTS

<b>NANOELECTRONIC SENSORS AND INFORMATION SYSTEMS. NANOELECTRONIC SENSORS FOR BIO-ENGINEERING</b>	<b>5</b>
Chichkov Boris, Muzyka Kateryna, Slipchenko Mykola, Slipchenko Olena, Vasytkovskyi Volodymyr, Zholudov Yuriy <b>RECENT RESEARCH ADVANCES OF USAGE OF LASER-FABRICATED NANOMATERIALS IN ELECTROANALYTICAL TECHNIQUES</b>	<b>6</b>
A.V. Borisov, S.N. Osinov, V.F. Zavorotnyi <b>RADIATION DETECTOR BASED ON THE SYMMETRIC SILICON STRUCTURE</b>	<b>10</b>
B.N. Chichkov, N.I. Slipchenko, V.G. Udovitskiy, P.V. Turbin, A.Yu. Kropotov, E.V. Slipchenko <b>CARBON NANOTUBE BASED NANOBIOSENSORS FOR THE DETECTION OF VIRUSES: ACHIEVEMENTS AND PROSPECTS</b>	<b>14</b>
Yuriy Zholudov, Ali Salman Aljebur, Dmytro Snizhko, Guobao Xu <b>ELECTROCHEMILUMINESCENT DETECTION OF TRYPTOPHAN AMINOACID</b>	<b>16</b>
Dmytro Snizhko, Yuriy Zholudov, Iaroslav Gnilitskiy, Alexander Kuznetsov, Guobao Xu <b>CARBON NANOTUBE ELECTRODES FOR NANOELECTROCHEMICAL SENSORS</b>	<b>20</b>
V.N. Borschev, A.M. Listratenko, A.V. Kravchenko, A.V. Syddia, N.I. Slipchenko, B.N. Chichkov <b>NANOMATERIALS IN OPTICAL AND OPTICAL-ELECTRONIC INSTRUMENT</b>	<b>23</b>
Nikolaenko V. A. <b>SHORT REVIEW OF FEATURES A LOW DIMENSIONAL ELECTRON SYSTEMS ON HELIUM LAYERS AT EXPERIMENTAL STUDY. POSSIBLE APPLICATIONS</b>	<b>28</b>
Volodymyr Hryha, Taras Benko, Igor Kogut, Oksana Dolishnyak <b>RECURSIVE DEVICES OF BINARY DATA SORTING DEVICES</b>	<b>33</b>
<b>METHODS OF FORMATION, DIAGNOSIS, AND RESEARCH OF NANOSTRUCTURES AND NANO-OBJECTS INCLUDING BIOLOGICAL</b>	<b>36</b>
Yaroslav Lepikh, Vitalii Borshchak, Nina Sadova, Nataliya Zatovskaya <b>BiO<sub>2</sub> AND RuO<sub>2</sub> BASED NANOCOMPOSITES FOR HYBRID INTEGRATED CIRCUITS</b>	<b>37</b>
Alexander Sorokin, Irina Ropakova, Roman Grynyov, Irina Bespalova, Svetlana Yefimova, Yuri Malyukin <b>FORMATION OF CYANINE DYES J-AGGREGATES IN THIN POLYMER FILMS</b>	<b>40</b>
Yevhenii Antonenko, Sergey Berdnik, Victor Katrich, Mikhail Nesterenko, Yuriy Penkin, Sergey Shulga <b>ESTIMATION OF WAVE PRESSURE ON SCATTERING CARBON NANOTUBES IN THZ RANGE</b>	<b>44</b>
A. Pogodin, I. Shender, S. Bereznyuk, M. Filep, O. Kokhan, I. Studenyak <b>ELECTRICAL CONDUCTIVITY OF (Cu<sub>1-x</sub>Ag<sub>x</sub>)<sub>7</sub>Si<sub>5</sub>I-BASED CERAMICS PREPARED FROM NANOPOWDERS</b>	<b>48</b>
M. Pop, M. Kranjčec, A. Bendak, A. Solomon, L. Suslikov, I. Studenyak <b>OPTICAL PROPERTIES OF X-RAY IRRADIATED (Ga<sub>0.1</sub>In<sub>0.9</sub>)<sub>2</sub>Se<sub>3</sub> THIN FILMS</b>	<b>52</b>

Tatiana Panchenko, Ludmila Karpova <b>EFFECT OF ANNEALING ON THE SURFACE PHOTOCONDUCTIVITY OF SILICOSILLENITE CRYSTALS</b>	<b>55</b>
Valentine Panarin, Nikolay Svavilny <b>CARBON NANOTUBES GROWN ON THE SURFACE OF TITANIUM ALLOY, FROM THE C<sub>2</sub>H<sub>2</sub> ATMOSPHERE, AT THE EQUIPMENT OF ION-PLASMA DEPOSITION</b>	<b>58</b>
Zaitseva N.V., Zakharov S.M., S. Kedrovskiy, Shmatko O.A., Shmatko I.O. <b>THE EFFECT OF VIBRATION PROCESSING ON THE TIN ELECTROSPARK COATING ON STEEL WITH NANOSTRUCTURED COMPONENTS</b>	<b>62</b>
Andrii Korotun, Nazar Pavlishche, Vitalii Reva, Igor Titov <b>THE OPTICAL PROPERTIES OF THE HYPERBOLIC METAMATERIALS WITH THE WHISKERS</b>	<b>64</b>
Andrii Korotun, Yan Karandas <b>MORE ON THE SIZE EFFECTS OF POLARIZABILITY OF THE SINGLE-WALL ACHIRAL CARBON NANOTUBES</b>	<b>69</b>
Mykola Kulish, Vitaliy Kostylyov, Anatoly Sachenko, Igor Sokolovskiy, Anatoly Shkrebti <b>LUMINESCENT SOLAR CONCENTRATOR: PHOTON TRANSPORT EFFICIENCY</b>	<b>74</b>
Ievgen Brytavskiy, Yaroslav Lepikh, Valentyn Smyntyna, Martin Heilmann, João Marcelo Lopes <b>DIELECTRIC PROPERTIES OF HEXAGONAL BORON NITRIDE NANOLAYERS</b>	<b>77</b>
V.A. Smyntyna, V.M. Skobeeva, K.A. Verheles, N.V. Malushin <b>EFFECT OF THE ACID-BASE COMPOSITION OF THE MEDIUM ON THE PHOTOLUMINESCENCE SPECTRUM OF CdS QDs</b>	<b>80</b>
Andrii Korotun <b>THE EFFECT OF DIELECTRIC ON THE POLARIZABILITY OF THE TWO-LAYER METAL-DIELECTRIC SEMISPHERE ON THE SUBSTRATE</b>	<b>83</b>
I.N. Bondarenko, V.A. Nikolaenko <b>THE HF-LF MINILAB FOR ANALYSING DIELECTRIC AND SEMICONDUCTOR MATTER WITH THE TUNNEL DIODES AND CORBINO-ELECTRODES IN RESONATOR</b>	<b>88</b>
Grigorii Milenin, Roman Redko <b>TRANSFORMATION OF DEFECTS IN THE NEAR-SURFACE LAYERS OF SEMICONDUCTOR STRUCTURES CAUSED BY ELECTRORESONANCE AND MAGNETIC RESONANCE PHENOMENA</b>	<b>92</b>
<b>MATHEMATICAL MODELING AND TECHNOLOGIES IN NANO-ELECTRONICS</b>	<b>94</b>
Yu.Ye. Gordienko, M.I. Slipchenko, I.M. Shcherban <b>NUMERICAL SIMULATION OF THE FIELD DISTRIBUTION OF A RESONATOR COAXIAL PROBE FOR SCANNING MICROWAVE MICROSCOPY</b>	<b>95</b>
Mayboroda D.V., Pogarsky S.A. <b>SIMULATION OF PARAMETERS OF FREQUENCY SELECTIVE SURFACE IN MICROWAVE BAND</b>	<b>99</b>

Aleksandr Galat, Aleksandr Sliusarenko <b>PROBLEMS OF SOLAR CELL SIMULATION</b>	<b>102</b>
Denis Grankin, Viktor Grankin <b>MODEL OF THE GROWTH MECHANISM OF WHISKER NANOCRYSTALS WITH THE PARTICIPATION OF HOT ADATOMS</b>	<b>105</b>
Aleksandr Tyurin, Sergei Zhukov, Aleksandr Bekshaev <b>MECHANISM OF THE DYE "SELF-DESENSITIZATION" EFFECT UPON EXCITATION OF ITS AGGREGATED STATES</b>	<b>108</b>
Nina Smirnova, Andrii Korotun, Valentina Tretiak, Igor Titov <b>THE SIZE EFFECTS IN VAN DER WAALS INTERACTION BETWEEN THE SPHERICAL METALLIC NANOPARTICLES</b>	<b>112</b>
Anatoly Sachenko, Vitaliy Kostilyov, Viktor Vlasiuk, Igor Sokolovskyi, Anatoly Shkrebtii, Mykhaylo Evstigneev <b>MODELING OF THE KEY CHARACTERISTICS OF HIGH-EFFICIENCY SILICON SOLAR CELLS WITH PLANAR SURFACES</b>	<b>117</b>
N.N. Chernyshov, A.V. Belousov, A.V. Razinka <b>MODELING OF PHOTOVOLTAIC CONVERTERS BASED ON NANOCRYSTALLINE MATERIALS IN THE COMSOL MULTIPHYSICS PROGRAM</b>	<b>122</b>

**Collection of scientific works**

**XI INTERNATIONAL SCIENTIFIC CONFERENCE**

# **Functional Basis of Nanoelectronics**

Responsible for the release of materials: Mykola Slipchenko, Volodymyr Vasylykovskiy

Collection materials are published in the author's version without  
editing

Format 60x84/8. A paper is offset. Garniture of Times New.  
Conditionally printed sheets 15,11. Drawing 60 things. Order 1123/20.

It is printed from prepared original iv in the printing-house of FOP Azamaev V.R.  
Testifying to state registration of V02 № 229278 from 25.11.1998.  
Testifying is to bringing of subject of publishing business in the state register of publishers,  
manufacturers and spreaders of publishing products. Series of HK № 135 from 23.02.05.  
City Kharkiv, street Poznanska 6, k. 84, tel. +7 (057) 78-17-137  
e-mail:bookfabrik@mail.ua